High-Pressure Vibrational Spectroscopic and Crystallographic Investigations of the N_2-Ar and N_2-Kr Binary Systems

Shawna Miles

Thesis submitted to the
Faculty of Graduate and Postdoctoral Studies
In partial fulfillment of the requirements for the degree of
M. Sc. in Physics

Department of Physics
Faculty of Science
University of Ottawa

Abstract

In this work, the phase behavior of binary systems comprising nitrogen and a noble element (nitrogen + argon and nitrogen + krypton) was studied at high density in the condensed state. Following the work of Lotz *et al.*[2001], the main goal of this work was to further investigate the pressure-concentration phase diagram as well as to look for the possible formation of van der Waals compounds at elevated pressures and room temperature and study their physical properties, using both vibrational spectroscopy and X-ray diffraction. The observed phases, formed by single atoms and/or simple molecules in the binary systems were solved and modeled for their corresponding crystalline structures. From experimental results, lattice parameters for all crystalline structures and phase transitions, if detected, have been observed to shift with respect to that of the pure substances. The analyses and characterization of these binary systems are discussed in detail.

Statement of Originality

To the best of my knowledge, I certify that the research presented in this thesis is the original work of the author. Any contributions to this work made by others with whom I have worked are expressly indicated and acknowledged in the text.

X-ray diffraction and Raman spectroscopic measurements on the sample *NAr1xx* were made by Catherine Aldous. X-ray diffraction measurements on the sample *NAr7xx* were performed by Prof. Serge Desgreniers.

Acknowledgements

I would like to express my gratitude to my supervisor, Prof. Serge Desgreniers, for giving me the opportunity to work in such a fascinating field of study. His guidance, understanding and patience these past couple of years have helped me to become a better physicist and have made my graduate experience rewarding. It will be a time in my life that I will never forget.

I would like to thank Dr. Ning Chen, Dr. Chang-Yong Kim and Dr. Weifeng Chen, Hard X-ray MicroAnalysis beamline scientists at the Canadian Light Source for their help in carrying out X-ray diffraction experiments, as well as Dr. Robert Gordon (formerly) at the CLS@APS (Sector 20) at the Advanced Photon Source. I would also like to acknowledge the financial support of the Canadian Light Source through the CLS Graduate and Post-Doctoral Student Travel Support Program.

I thank my fellow colleagues at the Laboratoire de physique des solides denses (*LPSD*): Akio Yoshinaka, who always found time to help me whenever I asked; Dominique Laniel for helping to train me in the lab and even though he is an ocean's distance away at present, has always informed me that he is only an email away. Last, but certainly not the least, I would like to genuinely thank Laurent Gagné-Dumais for his friendship and support. No matter how many times, or the time of day, that I asked for his advice, he has always been happy to help. I am grateful for that!

I would also like to thank my family for all of their love and support throughout my life. It pushed me to be the best that I could be. Above all, I thank God for giving me strength and perseverance during my graduate studies.

Table of Contents

List of Figures

List of Tables

Nomenclature

A	constant in the ruby luminescence empirical calibration scale
α	diameter ratio
APS	Advanced Photon Source
Ar	argon
B	constant in the ruby luminescence empirical calibration scale
c	speed of light
c	the number of components in a system (Gibb's phase rule)
cg	cubic gauche
CLS	Canadian Light Source
d	spacing between lattice planes
DAC	diamond anvil cell
EOS	equation of state
ε	Lennard-Jones parameter
f	the number of variables that can be independently changed (Gibb's phase rule)
FCC	face-centered cubic
F_{hkl}	structure factor
f_n	scattering factor of the n^{th} atom
FWHM	full width at half maximum
GPa	gigapascal
h	Planck's constant
HCP	hexagonal close-packed
hkl	Miller indices
HXMA	Hard X-ray MicroAnalysis

I_{hkl}	intensity of the (*hkl*) diffraction peak
K_o	bulk modulus
K_o'	pressure derivative of bulk modulus
Kr	krypton
λ	wavelength
λ_0	wavelength at ambient pressure
LP	layered polymeric
LPSD	Laboratoire de physique des denses
N	number of atoms within a molecule
N_2	molecular nitrogen
N_2-Ar	nitrogen + argon binary system
N_2-Kr	nitrogen + krypton binary system
NAr	nitrogen + argon binary system
NKr	nitrogen + krypton binary system
P	pressure
p	the number of thermodynamically stable phases for a system (Gibb's phase rule)
PN	polymeric nitrogen
pXRD	powder x-ray diffraction
r	distance between two particles
R_{wp}	weighted-profile factor
σ	Lennard-Jones parameter
S_y	residual function to be minimized via the Rietveld method
T	temperature
T*c*	critical temperature
θ	angle of incidence/reflection

V	volume
V_0	initial volume (ambient pressure volume)
vdW	van der Waals
w_i	weighting factor
x	nitrogen mole fraction
XRD	x-ray diffraction
XRDA	x-ray diffraction analysis program
y_i(calc)	intensities of the calculated diffraction pattern
y_i(obs)	intensities of the experimental diffraction pattern

Chapter 1
INTRODUCTION

Simple binary mixtures are model systems for studying phase behavior and mutual solubility in solids. Nitrogen (N_2) is the seventh most abundant element in the universe, makes up about 78 % of the air we breathe and represents an ideal component for such studies. Pure N_2 has been extensively studied and has had a considerable theoretical background. The N_2 molecule has a nearly spherical shape and, when paired with another simple molecule or atom such as that of a noble gas element (Ar, Kr, etc.), forms a mixture that resembles a hard-sphere binary system. Understanding the effects a second component has on the pure system, the corresponding structures that may evolve and the properties of the mixed system can aid in endeavors such as developing more accurate planetary models which are currently based on low pressure behavior. In addition, new beneficial materials may be created and better methods designed for shifting certain properties to a more practical region of the phase diagram.

Phase diagrams summarize the effect of temperature, pressure and concentration on a substance or a mixture. Every point on the phase diagram represents a possible combination of thermodynamic conditions for the system. A phase will have characteristic physical and chemical properties and will have the lowest possible energy for the specified thermodynamic conditions. When a variable is changed, such as increasing pressure or adding various concentrations of a second component, it can have a significant impact on the phase diagram of mixed components. A state of lower energy might be more preferential, phase transitions and possibly new phases will be observed. Mixing systems can alter the phase diagram of the pure components. Phase transitions may be shifted or

non-existent and new phases might be observed. Studies on simple binary systems have detected the formation of weakly bound stoichiometric solids, called van der Waals (vdW) compounds, which are stabilized under elevated pressures.

This work focuses on extending the pressure-concentration binary phase diagrams of N_2-Ar and N_2-Kr in the pressure range of 1-25 GPa at room temperature. The phase diagrams of the pure components, namely, N_2, Ar and Kr, have been studied extensively under a wide range of thermodynamic conditions. The main objectives are to study the effect on condensed phases upon mixing, to pinpoint the transition pressures for all concentrations studied between known and novel phase(s), to identify possible van der Waals binary solids present as a function of concentration, pressure and temperature and to understand the relationship among them. Raman spectroscopy was used to identify structural phase transitions as a function of pressure and XRD was employed to fully characterize these crystalline structures and their corresponding properties. XRD experiments were performed using synchrotron radiation primarily at the Hard X-ray MicroAnalysis (HXMA) 06ID-1 beamline at the Canadian Light Source (CLS) and also at CLS@APS (Sector 20) of the Advanced Photon Source (APS). The results of these studies and conclusions are presented in this work.

This work is divided into seven chapters: Chapter 1 is an introduction, Chapter 2 reviews the relevant literature and Chapter 3 outlines the experimental techniques employed in this work. Raman spectroscopic results for pure nitrogen and the calibration method for the spectrometer are described in Chapter 4. The results, followed by as discussion, for the N_2-Ar and N_2-Kr systems are given in Chapters 5 and 6, respectively. Chapter 7 will summarize this work and discuss possible future prospects for the project.

Chapter 2
LITERATURE REVIEW

This chapter will introduce the reader to the study of materials under extreme pressure and why it is useful for ascertaining properties from a material. A literature review of pure and compound systems under pressure will follow. There will also be a discussion regarding the motivations for studying the nitrogen-argon and nitrogen-krypton systems at various concentrations.

2.1 Materials Under Extreme Conditions

2.1.1 A Brief Introduction to Extreme Conditions

Near-ambient conditions are necessary for life; however, most matter in the universe is submitted to vacuum or extreme conditions such as high pressure and/or temperature. To understand the properties of matter it is essential to reproduce the extreme conditions in the laboratory. This can allow, for example the reproduction of conditions existing within the Earth (crust, mantle, core).

Materials are an important part of energy technology (i.e. steam and wind turbines, fuel efficient vehicles, energy sources) and there are continual demands on material performance with respect to extremes such as stress, temperature, pressure, chemical reactivity, and external fields. Extreme conditions can speed up the deterioration of materials and lead to reduced performance and eventual failure, which can be costly. There is a necessity to understand the chemical and physical processes involved with materials. This involves a comprehension of how atoms and electrons behave within a material under extreme conditions. This will provide insight into the structure,

defect production, phase transitions, chemical reactions, etc. It requires advanced characterization methods (e.g., x-ray diffraction, spectroscopy, and microscopy) to study materials *in situ* as the materials evolve under applied constraints and computational techniques to model and predict material behavior under extreme conditions.

Materials are primarily made by chemical and physical reactions whereby reactants, temperature, composition, and pressure are varied. Extreme conditions such high pressure can be used to manipulate the synthesis process. The main effect of high pressure on condensed matter, for example, is the modification of the interatomic distances and, in turn, change of crystal lattice parameters and electronic properties as well as the intensity of the different interactions involved in interatomic binding. As an example, we consider the case of H_2O. Over the years, the number of phases of condensed H_2O has continued to expand and show how extreme conditions can induce polymorphism. The phase diagram for H_2O now consists of over 18 or so crystalline phases and 3 amorphous phases.[1,2] The application of pressure has also aided in the production of superconductors that have higher critical transition temperatures (T_c) than ever before. Recent reports (Drozdov *et al.*, 2014) have claimed a T_c near 190 K, albeit at very high pressure, has been observed in H_2S.[3]

A better understanding of the processes involved will make it possible to predict the behavior of materials under extreme conditions. This will allow for the design and synthetization of revolutionary materials down to the chemical bond with unique properties, whether the purpose is for high strength components or energetic materials that can store vast amounts of chemical energy. In this work, the changes of physical properties of materials are examined at high pressures at room temperature.

2.1.2 The Effect of Pressure on Materials

Materials exhibit a wide range of pressure sensitivity which can lead to structural deformation and/or phase transitions. To study the properties and characterize materials with changing pressure, devices such as the diamond anvil cell (DAC) have been designed and constructed to create high pressures in the laboratory. Pressure is measured in units of force (N) over area (m^2), which is also called a Pascal (1 Pa = 1 N/m^2). In high pressure science, experimental pressures are on the order of tens of 10^9 Pa, or Gigapascals (1 GPa = 10^9 Pa ~ 10^4 atm). In this work, the DAC was utilized to reach pressures up to 25 GPa at room temperature. The DAC will be discussed in more detail in Chapter 3. Table 2.1 provides a few examples of pressures that are found in the universe.

Table 2.1: Examples of pressure found for various objects. *Temperatures will vary. Values are obtained from various sources.*[4,5,6,7]

Object	Pressure (atm)	Pressure (Pa)	Pressure (GPa)
Outer Space	~ 1.44×10^{-23}	1.46×10^{-18}	1.46×10^{-27}
Sea Level	1	1.01×10^{5}	1.01×10^{-4}
Center of the Earth	3.59×10^{6}	3.64×10^{11}	364
Highest Static Pressure Reached in Laboratory in a Diamond Anvil Cell	7.64×10^{6}	7.74×10^{11}	774
Center of the Sun	2.47×10^{11}	2.5×10^{16}	2.5×10^{7}

2.2 The Study of Nitrogen and Binary Systems Conditions

2.2.1 van der Waals Compounds

When two uncharged atoms or molecules approach one another, their electron clouds undergo deformation. An unsymmetrical electron cloud results in a temporary dipole moment or induced dipole moment. The duration is brief but in this time the atoms or molecules are attracted to one another. This intermolecular force is known as the van der Waals (vdW) force, named after the Dutch scientist Johannes Diderik van der Waals.[8] The vdW force is much weaker when compared to covalent bonds and vanishes quickly with distance.

Atoms or molecules can be attracted to each other at moderate distances (a few angstroms) and repel each other at close range. The vdW force can be approximated with a Lennard-Jones function. The Lennard-Jones potential is effective at describing the attractive and repulsive interactions between two uncharged atoms or molecules and is given by the following equation:

$$V(r) = 4\varepsilon\left[\left(\frac{\sigma}{r}\right)^{12} - \left(\frac{\sigma}{r}\right)^{6}\right] \tag{2.1}$$

where σ and ε are Lennard-Jones parameters and are dependent on the interacting particles. When the separation, r, is small the $\frac{1}{r^{12}}$ term dominates, giving a positive potential (short range repulsion). As r increases, the $\frac{1}{r^{6}}$ term prevails (long-range attraction). The resulting potential is shown in Figure 2.1. The minimum of the Lennard-Jones potential indicates the separation between the atoms or molecules at equilibrium.

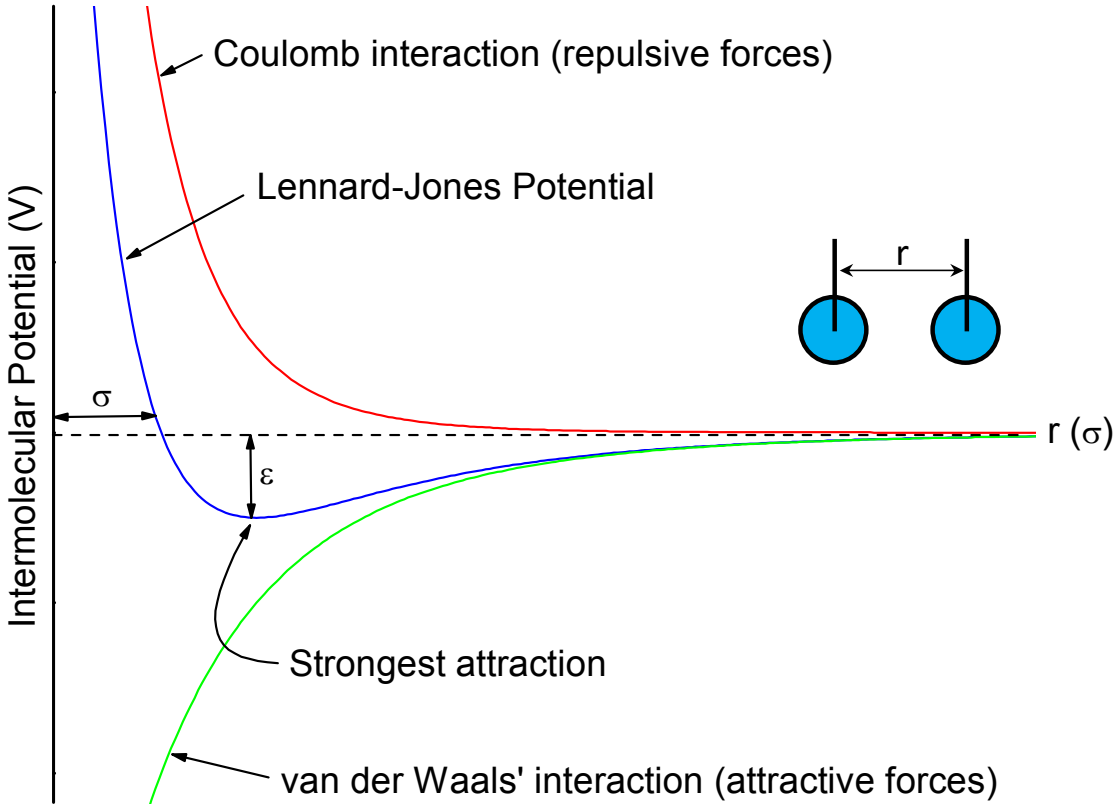

Figure 2.1: The van der Waals interaction is approximated with the Lennard-Jones function for intermolecular potential, V(r).

vdW forces can be categorized into three types: dipole-dipole, dispersion and hydrogen-bonding. Dipole-dipole forces occur in polar molecules such as HCl. In a solution of polar molecules, for example, there will be a number of molecules that have a slightly positive and a number that have a slightly negative region. They will orient themselves to accommodate the charge and the result is a weak intermolecular interaction during a close encounter. It should be noted that a molecule's momentum is often strong enough to overcome the attraction and prevents it from grouping closely (i.e. solid) with other molecules.

Dispersion forces exist between nonpolar molecules. Electrons move around an atom or molecule incredibly fast and this can result in temporary electron-rich or electron-poor regions. These

regions last very briefly, but if they can polarize the electron cloud on an adjacent molecule the electron clouds of each molecule may begin to oscillate with each other. The result is an alignment of dipoles and an attractive force between the molecules. Larger electron imbalances will lead to stronger forces. For example, the dispersion forces are harder to overcome giving a higher boiling point for Xe when compared to Ne due to having more electrons and a larger electron imbalance.

The third type of vdW force is hydrogen-bonding. This involves molecules with –OH, -FH and –NH groups. It behaves exactly like dipole-dipole forces; however, it is much stronger when compared to the other types of vdW forces. The result of a combination of hydrogen with oxygen, fluorine or nitrogen is an extreme dipole situation and the positive side of a molecule will orient itself with the negative side of another. For a comparison of the three forces, it would take more energy to overcome the vdW forces with H_2O molecules (hydrogen-bonding) than it would with HCl molecules (dipole-dipole). Dispersion forces are the weakest of the three and are a feature common to all atoms.[8,9,10]

2.2.2 Constructing Phase Diagrams

The properties of materials reflect their crystal structure as structures are controlled by composition and methods of processing. The state exhibited by a material depends on its chemical composition, temperature and pressure. A phase diagram is a type of graph to show the physical state of a material and provide some fundamental knowledge of what the equilibrium phase with a given structure (lowest possible energy) is as a function of temperature, pressure and composition in a closed system.[11]

The number of phases that are thermodynamically stable for a system is given by the Gibb's phase rule:

$$p = c - f + 2 \tag{2.2}$$

where the number of phases, p, is determined by the number of components, c, and the number of variables, f, that can be independently changed without changing the state of the system (i.e. the number of phases and composition are constant).[11,12]

Figure 2.2, (a) shows a general phase diagram for a single component system with gaseous, liquid and solid phases. There are distinct areas with only a single phase, and these regions can be explained with the Gibb's phase rule. If temperature and pressure are free to change, according to Eq. 2.2, $c = 1$, $f = 2$ giving a total of $p = 1 - 2 + 2 = 1$ phase for that particular region. At a triple point, pressure and temperature are constant ($f = 0$) which gives three phases. Along the two-phase lines, either pressure or temperature is changing ($f = 1$). To maintain a coexistence of the two phases along the line, the second variable must change by a corresponding fixed amount. The line separating the liquid to gas transition comes to a point (critical point) where their properties converge and become identical. This is referred to as supercritical fluid.

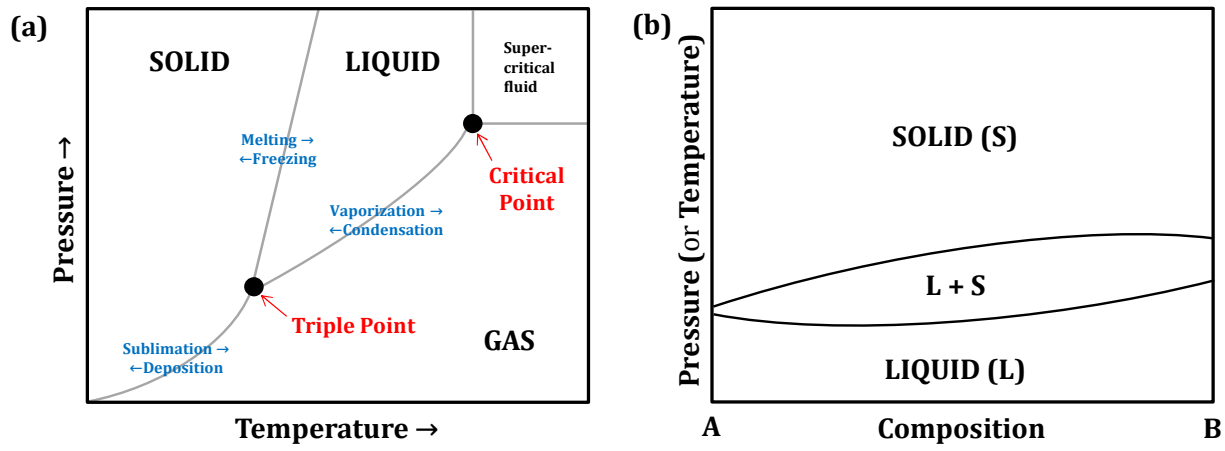

Figure 2.2: A general pressure-temperature phase diagram for a single component system. (b) A general binary phase diagram.

Figure 2.2, (b) shows a general binary phase diagram that displays the phases formed from differing mixtures of two elements over a range of pressures (or temperatures). The composition runs from 100 % of element A on the left, through mixtures of A and B, to 100 % of element B on the right. According to Eq. 2.2, for a binary system (c = 2) at constant temperature with varied pressure and composition (f = 2), there are expected to be a maximum of two phases that can be thermodynamically stable with each other. They might come in one of, or combinations of individually pure phases, a solid solution, or a compound consisting of the two components which has a different phase than that of the pure substances.

There are various tools that can be used to construct a phase diagram. In this work, the main techniques employed were Raman spectroscopy and x-ray diffraction (XRD) with synchrotron radiation. Raman spectroscopy is sensitive to changes in the environment and can provide some information on the orientational and translational behavior of atoms or molecules of the material by measuring the energy corresponding to characteristic vibrational modes. Regarding Raman spectroscopy, the terms energy, frequency and wavenumber will interchange to have the same meaning. In addition to Raman spectroscopy, XRD patterns can be used to determine crystalline structures corresponding to the phases. High quality x-ray diffraction patterns can provide information on the number of mixed phases and their corresponding unit cells, volumes, space groups, etc. These techniques are discussed in more detail in Chapter 3. The following section will introduce polymeric nitrogen, which is a single-bonded network of nitrogen, and motivations behind retrieving this structure under ambient conditions.

2.2.3 Polymeric Nitrogen

Dense forms of nitrogen are of great interest. The energy difference between single-bonded nitrogen (160 kJ/mol, or 0.83 eV/atom) and triple-bonded nitrogen (954 kJ/mol, or 4.94 eV/atom) is significant.[13] If single-bonded nitrogen (N-N) were to transform into triple-bonded nitrogen (N≡N), a large amount of energy would be released (about 444 kJ/mol, or 2.3 eV/atom). If this energy could be stored in a material containing a substantial network, or if possible, a complete network of single-bonded nitrogen, it would have the highest energy content of any known nonnuclear material.

Theoretical calculations on the structure of nitrogen by McMahon *et al.*[14] predicted that intramolecular interactions between nitrogen atoms would become competitive with intermolecular interactions at high pressures. The result would be an energetically favorable single-bonded network of nitrogen, also called polymeric nitrogen (PN). Over the years, PN structures have been predicted and in 1992 Mailhiot *et al.*[15] performed extensive *ab initio* pseudopotential total-energy calculations and found that a structure with a cubic gauche (cg) distortion characterized by all gauche (~60°) dihedral angles had the lowest energy of all the other proposed structures and was predicted to be stable at 50 ± 15 GPa. This structure is shown in Figure 2.3. Results from many other theoretical studies have also confirmed the stability of this structure (cg-N, space group $I2_13$).[16,17,18,19]

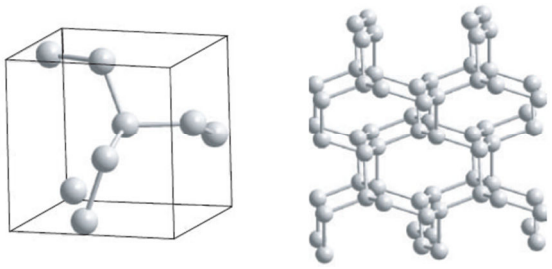

Figure 2.3: The cubic gauche structure of nitrogen (cg-N). Left: The unit cell. Right: An extended structure of the polymeric nitrogen. *Reprinted with permission from Macmillan Publishers Ltd., Nature, Copyright 2004.*[20]

Experimental results, however, did not agree with theoretical predictions. High pressure experiments (> 100 GPa) with nitrogen at room temperature produced the vibron associated with the stretching mode of molecular nitrogen (later called the η phase), but did not display any presence of PN.[21,22] Low temperature experiments (80 – 300 K) performed by Goncharov *et al.*[23] and Eremets *et al.*[24] produced the first non-molecular form of nitrogen. This phase was found to consist of an amorphous network of single-bonded nitrogen.

In 2004, Eremets *et al.*[20] successfully synthesized cg-N at extreme conditions. The process involved heating a sample at 140 GPa until the molecular nitrogen Raman modes disappeared. At temperatures above 2500 K, the sample was then reduced to 115 GPa and new Raman-active molecular stretching modes (also named vibrons) appeared and were in good agreement with theoretical cg-N. XRD experiments[20,25] confirmed the cg-N structure (Figure 2.3) exists above 110 GPa and temperatures above 2000 K.

In 2014, Tomasino *et al.*[26] reported the discovery of a nitrogen phase that consists of a single-bonded, layered polymeric (LP) structure.

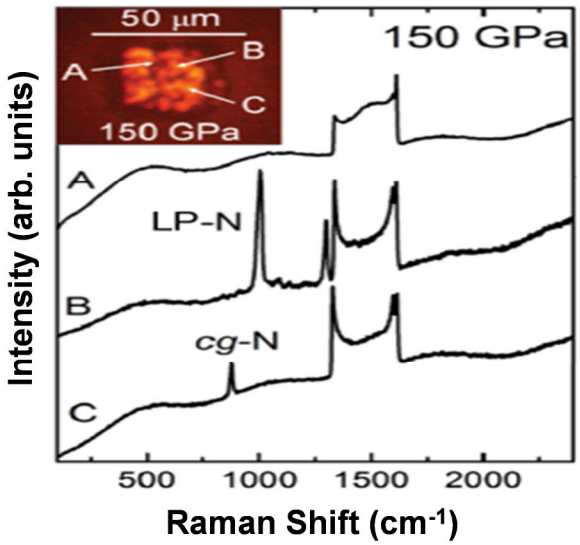

Figure 2.4: Vibrational spectra of laser-heated nitrogen at 150 GPa. *Reprinted with permission from the American Physical Society, Copyright 2014.*[26]

This structure was synthesized using laser heated diamond anvil cells at pressures from 120 – 180 GPa. In each experiment, a mixture of amorphous, LP-N and cg-N phases were produced. Two Raman-active modes were observed for LP-N at ~1005 cm^{-1} and 1300 cm^{-1} (Figure 2.4). The XRD pattern of LP-N at 112 GPa is shown in Figure 2.5. A majority of the peaks can be indexed to an orthorhombic unit cell of space group *Pba*2, which is a theoretically predicted structure for nitrogen.

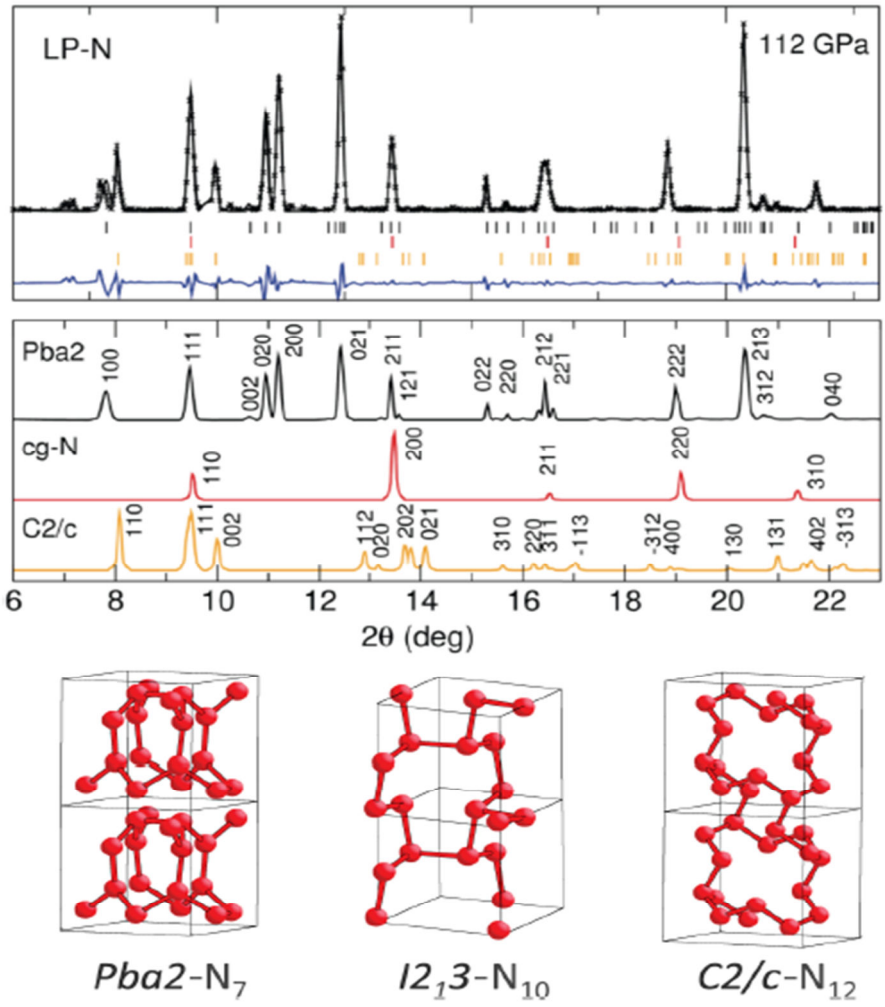

Figure 2.5: XRD pattern of LP-N compared to cg-N, its metastable form (*C*2/*c*) and to the theoretical structure *Pba*2. Bottom: Crystal structures of the proposed phases. *Reprinted with permission from the American Physical Society, Copyright 2014.*[26]

Recently, an effort has been made to use extensive theoretical predictions to construct a phase diagram that includes transition lines of molecular nitrogen into PN at elevated temperatures and extremely high pressures.[27] The phase diagram is shown in Figure 2.6.

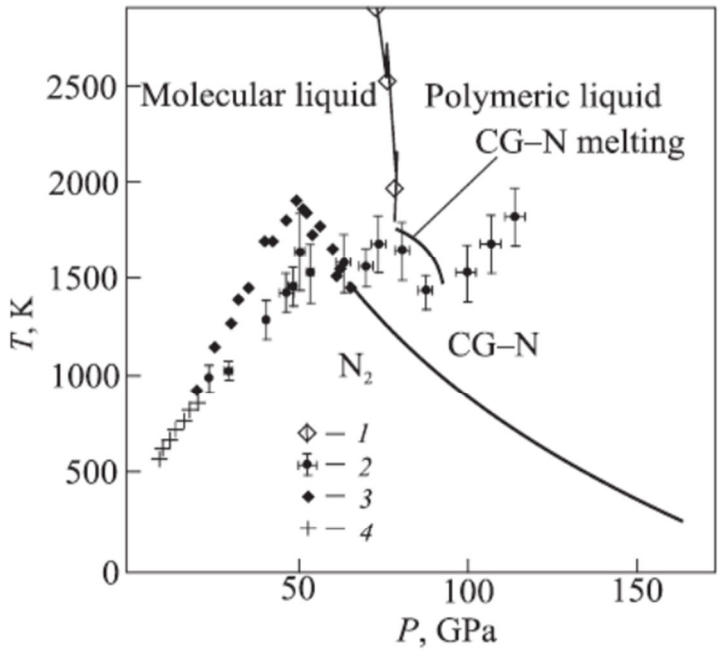

Figure 2.6: Phase diagram constructed to include theoretical predictions for transition lines between N_2 and PN. In the plot, "1" refers to computer simulated results while "2-4" refer to the experimental data on the melting line of the polymeric solid. *Reprinted with permission from the American Institute of Physics, Copyright 2015.*[27]

2.2.4 Recovering Polymeric Nitrogen (PN) at Ambient Conditions

Experimental attempts to recover predicted phases of PN have been challenging due to numerous reasons such as diamond anvil cell failure[28], cg-N transforming back to molecular nitrogen, etc. At room temperature, Eremets *et al.*[20] recovered cg-N down to 42 GPa before it transformed. At present, researchers are exploring possible methods of retrieving or synthesizing single-bonded nitrogen at ambient conditions.

Recent theoretical studies have predicted new PN structures utilizing numerous computer simulations at ambient pressure (1 atm). A discussion of the details for various simulations can be found in Hirshberg *et al.*[29]. In their work, they predict the existence of a solid consisting of N_8 molecules, which are not composed of N_2 molecules, that is metastable at ambient pressure. This phase is stabilized by van der Waals and electrostatic forces between the N_8 molecules. It is expected to be more stable than cg-N at pressures below 20 GPa. In 2014, Sun *et al*.[30] predicted another six PN structures ($P2_1/m$, $C2/c$, $P2_12_12_1$-500, $Pnnm$, $P2_1$, and $Cmc21$) between the pressures of 100 and 600 GPa. The prediction of new structures aids in stimulating the search for new methods of recovering polymeric nitrogen.

Other studies have looked at high nitrogen content compounds as a way to synthesize single-bonded nitrogen and theoretical studies have been promising. Wang *et al.*[31] utilized particle swarm optimization search (CALYPSO) in combination with density functional theory and were able to transform N_3^- ions into a polymeric form of nitrogen in CsN_3. It is expected to be stable at pressures above 51 GPa. In 2015, Zhang *et al.*[32] investigated KN_3 up to 400 GPa using a combination of structure searching methods and first principles density functional calculations. Above 274 GPa, their calculations revealed a stable phase of polymeric nitrogen ($C2/m$-N) that consists of "zig-zag" benzene-like N_6 rings.

Another possible method to recover PN under ambient conditions is using dopants such as noble gases or other molecules to act as polymer stabilizers. Recovery of PN upon decompression is hindered by an "unravelling" of the polymeric structure, which transforms to a molecular phase, and a dopant may help to avoid this.[13,20,33]

2.2.5 Binary Systems

The study of simple binary mixtures has and will continue to give us knowledge about phase behavior and mutual solubility in solids. Hard-sphere systems are a good starting point for developing phase diagrams of binary mixtures. At higher pressures, well above ambient pressure, it is believed that the solubility in solid systems is strongly affected by geometrical effects, which is described by the Hume-Rothery rules for compound formation.[34] Extensive computer simulations on hard sphere systems have shown that phase behavior strongly depends on the diameter ratio between the two species, α. According to the Hume-Rothery rules, an extensive substitutional solid solution, and compound formation, is expected if α is above 0.85. In addition, separate pure phases will be observed for intermediate size ratios and interstitial solids (small atoms/molecules located in the interstices of larger ones) may be observed up to $\alpha \sim 0.60$.[33,35]

The addition of a second component may alter the phase diagram of the pure substance and shift or eliminate phase transitions. Knowledge of the structure and properties of mixed systems can aid in our understanding of the planets and their satellites, as current planetary models are based on low pressure behavior.[33,34] If certain properties are required from a pure system, they might be shifted to a more practical region of the pressure-temperature diagram. An example would be developing an easier method for recovering metallic hydrogen.[36] In addition, a second component may create new physical properties and the formation of compounds might be observed.

When two components with different diameters are combined, stoichiometric compounds can form and are stabilized by entropy and efficiency packing.[35] In 1992, Vos *et al*.[33] claimed to have observed the first solid vdW compound in the nitrogen-helium binary system. During crystal growth, facets were observed as opposed to rounded surfaces expected for the pure components.

Raman experiments revealed a main vibron shifted with respect to that of pure nitrogen; with certain initial concentrations, this vibron was observed along with the vibrons of the pure nitrogen (N_2) phases. XRD patterns indicated high-quality crystals with a hexagonal unit cell that was distinct from those of the pure components in the same pressure-temperature regions. The lattice parameters of the new compound were a = 8.019 Å and c = 9.461 Å at 12.6 GPa and 295 K. The crystalline structure was found to contain 22 N_2 molecules and 2 He atoms per unit cell. Various initial bulk compositions were investigated and the unit cell volume remained unchanged. It was concluded that composition had no effect on the volume and this was indeed a stoichiometric compound, $He(N_2)_{11}$. In comparison to hard-sphere simulations, the stoichiometry of this compound is unusual and it differs with known hard-sphere solids in that the larger species is the major component. The diameter ratio for the nitrogen-helium system is 0.62. According to the Hume-Rothery rules, which do not take into account molecular shapes and intermolecular potentials, compound formation is expected for α above 0.85. Having a compound form at a lower α indicates that theoretical descriptions need improvement and the study of vdW compounds will aid in this endeavor.

Since the discovery by Vos *et al*.[33], many solid vdW compounds have been revealed. Under compression, stoichiometric vdW compounds with a variety of structures can form between noble elements and simple molecules such as hydrogen and nitrogen. Some stoichiometric compounds that have been observed include $Ne(He)_2$, $Ar(H_2)_2$, $(O_2)_3(H_2)_4$ and more recently $Kr(H_2)_4$.[37,38] Binary systems that are relevant to this work include N_2 with noble gases or simple molecules. The N_2 molecule has an almost spherical shape, well known interaction potential, and extensive theoretical background, which makes it ideal for studying phase behaviour and solubility in solids. Systems such as N_2-methane (α = 0.96), N_2-Xe (α = 0.88) and N_2-Ne (α = 0.73) have been found to stabilize in

stoichiometric compounds at high pressure.[39,40] In this work, the high-density nitrogen-argon and nitrogen-krypton binary systems are investigated in more detail.

2.2.6 The Nitrogen-Argon Binary System

The nitrogen-argon binary system presents yet another example of a simple system that is ideal for studying the properties and mutual solubility in a solid mixed system. With a diameter ratio of 0.94 and similar intermolecular interactions, it is expected that argon (Ar) atoms will dissolve substitutionally into nitrogen (N_2) structures, and possible stoichiometric compound formation may be observed.[41]

At room temperature, Ar solidifies at 1.3 GPa and N_2 at 2.4 GPa. The N_2-Ar system has been studied with Raman spectroscopy up to ~10 GPa and ~16 GPa for higher and lower concentrations of N_2, respectively.[39,41] The δ phase for pure nitrogen (δ-N_2) has a disordered cubic unit cell with spherically disordered molecules located at the corners and at the body-center. The others are located at the faces in a disk normal to the faces. They are referred to as sphere-like and disk-like nitrogen with a corresponding Raman spectrum containing two main vibrons.

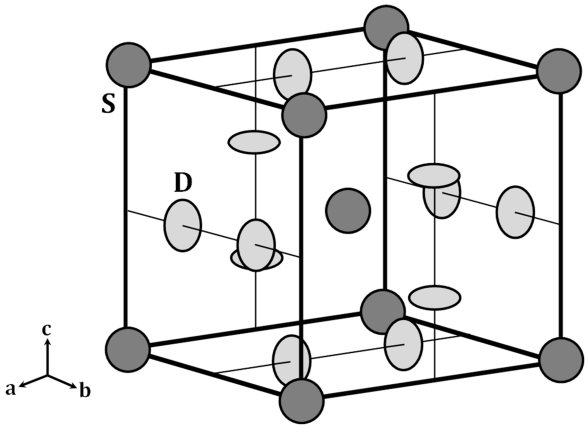

Figure 2.7: The δ-N_2 structure has a disordered cubic unit cell with disk-like (D) molecules on the faces and sphere-like molecules (S) on the corners.

This structure is discussed in more detail in Section 2.3.3. Figure 2.8 shows a comparison for pure N_2 (top) and that of the mixed N_2-Ar system (bottom), both in the δ phase. For pure N_2, both vibrons are well defined with an intensity ratio corresponding to the number of N_2 molecules at each location (more N_2 molecules at the disk-like sites, giving a higher intensity). After the addition of Ar, the vibron corresponding to the spheres has a lower intensity, indicating that the Ar atoms are preferentially occupying the sphere-like sites within the δ* phase (the asterisk represents a solid containing both components). These observations were in agreement with Monte-Carlo simulations.[41,42]

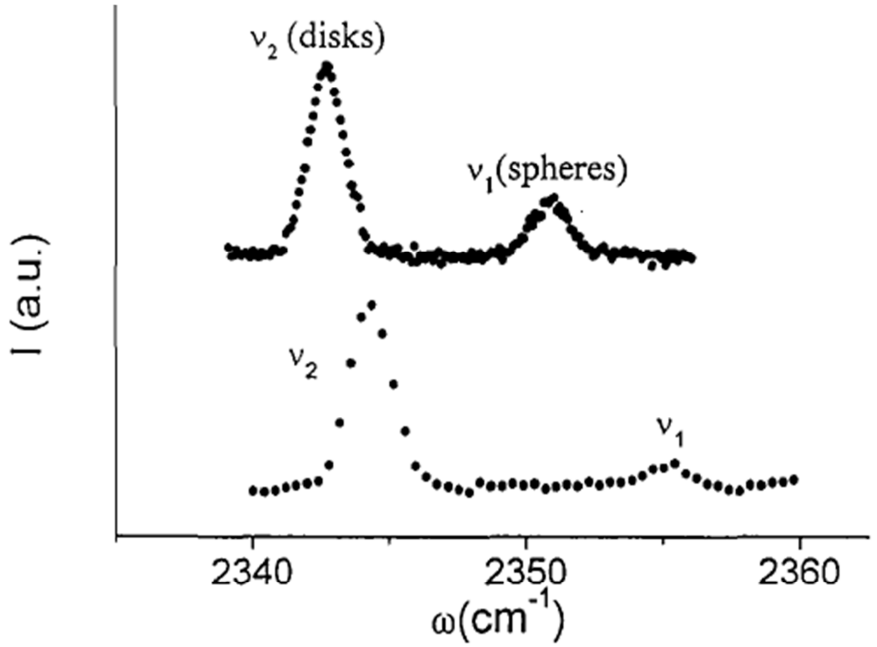

Figure 2.8: Vibrational Raman spectra comparing **(top)** pure N_2 at 5.9 GPa and 243 K and **(bottom)** that of the mixed N_2-Ar system with x = 0.85 at 6.7 GPa and 175 K. A lower intensity for υ_1 in the N_2-Ar spectrum indicates that argon atoms are mainly located at the sphere-like sites. The corresponding spectra at room temperature are similar. *Reprinted with kind permission from the Springer Science and Business Media, Copyright 1998.*[41]

In 2001, Lotz *et al.*[39] investigated this system at room temperature for various concentrations, including N_2 mole fractions (x) of 0.04, 0.10, 0.25, 0.50, and 0.75. Argon was found to affect the phases of N_2 significantly. Figure 2.9 presents their experimental Raman vibrational frequencies in comparison to that of pure nitrogen. At low pressure, a single vibron was observed for all

compositions. For the lowest concentrations, x = 0.04 and 0.10, only a single peak was observed up to the highest pressure investigated. As the concentration of N_2 was increased, the coexistence region of fluid and β phase nitrogen (β-N_2) was observed to increase from 1.7 to 2.4 GPa. This was suggested to be the outcome of Ar dissolving easily into β-N_2, making the fluid phase no longer favorable. They found that the amount of Ar dissolving into β- and δ-N_2 was significantly larger than N_2 in Ar. N_2 molecules located within solid Ar (S_{Ar^*})resulted in Raman signals with higher frequency compared to that of pure β-N_2. The β*- δ* transition was also found to shift to higher pressures as the concentration of N_2 was decreased. It is believed that N_2 molecules prefer the hexagonal close packed (HCP) structure as argon's smaller lattice parameters hinder the rotation of the N_2 molecules, indicating that orientational degrees of freedom must also be considered in the solubility of high pressure solids.

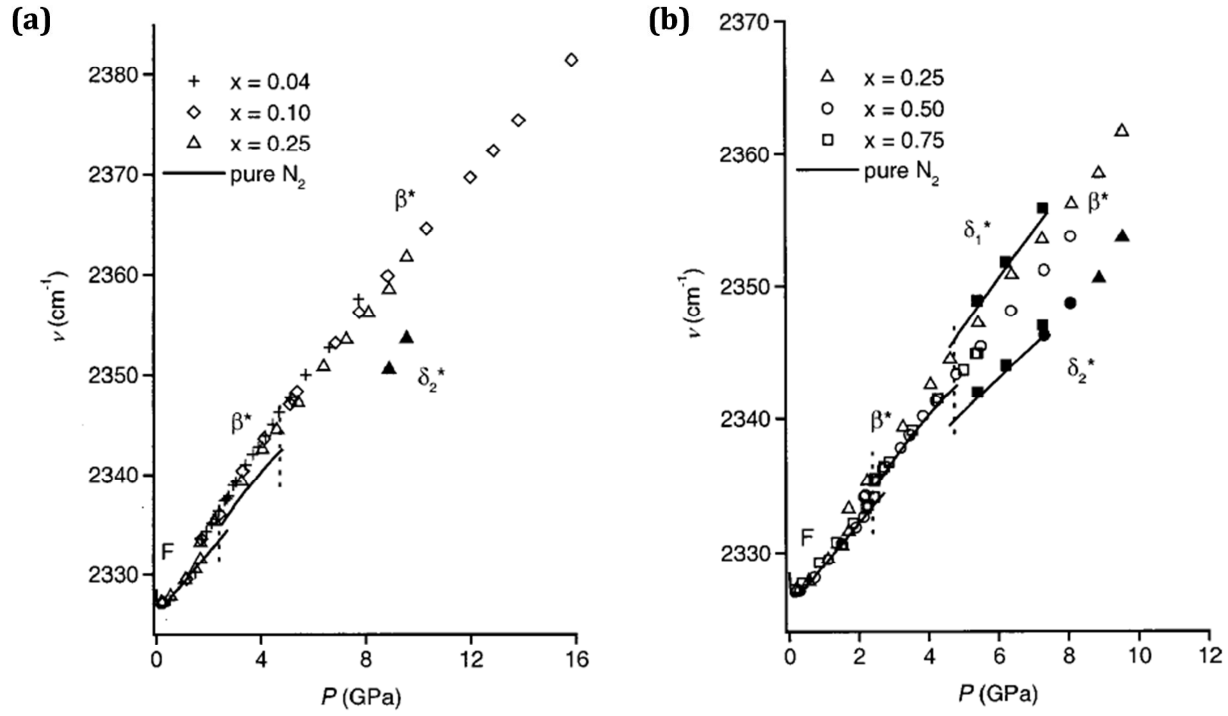

Figure 2.9: Vibrational frequencies for nitrogen obtained by Lotz *et al.*[39] as a function of pressure at 296 K. "x" denote the nitrogen concentration in the nitrogen + argon binary system. Full symbols represent the δ* phase and the dashed vertical lines indicate phase transitions in pure nitrogen. *Reprinted with permission from the American Physical Society, Copyright 2001.*[39]

Lotz *et al.*[39] determined the amount of Ar that was dissolving into solid N_2 had a limitation of ~35 % due to a decrease in volume and energy in the system, with Ar occupying the sphere-like sites. At x = 0.75, ~50 % of the sphere-like sites were occupied by Ar atoms. No stoichiometric compounds were observed in this system up to the highest pressures investigated. After considering all of their results, Lotz *et al.*[39] proposed a phase diagram for the N_2-Ar binary system, shown in Figure 2.10.

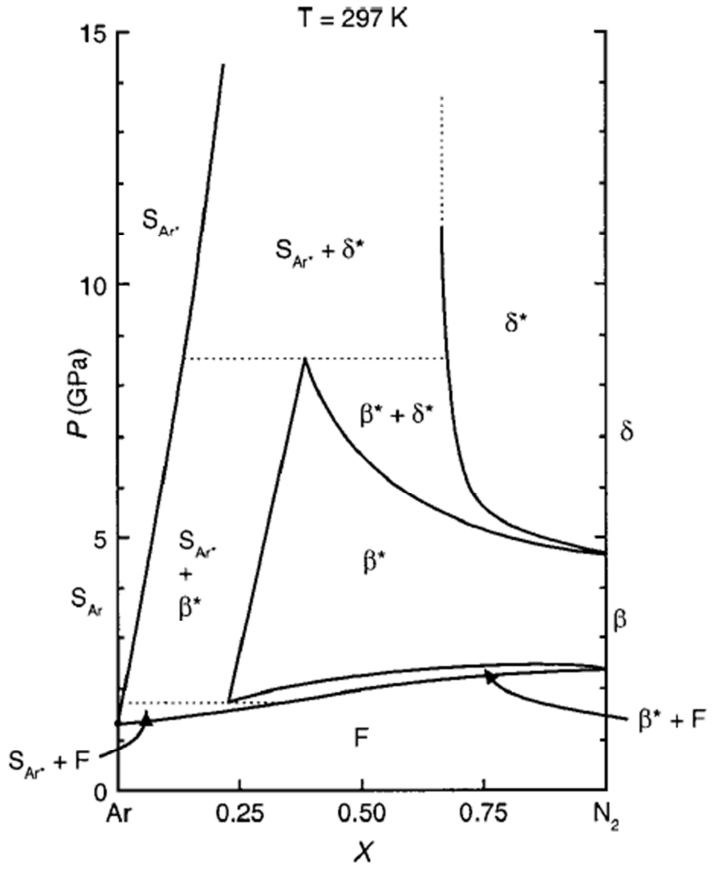

Figure 2.10: Proposed pressure-concentration phase diagram for the N_2-Ar binary system. *Reprinted with permission from the American Physical Society, Copyright 2001.*[39]

Following the work of Kooi *et al.*[41] and Lotz *et al.*[39], the main goals of this work are to verify their results, to further investigate the N_2-Ar pressure-concentration diagram and to search for possible van der Waals compounds at room temperature and elevated pressures using Raman spectroscopy and X-ray diffraction.

2.2.7 The Nitrogen-Krypton Binary System

In the nitrogen-krypton (N_2-Kr) system, the diameter of Kr is close to that of pure N_2, giving a diameter ratio that is ~1. As with N_2-Ar, Kr atoms are expected to dissolve substitutionally into nitrogen structures. Since the diameter ratio is nearly 1 ($\alpha \sim 1$), the solubility is expected to be higher than that of N_2-Ar and the formation of a van der Waals compound, though less likely, is still possible.[43]

Lotz *et al.*[43] also investigated the N_2-Kr system, using Raman spectroscopy at room temperature up to 15 GPa. Mixtures included various nitrogen mole fractions (x), including 0.06, 0.25, 0.50, 0.75 and 0.93. The experimental vibrational frequencies as a function of pressure are shown in Figure 2.11.

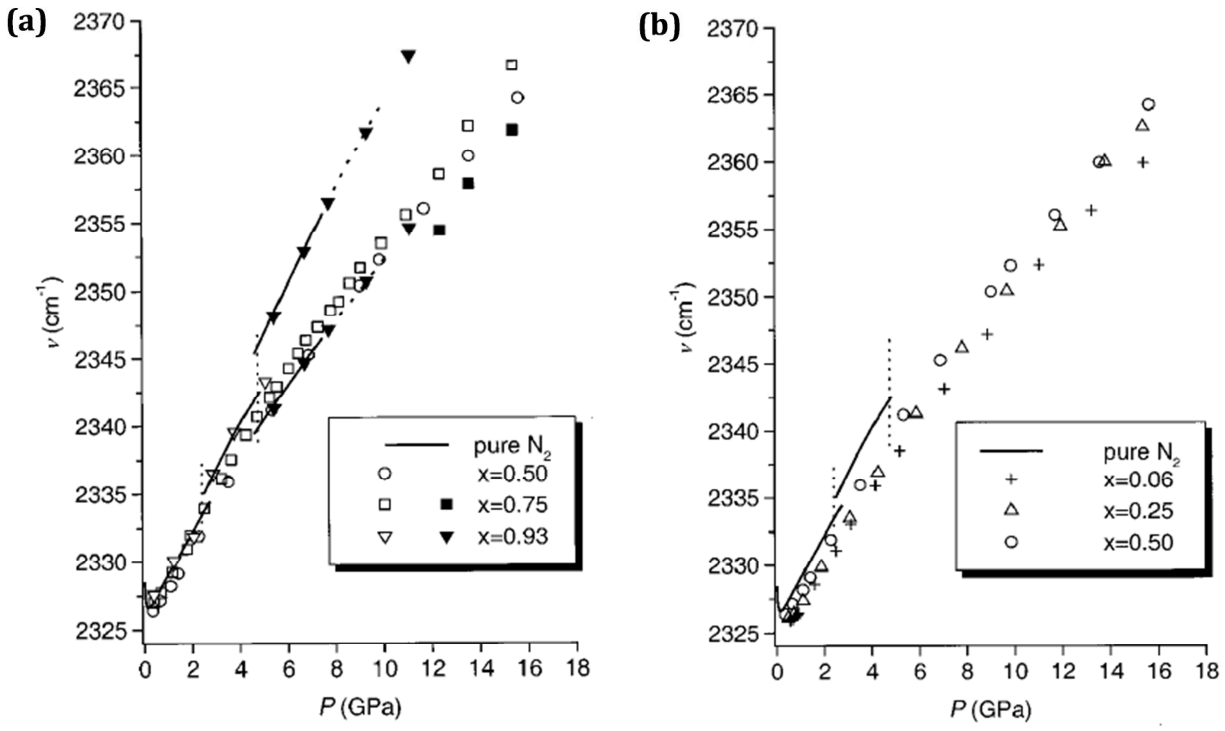

Figure 2.11: Vibrational frequencies for nitrogen obtained by Lotz *et al.*[43] as a function of pressure at 296 K. "x" denote the nitrogen concentration in the nitrogen + krypton binary system. Full symbols represent the δ* phase, solid lines represent pure nitrogen and the dashed vertical lines indicate phase transitions in pure nitrogen. *Reprinted with permission from the American Physical Society, Copyright 2001.*[43]

At room temperature, Kr solidifies at ~0.9 GPa and N_2 at 2.4 GPa. In the mixed system at low pressure, only a single vibron was observed for the various nitrogen mole fractions. The fluid-solid coexistence region was observed to be small for all compositions and increase from 0.9 to 2.2 GPa with increasing nitrogen mole fractions. The vibrational frequencies were found to be dependent on composition and shifted to lower values when compared to that of pure N_2. Smaller concentrations of N_2 resulted in a higher redshift. For $x < 0.75$, the spectra contained only one mode (no δ* phase) and the frequencies increased monotonically with pressure with no discontinuities. For the mixtures with higher N_2 concentrations, additional modes were observed. Figure 2.12 shows the Raman spectra of nitrogen in the mixed system with $x = 0.93$. In this mixture, the β-δ transition occurred at 5.5 GPa, about 0.5 GPa higher than pure N_2, and double peaks were observed within the two modes. The splitting of these modes is not fully understood. A single curve fit to each mode corresponds to main peak positions, within experimental accuracy, of pure N_2.

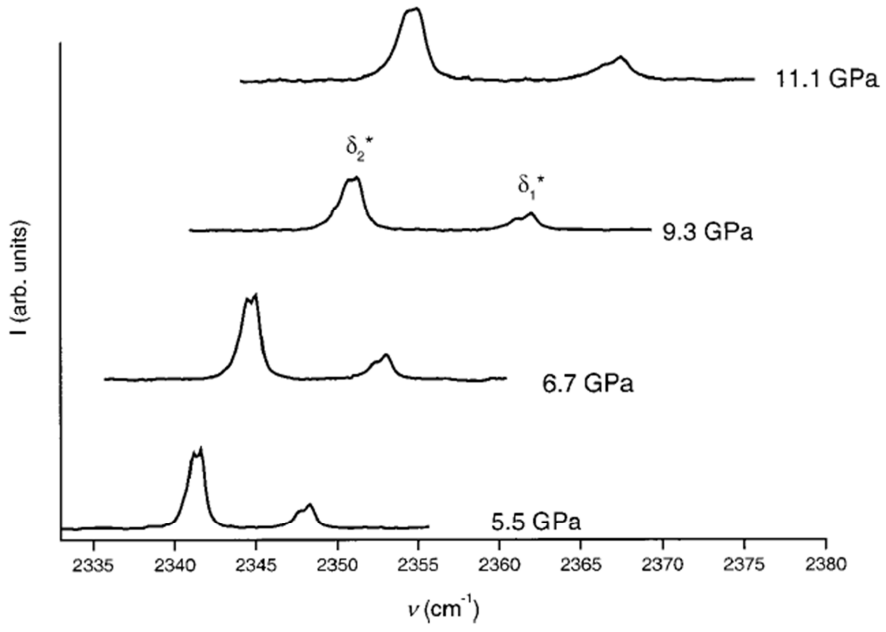

Figure 2.12: Raman spectra of the N_2-Kr system with $x = 0.93$ at room temperature. This mixture transitioned to the δ* phase at 5.5 GPa. Double peaks are observed in each mode. *Reprinted with permission from the American Physical Society, Copyright 2001.*[43]

For both x = 0.75 and 0.93 mixtures, the Raman signals were observed to broaden significantly with pressure. For pure N_2, the line shapes are Lorentzian for all phases while the line shape for the N_2-Kr system was found to be strongly dependent on composition and change from Lorentzian to almost Gaussian at the fluid-solid transition and remain Gaussian with pressure. For x = 0.50 mixtures, the full width at half maximum (FWHM) was at its largest with a width of about twice that of pure N_2.

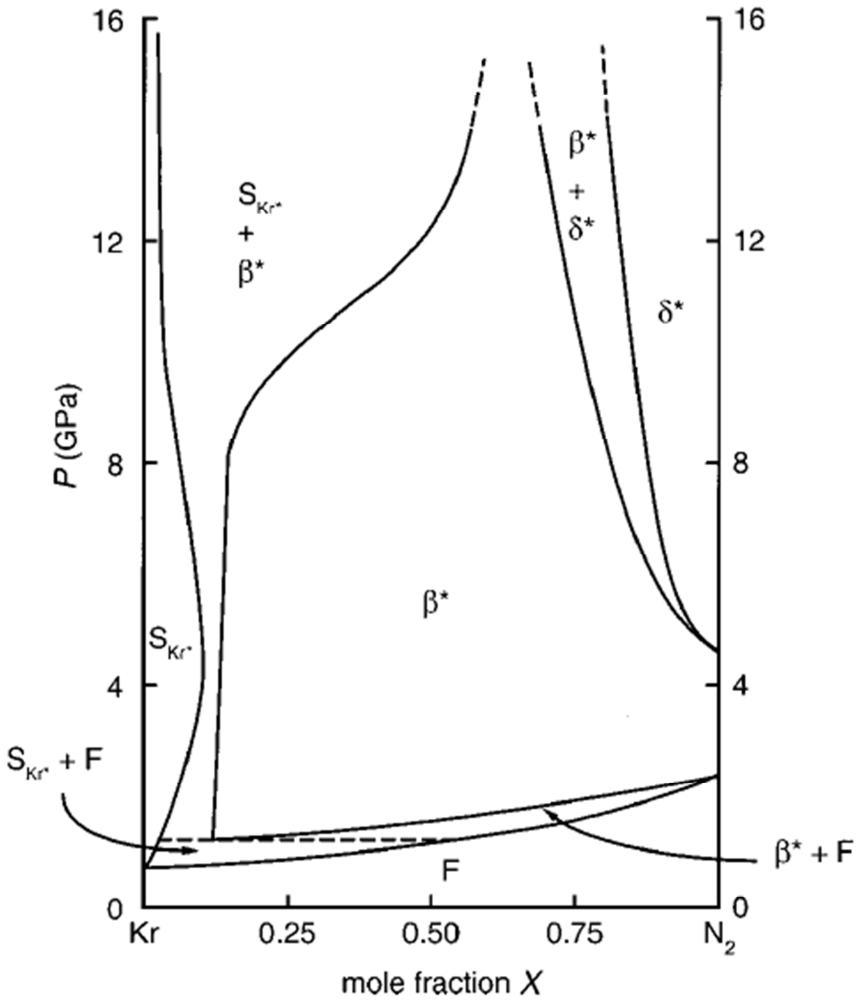

Figure 2.13: Proposed pressure-concentration phase diagram for the N_2-Kr binary system. *Reprinted with permission from the American Physical Society, Copyright 2001.*[43]

Lotz *et al*.[43,44] examined the N_2-Kr system by comparing their experimental results to molecular dynamics simulations as a function of nitrogen concentration. They concluded that the values for the vibrational frequencies suggest random configurations in the mixed solids and the linewidth may be attributed to a rapid exchange of the positions of the molecules. The maximum amount of Kr dissolving into N_2 structures was ~85 % while the maximum solubility of N_2 into Kr was ~10 %. The δ* phase intensity ratio for x = 0.75 and 0.93 mixtures were comparable to pure N_2, indicating the Kr atoms have no preference for either the sphere-like or the disk-like sites. The N_2-Kr phase diagram proposed by Lotz *et al*.[43] is presented in Figure 2.13.

In this work, in addition to N_2-Ar, the N_2-Kr system will be investigated with Raman spectroscopy and X-ray diffraction at room temperature and elevated pressures to verify and aid in extending the current pressure-concentration phase diagram and search for possible van der Waals compounds. Due to time constraints, this system will not be studied as extensively as the N_2-Ar system.

2.3 Solid Nitrogen

2.3.1 The Phase Diagram of N_2

Many attempts to identify the solid phases and their corresponding structures of nitrogen at room temperature with XRD occurred in the 1980's. Over the years, the phase diagram has been modified and improved by many research groups. Efforts are continually made to fully characterize the structures of solid nitrogen as there is still uncertainty with current descriptions. In 2007, the phase diagram was further extended when Gregoryanz *et al*.[45] identified new phases after XRD experiments were performed on nitrogen up to 170 GPa and 2500 K. Figure 2.14 shows the phase diagram presented by Gregoryanz *et al*.[45] Solid phases of N_2 have been designated Greek letters, in order of chronological discovery.

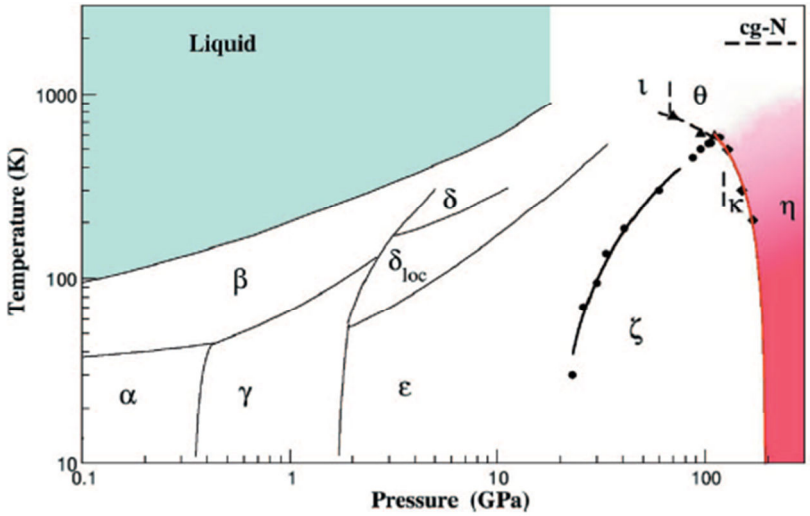

Figure 2.14: The phase diagram of nitrogen. *Reprinted with permission from the American Institute of Physics, Copyright 2007.*[45]

As previously discussed in Section 2.2.3, a motivation for studying and extending the phase diagram of nitrogen is the possible application to energetic materials. Currently, researchers have been trying to find a way to retrieve single-bonded nitrogen at room conditions, as this would represent an effective energetic material that could be used for fuels, explosives, etc.[46]

2.3.2 β-N_2

At room temperature, nitrogen exists in the β phase (β-N_2) between 2.4 and 4.9 GPa.[47,48,49] This phase is also observed at ambient pressure between 35.6 K and 63.1 K.[50] The β-N_2 structure has a disordered hexagonal unit cell with space group $P6_3/mmc$. The unit cell contains two nitrogen molecules and has a c/a ratio similar to the ideal value of $\sqrt{8/3} \cong 1.663$ for close-packed spheres.[51,52,53,54]

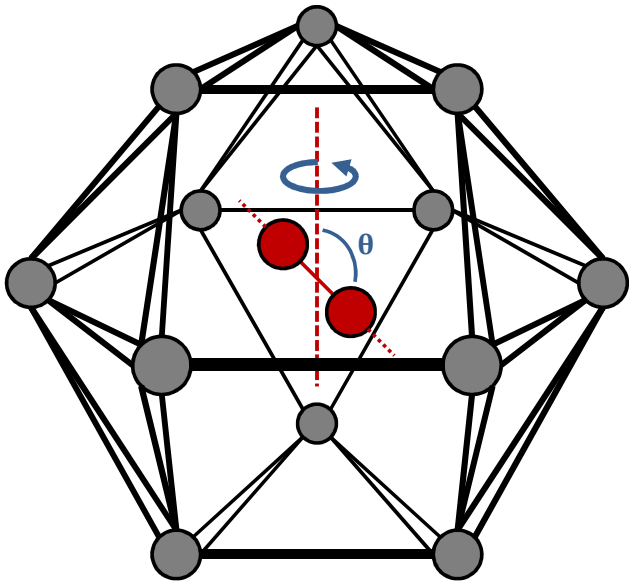

Figure 2.15: The β-N_2 structure has a disordered hexagonal unit cell; a precessing molecule in a cage of hexagonal close-packed (HCP) lattice points. Each point represents the center of another precessing molecule. [51,55]

The vibrational spectrum for β-N_2 consists of lattice modes and a single vibron, corresponding to the stretching mode in nitrogen. In this work, the focus will be on the stretching mode unless otherwise stated. Westerhoff *et al.*[49] showed that anomalies with the linewidth of the N_2 vibron are connected with phase transitions. A Raman spectrum of N_2 is shown in Figure 2.16.

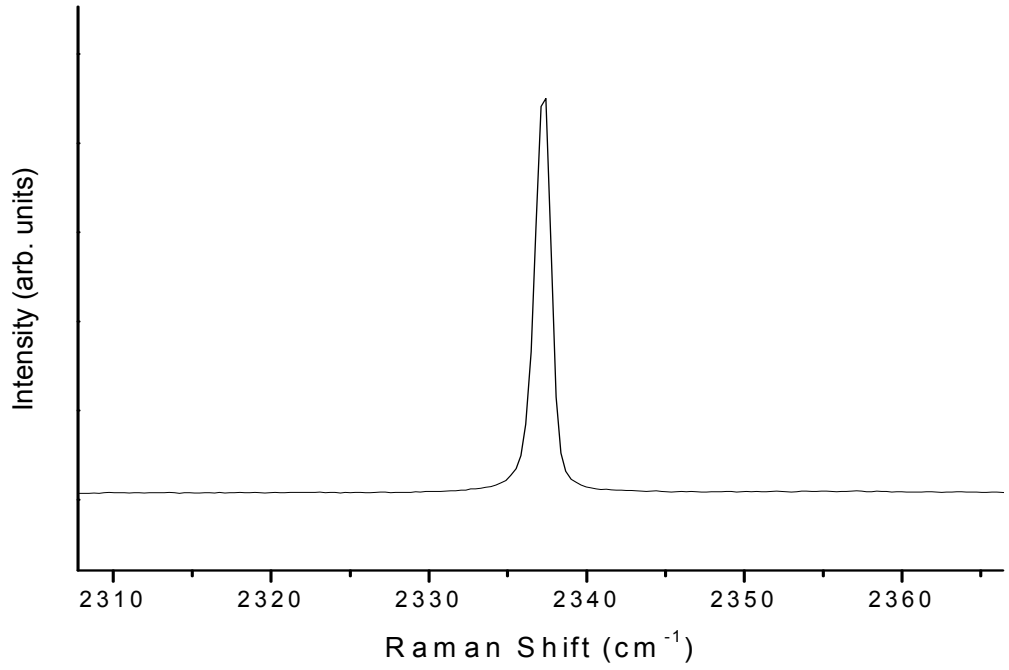

Figure 2.16: Experimental Raman spectrum of nitrogen in the β phase, from this work, taken at room temperature and 2.92 GPa**.**

Swenson *et al.*[56] determined that nitrogen crystallizes as a molecular solid with β-N_2 having a disordered hexagonal structure and speculated that a closed packed structure may exist with pressure. In this structure, it was proposed that each individual molecule rotates, or precesses, about their center of gravity. From single crystal XRD, Streib *et al.*[51] proposed that the molecules had a precession angle (θ) of 54.5˚ with respect to the c-axis. This was later refined to 56˚ by Jordan *et al.*[52] The orientational order of β-N_2 has been under debate over the years as the evidence has been conflicting. Press *et al.*[57] investigated the two proposed molecular orientations: static and disordered or precessing molecules. Their results were inconclusive as they found it difficult to distinguish between them. Figure 2.17, below, shows an example XRD pattern for N_2 at 2.94 GPa.

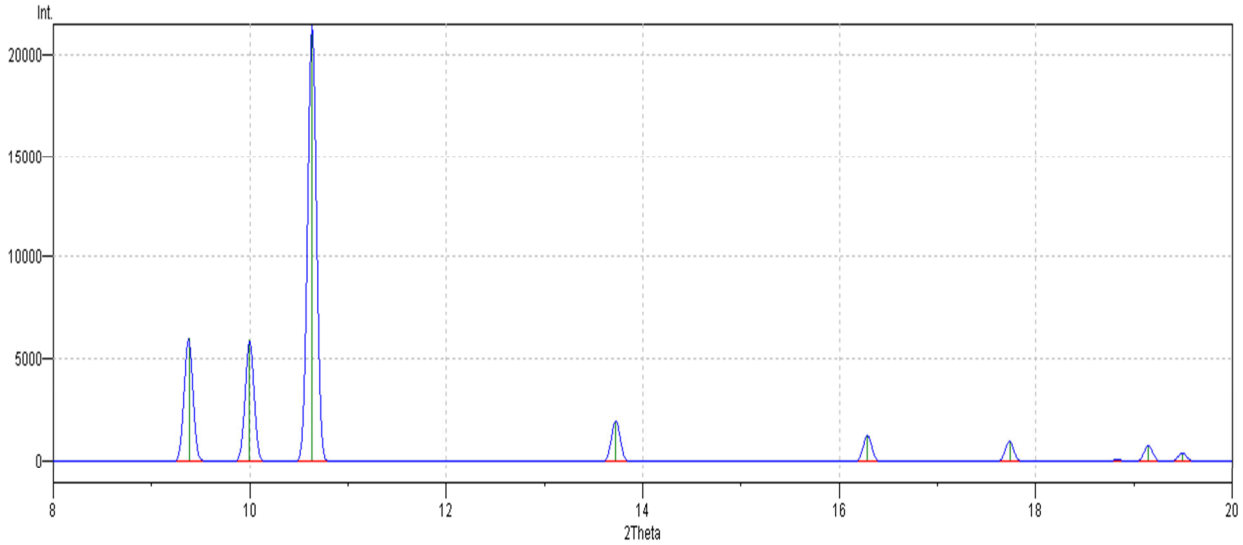

Figure 2.17: The x-ray diffraction pattern of β-N_2 at 2.94 GPa and 300 K, generated from the unit cell parameter, space group and atomic positions obtained by Schiferl *et al.*[47] with λ = 0.509176 Å.

2.3.3 δ-N_2

Nitrogen undergoes a phase transition from β- to δ-N_2 at 4.9 GPa at room temperature. The δ phase has a disordered cubic unit cell containing 8 molecules with space group *Pm*3*n*.[58] Figure 2.18 shows the basic structure of δ-N_2, which includes sphere-like molecules that are centered on the 2a Wyckoff sites at (0,0,0) and $\left(\frac{1}{2},\frac{1}{2},\frac{1}{2}\right)$, and disk-like molecules that are centered on the 6d Wyckoff sites at $\left(0,\frac{1}{4},\frac{1}{2}\right)$.[59,60]

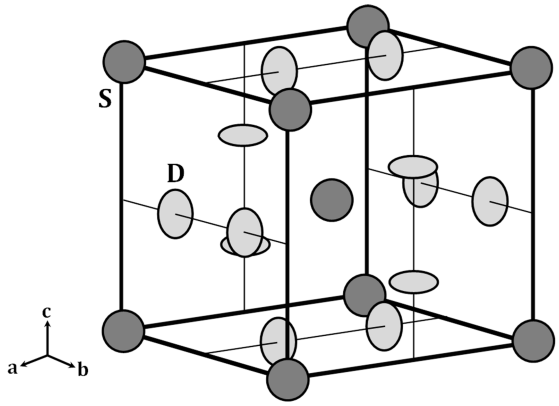

Figure 2.18: The δ-N_2 structure has a disordered cubic unit cell with disk-like (D) molecules on the faces and sphere-like molecules (S) on the corners.

The vibrational spectrum consists of two molecular stretching modes (Figure 2.19) corresponding to two different lattice sites. The low-frequency peak (ν_2) and the higher-frequency peak (ν_1) correspond to disk-like and sphere-like sites, respectively. The greater number of disk-like sites results in a higher intensity for the ν_2 vibron.

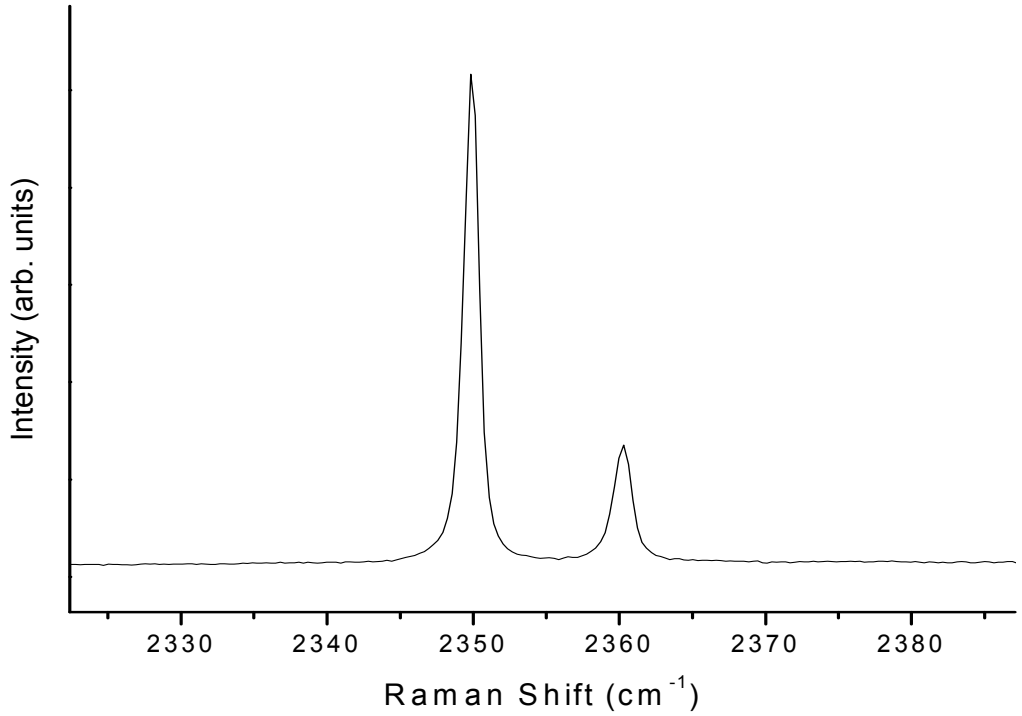

Figure 2.19: Experimental Raman spectrum of nitrogen in the δ phase, from this work, taken at room temperature and 8.83 GPa.

There has been a great deal of debate concerning the orientational behavior of the molecules. Westerhoff *et al.*[49] suggested that the sphere-like molecules had spherical disorder and the disk-like molecules favored an alignment of 45˚ to the unit cell faces. Belak *et al.*[61] found that a possible preference existed for the disk-like molecules to be parallel or perpendicular to the unit cell faces.

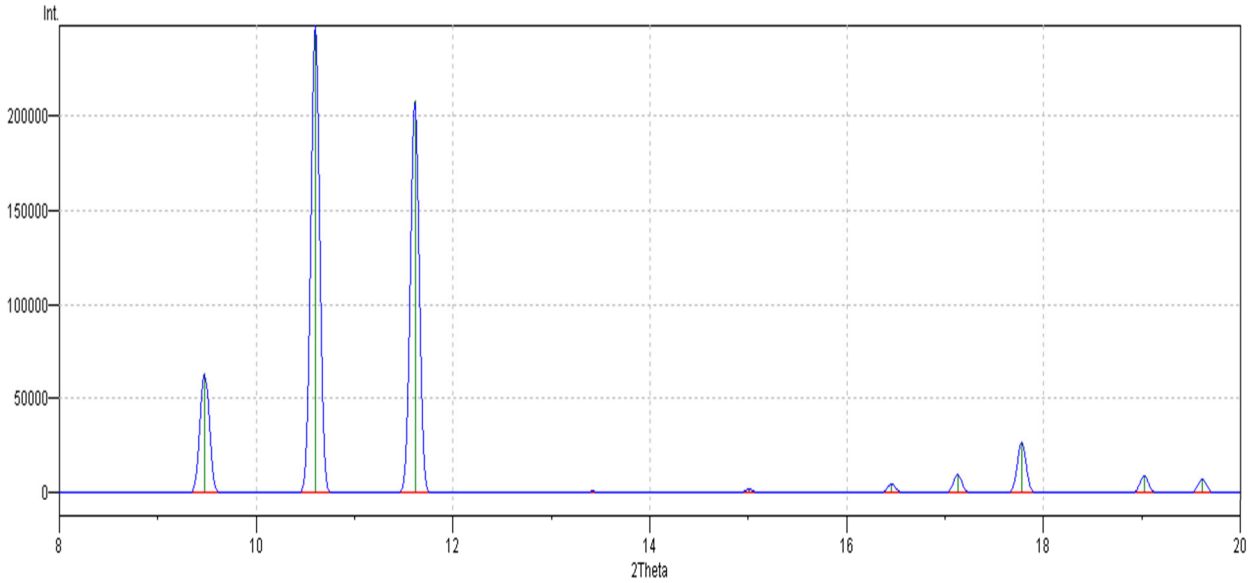

Figure 2.20: The x-ray diffraction pattern of δ-N_2 at 4.9 GPa and 299 K, generated from the unit cell, space group and atomic positions obtained by Cromer *et al.*[59] with λ = 0.509176 Å.

Mulder *et al.*[62] and Scheerboom *et al.*[63] were in agreement of a structure with a nearly spherical disorder of the sphere-like molecules and a preference for alignment with the disk-like molecules. Stinton *et al.*[60] utilized high-pressure single crystal techniques and synchrotron radiation to investigate the δ phase of nitrogen. They concluded that the spherically rotating molecules show some preference for avoiding pointing along the ⟨0,0,1⟩ directions, and the orientation of the disk-like molecules was in agreement with Cromer *et al.*[59] and Westerhoff *et al.*[49]

2.3.4 δ_{loc}-N_2

In 1993, Scheerboom *et al.*[64] discovered anomalous behavior with the orientationally disordered δ phase of nitrogen. Vibrational spectra of nitrogen as a function of temperature revealed a noticeable change of slope which is indicative of a phase change (Figure 2.21).

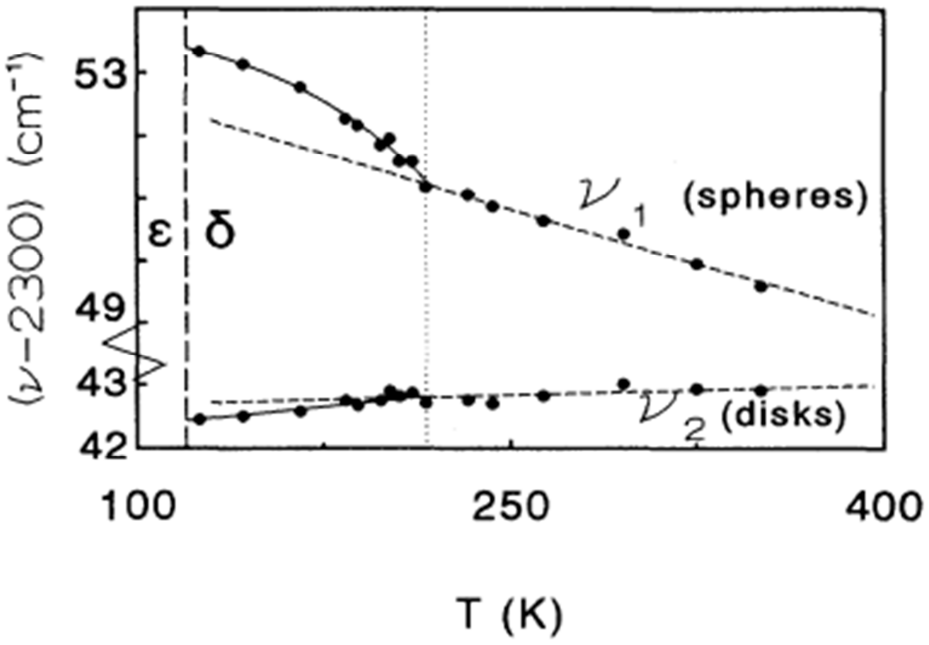

Figure 2.21: ν_1 and ν_2 (vibrons) as a function of temperature at 5.9 GPa. The vertical dotted line represents the δ- to δ_{loc}-N_2 phase transition. *Reprinted with permission from the American Physical Society, Copyright 1992.*[63]

XRD experiments were similar to δ-N_2, however, additional diffraction lines were observed above 11 GPa through to 16 GPa.[65] The XRD patterns were indexed with a tetragonal structure having 16 molecules per unit cell. The suggested structure was called δ_{loc} with space group $P4_2/ncm$ and a c/a ratio of $1/\sqrt{2}$ ~0.707. Hanfland *et al.*[65] proposed a relation between the lattice parameters of δ_{loc} and δ nitrogen with $a_{\delta_{loc}} \cong a_\delta\sqrt{2}$ *and* $c_{\delta_{loc}} \cong a_\delta$. More recent studies of δ_{loc}-N_2 by Hellwig *et al.*[66] and Stinton *et al.*[60] were in complete agreement with these conclusions, rejecting other structures and symmetries offered in the literature.

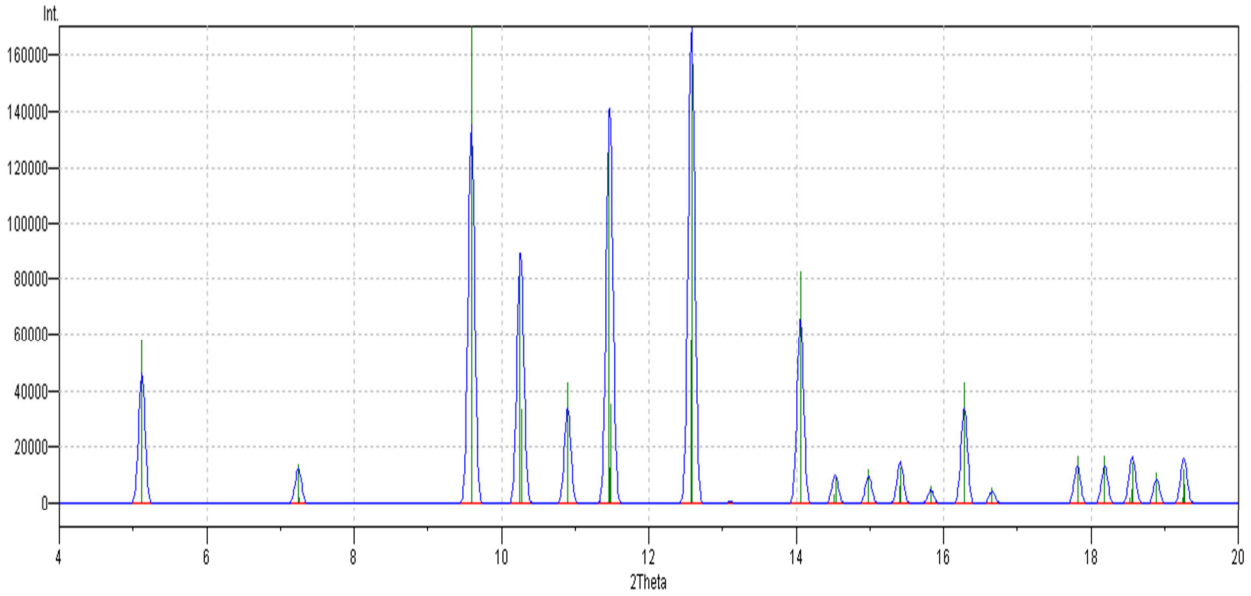

Figure 2.22: The x-ray diffraction pattern of δ_{loc}-N_2 at 14.5 GPa and 293 K, generated from the unit cell parameters, space group and atomic positions obtained by Stinton *et al.*[60] with λ = 0.509176 Å.

Similar to δ-N_2, the δ_{loc}-N_2 structure contains sphere-like and disk-like molecules. The predicted structure by Stinton *et al.*[60] is shown in Figure 2.23 and has three symmetry independent molecules. One of sphere-like molecules and two derived from the disk-like molecules. The symmetry and space group may have been confirmed by Stinton *et al.* and others; however, there are still unanswered questions. The Raman and IR-active modes observed do not match the number that has been calculated for the structure.[67,68] Stinton *et al.*[60] notes that no structure yet proposed have been able to fully characterize δ_{loc}-N_2 and further studies are required.

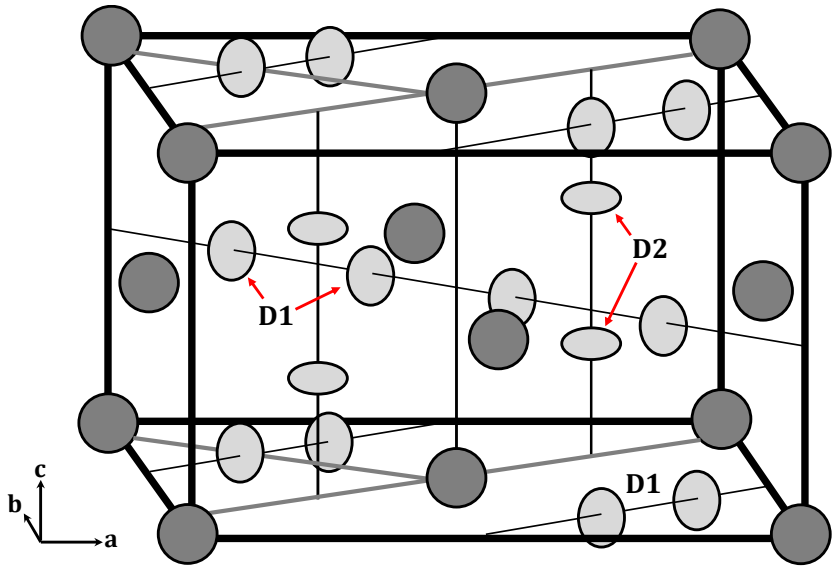

Figure 2.23: The δ_{loc}-N_2 structure has a disordered tetragonal unit cell with disk-like (D1 & D2) and sphere-like molecules (S).[60]

2.3.5 ε-N_2

The δ_{loc}- to ε-N_2 phase transition occurs at 16.3 GPa at room temperature. The ε phase has a rhombohedral unit cell containing 8 molecules with space group *R*3*c*. The rhombohedral unit cell is an extension of the cubic unit cell of δ-N_2 along the cube diagonal, together with a small displacement and ordering of the molecules. This results in a shift in the angle, α, between the axes from 90° (cubic) to 84.68° (rhombohedral ε-N_2).[69]

For ε-N_2, the sphere-like molecules of δ-N_2 (located at the center and corners of the cubic unit cell) align with the body diagonal (111). The disk-like molecules of the δ phase align 45° in the plane of the disk with respect to the normal of each face. Dependent on the angles of the unit cell, they also align at an angle, θ_d, with respect to the normal of the disk. Figure 2.24 shows the ε-N_2 structure as described by Mulder et al.[62,70]

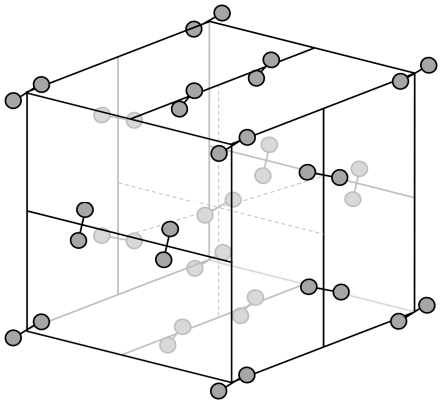

Figure 2.24: The ε-N_2 structure with a rhombohedral unit cell as described by Mulder *et al.*[62,70]

The vibrational spectrum has revealed evidence for the ε phase of nitrogen at room temperature. Two vibrons, υ_1 and υ_2, are observed for both δ- and δ_{loc}-N_2 and as pressure is increased, the ε phase is observed by a splitting of the υ_2 vibron at 16.3 GPa (Figure 2.25, (a)). In addition, the linewidths of both vibrons (υ_1 and υ_2) decrease noticeably between 16 and 18.5 GPa (Figure 2.25, (b)). Westerhoff *et al.*[49] determined that nitrogen dephasing was the dominant process for vibrational relaxation.

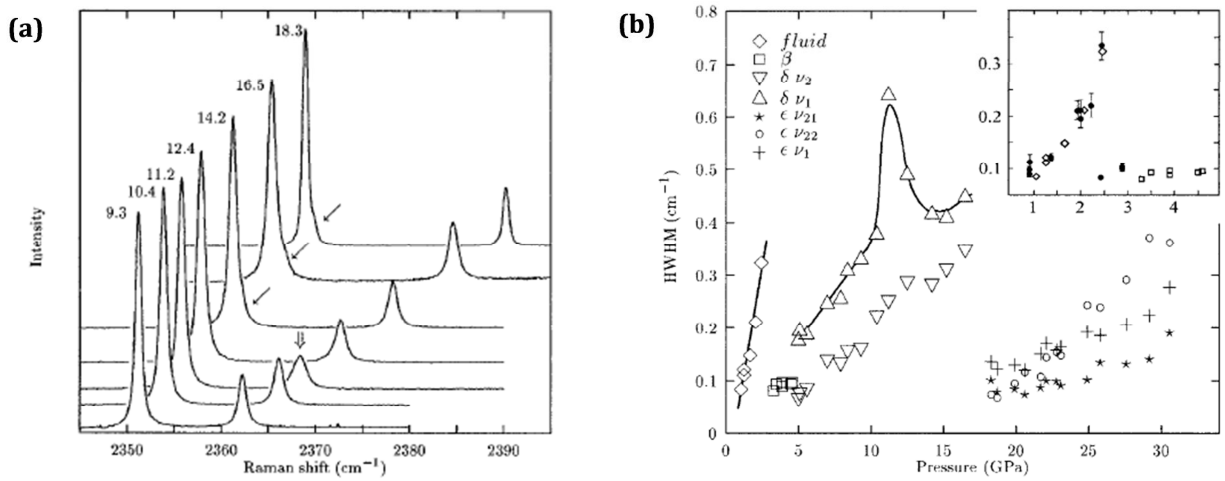

Figure 2.25: (a) The Raman shift of nitrogen at higher pressures. Single arrows on spectra at 14.2 GPa and higher indicate a splitting of the vibron in the ε phase. The double arrow at 11.2 GPa shows an anomalously broadened υ_1 vibron that is briefly discussed in Westerhoff *et al.*[49] **(b)** The half width at half maximum (HWHM) of nitrogen Raman spectra, showing the δ-ε transition around 16 GPa. The shoulder on the high frequency side of υ_2 becomes stronger with increased pressure and eventually separates from the main vibron (υ_{21}) into a new vibron (υ_{22}) above 20 GPa. The figure in the top right shows the FWHM for nitrogen at the liquid to β phase transition, which also displays a change in the slope. *Reprinted with permission from the American Physical Society, Copyright 1996.*[49]

The XRD patterns obtained at higher pressures indicate an obvious change of phase for the δ_{loc}- to ε-N_2 transition. Figure 2.26 shows an XRD pattern of ε-N_2 at lower temperature, which has a similar structure at room temperature.

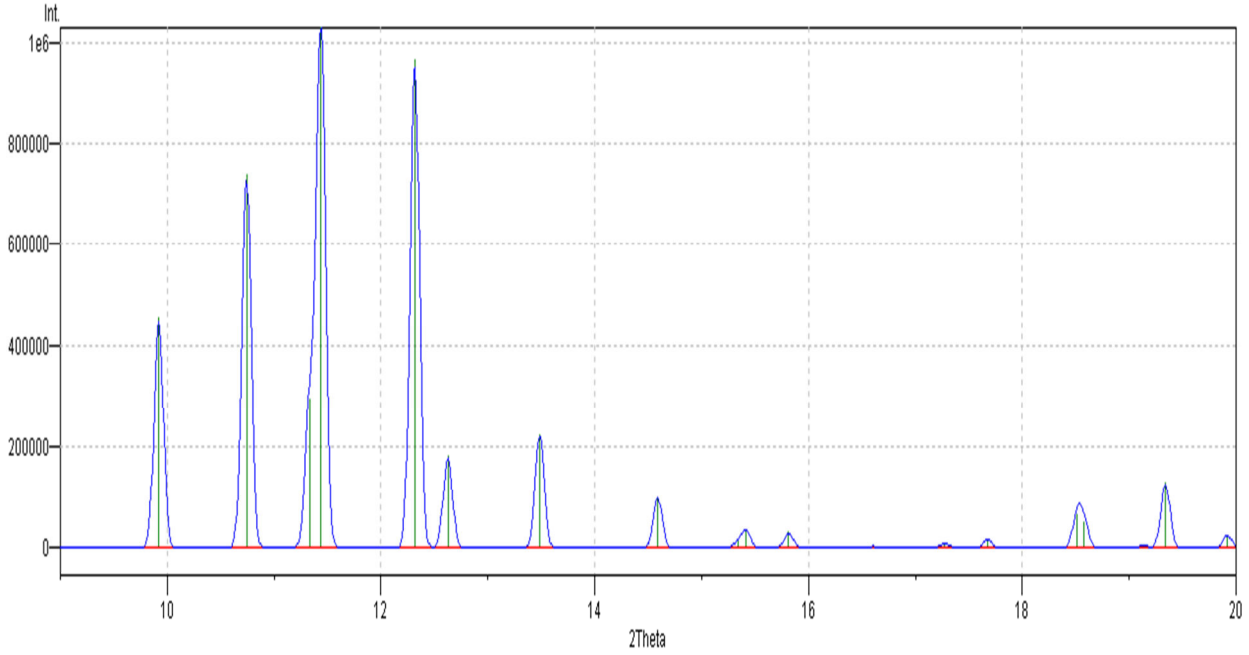

Figure 2.26: The x-ray diffraction pattern of ε-N_2 at 7.8 GPa and 110 K, generated from the unit cell parameters, space group and atomic positions obtained by Mills *et al.*[58] with λ = 0.509176 Å. At room temperature the structure is similar, with lattice parameters varying slightly.

2.3.6 Additional Phases for N_2

The complexity of the phase diagram for nitrogen is shown in Figure 2.14. Additional structures exist and are dependent on temperature and pressure. The α, γ, and ζ phases are found at lower temperatures with pressure. The ί, θ, κ and η phases have been discovered more recently and require both higher temperatures and pressures. Table 2.2 summarizes these structures.

Table 2.2: Additional structures of nitrogen found at various temperatures with pressure.

Name:	Structure:	Space Group:	Temperature Range:	Pressure Range:	References:
α	Ordered cubic	*Pa*3	Low (up to ~ 36 K)	Low (Up to 0.4 GPa)	Zinn, 1987 Olijnyk, 1990
γ	Ordered tetragonal	$P4_2/mnm$	Low (< 100 K)	Higher than α (0.4 – 2 GPa)	Mills, 1985 Olijnyk, 1990
ζ	Rhombohedral*	*R*3*c*	Lower than the ί and θ phases	High	Gregoryanz, 2007
ί	N/A**	N/A	High	High	Gregoryanz, 2002
θ	Orthorhombic**	N/A	High	High	Gregoryanz, 2002
κ	Monoclinic*	N/A	Lower than the ί and θ phases	High	Gregoryanz, 2007
η	Non-molecular*	N/A	All	High	Gregoryanz, 2002
LP-N	Layered-polymeric*	Similar to *Pba*2	High	120-180 GPa	Tomasino, 2014
cg-N	Cubic gauche*	$I2_13$	High (above 2000 K)	High (above 110 GPa)	Eremets, 2004

* *Recently discovered; more studies are required to determine exact structures and phase boundaries.*
** *Requires further investigation. Both phases are observed over a wide P-T range (30 – 1000 K and 20 – 100 GPa).*

2.3.7 The Raman Spectrum of N_2

At room temperature, the molecular stretching modes (vibrons) of nitrogen undergo changes in linewidth, splitting and shift in frequency with increasing pressure that are connected with phase transitions. The vibrational spectra consists of a single stretching mode in the fluid (P < 2.5 GPa) and β phases (2.4 < P < 4.9 GPa). The δ phase (4.9 < P < ~10.5 GPa) consists of two modes, ν_1 and ν_2, corresponding to two different lattice sites. These vibrons shift to higher frequency with increasing pressure. The δ phase transforms into the δ_{loc} phase and is observed by a change in the slope of the Raman shift of nitrogen as a function of temperature. The ε phase is observed as a splitting of the ν_2 vibron around 16.3 GPa. Figure 2.27 summarizes results for these solid phases of nitrogen.

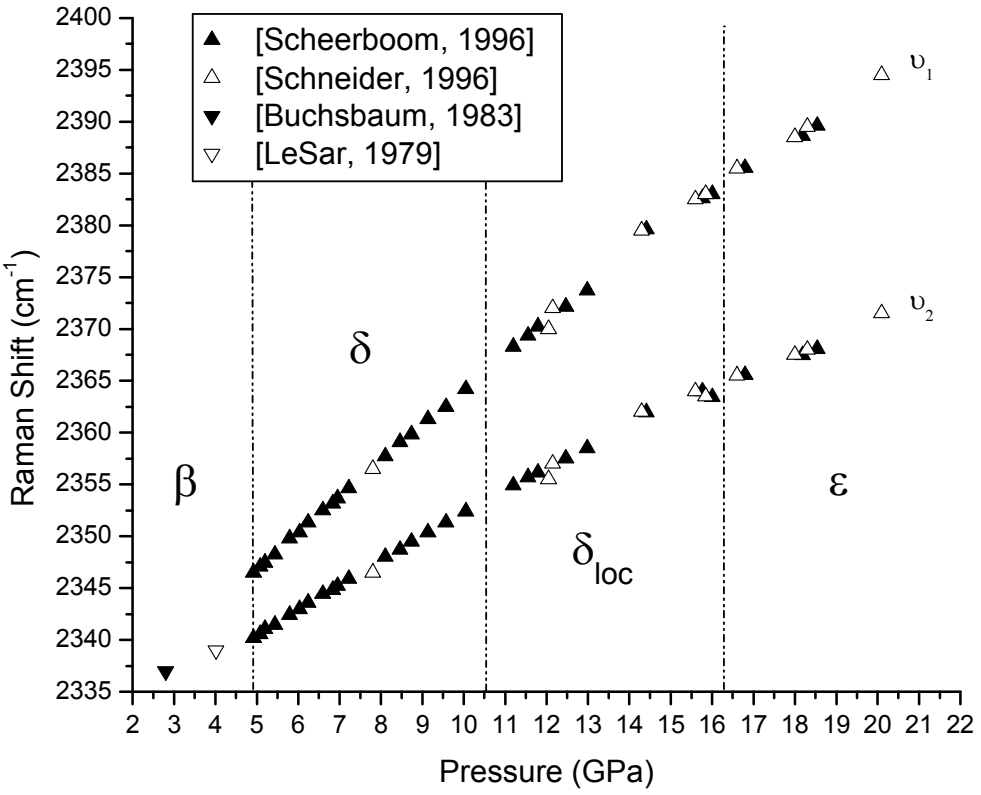

Figure 2.27: The Raman shift of nitrogen in the relevant pressure range at room temperature. In this figure the ε phase is represented with one vibron, however, this phase is usually observed by the splitting of the υ_2 vibron.

2.3.8 Equation of State of N_2

The molecular and molar volumes of solid nitrogen as a function of pressure are shown in Figure 2.28. The data was acquired from various sources. Due to a lack of data regarding δ_{loc} lattice parameters, the relation given by Hanfland *et al.*[65] ($a = a_\delta\sqrt{2}$, $c = a_\delta$ and 16 molecules per unit cell), was used to extrapolate volumes for δ_{loc} between 10.5 and 16.3 GPa.

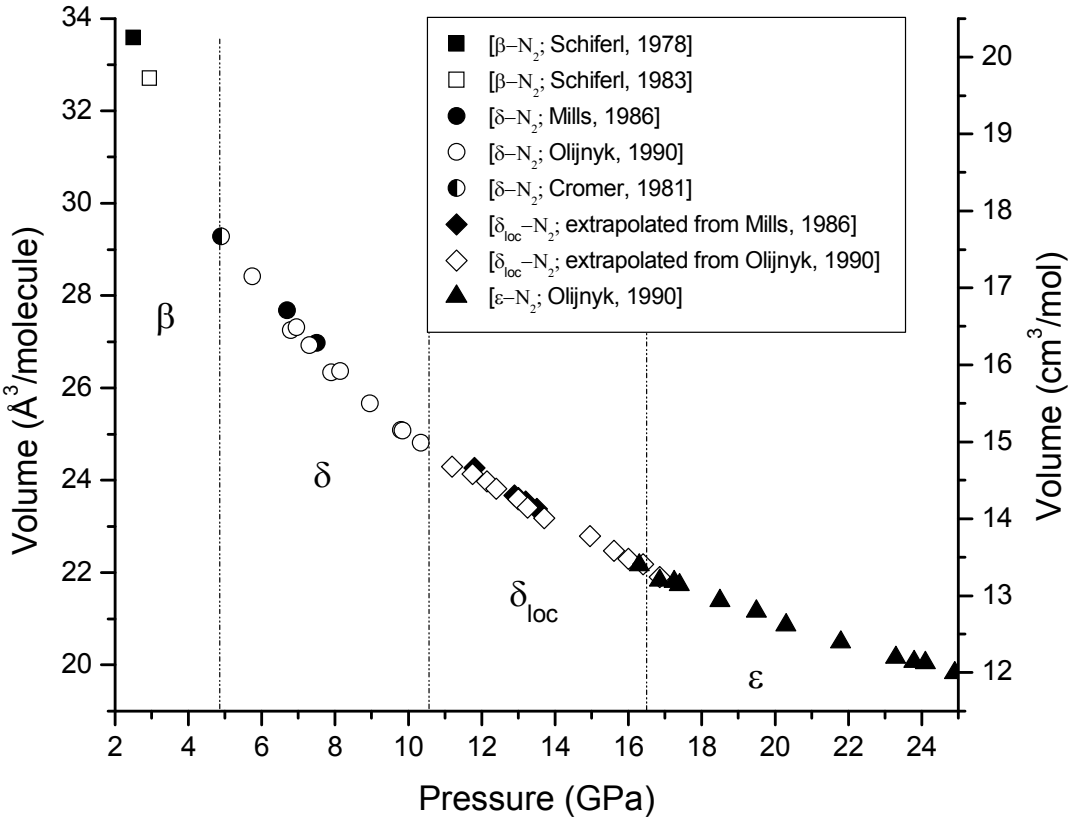

Figure 2.28: The equation of state of nitrogen. The volumes for δ_{loc}–N_2 were extrapolated from δ-N_2 results from Mills *et al.*[58] and Olijnyk *et al.*[69], and cell dimensions proposed by Stinton *et al.*[60]

2.4 Argon

2.4.1 The Phase Diagram of Argon

High-pressure experiments have shown that argon is stable in a face-centered cubic (FCC) structure at all temperatures upon compression.[71] Argon can also crystallize in a metastable form with the HCP structure. At room temperature, Errandonea *et al.*[72] observed the coexistence of FCC and HCP phases of argon at 49.6 GPa with the HCP/FCC ratio increasing with pressure. At 114 GPa, the transition was not complete and they predict that a full FCC-to-HCP transition will occur at ~300 GPa. The close packed arrangements (FCC and HCP) of atoms are the most efficient ways of filling space with identical spheres. Atoms which are attracted to each other by non-directional forces, such as noble gases, will crystallize in the FCC structure. The exception is helium which crystallizes in the HCP structure.[73] The phase diagram of argon is shown in Figure 2.29. Argon atoms are weakly bonded by van der Waals forces in the solid and liquid phases.

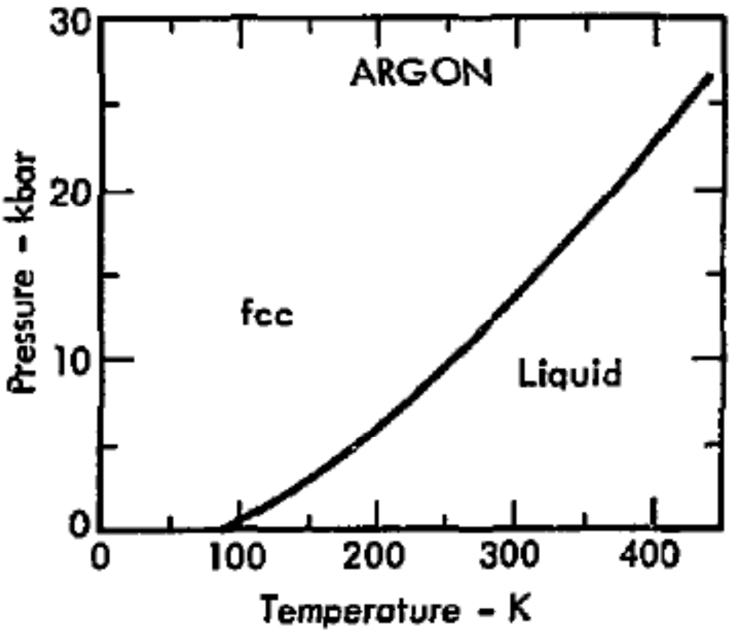

Figure 2.29: The phase diagram of argon. *Figure courtesy of David Young – Lawrence Livermore Lab.*[71,74]

2.4.2 FCC Argon

The FCC-Ar structure contains four atoms per unit cell and has space group *Fm*3*m*. The unit cell is shown in Figure 2.30. Finger *et al.*[75] found that argon has a high compressibility and produces a hydrostatic environment at high pressures. They observed that argon recrystallized and conformed to the shape of the sample chamber with a change of pressure greater than 0.3 GPa.

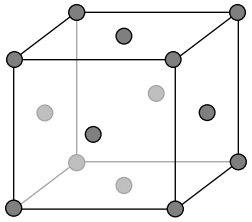

Figure 2.30: The unit cell for solid FCC-Ar.

The lattice constants of argon are sensitive to pressure and there are developments to use it as an internal x-ray pressure calibration, as an alternative to the ruby luminescence method. In addition to its high compressibility, argon has intense, well known diffraction peaks that aid in measuring the bulk modulus and pressure.[75,76]

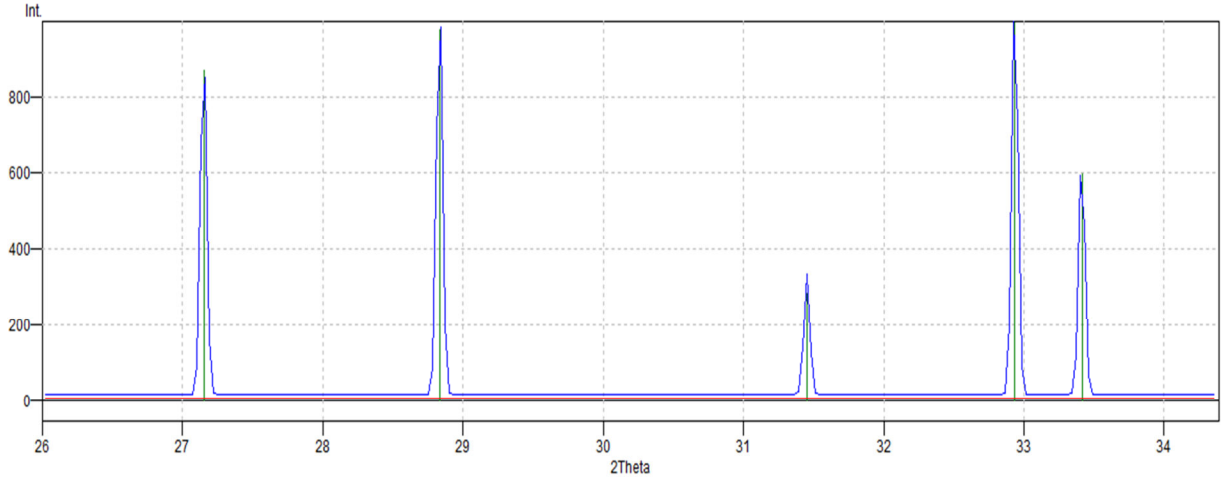

Figure 2.31: The x-ray diffraction pattern of FCC-Ar at atmospheric pressure and 20 K, generated from the unit cell parameter, the space group and atomic positions obtained by Dobbs *et al.*[77] with λ = 0.509176 Å. At room temperature with increasing pressure the structure is similar, with parameters varying slightly.

2.4.3 FCC Argon Equation of State

The solid structure preferred by argon at room temperature with pressure is face-centered cubic. Figure 2.32 summarizes the molecular and molar volume of FCC-Ar plotted as a function of pressure. Lattice parameters for the volume calculations were obtained from various sources.

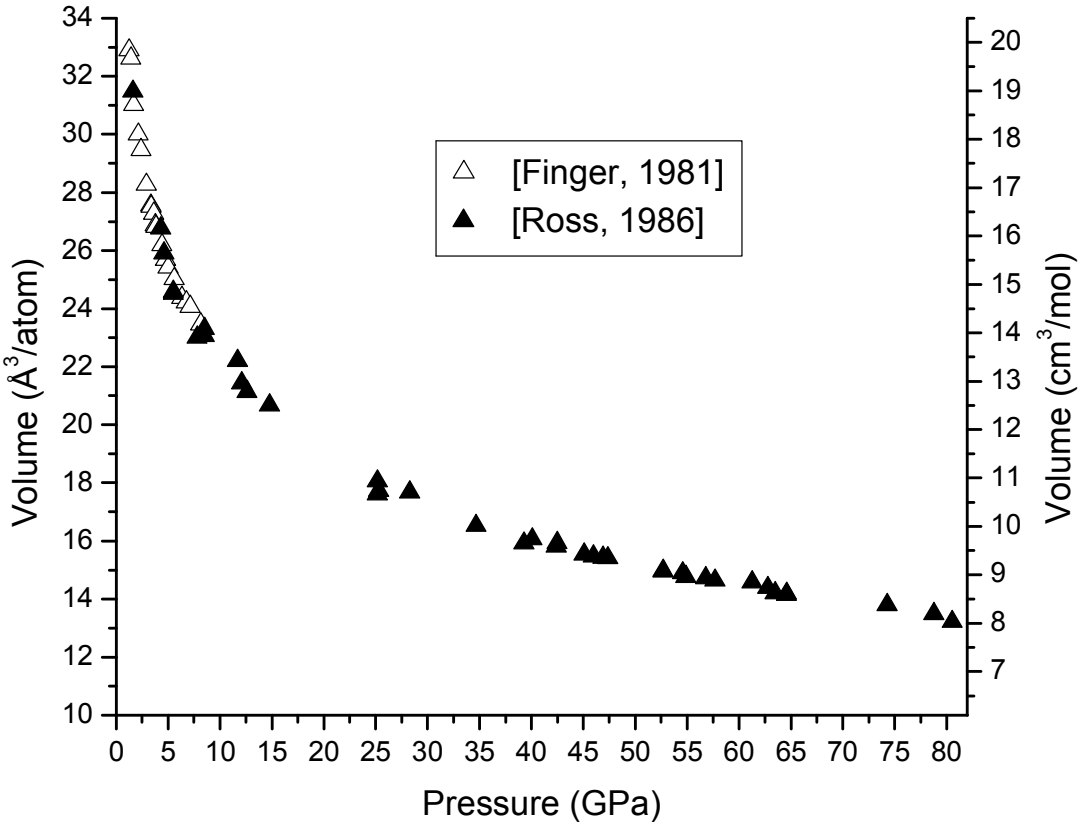

Figure 2.32: The equation of state (EOS) of FCC-Ar. The volumes were calculated from data points obtained by digitizing the published graph of Finger *et al.*[75] and Ross *et al.*[76]

2.4.4 HCP Argon

Hexagonal close packed (HCP) structures can also be observed in XRD patterns of solid argon due to similarities of the FCC and HCP structures which are composed of stacked hexagonal layers. Both structures are close packed with nearly equivalent energy levels, have a packing factor of 0.74 and a coordination number of 12. The difference between them is the packing sequence, shown in Figure 2.33. The HCP structure contains two types of planes with an alternating ABAB arrangement, while the FCC structure contains three types of planes with an alternating ABCABC arrangement.

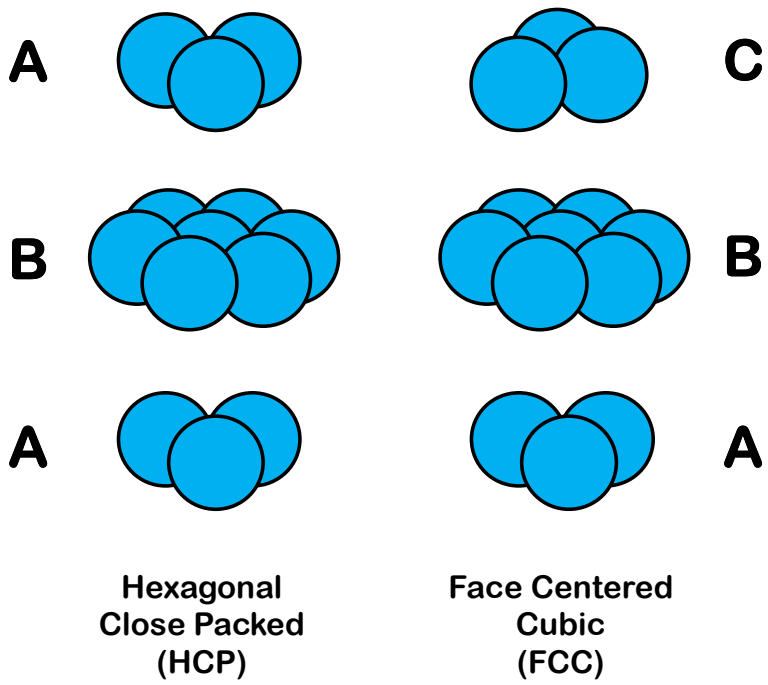

Figure 2.33: The stacking sequence of HCP and FCC structures.

All solids that form from noble gases will be close packed structures because they are considered spherical. When a crystal forms, faults in the stacking can result in an ABAB arrangement and a HCP structure (Figure 2.34) will be observed. If these stacking faults are observed with XRD, they will be far less intense than the FCC structure.

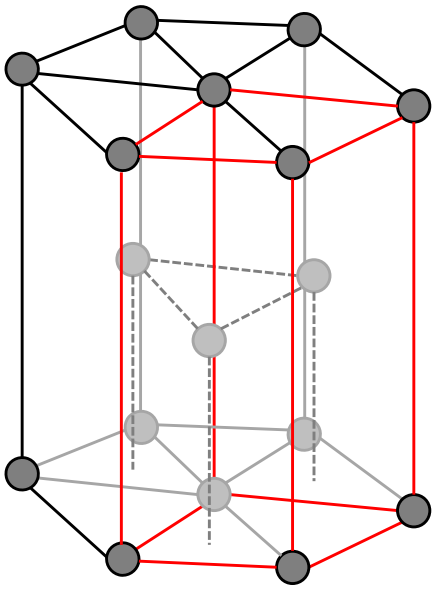

Figure 2.34: The structure of HCP-Ar. The unit cell is shown in red.

At room temperature, the FCC structure is preferred at higher pressures, however, dependent on the method employed to crystallize argon, individual HCP crystals may be grown. Low-temperature experiments have led to metastable HCP phases which become more stable with the addition of impurities (oxygen, nitrogen).[78] Wittlinger *et al.*[79] found a way to crystallize argon in the HCP structure (space group: $P6_3/mmc$) by cryogenically loading a sample in a diamond anvil cell and subsequently heating it up to room temperature. It was discovered that if a pressure above 1.2 GPa was reached under liquid argon conditions (Ar boiling point: 87.3 K, -185.9 °C) and then heated to room temperature, the HCP structure would then crystallize. However, if the pressure was initially lower than 1.2 GPa before heating, the FCC structure will be observed. The quality of the HCP crystals was found to deteriorate with increasing pressure up to 8.5 GPa. The crystals could be recreated by heating the cell to 393 K at 8.5 GPa, accompanied by a pressure decrease (>1 GPa). Figure 2.35 shows an XRD pattern for HCP-Ar generated from results obtained by Wittlinger *et al.*[79] In additions, mixed FCC-HCP argon has also been reported in the literature.[80]

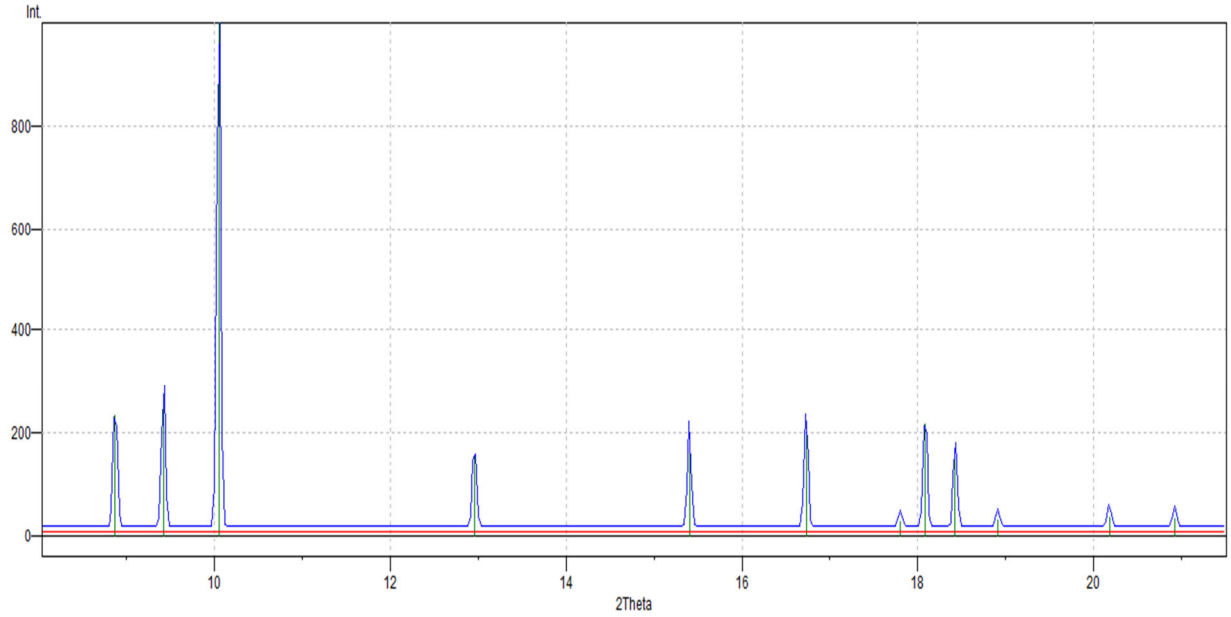

Figure 2.35: The x-ray diffraction pattern of HCP-Ar at 6.5 GPa and 299 K, generated from the unit cell parameters, the space group and atomic positions obtained by Wittlinger *et al.*[79] with λ = 0.509176 Å.

2.4.5 HCP Argon Equation of State

Wittlinger et al.[79] described the pressure dependence on the HCP-Ar structure they observed with the following third order Birch-Murnaghan equation of state (EOS):

$$P(V) = \frac{3K_0}{2}\left[\left(\frac{V_0}{V}\right)^{\frac{7}{3}} - \left(\frac{V_0}{V}\right)^{\frac{5}{3}}\right]\left\{1 + \frac{3}{4}(K_0{}' - 4)\left[\left(\frac{V_0}{V}\right)^{\frac{2}{3}} - 1\right]\right\} \quad (2.3)$$

with the bulk modulus, K_0, the derivative of the bulk modulus, K_0', the initial volume (ambient pressure volume),V_0, the corresponding volume of the unit cell, V, with pressure, P. Measurements taken by Wittlinger *et al.*[79] occurred in a small pressure range, so K_0' was set equal to 4 to omit the

last term in Equation 2.3 as its effects would be negligible. Their fit gave a bulk modulus of K_0 = 6.5 GPa, V_o = 78 Å^3, which corresponds to a HCP structure with lattice constants a = 3.8 Å, and c = 6.2 Å. The molecular and molar volumes of HCP-Ar as a function of pressure are shown in Figure 2.36. The data was acquired from Wittlinger *et al*.[79]

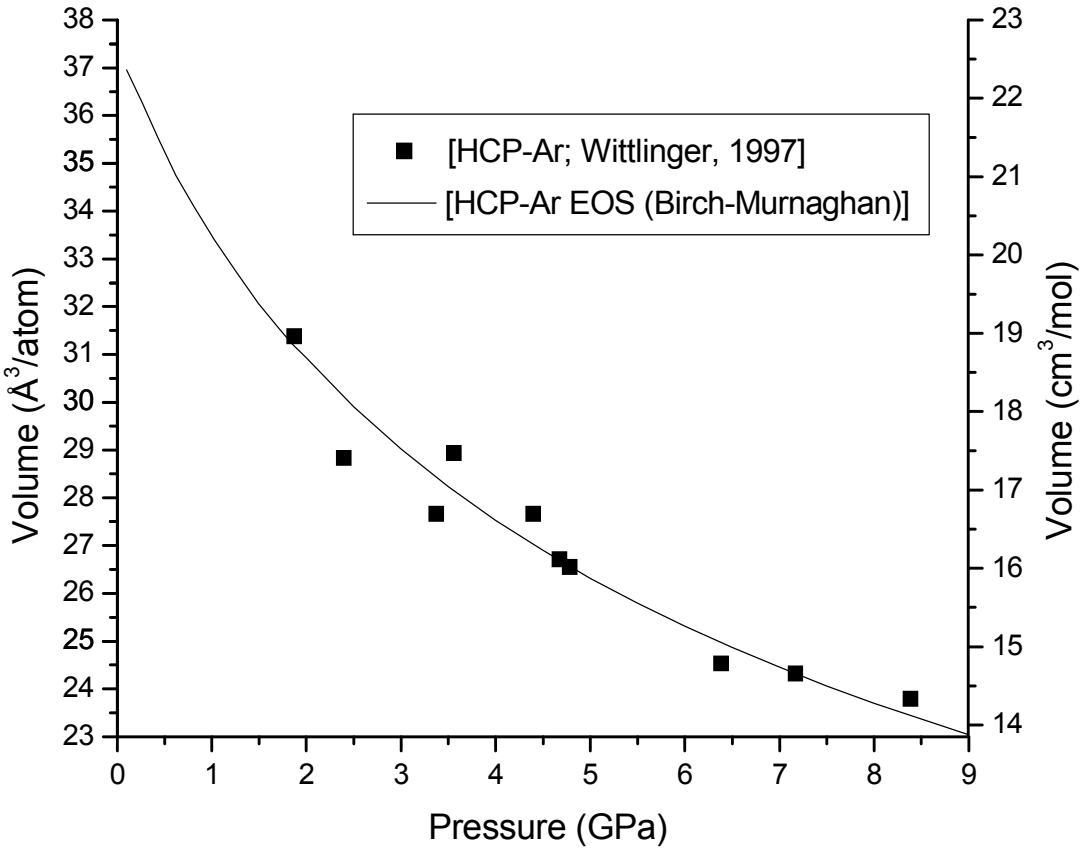

Figure 2.36: The equation of state of HCP-Ar at room temperature with a bulk modulus of K_0 = 6.5 GPa and V_o = 78 Å^3. The volumes were calculated from data points obtained by digitizing the published graph of Wittlinger *et al.*[79]

2.5 Krypton

2.5.1 The Phase Diagram of Krypton

Krypton, a noble gas, will crystallize similar to argon in the FCC structure with four atoms per unit cell and space group *Fm*3*m*. High pressure experiments have shown that krypton is also stable in the FCC structure at all temperatures with pressure. High pressure melting curves of krypton have been studied and up to about 30 GPa the measurements for krypton were in good agreement with theoretical predictions. Above 30 GPa an anomalous lowering in the melting slope was observed and it was attributed to the presence of stacking faults.[81] The phase diagram of krypton is presented below in Figure 2.37.

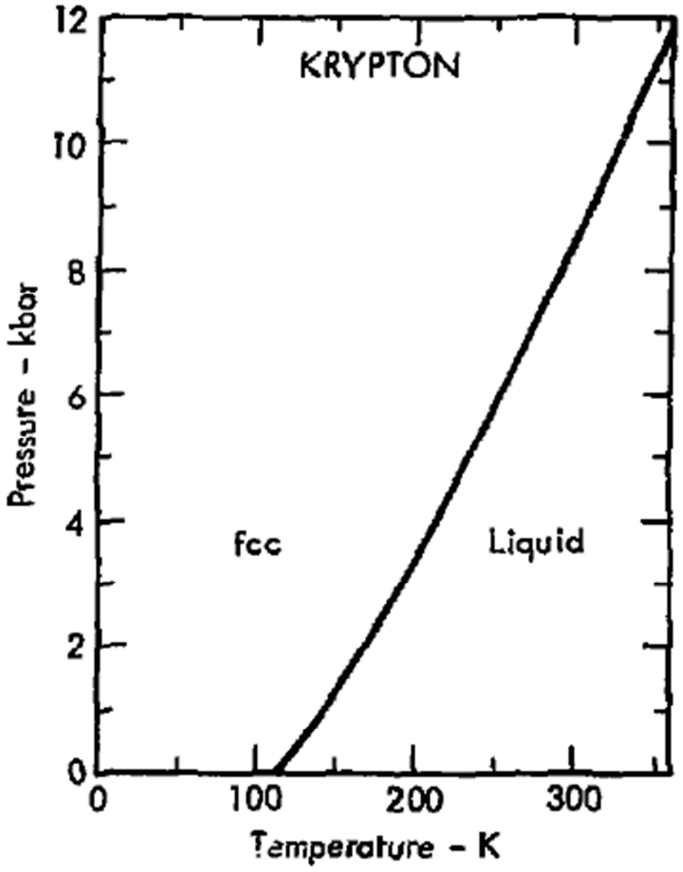

Figure 2.37: The phase diagram of krypton. *Figure courtesy of David Young – Lawrence Livermore Lab.*[74,82,83]

2.5.2 The Structure of Krypton and the Equation of State

The solid structure of krypton at room temperature with pressure is the face-centered cubic structure. Figure 2.38 summarizes the molecular and molar volume of FCC-Kr plotted as a function of pressure. Lattice parameters for the volume calculations were obtained from various sources. Similar to the pure Ar system, stacking faults resulting in an HCP structure have also been observed for Kr.[81,84]

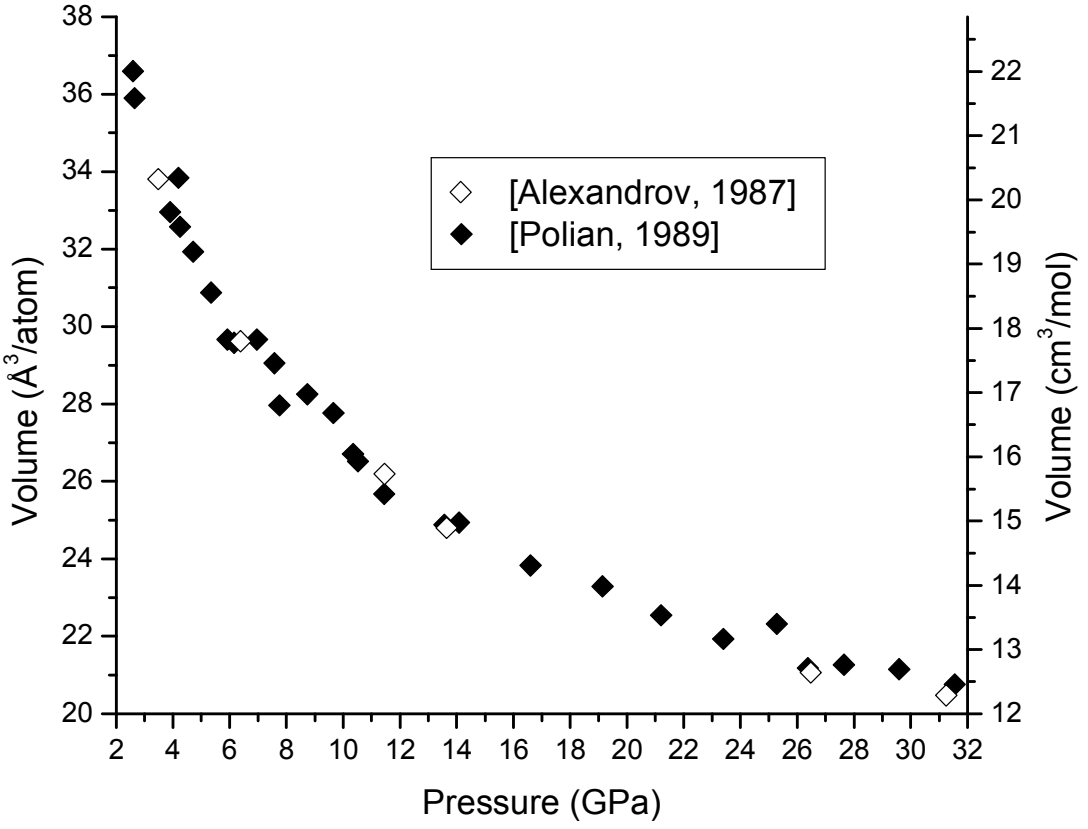

Figure 2.38: The equation of state of FCC-Kr. The volumes were calculated from data points obtained by digitizing the published graph of Alexandrov *et al.*[85] and Polian *et al.*[86]

References

1. Bartels-Rausch, T. *et al.* Ice structures, patterns, and processes: A view across the icefields. *Rev. Mod. Phys.* **84,** 885–944 (2012).

2. Debenedetti, P. G., Ricci, M. A. & Bruni, F. *Proceedings of the International School of Physics 'Enrico Fermi' Course 187; Water: Fundamentals as the Basis for Understanding the Environment and Promoting Technology*. (IOS, Amsterdam; SIF Bologna, 2015).

3. Hirsch, J. E. & Marsiglio, F. Hole superconductivity in H2S and other sulfides under high pressure. *Phys. C Supercond. its Appl.* **511,** 45–49 (2015).

4. Dziewonski, A. M. & Anderson, D. L. Preliminary reference Earth model. *Phys. Earth Planet. Inter.* **25,** 297–356 (1981).

5. Halliday, D. *Fundamentals of Physics 6 E*. (Wiley, New York, 2001).

6. Williams, R. Sun Fact Sheet. (2015). at <http://nssdc.gsfc.nasa.gov/planetary/factsheet/sunfact.html>

7. Dubrovinsky, L. *et al.* The most incompressible metal osmium at static pressures above 750 gigapascals. *Nature* **525,** 226–229 (2015).

8. Parsegian, V. A. *Van der Waals Forces: A Handbook for Biologists, Chemists, Engineers, and Physicists*. (Cambridge University Press, New York, 2005).

9. Hiemenz, P. C. & Rajagopalan, R. *Principles of Colloid and Surface Chemistry, Third Edition, Revised and Expanded*. (CRC Press, Roca Raton, FL, 1997).

10. Masuda, H., Higashitani, K. & Yoshida, H. *Powder Technology: Fundamentals of Particles, Powder Beds, and Particle Generation*. (CRC Press, Roca Raton, FL, 2006).

11. Hillert, M. *Phase Equilibria, Phase Diagrams and Phase Transformations: Their Thermodynamic Basis*. (Cambridge University Press, New York, 2007).

12. Kakani, S. L. & Kakani, A. *Material Science*. (New Age International Pvt Ltd, New Delhi, 2010).

13. Ciezak, J. Metastable Polymeric Nitrogen: The Ultimate Green High-Energy-Density Material. *Army Res. Lab. Tech. Rep. No. ARL-TR-4478* (2008).

14. McMahan, A. K. & Lesar, R. Pressure dissociation of solid nitrogen under 1 Mbar. *Phys. Rev. Lett.* **54,** 1929–1932 (1985).

15. Mailhiot, C., Yang, L. H. & McMahan, A. K. Polymeric nitrogen. *Phys. Rev. B* **46,** 14419–14435 (1992).

16. Barbee, T. W. Metastability of atomic phases of nitrogen. *Phys. Rev. B* **48,** 9327–9330 (1993).

17. Mitáš, L. & Martin, R. Quantum Monte Carlo of nitrogen: atom, dimer, atomic, and molecular solids. *Phys. Rev. Lett.* **72,** 2438–2441 (1994).

18. Yakub, E. S. Diatomic fluids at high pressures and temperatures: a non-empirical approach. *Phys. B Condens. Matter* **265,** 31–38 (1999).

19. Alemany, M. & Martins, J. Density-functional study of nonmolecular phases of nitrogen: Metastable phase at low pressure. *Phys. Rev. B* **68,** 1–4 (2003).

20. Eremets, M. I., Gavriliuk, A. G., Trojan, I. A., Dzivenko, D. A. & Boehler, R. Single-bonded cubic form of nitrogen. *Nat. Mater.* **3,** 558–563 (2004).

21. Reichlin, R., Schiferl, D., Martin, S., Vanderborgh, C. & Mills, R. L. Optical studies of nitrogen to 130 GPa. *Phys. Rev. Lett.* **55,** 1464–1467 (1985).

22. Bell, P. M., Mao, H. K. & Hemley, R. J. Observations of solid H2, D2 and N2 at pressures around 1.5 Mbar at 25°C. *Phys. B+C* **139-140,** 16–20 (1986).

23. Goncharov, A. F., Gregoryanz, E., Mao, H. K., Liu, Z. & Hemley, R. J. Optical evidence for a nonmolecular phase of nitrogen above 150 GPa. *Phys. Rev. Lett.* **85,** 1262–1265 (2000).

24. Eremets, M. I., Hemley, R. J., Mao Hk & Gregoryanz, E. Semiconducting non-molecular nitrogen up to 240 GPa and its low-pressure stability. *Nature* **411,** 170–174 (2001).

25. Eremets, M. I., Gavriliuk, a. G. & Trojan, I. a. Single-crystalline polymeric nitrogen. *Appl. Phys. Lett.* **90,** 1–4 (2007).

26. Tomasino, D., Kim, M., Smith, J. & Yoo, C.-S. Pressure-Induced Symmetry-Lowering Transition in Dense Nitrogen to Layered Polymeric Nitrogen (LP-N) with Colossal Raman Intensity. *Phys. Rev. Lett.* **113,** 1–5 (2014).

27. Yakub, L. N. Phase Diagram of Polymeric Nitrogen. *Low Temp. Phys.* **41,** 576–581 (2015).

28. Eremets, M. I. *High Pressure Experimental Methods*. (Oxford University Press, New York/Tokyo, 1996).

29. Hirshberg, B., Gerber, R. B. & Krylov, A. I. Calculations predict a stable molecular crystal of N8. *Nat. Chem.* **6,** 52–6 (2014).

30. Sun, M., Yin, Y. & Pang, Z. Predicted new structures of polymeric nitrogen under 100–600GPa. *Comput. Mater. Sci.* **98,** 399–404 (2015).

31. Wang, X., Li, J., Zhu, H., Chen, L. & Lin, H. Polymerization of nitrogen in cesium azide under modest pressure. *J. Chem. Phys.* **141,** (2014).

32. Zhang, M., Yan, H., Wei, Q. & Liu, H. A new high-pressure polymeric nitrogen phase in potassium azide. *RSC Adv.* **5,** 11825–11830 (2015).

33. Vos, W. L. *et al.* A high-pressure van der Waals compound in solid nitrogen-helium mixtures. *Nature* **358,** 46–48 (1992).

34. Schouten, J. A. Recent advances in the study of high-pressure binary systems. *J. Phys. Condens. Matter* **7,** 469–482 (1995).

35. Kooi, M. & Schouten, J. High-pressure Raman investigation of mutual solubility and compound formation in Xe-N2 and Ne-N2. *Phys. Rev. B* **60,** 12635–12643 (1999).

36. Loubeyre, P. *et al.* X-ray diffraction and equation of state of hydrogen at megabar pressures. *Nature* **383,** 702–704 (1996).

37. Loubeyre, P. Compounds of simple molecular systems at high pressure. *High Press. Res.* **14,** 353–361 (1996).

38. Kleppe, A. K., Amboage, M. & Jephcoat, A. P. New high-pressure van der Waals compound Kr(H2)4 discovered in the krypton-hydrogen binary system. *Sci. Rep.* **4,** 4989 (2014).

39. Lotz, H. & Schouten, J. Phase behavior of the N2-Ar system at high pressures: A Raman spectroscopy study. *Phys. Rev. B* **64,** 1–6 (2001).

40. Aldous, C. *Novel van der Waals Compounds in the Nitrogen-Methane Binary System at Room Temperature and High Pressure. Thesis*. (University of Ottawa, 2010).

41. Kooi, M. E. & Schouten, J. A. Raman spectra and phase behavior of the mixed solid N2 -Ar at high pressure. *J. Low Temp. Phys.* **57,** 407–413 (1998).

42. Kooi, E. & Schouten, J. Influence of Argon on the Phase Behavior and Vibrational Properties of Solid Nitrogen at High Pressure. *J. Low Temp. Phys.* **111,** 349–355 (1998).

43. Lotz, H. & Schouten, J. Vibrational line broadening in the mixed solid N2–Kr: A high-pressure Raman study of the phase diagram. *Phys. Rev. B* **64,** 1–8 (2001).

44. Lotz, H. T., Michels, J. P. J. & Schouten, J. A. Vibrational line broadening in the solid system N2-Kr: A molecular dynamics study. *J. Chem. Phys.* **117,** 7245 (2002).

45. Gregoryanz, E. *et al.* High P-T transformations of nitrogen to 170 GPa. *J. Chem. Phys.* **126,** 1–5 (2007).

46. Peiris, S. M. & Piermarini, G. J. *Static Compression of Energetic Materials*. (Springer-Verlag, Heidelberg, Germany, 2008).

47. Schiferl, D. *et al.* Structure of N2 at 2.94 GPa and 300 K. *Acta Crystallogr. Sect. C Cryst. Struct. Commun.* **39,** 1151–1153 (1983).

48. Schiferl, D., Buchsbaurn, S. & Mills, R. L. Phase Transitions in Nitrogen Observed by Raman Spectroscopy from 0.4 to 27.4 GPa at 15 K. *J. Phys. Chem.* **89,** 2324–2330 (1985).

49. Westerhoff, T., Wittig, a. & Feile, R. High-pressure Raman scattering of the stretching mode in nitrogen along the 300-K isotherm. *Phys. Rev. B* **54,** 14–17 (1996).

50. Zinn, A. S., Schiferl, D. & Nicol, M. F. Raman spectroscopy and melting of nitrogen between 290 and 900 K and 2.3 and 18 GPa. *J. Chem. Phys.* **87,** 1267 (1987).

51. Streib, W. E., Jordan, T. H. & Lipscomb, W. N. Single-Crystal X-Ray Diffraction Study of β Nitrogen. *J. Chem. Phys.* **37,** 2962 (1962).

52. Jordan, T. H., Smith, H. W., Streib, W. E. & Lipscomb, W. N. Single-Crystal X-Ray Diffraction Studies of α-N2 and β-N2. *J. Chem. Phys.* **41,** 756 (1964).

53. Schuch, A. F. Crystal Structures of the Three Modifications of Nitrogen 14 and Nitrogen 15 at High Pressure. *J. Chem. Phys.* **52,** 6000 (1970).

54. Buchsbaum, S., Mills, R. L. & Schiferl, D. Phase diagram of nitrogen determined by Raman spectroscopy from 15 to 300 K at pressures to 52 GPa. *J. Phys. Chem.* **88,** 2522–2525 (1984).

55. Hemley, R. J. Effects of High Pressure on Molecules. *Annu. Rev. Phys. Chem.* **51,** 763–800 (2000).

56. Swenson, C. A. New Modification of Solid Nitrogen. *J. Chem. Phys.* **23,** 1963 (1955).

57. Press, W. & Hüller, a. On the orientational order in β-nitrogen. *J. Chem. Phys.* **68,** 4465 (1978).

58. Mills, R. L., Olinger, B. & Cromer, D. T. Structures and phase diagrams of N2 and CO to 13 GPa by x-ray diffraction. *J. Chem. Phys.* **84,** 2837 (1986).

59. Cromer, D. T., Mills, R. L., Schiferi, D. & Schwalbe, L. A. The structure of N2 at 49 kbar and 299 K. *Acta Crystallogr. Sect. B Struct. Crystallogr. Cryst. Chem.* **37,** 8–11 (1981).

60. Stinton, G. W., Loa, I., Lundegaard, L. F. & McMahon, M. I. The crystal structures of δ and δ* nitrogen. *J. Chem. Phys.* **131,** (2009).

61. Belak, J., LeSar, R. & Etters, R. D. Calculated thermodynamic properties and phase transitions of solid N2 at temperatures 0≤T≤300 K and pressures 0≤P≤100 GPa. *J. Chem. Phys.* **92,** 5430 (1990).

62. Mulder, A., Michels, J. & Schouten, J. ε-δ phase transition of nitrogen and the orientational behavior of the second-order transition within the δ phase: A Monte Carlo study at 7.0 GPa. *Phys. Rev. B* **57,** 7571–7580 (1998).

63. Scheerboom, M. I. M. & Schouten, J. A. Anomalous behavior of the vibrational spectrum of the high-pressure delta phase of nitrogen: A second-order transition. *Phys. Rev. Lett.* **71,** 2252–2255 (1993).

64. Scheerboom, M. I. M. & Schouten, J. A. Anomalous Behaviour of the Vibrational Spectrum of the High-Pressure Delta Phase of Nitrogen: A Second-Order Transition. **71,** 2252–2255 (1993).

65. Hanfland, M., Lorenzen, M., Wassilew-Reul, C. & Zontone, F. Structures of Molecular Nitrogen at High Pressures. *Rev. High Press. Sci. Technol.* **7,** 787–789 (1998).

66. Hellwig, H. *et al.* Coherent anti-Stokes Raman scattering spectroscopy of solid nitrogen to 22 GPa. *J. Chem. Phys.* **115,** 10876–10882 (2001).

67. Bini, R., Jordan, M., Ulivi, L. & Jodl, H. J. Infrared and Raman studies on high pressure phases of solid N[sub 2]: An intermediate structural modification between ε and δ phases. *J. Chem. Phys.* **108,** 6849 (1998).

68. Bini, R., Ulivi, L., Kreutz, J. & Jodl, H. J. High-pressure phases of solid nitrogen by Raman and infrared spectroscopy. *J. Chem. Phys.* **112,** 8522 (2000).

69. Olijnyk, H. High pressure x-ray diffraction studies on solid N2 up to 43.9 GPa. *J. Chem. Phys.* **93,** 8968 (1990).

70. Mulder, A., Michels, J. P. J. & Schouten, J. The importance of the anisotropic energy term for the structure of the solid phases of nitrogen. *J. Chem. Phys.* **105,** 3235 (1996).

71. Grace, J. D. & Kennedy, G. C. The melting curve of five gases to 30 kb. **28,** 977–982 (1967).

72. Errandonea, D., Boehler, R., Japel, S., Mezouar, M. & Benedetti, L. R. Structural transformation of compressed solid Ar: An x-ray diffraction study to 114 GPa. *Phys. Rev. B - Condens. Matter Mater. Phys.* **73,** 2–5 (2006).

73. Atkins, P. W., Rourke, J. P., Weller, M. T. & Armstrong, F. A. *Shriver and Atkins' Inorganic Chemistry 5th Edition*. (Oxford University Press, New York, 2010).

74. Young, D. Phase diagrams of the elements. *Lawrence Livermore Lab.* 64 (1975). doi:10.2172/4010212

75. Finger, L. W., Hazen, R. M., Zou, G., Mao, H. K. & Bell, P. M. Structure and compression of crystalline argon and neon at high pressure and room temperature. *Appl. Phys. Lett.* **39,** 892–894 (1981).

76. Ross, M., Mao, H. K., Bell, P. M. & Xu, J. A. The equation of state of dense argon: A comparison of shock and static studies. *J. Chem. Phys.* **85,** 1028–1033 (1986).

77. Dobbs, E. R., Figgins, B. F., Jones, G. O., Piercey, D. C. & Riley, D. P. Density and Expansivity of Solid Argon. *Nature* **178,** 483 (1956).

78. Meyer, L., Barrett, C. S. & Haasen, P. New Crystalline Phase in Solid Argon and Its Solid Solutions. *J. Chem. Phys.* **40,** 2744 (1964).

79. Wittlinger, J., Fischer, R., Werner, S., Schneider, J. & Schulz, H. High-Pressure Study of h.c.p. Argon. *Acta Crystallogr. Sect. B Struct. Sci.* **53,** 745–749 (1997).

80. Danil'chenko, A. G., Kovalenko, S. I. & Samovarov, V. N. Electron diffraction analysis of the FCC–HCP transition in argon clusters with a change in cluster size. *Low Temp. Phys.* **34,** 966 (2008).

81. Boehler, R., Ross, M., Söderlind, P. & Boercker, D. B. High-pressure melting curves of argon, krypton, and xenon: Deviation from corresponding states theory. *Phys. Rev. Lett.* **86,** 5731–5734 (2001).

82. Lahr, P. H. & Eversole, W. G. Compression Isotherms of Argon, Krypton, and Xenon Through the Freezing Zone. *J. Chem. Eng. Data* **7,** 42 (1962).

83. Crawford, R. K. & Daniels, W. B. Experimental Determination of the P-T Melting Curves of Kr, Ne, and He. *J. Chem. Phys.* **55,** 5651–5656 (1971).

84. Sonnenblick, Y., Alexander, E., Kalman, Z. H. & Steinberger, I. T. Hexagonal close packed krypton and xenon. *Chem. Phys. Lett.* **52,** 276–278 (1977).

85. Alexandrov, I. V., Zisman, A. N. & Stishov, S. M. An investigation of the equations of state of the isoelectronic substances Csl-Xe and RbBr-Kr. Phase transitions in Csl and Rbl. *JETP* 371–375 (1987).

86. Polian, A., Besson, J. M., Grimsditch, M. & Grosshans, W. A. Solid krypton: Equation of state and elastic properties. *Phys. Rev. B* **39,** 1332–1336 (1989).

Chapter 3
EXPERIMENTAL METHODS

This section will outline the experimental techniques used for the investigation and construction of phase diagrams of binary systems at high pressure and room temperature. The discussion will focus on the diamond anvil cell (DAC), vibrational (Raman) spectroscopy and powder X-ray diffraction (pXRD) using synchrotron radiation.

3.1 Diamond Anvil Cell (DAC)

3.1.1 A Brief Introduction to the DAC

Introduced in 1959,[1,2] improvements to the design of the DAC throughout the years have allowed for ultra-high pressures to be achieved in the laboratory. Pressure is defined as the force applied to a given area. When the area is smaller, less force is required to obtain extreme pressures. With this versatile device, samples are microscopic and high pressures can be reached with a turn of the screw. The components of a DAC include opposing diamond anvils with culets (flat face on the bottom of the diamond) that are parallel to each other, a metallic gasket placed between these anvils, constraining a compression chamber that houses the sample, and the seats. Figure 3.1 shows the basic schematic of a diamond anvil cell. At present, the highest pressure attained in a DAC, utilizing micro-ball nano-diamond anvils[3], has reached 774 GPa (1 GPa = 10^9 Pa = 10^4 atm).

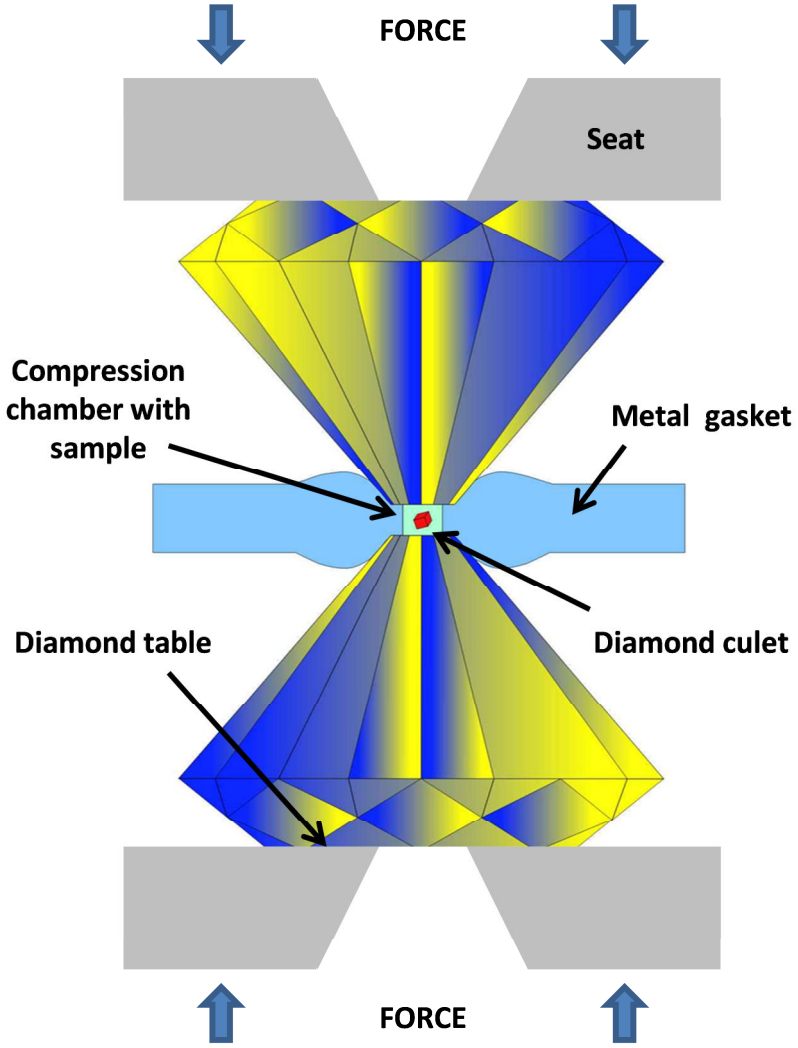

Figure 3.1: Schematic diagram of the diamond anvil cell. The components include: the opposing diamond anvils with culets parallel to each other, the metallic gasket, the compression chamber that houses the sample, and the seats. *Figure courtesy of S. Desgreniers*.

3.1.2 Membrane DAC

Diamond anvil cells can be designed for many diverse experiments such as ultra-high pressures, various temperatures, spectroscopic studies, X-ray scattering experiments on fluids and solids. The compressed sample remains in position within the cell and this allows it to be used with optical

microscopes, at synchrotron radiation beam lines, etc. Experiments were performed with membrane DACs in the present work; they were chosen for their capability to have gas loaded samples and pressures in the desired range. Membrane DACs consist of a cylinder and a piston each with mounted diamond anvils. The cell body is precision-machined out of strong, stainless steel (Figure 3.2).

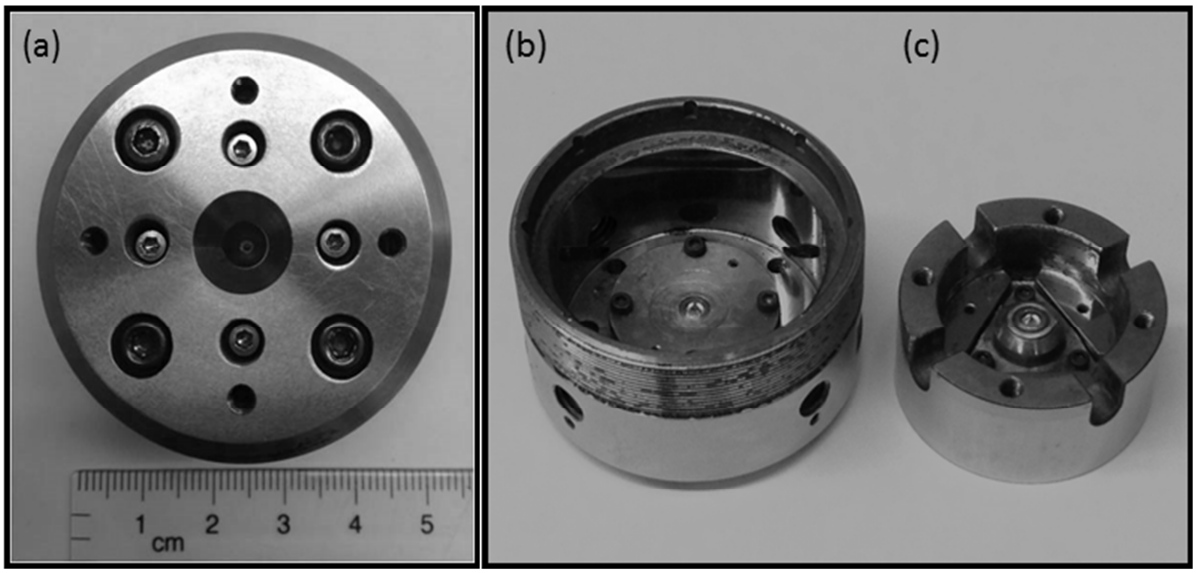

Figure 3.2: (a) Top of the diamond anvil cell. **(b)** The cylinder and **(c)** the piston of the cell with mounted diamond anvils.

Within the DAC, the diamond anvils reside on "seats" made of a strong material so as to transmit the load of the cell to the anvils. Depending on the application the seats may need to be X-ray transparent, withstand temperatures, etc. For experiments involving X-ray diffraction, a beryllium seat is a good choice as it is nearly transparent to hard X-rays (high energy)[4]. A stronger material that is commonly used for seats is tungsten carbide. This material is two times stronger than steel and denser than titanium[5] and when used as a seat, it allows for a larger optical and X-ray aperture. The opposing anvils must be mounted so that they are perfectly parallel and concentric to each other. If there is misalignment, there will be high stress on the system and this could result in positional instability of the sample and possibly fractured anvils.

The pressure increase mechanism in a membrane DAC is accomplished by adjusting the distance between the anvils while they remain in position, mounted on the cylinder and piston. By turning the four large screws located on the top of the DAC (see Figure 3.2, (a)), the piston is brought into the cylinder and the pressure is increased. Likewise, turning the screws in the opposite direction will increase the distance between the diamonds and decrease the pressure. The same action can be accomplished by a pneumatically driven membrane (hence the name of membrane DAC) for an improved control of the pressure.

3.1.3 Diamond Anvils

Robertson *et al*.[6] were the first to organize diamonds into a formal classification system. They divided the "colorless" diamonds into two categories, type I and type II. They were categorized based on their transparency to both UV (100 nm to 400 nm) and infrared (IR; 750 nm to ~1 mm) wavelengths. It should be noted that the band gap for pure diamond is ~5.4 eV and UV radiation with a wavelength shorter than ~230 nm will be absorbed. Type II, containing sub-groups IIa and IIb, are almost free of impurities and occur very rarely in nature[7]. Type IIa are normally very pure and transparent while type IIb are bluish in color and exhibit electrical conductivity due to boron impurities.[8] Type I diamonds account for the vast majority of natural diamonds. They contain nitrogen impurities and have also been split into sub-groups with aggregated (type Ia) and isolated (type Ib) nitrogen atoms[9]. The most common types of diamonds used as anvils are type Ia and type IIa.

In this work, experiments were performed with type Ia diamond anvils that were typically $^1/_4 - ^1/_3$ carat in weight (1 carat = 200 mg). Diamonds that are used as anvils differ from diamonds that are cut for jewelry as there is a small culet face where the point would normally be (Figure 3.3). The

pressure that can be achieved is dependent on culet size. Pressure becomes larger as the culet becomes smaller. Flat culets of either 200 μm, 300 μm or 500 μm in diameter were utilized.

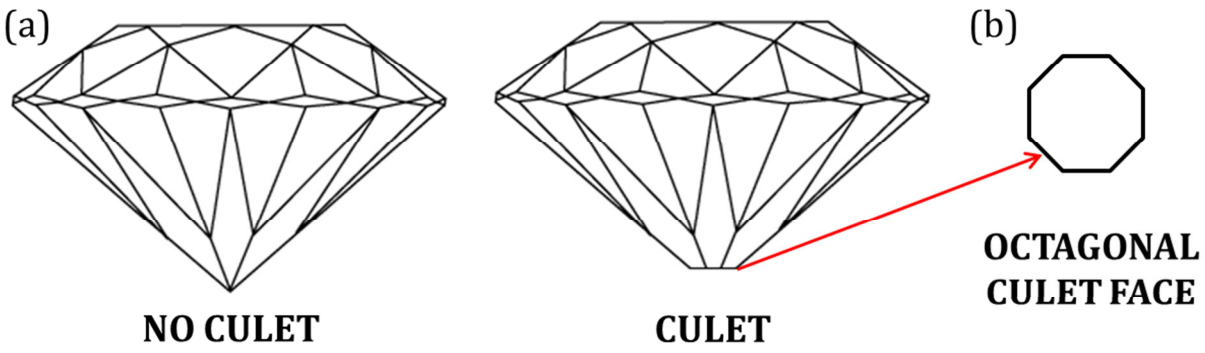

Figure 3.3: (a) Side views of diamonds with and without a culet. **(b)** A closer look at the culet surface, which can have 8 (as illustrated) or 16 sides.

There are pros and cons for using diamonds in a pressure cell. Diamonds are very strong and hard, and tend not break or deform under the high forces involved. Their transparency to many types of radiation is useful as it allows us to see the sample inside the cell, and allows for experiments such as X-ray diffraction to be performed. Diamonds can, however, be a hindrance when performing Raman spectroscopy (discussed in Section 3.4) as they have intense first and second order Raman scattering corresponding to vibrational modes occurring at 1333 cm^{-1} and mostly at 2300-2700 cm^{-1}, respectively, at room conditions. The intensity of these Raman modes can be magnitudes higher in intensity than that of the sample due to their corresponding thicknesses, with the sample being about $^{1}/_{50}$ the thickness of the diamond. Any signals that might be coming from the sample may be lost to the diamond. If this is the case a different choice of anvil material such as moissanite (a dense form of SiC), which has no overlapping vibrational modes with diamond, might be preferred.[10,11] The use of moissanite as the anvil material limits the pressure that one can attain with the pressure cell and is less appropriate for X-ray diffraction experiments given the high X-ray absorption.

3.1.4 Gasket and Compression Chamber

A gasket used in the DAC is a thin sheet of hard metal of about 250 μm in initial thickness that is compressed between the diamond anvils. It is required to withstand great pressure, so metals such as rhenium or tungsten are chosen. For low pressure experiments (<25 GPa), full-hard ANSI T301 stainless steel is a cheaper alternative. When preparing a sample, a gasket is pre-indented using the anvils within the cell to help provide a stable compression chamber. The gasket is positioned over one of the diamonds and fastened in place with putty (Figure 3.4, (a),(b)). The piston and cylinder are placed together and the pressure is increased with the top screws, indenting the metal. The extrusion around the culet is measured under a microscope and its diameter is used to determine a "rough" thickness of the metal. The actual thickness is measured with a fine-tipped micrometer with precision of 1 μm. Indentation thicknesses ranging from 80 to 120 μm are chosen for the experiment; higher pressures require thinner indentations which will further work to harden the gasket material.

After indentation, the gasket is removed from the DAC to prepare it for compression chamber forming by microdrilling and sample loading. Dependent on the metal used for the gasket, a hole is drilled with either a pulsed laser or mechanical drill in the center of this indentation. The hole is smaller than the culet and is usually about one third of its diameter (50-150 μm). The drilled gasket is then placed back in the cell with the same orientation on the anvil that it was indented with. It will be used as the compression chamber which holds the sample.

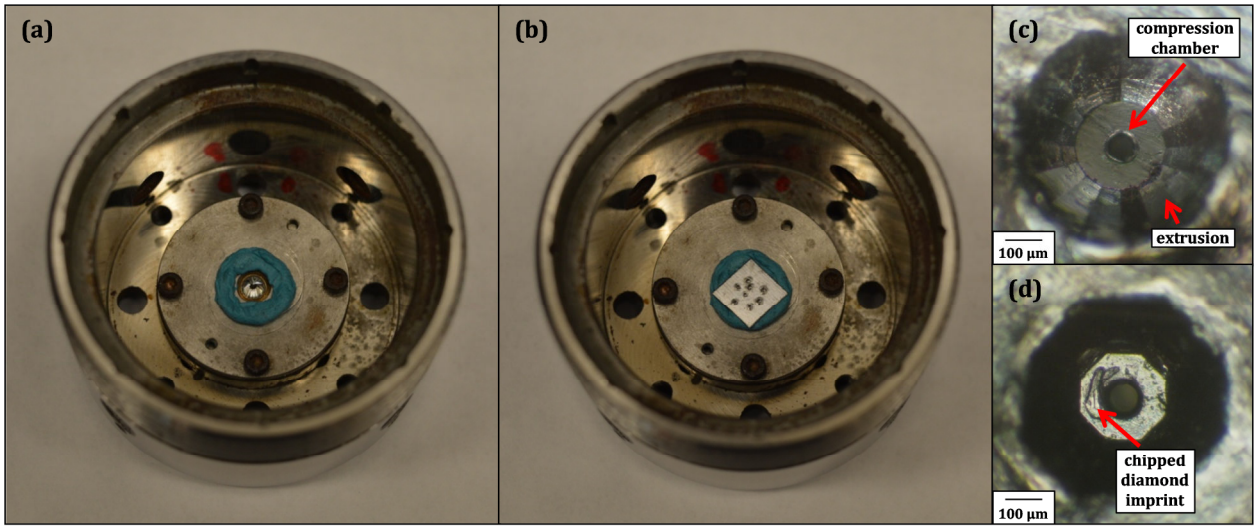

Figure 3.4: The DAC cylinder **(a)** with putty and **(b)** with the gasket aligned on top of the diamond. In this case, the gasket has many indentations **(c)** A gasket showing a diamond indentation with extrusion and the drilled compression chamber which holds the sample. **(d)** A gasket indentation showing eight-sided anvil and culet with defects.

3.2 Pressure Measurement

The ruby luminescence method was employed for *in-situ* pressure measurements. The set up consists of a green (doubled Nd:YAG at 532 nm) or green-blue laser (argon ion at 488 nm) laser to excite the luminescence of a ruby microsphere which is measured with an appropriate spectrograph equipped with a cooled CCD detector. The apparatus is also equipped with a microscope for observation.

A ruby (α- Al_2O_3:Cr^{3+}) will absorb radiation and excite the Cr^{3+} ions in the aluminum oxide host crystal, then decay rapidly to a metastable state. The energy lost in this process is nonradiative and vibrationally excites the crystal atoms. The Cr^{3+} ions emit luminescence as they decays back to

ground state and a spectrograph is used to measure the ruby R_1-R_2 doublet (Figure 3.5). With as little as 2.33 eV (532 nm), a ruby will fluoresce.

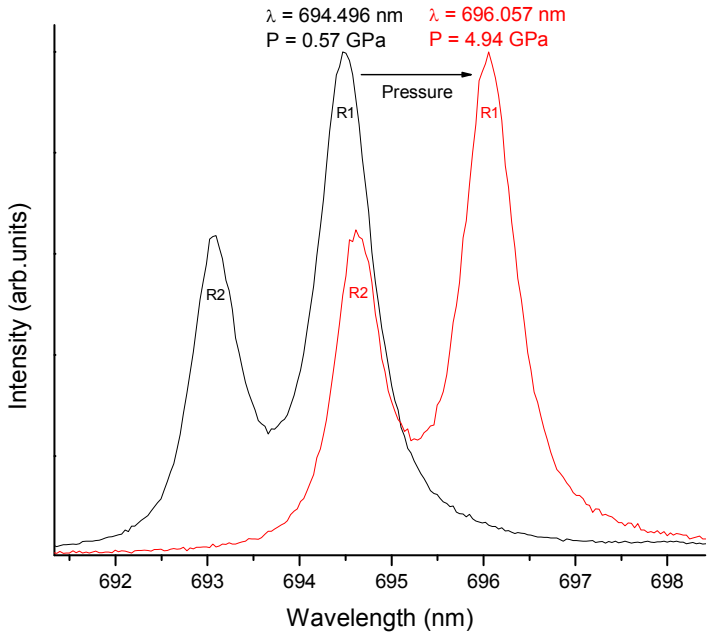

Figure 3.5: Ruby fluorescence; the R_1-R_2 doublet measured at 0.57 GPa and 4.94 GPa to demonstrate the shift in wavelength with pressure. Pressure is determined using Equation (3.1).

The R_1-R_2 doublet was found to move with pressure and a great effort was made to calibrate and develop empirical formulae that describe the changes in wavelength, $\Delta\lambda$, with pressure (Figure 3.5). The pressure-$\Delta\lambda$ relation is linear to about 20 GPa, where it begins to deviate from linearity.[12]

To determine which pressure corresponds to a given wavelength, the ruby pressure-$\Delta\lambda$ relation requires calibration against a material that is almost absolute. Thermodynamic models relate volume to pressure at different temperatures. Shockwave studies of metals with high symmetry such as gold and tungsten have led to the derivation of isothermal equations of state (EOS) for high pressures. Mao *et al.*[13,14] studied the ruby pressure-$\Delta\lambda$ relation by simultaneously measuring the

specific volume of Cu, Mo, Ag, and Pd and referring to isothermal EOS. They developed the following empirical pressure calibration scale:

$$P(GPa) = \frac{A}{B}\left[\left(\frac{\lambda}{\lambda_0}\right)^B - 1\right] \quad (3.1)$$

where pressure, P, is dependent on the position of the R_1-line at ambient pressure, λ_0, and at the current pressure, λ. A and B are constants having values of 1904 GPa and 5, respectively, for non-hydrostatic conditions. More recently, the calibration has been improved for hydrostatic systems by Dewaele *et al.*[15] using various metals with helium as a pressure transmitting medium. Using the equation proposed by Mao *et al.*[13,14], the parameters they obtained for A and B were 1920 GPa and 9.61, respectively. These pressure scales are accurate up to 180 GPa.[12]

In this work, at least one ruby microsphere is placed within the compression chamber, prior to sample loading. The rubies are small, about 5 – 15 μm in diameter, and do not hinder sample size or experiments as they only occupy a small space. The pressures measured have an uncertainty of ± 0.01 GPa.[16]

3.3 Sample Preparation

3.3.1 Loading Procedure

Samples of various concentrations were studied to extend the nitrogen-argon pressure-concentration phase diagram proposed by Lotz *et al.*[17] to higher pressures. To produce a sample, a prepared gasket is placed on a diamond that is mounted on either the cylinder or piston of the DAC. Ruby microspheres are then inserted into the compression chamber. The piston is placed in the cylinder but only far enough to create a gap of about 1 mm between the opposing diamond. This

will allow space for the gaseous or liquid sample mixture to enter the compression chamber. Mixtures of nitrogen and argon were loaded with one of two methods, either gas or cryogenically to high pressures.

The gas loading method involves placing the "prepared" DAC into a clamping mechanism which is then placed into the pressure vessel of the gas loading apparatus. Nitrogen and argon are individually inserted into the chamber in volumes that would result in desired final concentrations. After time is allowed for the gases to mix at the required pressures (about 0.18 GPa or 1800 bars), the sample of mixed species is contained inside the compression chamber by closing the DAC with motorized controls. After a desired pressure is reached for the sample (~2-5 GPa) inside the DAC, the chamber and in turn the DAC are removed and the sample is inspected under a microscope. If the sample is not present or has reduced in size due to gasket failure, the sample is re-loaded. An ideal sample will have a good powder in a circular compression chamber, which has not started to collapse. The DAC and sample remain close to room temperature during the entire process.

The second method to prepare a mixed sample involves loading the species cryogenically. At atmospheric pressure, the boiling temperatures of nitrogen (77.2 K, -195.8 °C) and argon (87.3 K, -185.8 °C) are close, so liquid argon is produced by flowing argon gas into a flask that is cooled in a bath of liquid nitrogen. The flask is sealed with a rubber stopper containing a tube for the insertion of argon gas and a vent to prevent pressure build-up. When the desired volume of liquid argon is reached (~100–150 mL), a solid stopper is placed on the flask to prevent contamination and the liquid argon is kept at liquid nitrogen temperature. The DAC and glassware that will hold the N_2-Ar mixture are then cooled in liquid nitrogen baths. Care must be taken not to allow liquid nitrogen into the opening of the DAC or the rubies may be lost. The desired proportion of liquid nitrogen and argon are measured and mixed in a Pyrex bowl that is placed in a liquid nitrogen bath. The mixture

will have a total volume of 150-250 mL, as this allows for the complete submersion of the DAC. After the pre-cooled DAC has been submerged in the mixture and the boiling of the liquid has slowed, the mixture is trapped and solidified in the compression chamber as the screws are tightened to increase the pressure. The DAC and sample are then warmed to room temperature while a sufficient pressure is applied to maintain the mixture in a solid phase.

3.3.2 Concentration

The concentration of the mixed sample can be roughly obtained by using the volumes of nitrogen and argon that are put into the mixture; however, there is a large uncertainty with this method alone, about ±10%. At room temperature, gas loading errors can occur if, for example, the gases have not had sufficient time to properly mix and/or enter the compression chamber area of the DAC. Cryogenically, ambient conditions surrounding the loading mechanism causes the liquids to boil. The boiling temperatures are close for liquid nitrogen and argon which minimizes evaporative losses; nevertheless, their slight difference will cause unequal boiling of the components. Attempts are made to avoid additional boiling, such as pouring the liquid with lower boiling temperature (nitrogen) into that of higher boiling temperature (argon) when mixing.

Raman spectroscopy is employed to aid in more accurately determining the final concentration. Figure 3.6 shows the characteristic Raman frequencies of the vibrons of molecular nitrogen of a mixed sample compared to that of the pure substance[18,19,20,21] and to the N_2-Ar concentrations obtained by Lotz *et al*.[17] after allowing their samples to mix for 60 hours. Due to time constraints, it was not possible to allow for a similar duration for mixing, which is why the experimental frequencies in this work were compared to the literature. The shift in Raman frequencies of nitrogen in the mixture can be used to get the concentration. In addition, the intensity of the

vibronic peaks may also be used to estimate the concentration. At a given pressure, the relative intensity is proportional to the amount of nitrogen present in the sample. It should be noted that the intensity of the peak is also dependent on parameters such as sample volume and laser power, so this will only give a relative comparison. Using a combination of these methods, the uncertainty for the final concentration is about ±2%.

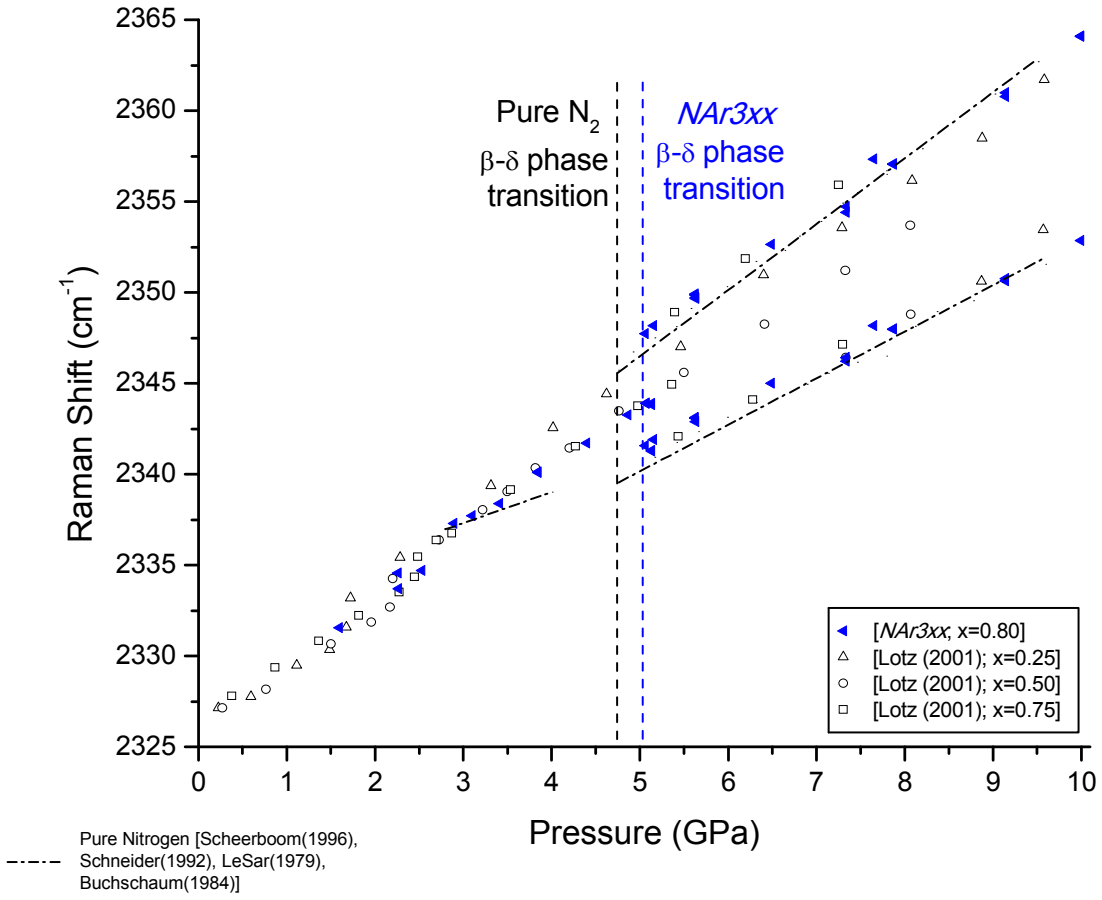

Figure 3.6: Final concentrations were determined by a comparison of N_2 vibrons as a function of pressure to that of the pure substance and concentrations obtained by Lotz *et al*.[17]

3.4 Vibrational Raman Spectroscopy

3.4.1 A Brief Introduction to Raman Scattering

Raman spectroscopy, introduced in Section 2.2.2, is one of the most common methods for assessing molecular motion and environment, and sample identification. This technique involves shining a laser beam (monochromatic light) at a sample and detecting the quasi-elastic scattered light. When a molecule absorbs radiation, there can be a change in bond length or positions with respect to the other atoms in the molecule. In three-dimensional space, a molecule will have 3N degrees of freedom, where N is the number of atoms within the molecule. A molecule as a whole will experience translational and rotational motion, as well as individual motion of the atoms, or vibration. Molecular vibrations are categorized into normal modes. A normal mode occurs when some or all of the atoms in a molecule vibrate with the same frequency in a particular motion (Figure 3.7). The number of modes is equal to the vibrational degree of freedom for the molecule, which is 3N-6 and 3N-5 for non-linear and linear molecules, respectively.[22] The corresponding frequencies and intensities of these modes, however, depend on other parameters such as state populations, polarizability derivatives, vibrational partition functions, etc.[23] In a molecular solid, different orientations of the molecules (lattice sites) within the solid can lead to additional intensities with distinct frequencies. An example would include the δ-N_2 structure (Section 2.3.3), which has two lattice sites that correspond to a high- and a low-frequency peak.

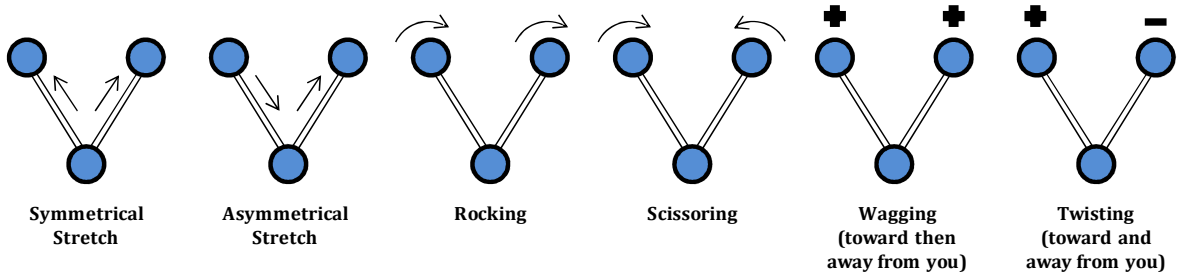

Figure 3.7: The normal modes of vibrations for polyatomic molecules. It should be noted that N_2 is a much simpler molecule to study as it is a linear diatomic molecule.

Most of the scattered light will have the same frequency as the laser, and this is referred to as Rayleigh scattering (Figure 3.8). However, not all of the scattered light will be elastic. Few photons (about 1 in 10^6) will be shifted with respect to the laser frequency due to interactions between the incident light and the vibrational energy levels of the molecule.[24] In classical terms, light is an electromagnetic radiation which contains an oscillating electric field that interacts with a molecule through its polarizability. Polarizability is determined by how the electron cloud distorts when in the presence of an electric field, causing an induced dipole moment in the molecule or atom. Molecules with higher polarizability tend to be strong Raman scatterers.[23,24]

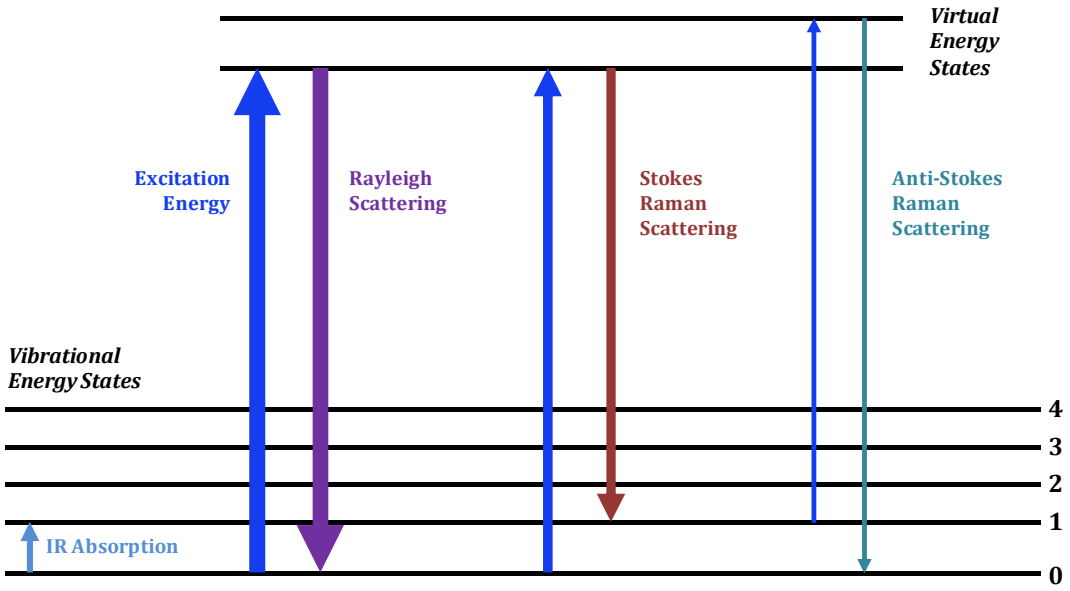

Figure 3.8: Energy levels and transitions related to Raman scattering. The line thickness is roughly proportional to signal intensity where Rayleigh scattering is typically six orders of magnitude larger than that of the Raman scattering.

Scattered light with a decrease in energy (emission of a phonon) will result in Stokes scattering while an increase in energy (absorption of a phonon) will give anti-Stokes scattering (Figure 3.8). The energy shift is independent of wavelength and characteristic to the molecule, giving a direct measure of its vibrational energies. A Raman spectrum is a measure of the intensity of the shifted light as a function of frequency, with respect to the laser frequency in units of wavenumber (cm^{-1}).[16,25] The wavenumber is the reciprocal of wavelength (λ^{-1}) and is directly proportional to

energy (E = [Planck's Constant (h)] x [Speed of light (c)] x [λ^{-1}] = hcλ^{-1}). In this case, it is proportional to the energy of a transition between states in a molecule.[26] The shifted wavelengths, or Raman shifts, provide information about the chemical properties of the sample and appear in the range of 400 and 4000 cm^{-1} (corresponding to energy of mid-infrared radiation) for intra-molecular interactions (e.g. bending and stretching vibrations). The range found between 0 and 400 cm^{-1} (corresponding to energy of far-infrared radiation), contains lattice vibrations from which information can be obtained on intermolecular forces. The area of a Raman line is proportional to concentration, making Raman spectroscopy a good tool for quantitative analysis.[26,27]

A typical Raman spectrum will have the Rayleigh line centered at 0 cm^{-1}, with the Stokes and anti-Stokes lines equally displaced from it. For anti-Stokes scattering to occur, a transition is required from an atom that is initially in an excited state to the ground state. Stokes scattering relies on a transition from ground to an excited vibrational state. At thermal equilibrium, the population of the ground state is higher than that of the excited state, following the Boltzmann distribution for populations of states.[26] The Stokes transition is much more probable; hence, there will be a more intense Stokes line when compared to the anti-Stokes line. In this work, Stokes scattering was measured.

3.4.2 Experimental Setup

Raman spectroscopy experiments were performed using two different setups at Laboratoire de physique des solides denses (*LPSD*) at the University of Ottawa and *in situ* at the Canadian Light Source (CLS) using instrumentation recently installed at the Hard X-ray Microanalysis (HXMA) beamline. The setups at *LPSD* include a Coherent Innova 70 argon ion laser (488 nm) and a Spectra Physics Centennia TD5 solid state frequency doubled Nd:YAG laser (532 nm), with spectrographs of

spectral resolution of 1 cm^{-1} and 4 cm^{-1}, respectively. Neon and/or argon emission lines were used to perform spectral calibration of the systems to within ±1 cm^{-1}.

The Nd:YAG laser setup (Figure 3.9, left) includes an Olympus BH-2 microscope with interchangeable 10x and 50x long-working distance Mitutoyo objectives which were used for visual observations and to focus the laser beam onto the sample. Manual positional adjustments were made with an x,y,z stage (resolution = +- 2 μm) viewed with a CCD video camera connected to a monitor. Scattered light was collected and refocused with the same 50x objective a near-backscattering geometry and directed to an optical fiber (multimode, 200 μm diameter core, numerical aperture = 0.22) where it was dispersed with an Andor Shamrock SR-303i spectrometer using a 1200 lines/mm grating. The light was then detected with a thermoelectrically cooled (-70˚C) Andor Newton DU971N-BV charge-coupled device (CCD) detector. The Raman spectrum was acquired using Andor Solis software. The laser was run at 200 mW at the source. After the beam was directed through a 50:50 beam splitter, optical filters and mirrors, the excitation power at the sample was no more than 60 mW.

The argon ion laser setup (Figure 3.9, right) utilizes a 50x long-working distance Mitutoyo objective for laser beam focusing and a Mightex SCE-B013-U video camera for viewing the sample. A Newport ESP301-3G motion controller was employed for the motorized x,y,z positional adjustments (resolution = +- 0.5 μm). Scattered light, directed to an optical fiber (multimode, 50 μm diameter core, numerical aperture = 0.22), was dispersed by an Andor Shamrock SR-500-B1 spectrometer using a 2400 lines/mm grating and detected with an Andor Newton DU940N-BV CCD. Unwanted argon emission lines were removed from Raman spectra with an ultra-steep edge filter. Laser power was controlled by current sent to the laser tube and adjustments were made on the power

supply to give a laser power output of 50 mW at the source. Laser excitation powers at the sample were about 35 mW.

Acquisition parameters included an exposure duration of 1 second with 30 accumulations. The "Step and Glue" function on Andor Solis takes multiple exposures centered at different wavelengths. It was used for spectra containing larger Raman shift ranges (e.x. 488nm to 570 nm). Slit width was 100 µm and 10 µm for the argon ion and Nd:YAG lasers, respectively. Raman line profiles, were analyzed using XRDA[28] using either a Gaussian or Lorentzian peak fitting function to extract Raman peak positions, line widths (full-widths at half maximum), and integrated intensities.

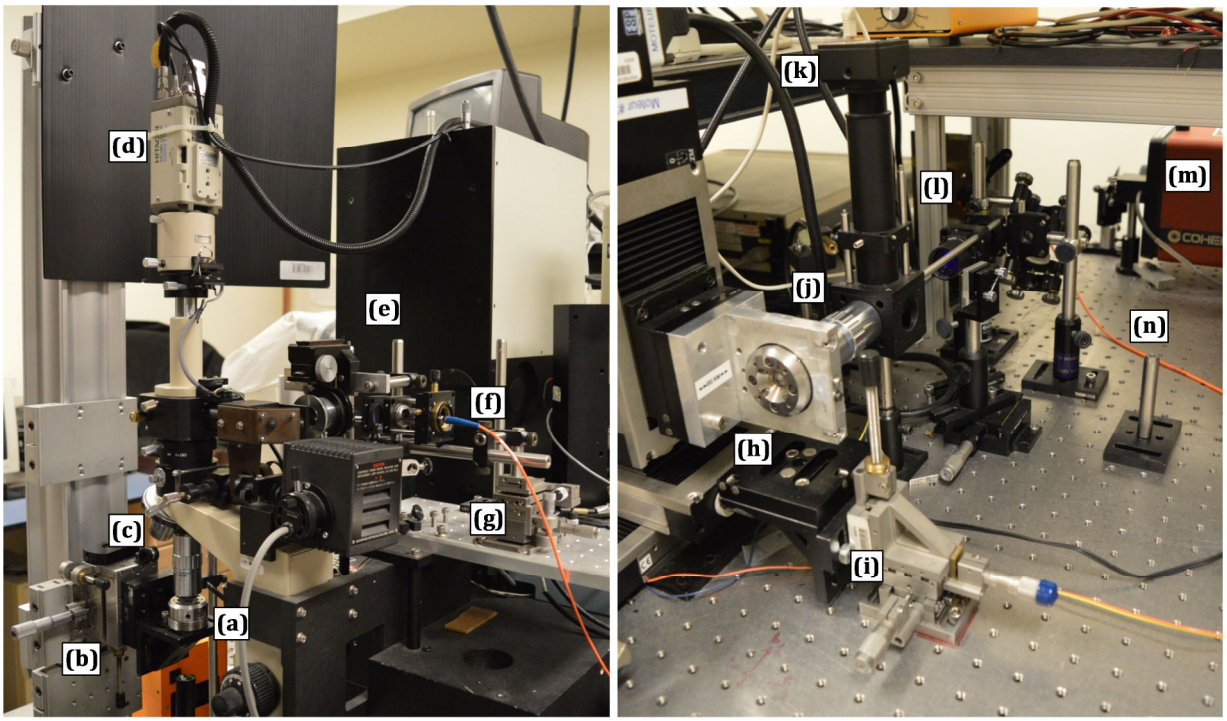

Figure 3.9: Raman spectroscopic setups at the Laboratoire de physique des solides denses. LEFT: Nd:YAG 532 nm laser system with **(a)** a holder for the DAC attached to a **(b)** 3-way stage. **(c)** Interchangeable 10x or 50x objectives to focus the laser beam and for visual observations via the **(d)** CCD camera. **(e)** Optical setup for focusing/directing the laser beam into the **(f)** optical fiber attached to the spectrograph (not shown). **(g)** Stages for positioning the optical fiber. RIGHT: Argon ion 488 nm laser system with **(h)** DAC holder, **(i)** 3-way motorized stage, **(j)** 50x objective, (k) CCD camera, **(l)** optical set-up, **(m)** laser, and **(n)** optical fiber.

3.5 Powder X-ray Diffraction Using Synchrotron Radiation

3.5.1 A Brief Introduction to X-ray Diffraction

The corresponding wavelengths of hard X-rays are small and on the order of atomic distances, around an angstrom. X-rays were discovered in 1895 by Wilhelm Rontgen. In 1912, Max von Laue discovered that when x-ray wavelengths are similar in size to the spacing of planes in a crystal lattice, the crystalline substance will act as a three-dimensional grating.[29] In 1913, physicists Sir W. H. Bragg and his son Sir W. L. Bragg developed a relationship to explain why x-ray beams appear to be reflected from planes of a crystal at certain angles with respect to the incident beam. The interaction of the incident rays with the electrons surrounding the atoms in the crystal produces constructive interference and a diffracted ray when conditions satisfy

$$n\lambda = 2d \sin\theta \tag{3.2}$$

Better known as Bragg's Law,[29,30] it relates the wavelength of the electromagnetic radiation, λ, to the diffraction angle, θ, and the lattice spacing in the crystal, d, where *n* is an integer multiple of λ.

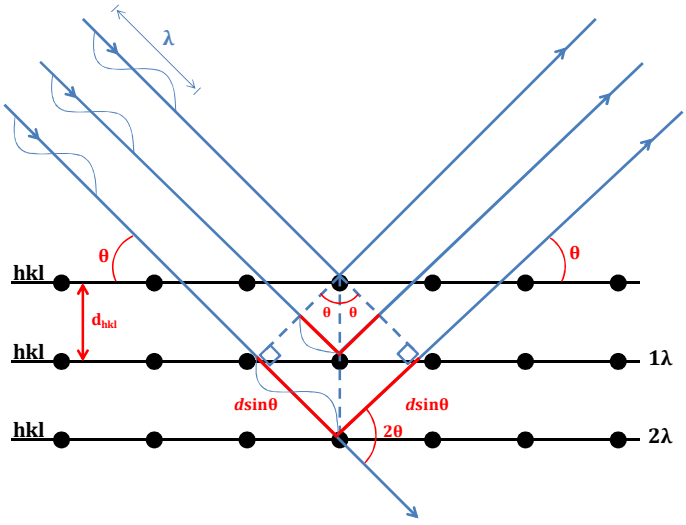

Figure 3.10: X-rays are directed at the sample and diffracted rays that are in phase will be collected. The XRD spectrum is represented as intensity vs. 2θ. Beyond this, powder and single crystal XRD vary in instrumentation.

X-rays that are diffracted in phase (Figure 3.10) will produce a signal which is counted and collected. The resulting x-ray diffraction (XRD) spectrum is a measure of the intensity as a function of 2θ in units of degrees (°). 2θ is measured with respect to the incident beam. XRD is now a technique used in a variety of fields from mineralogists to solid state physicists. In addition to atomic spacing, the size, shape, internal stress, and orientations of single crystals or grains can all be measured. The information obtained from XRD allows for the determination of the crystal structure of an unknown material.

A unit cell is the smallest building block in a crystal and consists of a fixed arrangement of a single atom or multiple atoms. Unit cells are periodically arranged into a lattice and a crystal consists of planes of atoms that are spaced apart by a distance *d* (Figure 3.10). Different planes will have different spacing and to satisfy Equation 3.2, θ must change as *d* changes. XRD can be used to determine lattice parameters and space group of a unit cell. For a generalized cell, shown in Figure 3.11, there will be six parameters: *a*, *b* and *c* (length) and α, β and γ which are the angles between the lengths. Table 3.1 shows the 7 crystal systems further divided into 14 groups called Bravais lattices based on symmetries of these parameters.

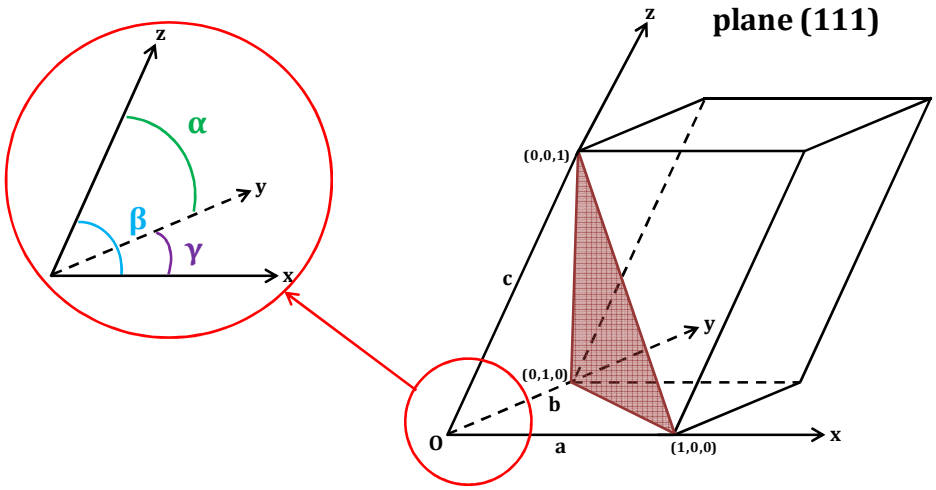

Figure 3.11: A general unit cell showing hkl plane (111). This cell contains six lattice parameters: lengths a, b, and c, and the three angles between these lengths α, β, and γ.

Table 3.1: Crystal Systems and Bravais Lattices

Bravais Lattice Examples:	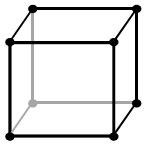 **Simple (S)**	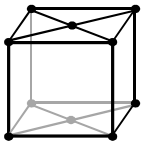 **Base Centered (bC)**	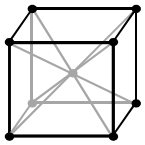 **Body Centered (BC) (Cubic = BCC)**	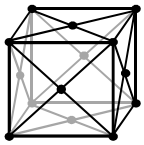 **Face Centered (FC) (Cubic = FCC)**

System:	**Angles & Dimensions:**	**Bravais Lattices**
Cubic	a=b=c, α=β=γ=90°	S, BCC, FCC
Tetragonal	a=b≠c, α=β=γ=90°	S, BC
Rhombohedral	a=b=c, α=β=γ≠90°	S
Hexagonal	a=b≠c, α=β=90°, γ=120°	S
Orthorhombic	a≠b≠c, α=β=γ=90°	S, bC, BC, FC
Monoclinic	a≠b≠c, α≠90°, β,γ=90°	S, BC
Triclinic	a≠b≠c, α,β,γ≠90°	S

Describing the directions and planes is important when determining crystal properties and structure. Many properties such as electrical and thermal conductivity and elastic modulus can vary with direction in a crystal.[30] The orientation of a crystal plane can be defined by how the plane intersects with the main axes of the crystal's unit cell. The Miller indices (*hkl*) are a set of integers that quantify infinite intercepts and identify the specific plane or surface. To assign Miller indices, the first step is to identify the intercepts on the x, y, and z axes. The next step is to specify the intercepts in fractional coordinates. For example, a point (x,y,z) in a unit cell ($a \times b \times c$) will have fractional coordinates $\left(\frac{x}{a}, \frac{y}{b}, \frac{z}{c}\right)$. The last step is to take reciprocals of the fractional intercepts and simplify by clearing fractions and reducing to the lowest terms.[31] As an example, the plane shown in Figure 3.11 would be assigned as follows:

Intercepts: a, b, c

Fractional Intercepts : $\frac{a}{a}, \frac{b}{b}, \frac{c}{c}$

Miller Indices: (111)

By removing a common factor a parallel plane a certain distance away from the origin is generated (e.x. (222) becomes (111) by dividing by 2). Some other general rules for assigning Miller indices include negative intercepts being denoted by over-striking the number (-1 becomes $\bar{1}$), and symmetry equivalent surfaces by using curly brackets (the six surfaces related to (100) become {100}).[31] For a generalized (triclinic) cell, the d-spacing in terms of the hkl plane (or reflection) and six lattice parameters is given by

$$d_{hkl} = V[h^2b^2c^2\sin^2\alpha + k^2a^2c^2\sin^2\beta + l^2a^2b^2\sin^2\gamma + 2hlab^2c(\cos\alpha\cos\gamma - \cos\beta) + 2hkabc^2(\cos\alpha\cos\beta - \cos\gamma) + 2kla^2bc(\cos\beta\cos\gamma - \cos\alpha)]^{-1/2} \quad (3.3)$$

with a volume of

$$V = abc\sqrt{1 - \cos^2\alpha - \cos^2\beta - \cos^2\gamma + 2\cos\alpha\cos\beta\cos\gamma} \quad (3.4)$$

The positions (2θ or d-spacings) of the diffraction peaks will provide information on the geometry of the unit cell while the intensities of these peaks can be used to determine the composition of the unit cell. The structure factor, F_{hkl}, is the resultant of the waves that are scattered by all the atoms in the units cell at a given *hkl* reflection. The structure factor depends on atomic species and provides information on their positions within the unit cell. For n atoms in a unit cell,

$$F_{hkl} = \sum_n^N f_n e^{2\pi i(hx_n + ky_n + lz_n)} \quad (3.5)$$

where f_n is the scattering factor for the n^{th} atom and x_n, y_n and z_n are its coordinates in a unit cell of N atoms. When the structure factor is multiplied by its complex conjugate it is proportional to the intensity of an *hkl* reflection, $I_{hkl} \propto |F_{hkl}|^2$.[31,32] The structures most relevant to this work are the cubic, hexagonal and rhombohedral cells. Their corresponding d_{hkl} and volumes are presented in Table 3.2.

Table 3.2: Volume and d_{hkl} for structures relevant to this work.

Cell:	**d_{hkl}:**	**V:**
Cubic	$\left[\frac{h^2+k^2+l^2}{a^2}\right]^{-1/2}$	a^3
Hexagonal	$\left[\frac{4}{3}\left(\frac{h^2+hk+k^2}{a^2}\right)+\frac{l^2}{c^2}\right]^{-1/2}$	$\frac{\sqrt{3}}{2}a^2c$
Rhombohedral	$\left[\frac{(h^2+k^2+l^2)\sin^2\alpha+2(hk+kl+hl)(\cos^2\alpha-\cos\alpha)}{a^2(1-3\cos^2\alpha+2\cos^3\alpha)}+\frac{l^2}{c^2}\right]^{-1/2}$	$a^3\sqrt{1-3\cos^2\alpha+2\cos^3\alpha}$

3.5.2 Powder X-ray Diffraction *vs* Single Crystal X-ray Diffraction

X-ray diffraction occurs when x-rays are scattered by a periodic array with long-range order, such as the electron density distribution in atoms of a crystal lattice. Constructive interference will occur at specific angles according to Bragg's Law (Equation 3.2). The electrons of an atom coherently scatter light, and the strength of this scattered light is proportional to the number of electrons in the atom. Crystals with different arrangements of atoms will produce different and unique diffraction patterns. A single crystal will produce only one "set" of peaks in the diffraction pattern. The "set" of peaks will correspond to all that are parallel (e.g. (200) are parallel to (100) planes). Figure 3.12 shows that in order to observe peaks corresponding to other planes, the sample will need to be realigned with respect to the incident and diffracted beam.[33]

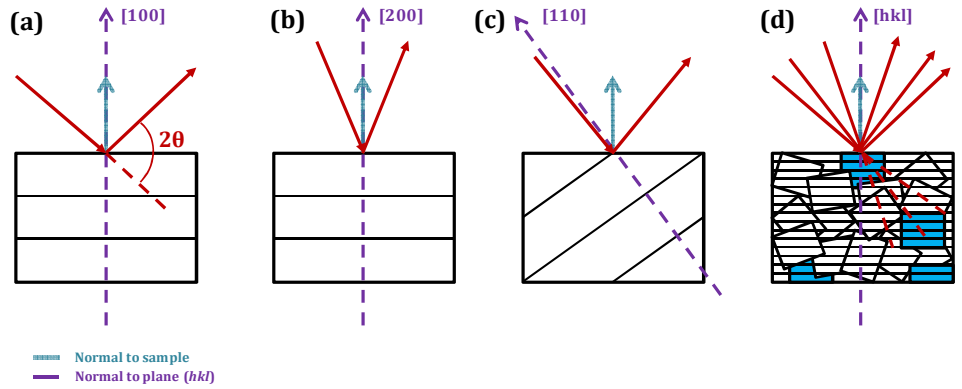

Figure 3.12: Planes **(a)** (100) and **(b)** (200) are both observed as they are parallel; d_{200} is ½ d_{100}. According to Bragg's Law, if 2θ = x for plane (100), then 2θ ~ 2x for the plane (200). **(c)** The perpendicular to the planes does not bisect the incident and diffracted beams. The planes would require realignment to produce a diffraction peak. **(d)** Polycrystalline sample where all crystal planes are observed at once.

A polycrystalline sample (powder) contains thousands of crystals, or grains about a micron in size. If monochromatic light is used then according to Bragg's Law, the wavelength will be fixed and each d-spacing will produce a cone of diffracted x-rays at a fixed angle, θ (Figure 3.13). A small percentage of the grains will be properly aligned to diffract for all planes (Figure 3.12, (d)). By scanning the sample through a range of 2θ angles, all possible diffraction directions of the lattice should be observed due to the random orientations of the grains in the powder.[34]

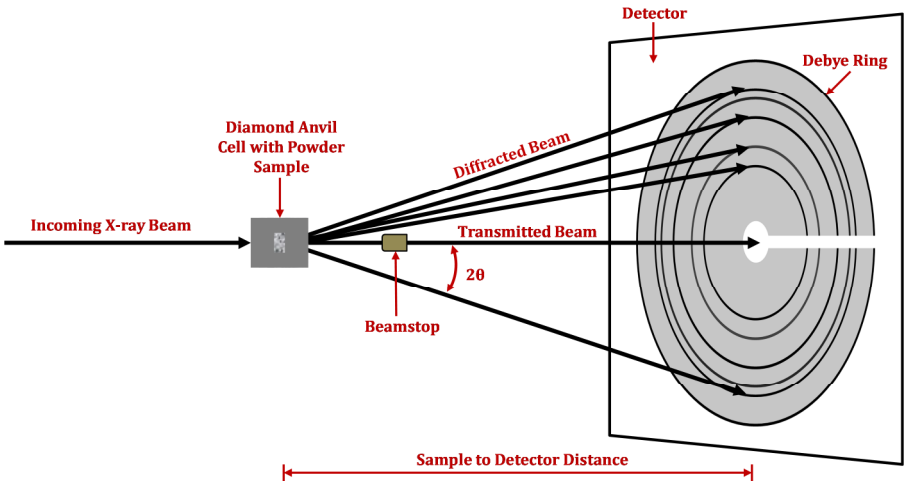

Figure 3.13: All crystal planes are observed with powder samples. Debye rings are observed due to the random orientation of the grains in the sample.

Powder and single-crystal x-ray diffraction are the two main methods employed to study crystal structures of materials. Each has their advantages and disadvantages. Single-crystal techniques are nearly always successful with accurate cell parameter measurements; however, culturing single crystals can be difficult and time consuming. Also, not every material can be prepared in a stable single-crystal form, or of sufficient size. Structure determination by powder x-ray diffraction (p-XRD) may not be as accurate as that of single-crystal, yet it is still a powerful technique. In addition to simplified sample preparation, some advantages of p-XRD would include shorter collection times for a measurement and the ability to study mixed phases.[35] In this work, p-XRD was utilized.

3.5.3 X-ray Diffraction and Synchrotron Radiation

The discovery of synchrotron radiation was published in a letter entitled "Radiation from Electrons in a Synchrotron" in 1947.[36] In 1961, the National Bureau of Standards created the first experimental program using synchrotron radiation.[37] Facilities have been continually improving and synchrotron radiation has become a valuable research tool for the study of matter in all its forms.

When charged particles are accelerated, in a curved orbit for example, they emit electromagnetic radiation. Figure 3.14 shows the dipole emission pattern of such a charged particle. When the speed of the charged particle is on close to the speed of light, the emission of energy is peaked in the forward direction, making synchrotron light focused radiation in space. Emitted radiation ranges from microwaves to hard X-rays, making it tunable with the use of monochromators.[38]

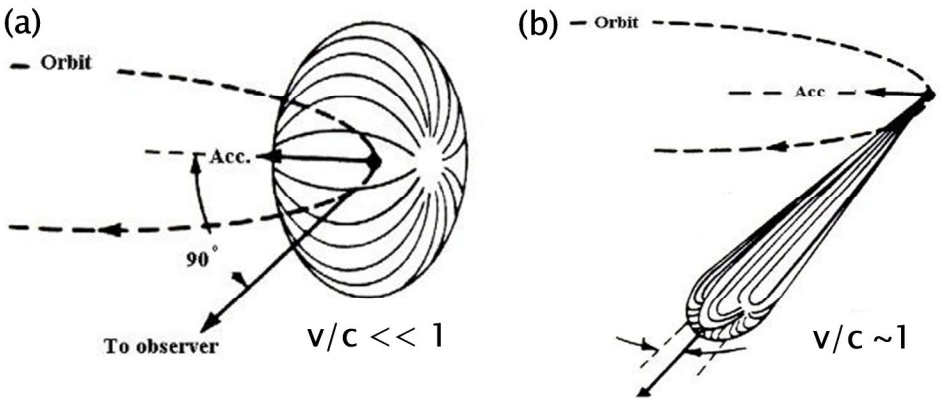

Figure 3.14: The dipole emission pattern of a charged particle accelerating in an orbit at a velocity **(a)** much less than the speed of light and **(b)** close to the speed of light. *Figure courtesy of R. Bartolini - John Adams Institute.*

According to Bragg's Law, increased energy (decreased wavelength) will result in smaller d-spacings at given angles (2θ). The aperture on the DAC is limited by the diamond anvil seats, which in turn limits the range of the d-spacings that can be observed. In this work, the maximum 2θ achieved was about 30°. With typical copper x-ray tubes used in laboratory x-ray diffractometers, smaller d-spacings correspond to much larger 2θ's and would not be observable in an experiment with the DAC. For example, high-quality structural determination requires the recording of d-spacings to about 1.5 Å. At this d-spacing, a copper source giving off photons of about 8 keV (~1.5 Å) would correspond to a 2θ of 62°. The energy at Hard X-ray MicroAnalysis (HXMA) beamline at the Canadian Light Source (CLS) is tunable, in a range of 5-40 keV, allowing for a large range of accessible d-spacings.

Other benefits of hard x-rays produced by synchrotron radiation include high transmission through the diamond, high photon flux and very low divergence in the plane of travel.[39] In regular laboratory XRD setups (e.g. copper source), the diamond anvils in the DAC, with a total diamond material thickness of about 4 mm, will absorb most of the radiation. When x-rays are of high energies, such as those produced at HXMA, the diamond will become more transparent, allowing

the radiation to pass through the sample. Synchrotron radiation produces a large amount of photons emitted per second per mm^2, or flux. The quality of the light source is measured in brilliance, which is proportional to flux and has units of photons/s/mm^2/$mrad^2$/0.1%bandwidth(BW).[40] For comparison, the flux at the CLS is overall almost 8 orders of magnitude larger than that of a conventional laboratory source.[41] This will reduce the time it takes to conduct an experiment. The size of the sample is limited by the DAC, so higher flux and a small parallel beam due to low divergence are beneficial for high pressure XRD experiments.

3.5.4 CLS HXMA 06ID-1 and APS Sector 20 ID Beamlines

Powder x-ray diffraction measurements were carried out using synchrotron radiation at the Canadian Light Source (CLS) Hard X-ray MicroAnalysis (HXMA) 06ID-1 and the Advanced Photon Source (CLS@APS) Sector 20 ID beamlines. All experiments, except for the *NAr7xx* series, were performed at the CLS utilizing a wavelength of 0.509176 Å (24.350 keV). Experiments with the *NAr7xx* series were performed at the CLS@APS beamline with a wavelength of 0.47684 Å (26.001 keV).

At the CLS, an electron gun runs high voltage electricity through a heated tungsten-oxide disk (cathode) to produce pulses of electrons. The electrons are then injected into a linear accelerator where microwave radio frequency fields accelerate them to 99.999998% of the speed of light, giving them energy of 250 MeV. The electrons then circulate in a booster ring that employs a radio frequency cavity to further accelerate the electrons to 2.9 GeV. After the booster ring, the electrons are transferred to the storage ring where they emit synchrotron radiation each time their path is bent by magnets. Insertion devices, such as wigglers and undulators, are located in straight sections

and help to increase the brightness and produce intense synchrotron light before entering a beamline. During the process of synchrotron radiation production, the electrons and photons travel in a vacuum chamber with a pressure of less than 1.33×10^{-9} Pa (1.32×10^{-14} atm) to avoid collisions with atoms or molecules.[41]

Synchrotron radiation is focussed and controlled in a beamline using an optics hutch and an experimental hutch where it is further focussed and the beam intensity and energy are monitored. The HXMA 06ID-1 beamline includes a 63 pole superconducting wiggler and Si(111) or Si(220) double crystal monochromators to tune the wavelength from 0.3 to 2.5 Å. The experimental setup for XRD experiments at HXMA is shown in Figure 3.15. The x-ray beam is collimated down to 30 μm and further refined with a cleanup aperture made in a rhenium foil with a choice from six holes that are drilled into it, ranging from 40 – 61 μm in diameter. After the beam passes through the sample, diffracted x-rays are collected with a Marresearch MAR345 area detector. The detector records diffraction images that are 345 mm in diameter with a pixel resolution of 100 μm x 100 μm. An area detector was chosen as it allows for numerous reflections (Debye ring) to be recorded in each exposure. The Debye rings can be used to calculate the *hkl*s from their positions[42] and will also give an indication of the quality of the sample.[43] A beamstop is placed to protect the detector from the direct beam while monitoring its intensity with a Si PIN diode. The sample, located ~400 mm away from the detector, is centered with motorized stages (four translational and one rotational) using a method described by Smith and Desgreniers.[43] This method measures the intensity of the x-rays transmitted though the sample as x, y, z and ω are scanned. The sample is repositioned until optimal values are reached, which indicates the sample is centered. After the sample has been centered, measurements may begin. To improve the quality of the data, the sample is rotated, or rocked, by a small angle (typically less than 10 degrees) while being exposed to hard x-rays for a duration of at least 5 minutes. Rocking the sample allows the x-rays to encounter more crystallites

at various orientations and reduces detector saturation. This helps to produce diffraction patterns with uniform Debye rings, which in turn increases diffraction peak resolution.[43]

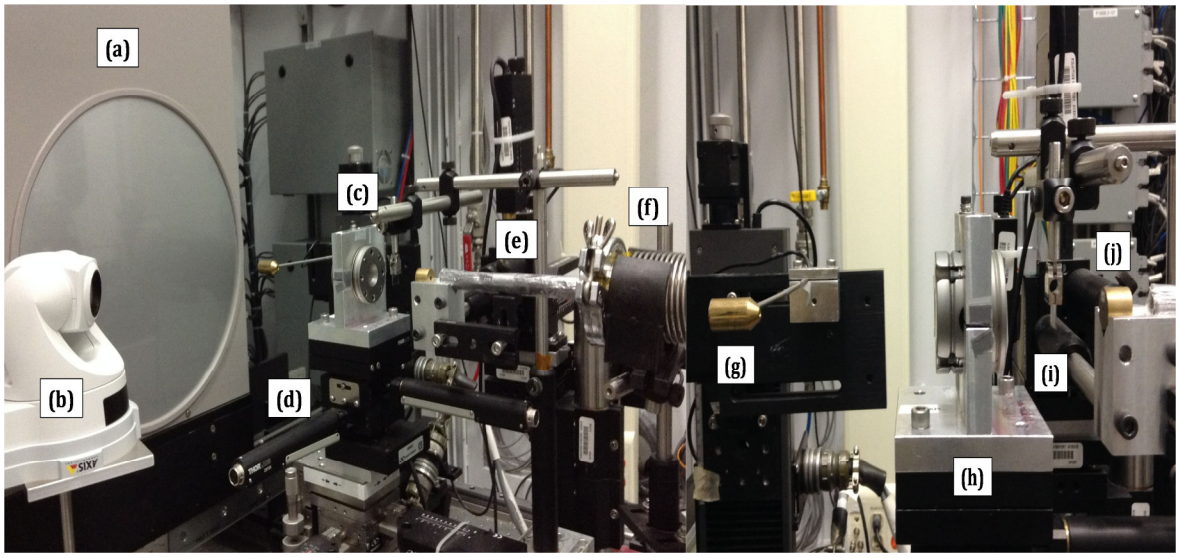

Figure 3.15: The experimental setup for XRD experiments at the HXMA beamline showing **(a)** the Marresearch MAR345 area detector, **(b)** a video camera to observe the setup remotely, **(c,h)** a DAC in a holder that has been mounted to **(d)** motorized stages, **(e)** a lead tube to aid in shielding scattered radiation, **(f)** the end of the beam pipe, **(g)** the beamstop assembly containing a Si PIN diode, **(i)** the cleanup aperture and **(j)** 30 or 45 μm collimator. The X-ray beam travels right to left.

The CLS@APS (Advanced Photon Source in Argonne, Illinois) is larger than the CLS facility in Saskatoon, Saskatchewan and also includes a linear accelerator, booster synchrotron (ring), storage ring, insertion devices and experimental sections. In the linear accelerator, electrons are accelerated to 450 MeV, traveling at 299 792 458 m/s, greater than 99.999 % the speed of light. The booster ring further accelerates the electrons to 7 GeV and then they are injected into the storage ring which has a circumference of 1104 m and contains more than 1000 electromagnets and equipment. Insertion devices are also used to aid with intensifying the synchrotron light before it enters the beamline. The XRD experimental setup at the CLS@APS is very similar to that of the CLS. Differences include a 3.3m long undulator as the source and Kirkpatrick-Baez mirrors to focus the beam at the sample to a spot of 5×5 μm^2.[44]

3.5.5 Data Analysis

To properly analyze and assign lattice parameters and space groups, the set-up must be optimized and calibrated. Calibration is done by taking an XRD image of an X-ray standard (Figure 3.16). In this work, LaB_6 and Si were used at the CLS and CLS@APS, respectively. Once the two-dimensional diffraction image is taken, a program called Fit2D[45] integrates the intensities to produce a one-dimensional diffraction pattern, displaying intensity as a function of 2θ. Each diffraction peak corresponds to a Debye ring. Fit2D aids with refining parameters such as sample-to-detector distance, pixel coordinates of the direct beam, and orientation of the detector plane with respect to the direct X-ray beam, parameters which are necessary for proper calibration. Figures 3.16 and 3.17 show the calibration of a LaB_6 diffraction image with Fit2D.

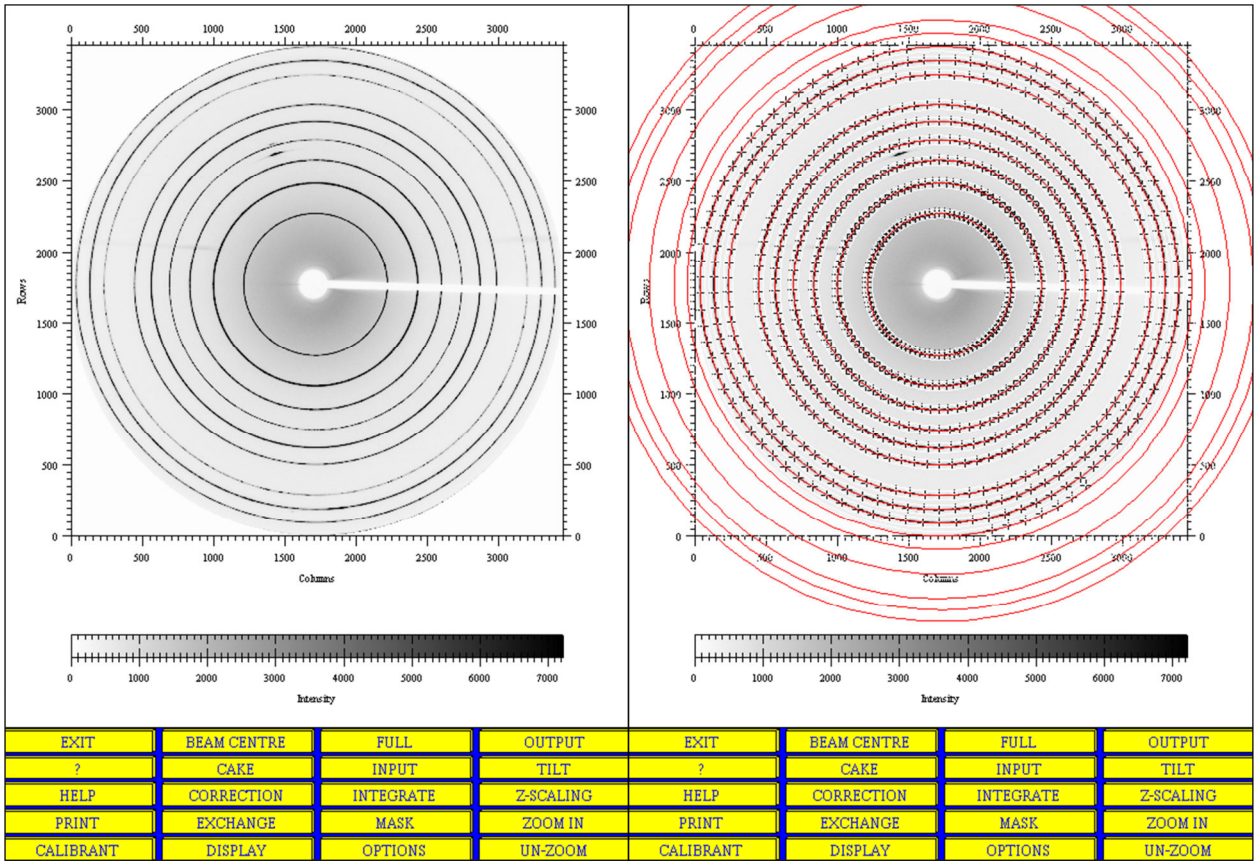

Figure 3.16: A LaB_6 diffraction image used for calibration and processed via Fit2D.

The X-ray diffraction pattern obtained from the integration of the image (Fig. 3.17) is then imported into a program called XRDA[28] where it is indexed. In XRDA, the peaks are fit with either Gaussian or Lorentzian profiles which provide the corresponding d-spacings.

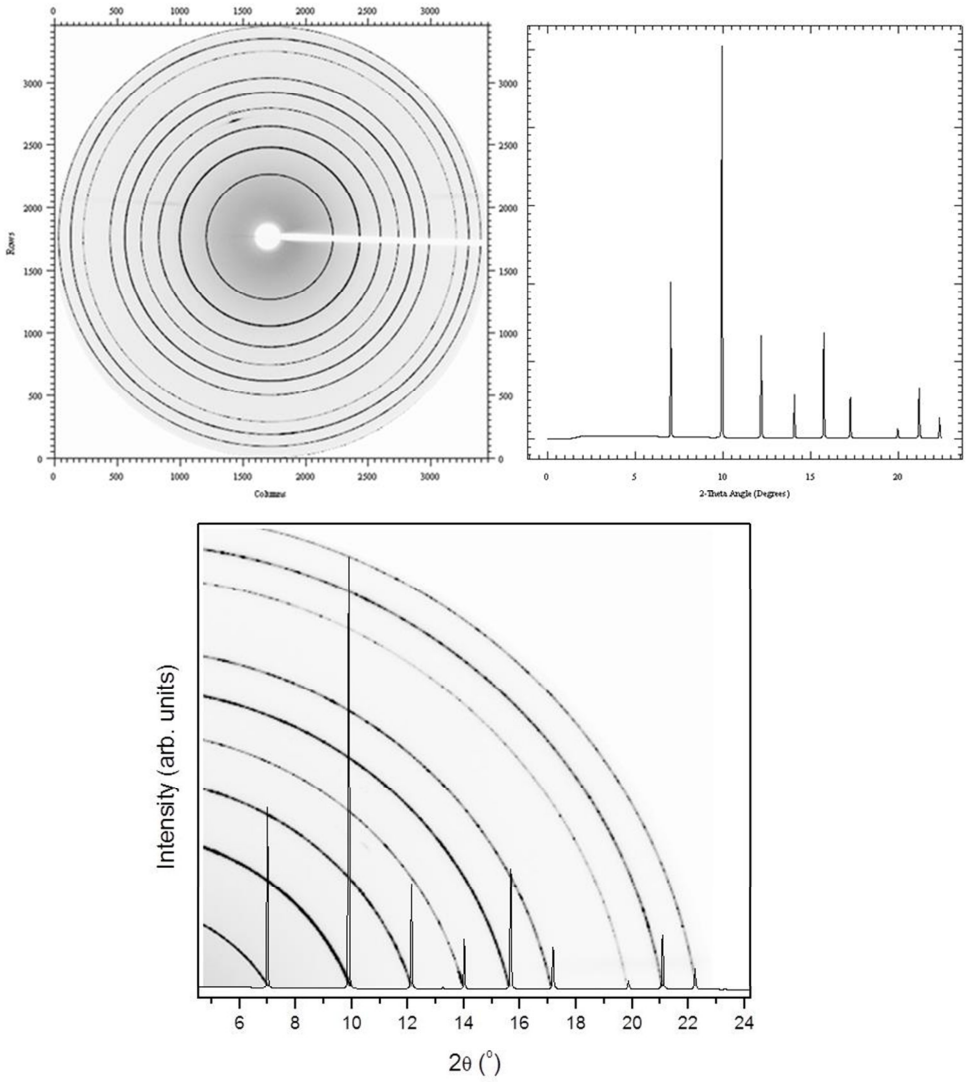

Figure 3.17: LaB_6 images showing the relation between the Debye rings and integrated intensities.

For the standard, the unit cell is known and the Bravais lattice and parameters are entered into the program. A simulated diffraction pattern is created showing a set of expected reflections for the known unit cell. Figure 3.18 shows (hkl) values that have been assigned to observed peaks, from which the lattice parameters are obtained.

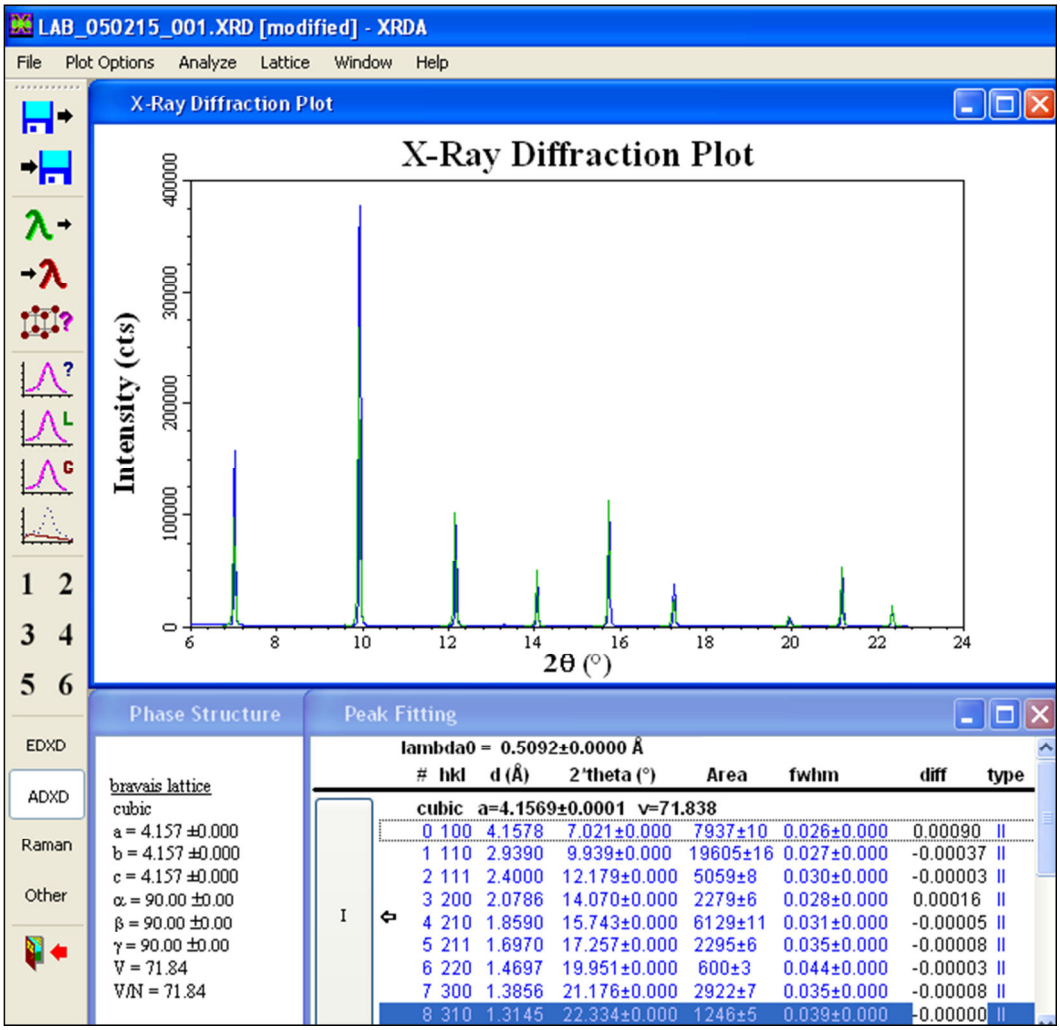

Figure 3.18: An analysis of a LaB_6 diffraction pattern with XRDA. The (*hkl*) have been assigned and the lattice parameter of 4.1569 Å has been obtained. The lattice parameters for the standard should be within 0.001 Å for successful calibration. LaB_6 is a NIST standard with a lattice parameter of 4.156826 Å ± 0.00008 Å at 22.5 °C.[46]

For cases where no information is known about the unit cell, software included in the Crysfire suite[47] can aid with indexing diffraction patterns. Crysfire uses several algorithms to search for unit cells and structures that best match the observed d-spacings. Different algorithms are used and the proposed structures are compared to the experimental data to verify that all of the reflections can be accounted for. Once a suitable unit cell has been found, XRDA will provide the lattice parameters and unit cell volume and programs such as Chekcell[48] can aid with assigning a space group to the

structure. Space groups describe the symmetry of a crystal and positions of the atoms in the unit cell. A space group will provide information on peak intensities and absences that will be expected in the diffraction pattern. Assigning space groups can be difficult and may not be possible at times if conditions for the sample are not ideal. Non-hydrostatic conditions, for example, can cause ambiguous reflections in a diffraction pattern.

To aid in verifying a structure, the reflection intensities can be analyzed with Le Bail[49] and Rietveld[50] methods using programs such as FullProf[51] suite. These methods use least-squares algorithms to minimize the difference between the calculated and observed diffraction patterns. The Le Bail method does not require atomic positions or space group and is a full pattern refinement procedure to extract the intensities and structural parameters. It does not provide a space group, but gives a comparison between the intensities for all indexed peaks. A probable structure will have a small deviation. The Rietveld method requires a model (space group) and is a full pattern refinement procedure to refine a known crystal structure by calculating intensities from the structural information. The goal of the Rietveld method is to minimize the following residual function:

$$S_y = \sum_i w_i [y_i(obs) - y_i(calc)]^2 \tag{3.6}$$

where y_i(obs) and y_i(calc) are the intensities of the experimental and calculated diffraction patterns, respectively, of the i^{th} point with a weighting factor of w_i. R-factors show how well the calculated pattern matches the experimental data. The weighted-profile R-factor, R_{wp}, provides the quality of the refinement and is defined as

$$R_{wp} = \sqrt{\frac{\sum_i w_i [y_i(obs) - y_i(calc)]^2}{\sum_i w_i [y_i(obs)]^2}} \tag{3.7}$$

Ideally, the R_{wp} should be less than 10%. In addition to the parameters refined by the Le Bail method, proper intensity profiles and atomic positions are also refined with the Rietveld method.[50]

References

1. Jamieson, J. C., Lawson, A. W. & Nachtrieb, N. D. New device for obtaining X-ray diffraction patterns from substances exposed to high pressure. *Rev. Sci. Instrum.* **30,** 1016–1019 (1959).

2. C. E. Weir, E. R. Lippincott, A. Van Valkenburg, E. N. & Bunting. Infrared Studies in the 1- to 15 micron region to 30,000 atmospheres. *J. Reasearch Natl. Bur. Stand. - A. Phys. Chem.* **63,** 55 – 62 (1959).

3. Dubrovinsky, L., Dubrovinskaia, N., Prakapenka, V. B. & Abakumov, A. M. Implementation of micro-ball nanodiamond anvils for high-pressure studies above 6 Mbar. *Nat. Commun.* **3,** 1163 (2012).

4. Jayaraman, A. Diamond anvil cell and high-pressure physical investigations.pdf. *Reviews of Modern Physics* **55,** 65–108 (1983).

5. Ashby, M. F. *Materials Selection in Mechanical Design*. (Elsevier Butterworth-Heinemann, Oxford, 2005).

6. Sir, B. & Robertson, R. Philosophical Transactions of the Royal Society of London. Series A Containing Papers of a Mathematical or Physical Character 1915 Bragg.pdf. **232,** 463–535 (2015).

7. Custers, J. F. H. Unusual phosphorescence of a diamond. *Physica* **18,** 489–493 (1952).

8. Wentorf, R. H. & Bovenkerk, H. P. Preparation of Semiconducting Diamonds. *J. Chem. Phys.* **36,** 1987 (1962).

9. Dyer, H. B., Raal, F. A., Du Preez, L. & Loubser, J. H. N. Optical absorption features associated with paramagnetic nitrogen in diamond. *Philos. Mag.* **11,** 763–774 (1965).

10. Xu, J. & Mao, H. Moissanite: a window for high-pressure experiments. *Science* **290,** 783–785 (2000).

11. Xu, J., Mao, H., Hemley, R. J. & Hines, E. The moissanite anvil cell: a new tool for high-pressure research. *J. Phys. Condens. Matter* **14,** 11543–11548 (2002).

12. Katrusiak, A. High-pressure crystallography. *Acta Crystallogr. Sect. A Found. Crystallogr.* **64,** 135–148 (2007).

13. Mao, H. K., Bell, P. M., Shaner, J. W. & Steinberg, D. J. SPECIFIC VOLUME MEASUREMENTS OF Cu, Mo, Pd, AND Ag AND CALIBRATION OF THE RUBY R1 FLUORESCENCE PRESSURE GAUGE FROM 0. 06 TO 1 MBAR. *J. Appl. Phys.* **49,** 3276–3283 (1978).

14. Mao, H. K., Xu, J. & Bell, P. M. Calibration of the Ruby Pressure Gauge to 800 kbar Under Quasi-Hydrostatic Conditions. *J. Geophys. Res.* **91,** 3276–4676 (1986).

15. Dewaele, A., Torrent, M., Loubeyre, P. & Mezouar, M. Compression curves of transition metals in the Mbar range: Experiments and projector augmented-wave calculations. *Phys. Rev. B - Condens. Matter Mater. Phys.* **78,** 1–13 (2008).

16. Eremets, M. I. *High Pressure Experimental Methods*. (Oxford University Press, New York/Tokyo, 1996).

17. Lotz, H. & Schouten, J. Phase behavior of the N2-Ar system at high pressures: A Raman spectroscopy study. *Phys. Rev. B* **64,** 1–6 (2001).

18. Scheerboom, M. I. M. & Schouten, J. A. Orientational behavior of solid nitrogen at high pressures investigated by vibrational Raman spectroscopy. *J. Chem. Phys.* **105,** 2553 (1996).

19. Schneider, H., Häfner, W., Wokaun, a. & Olijnyk, H. Room temperature Raman scattering studies of external and internal modes of solid nitrogen at pressures 8≤P≤54 GPa. *J. Chem. Phys.* **96,** 8046 (1992).

20. LeSar, R. *et al.* Raman spectroscopy of solid nitrogen up to 374 kbar. *Solid State Commun.* **32,** 131–134 (1979).

21. Buchsbaum, S., Mills, R. L. & Schiferl, D. Phase diagram of nitrogen determined by Raman spectroscopy from 15 to 300 K at pressures to 52 GPa. *J. Phys. Chem.* **88,** 2522–2525 (1984).

22. Moudgil, H. K. *Textbook of Physical Chemistry*. (PHI Learning Pvt. Ltd., Delhi, 2015).

23. Bernath, P. F. *Spectra of Atoms and Molecules*. (Oxford University Press, New York, 2005).

24. Harris, D. D. & Bertolucci, M. D. *Symmetry and Spectroscopy: An Introduction to Vibrational and Electronic Spectroscopy*. (Oxford University Press & Dover Publications, New York, 1989).

25. Long, D. A. *The Raman Effect: A Unified Treatment of the Theory of Raman Scattering by Molecules*. (John Wiley & Sons Ltd., Chichester, England, 2002).

26. Ferraro, J. R. & Nakamoto, K. *Introductory Raman Spectroscopy*. (Academic Press, San Diego, 2012).

27. Anderson, A. *The Raman Effect: Principles, Volume 1*. (Marcel Dekker Inc., New York, 1971).

28. Desgreniers, S. & Lagarec, K. XRDA: a program for energy-dispersive X-ray diffraction analysis on a PC. *J. Appl. Crystallogr.* **27,** 432–434 (1994).

29. Michette, A. G. & Pfauntsch, S. *X-rays: the first hundred years*. (John Wiley & Sons Ltd., Chichester, England, 1996).

30. Kittel, C. *Introduction to Solid State Physics*. (John Wiley & Sons, Inc., Hoboken, NJ, 2005).

31. Cullity, B. D. & Stock, S. R. *Elements of X-ray Diffraction*. (Prentice Hall, Upper Saddle River, NJ, 2001).

32. Ashcroft, N. W. & Mermin, N. D. *Solid State Physics*. (Thomson Learning, Inc., New York, 1976).

33. Bennet, D. W. *Understanding Single-Crystal X-ray Crystallography*. (WILEY-VCH Verlag GmbH & Co. KGaA, Weinheim, 2010).

34. David, W. I. F., Shankland, K. & McCusker, L. B. et al. *Structure Determination from Powder Diffraction Data*. (Oxford University Press, Oxford, 2006).

35. Harris, K. D. M., Tremayne, M. & Kariuki, B. M. Contemporary Advances in the Use of Powder X-Ray Diffraction for Structure Determination. *Angew. Chem. Int. Ed. Engl.* **40,** 1626–1651 (2001).

36. Elder, F. R., Gurewitsch, a. M., Langmuir, R. V. & Pollock, H. C. Radiation from electrons in a synchrotron [8]. *Phys. Rev.* **71,** 829–830 (1947).

37. Kleppner, D. & Pipkin, F. *Atomic Physics 7*. (Plenum Press, New York, 1981).

38. Hammond, C. *The Basics of Crystallography and Diffraction*. (Oxford University Press, New York, 2009).

39. Jørgensen, M. R. V. *et al.* Contemporary X-ray electron-density studies using synchrotron radiation. *IUCrJ* **1,** 267–280 (2014).

40. Kunz, C. Synchrotron radiation: third generation sources. *J. Phys. Condens. Matter* **13,** 7499–7510 (2001).

41. Canadian Light Source. What is a Synchrotron? at <http://www.lightsource.ca>

42. Ladd, M. & Palmer, R. *Structure Determination by X-ray Crystallography*. (Kluwer Academic/Plenum Publishers, New York, 2003).

43. Smith, J. S. & Desgreniers, S. Selected techniques in diamond anvil cell crystallography: Centring samples using X-ray transmission and rocking powder samples to improve X-ray diffraction image quality. *J. Synchrotron Radiat.* **16,** 83–96 (2008).

44. Advanced Photon Source. Introduction to APS. at <www1.aps.anl.gov>

45. Hammersley, A. P., Svensson, S. O., Hanfland, M., Fitch, A. N. & Hausermann, D. Two-Dimensional Detector Software: From Real Detector to Idealised Image or Two-Theta Scan. *High Press. Res.* **14,** 235–248 (1996).

46. NIST. Line Position and Line Shape Standard for Powder Diffraction (Lanthanum Hexaboride Powder). *National Institute of Standards and Technology; US Department of Commerce Gaithersburg, MD* 1–5 (2015). at <https://www-s.nist.gov/srmors/certificates/660C.pdf?CFID=35608137&CFTOKEN=7e602cd95cb32152-D56C3582-CDD9-D727-1A32D16FDB2CF208>

47. Shirley, R. *The Crysfire System for Automated Powder Indexing: User's Manual*. (The Lattice Press, Guilford, England, 2000).

48. Shirley, R. et al. CRYSFIRE Powder Indexing System for DOS/Windows. at <http://www.ccp14.ac.uk/tutorial/crys/index.html>

49. Le Bail, A. & Fourquet, J. L. Ab-initio structure determination of LiSbWO6 by X-ray powder diffraction. *Mater. Res. Bull.* **23,** 447 (1988).

50. McCusker, L. B., Von Dreele, R. B., Cox, D. E., Louër, D. & Scardi, P. Rietveld refinement guidelines. *J. Appl. Crystallogr.* **32,** 36–50 (1999).

51. Rodriguez-Caravajal, J. Recent advances in magnetic structure determination by neutron powder diffraction. *Phys. B* **192,** 55 (1993).

Chapter 4
NITROGEN

In the present work, Raman measurements were taken on condensed samples of pure nitrogen and used as an aid for comparison and calibration of the data obtained for the nitrogen/noble element mixed systems. This chapter outlines the results of these measurements and the corresponding calibrations that were required.

4.1 Calibration for Raman Spectroscopy

Samples of pure nitrogen (N_2) were loaded into a diamond anvil cell (DAC) for Raman spectroscopic measurements at room temperature and elevated pressures to compare the experimental vibrational frequencies and the corresponding linewidths obtained in this work to those in the literature.[1,2,3,4] An argon ion laser (wavelength at 488 nm) was utilized as the excitation light source for these measurements. The experimental set-up was calibrated with both neon and argon emission wavelengths. Spectra were obtained with Andor Solis software driving the Raman spectrometer utilizing the "Step-and-Glue" function, where multiple exposures were taken at different central wavelengths and "stitched" together by the program to achieve full Raman spectra. This setting was chosen as it provides the most vibrational information over a wide spectral range. As the vibrational frequencies recorded for N_2 presented an offset from the actual laser wavelength which had to be accounted for by a proper calibration. Figure 4.1 displays a typical Raman spectrum of condensed N_2 (β phase) recorded at 2.92 GPa. The N_2 vibron shown was measured to be 2340.8 cm^{-1} and, when compared to value reported in the literature for the same conditions, is

shifted by ~3.6 cm^{-1}. This amount corresponds to the laser offset, as recorded by the instrument (Figure 4.1). With a proper spectrometer calibration the observed vibrational frequency is corrected and in agreement with the reported value.[4]

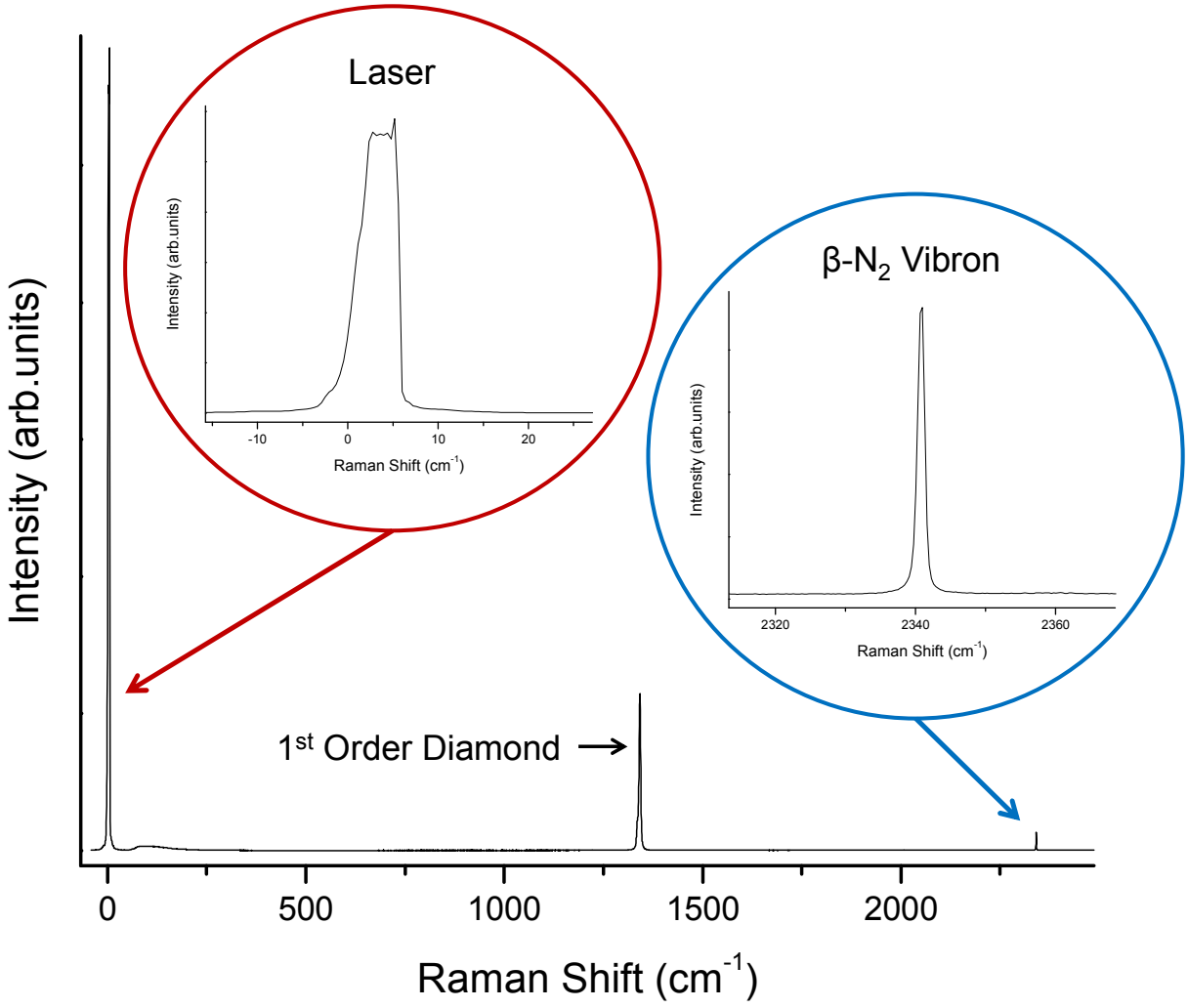

Figure 4.1: Raman spectrum of β-N_2 at 2.92 GPa and 300 K. A consequence of using the "Step-and-Glue" function of the recording software (Andor Solis) is that the measurement will have an offset that is equal to the laser offset. The offset depicted in this figure is about 3.6 cm^{-1}. The observed offset is applied to correct all recorded spectra.

4.2 Raman Spectroscopy Results

Pure condensed N_2 at room temperature is expected to undergo phase transitions from liquid to solid β-phase with pressure at ~2.4 GPa, from β- to δ-phase at ~4.9 GPa, and from δ- to ε-phase at ~16.3 GPa.[2] The phase diagram for pure N_2 was presented earlier in this work in Chapter 2, Section 3. These transitions were clearly visible from the Raman spectra, and in addition, the δ-ε transition was observed visually. As an example, Figure 4.2 displays the Raman spectra that correspond to the β-δ phase transition.

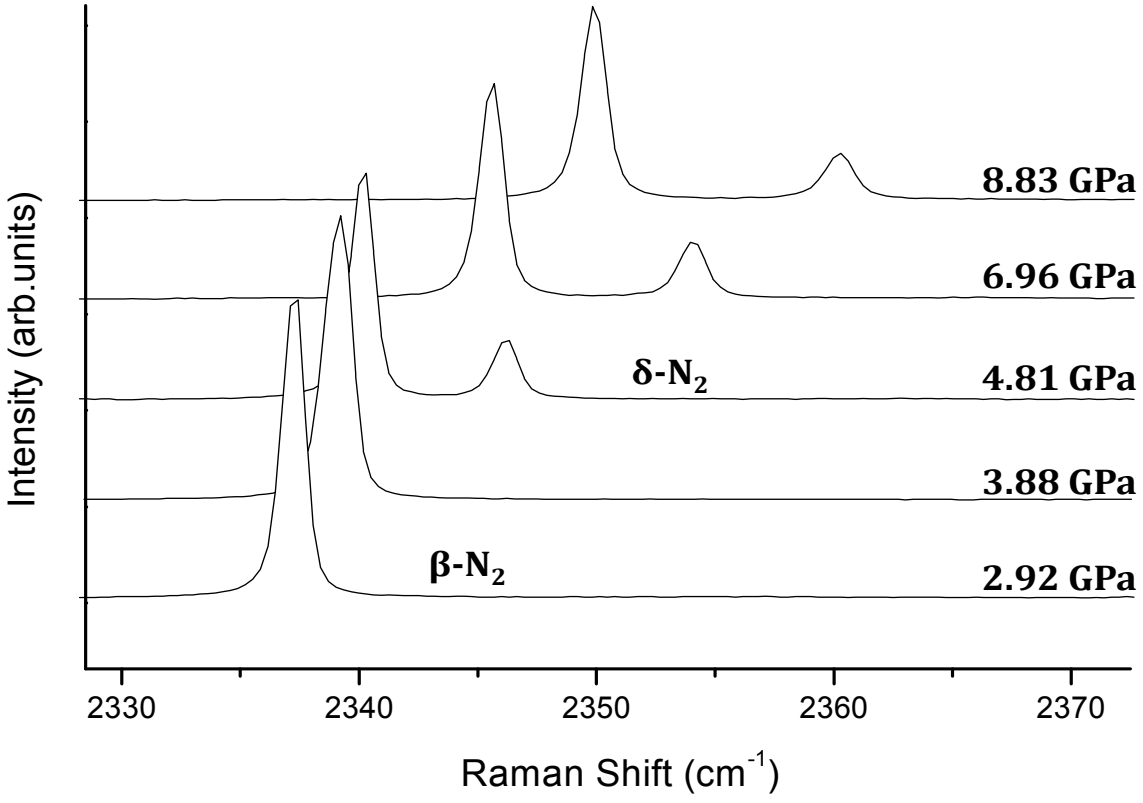

Figure 4.2: Experimental Raman spectra obtained for pure condensed N_2 showing the obvious solid-to-solid phase transition from β- to δ-N_2.

Regarding Raman spectroscopy, the focus in this work was on the high energy (intra-molecular or stretching modes) modes, however it should be noted that low energy (extra-molecular or lattice) modes are also expected to change with the different high pressure phases of nitrogen, such as the ε phase. Figure 4.3 shows the low energy Raman spectra observed for pure nitrogen from this work and by Schneider *et al*.[2] The experimental Raman spectra from this work display peaks similar to those observed by Schneider *et al*., indicative of the δ- to ε-N_2 phase transition.

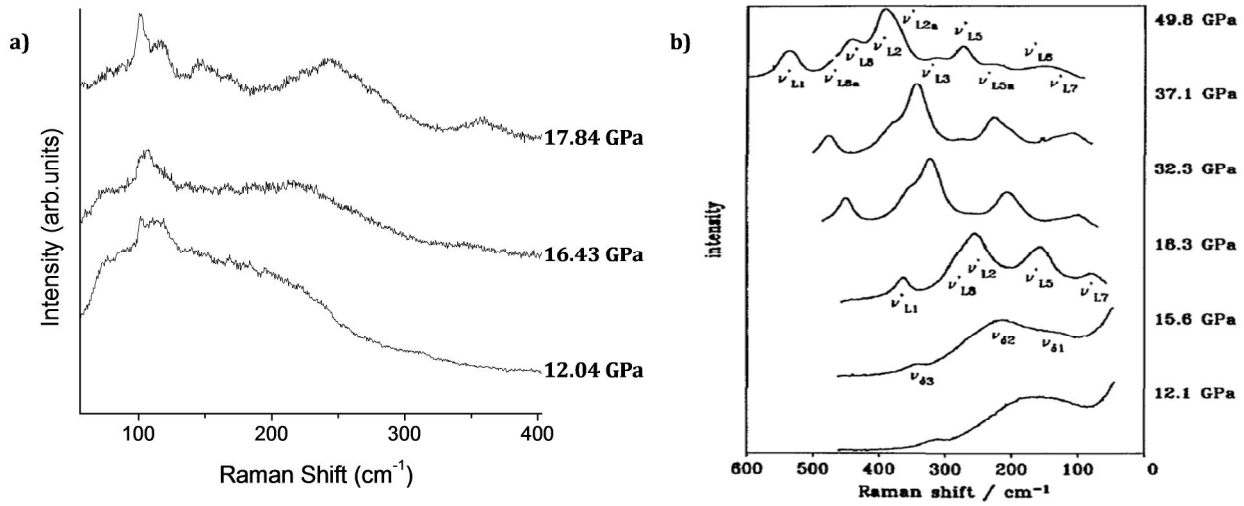

Figure 4.3: Raman spectra of the low energy lattice modes of pure nitrogen from **(a)** this work and by **(b)** Schneider *et al*.[2] Additional modes are expected around 16 GPa due to the δ- to ε-N_2 phase transition. *NOTE: **(b)** Reprinted with permission from the American Institute of Physics, Copyright 1992.*[2]

Solid N_2 is transparent and the only visually observable phase transitions for N_2 occur at the fluid-solid transition and at the δ-ε transition. Figure 4.4, below, shows the observable change (texture) in the sample as it undergoes transformation from δ- to ε-N_2.

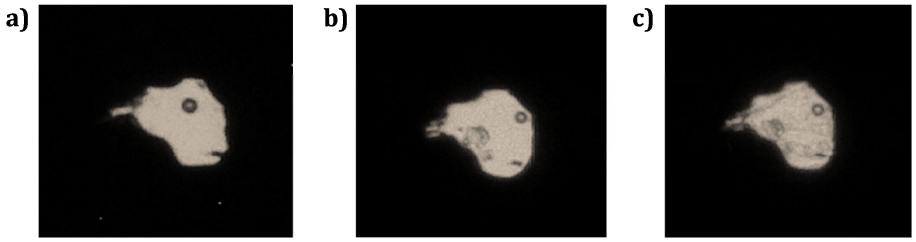

Figure 4.4: A sample of pure N_2 at **(a)** 13.8 GPa, **(b)** 16.43 GPa, and **(c)** 17.84 GPa. Once in the ε phase, N_2 is observed to be "textured".

After the offset corresponding to the known laser wavelength was taken into account, the vibrational frequencies for pure nitrogen were in good agreement with those in the literature. These vibrational frequencies as a function of pressure are presented in Figure 4.5. The uncertainty for each frequency is about ± 1 cm^{-1} and is incorporated into the size of the data point. The Raman spectroscopic data for N_2 is important for this work as the data will be used as the basis for comparison when N_2 is mixed with noble element species. It also ensures proper calibration the spectrometer.

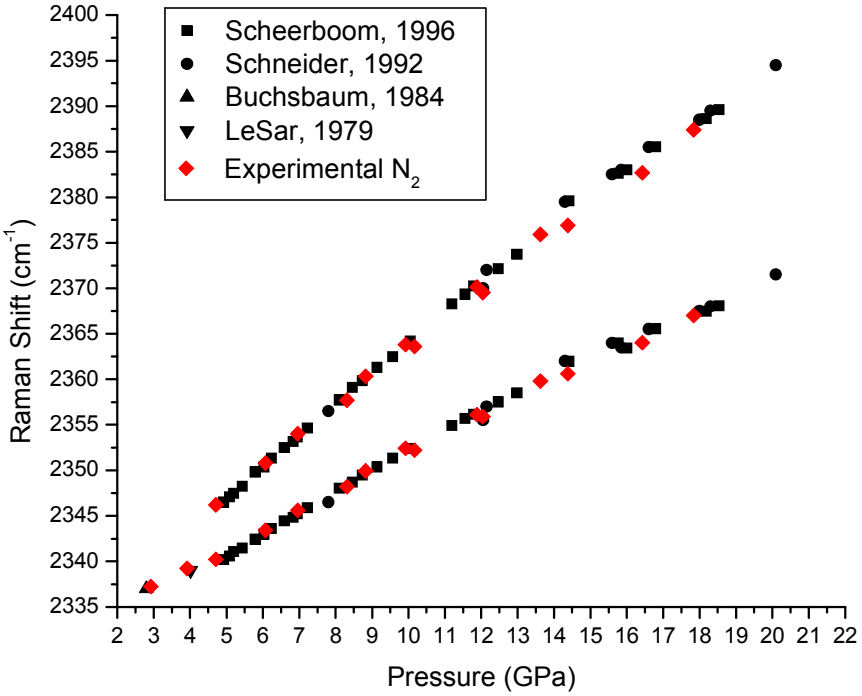

Figure 4.5: Experimental vibrational frequencies obtained for pure N_2 compared to the literature values in the relevant pressure range at room temperature. The ε phase is usually observed by the splitting of the υ_2 vibron above 16.3 GPa. In this figure it is represented with one data point. Note that data points at 14.38 GPa and 16.43 GPa correspond to single measurements.

References

1. Scheerboom, M. I. M., Michels, J. P. J. & Schouten, J. A. High pressure study on the Raman spectra of fluid nitrogen and nitrogen in helium. *J. Chem. Phys.* **104,** 9388 (1996).

2. Schneider, H., Häfner, W., Wokaun, A. & Olijnyk, H. Room temperature Raman scattering studies of external and internal modes of solid nitrogen at pressures 8≤P≤54 GPa. *J. Chem. Phys.* **96,** 8046 (1992).

3. Buchsbaum, S., Mills, R. L. & Schiferl, D. Phase diagram of nitrogen determined by Raman spectroscopy from 15 to 300 K at pressures to 52 GPa. *J. Phys. Chem.* **88,** 2522–2525 (1984).

4. LeSar, R. *et al.* Raman spectroscopy of solid nitrogen up to 374 kbar. *Solid State Commun.* **32,** 131–134 (1979).

Chapter 5
NITROGEN-ARGON

In this work, the focus for experiments was on the study of the nitrogen-argon binary system. Raman spectroscopy and XRD measurements were taken on mixed samples with various concentrations of nitrogen and argon. The results and a discussion of these experiments are reported in this chapter.

5.1 N_2-Ar Samples

Table 5.1 summarizes the N_2-Ar samples studied in the present work in chronological order. Note, however, that these samples are organized in this chapter by low and high concentrations of N_2.

Table 5.1: Summary of the N_2-Ar samples studied in this work and the corresponding experiments performed on the samples.

Sample	Sample Loading Procedure	Concentration (x = N_2 mole fraction)	Pressure Range (GPa)	Experiment
*NAr1xx**	Cryogenic	0.60	2.71 - 9.39	Raman, XRD
NAr2xx	Gas	0.04	0.56 – 18.93	Raman
NAr3xx	Gas	0.80	1.60 – 21.46	Raman
NAr4xx	Gas	0.15<x<0.25	1.65 – 10.09	Raman†, XRD
NAr5xx	Gas	0.06<x<0.10	10.9	Raman, XRD
NAr6xx	Gas	0.04<x<0.08	1.57 – 10.98	Raman†, XRD
NAr7xx	Cryogenic	0.65	2.35 – 16.04	Raman, XRD
NAr8xx	Gas	0.10<x<0.20	1.65 – 20.13	Raman, XRD
NAr9xx	Gas	0.75	5.63 – 22.82	Raman, XRD

(*) *Sample was prepared and experimented on by Catherine Aldous.* (†) *Raman spectroscopy performed at the CLS with excitation light at λ=532 nm. All others performed at the LPSD with excitation light at λ=488 nm.*

5.2 Raman Spectroscopy Results

5.2.1 Low N_2 Concentrations

All of the Raman spectroscopy experiments in this work were performed at room temperature. The uncertainty for each vibrational frequency and linewidth (FHWM) is 1 cm^{-1}. By comparing the intensity of the Raman line associated with the N_2 stretching mode (vibron) with respect to the 2nd order Raman intensity of diamond (anvil), a rough estimate of the concentration of the sample is obtained. A lower relative intensity indicates a lower concentration

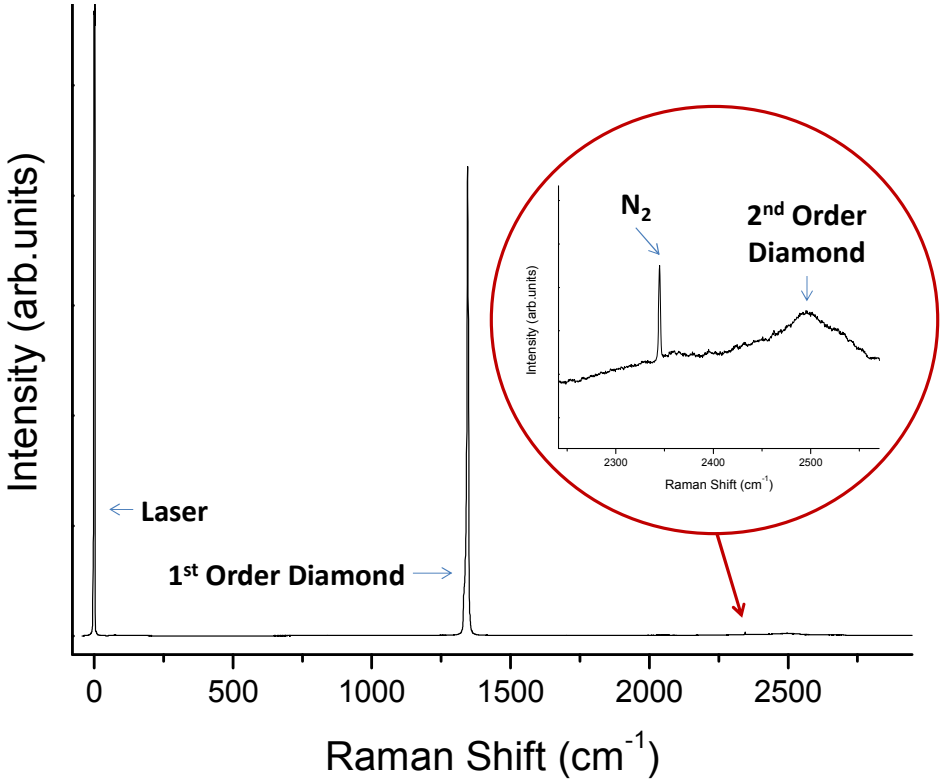

Figure 5.1: Raman spectrum of *NAr8xx* (0.10<x<0.20) at 4.43 GPa showing the intensities from the attenuated laser light, and Raman signals from diamond and N_2. It should be noted that the 2nd order Raman signal is not just a 'peak' as the arrow in the plot suggests. It actually extends from low Raman shift to twice that of the maximum of the first order (at ambient conditions), following the density of state.

of N_2 and vice-versa. Figure 5.1 provides an example of the nitrogen vibron intensity of a sample of N_2-Ar that contained less than x = 0.20 at 4.43 GPa, where "x" denotes the mole fraction of N_2 in the N_2-Ar system.

For samples containing a low concentration of N_2, less than x = 0.25, only a single vibron line was observed up to the highest pressure investigated. Figure 5.2 shows Raman spectra of sample *NAr8xx* up to 24.75 GPa. The vibron line is observed to broaden with pressure. Figure 5.3 gives the spectral linewidth (full-width-half-maximum, FWHM) for samples with low N_2 concentration. *NAr5xx* and *NAr6xx* are omitted from this plot as the resolution was low and the spectra gave unreliable vibrational linewidths. The FWHM increases with pressure with no obvious changes in the slope. Jumps or changes in the slope of the FWHM as a function of pressure are indicators of possible phase transitions.

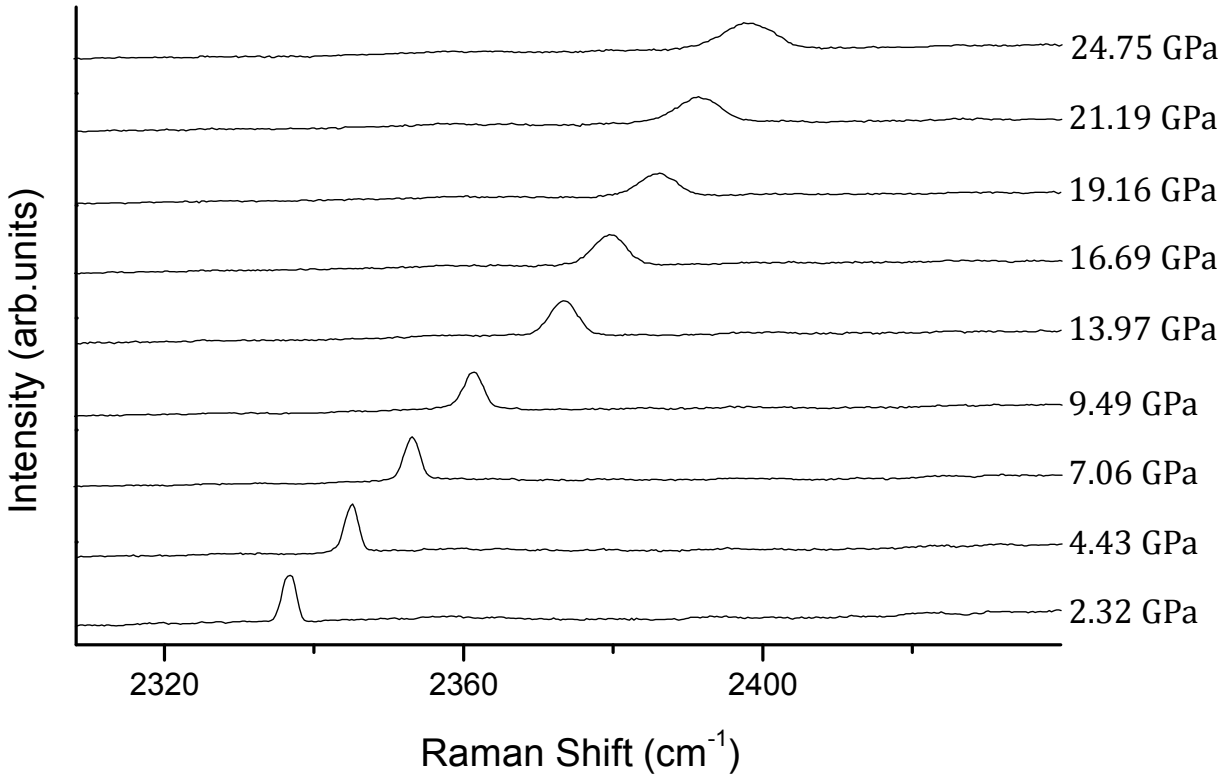

Figure 5.2: Raman spectra of the nitrogen (vibrational mode) in *NAr8xx* with 0.10<x<0.20. The sample is showing line broadening at higher pressures, most likely due to strain on crystals.

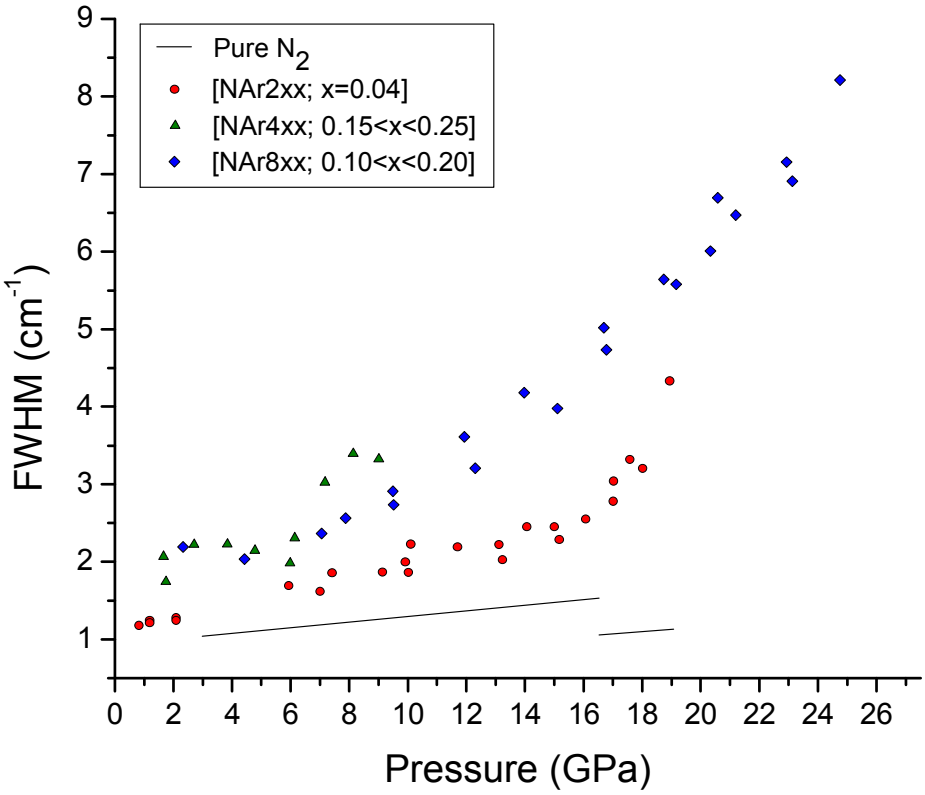

Figure 5.3: The FWHM of N_2 vibron lines as a function of pressure. Solid lines correspond to data points for pure N_2 from this work.

In Chapter 4, it was discussed how new lattice modes will appear in the lower energy Raman spectra at higher pressures. New vibrational modes appear around 16 GPa and are due to the δ to ε phase transition in pure nitrogen as observed in this work and reported in the literature.[1] Figure 5.4 presents the low energy Raman spectra for *NAr8xx* at various pressures. The spectra look similar for most pressures, with certain parts having slightly higher intensities at various pressures, but the peaks do not appear to be dependent on pressure. The peak labelled with an asterisk (*) at around 100 cm^{-1} and 7.06 GPa disappears above and below that pressure but is observed all other pressures investigated and does change with pressure. At 2.32 GPa, there is a weak band around 200 cm^{-1}. It is a little more pronounced at higher pressure. A recording of the spectrum from the gasket area (i.e., beside the sample) is a good way to double check whether a signal is genuinely

arising from the sample or not. There is a possibility that what has been recorded in the spectra of Figure 5.4 arose from the stressed diamond anvil. The lattice modes associated with δ to ε phase change of N_2 are not detected and the spectra observed in Figure 5.4 may not belong to the sample but to the apparatus.

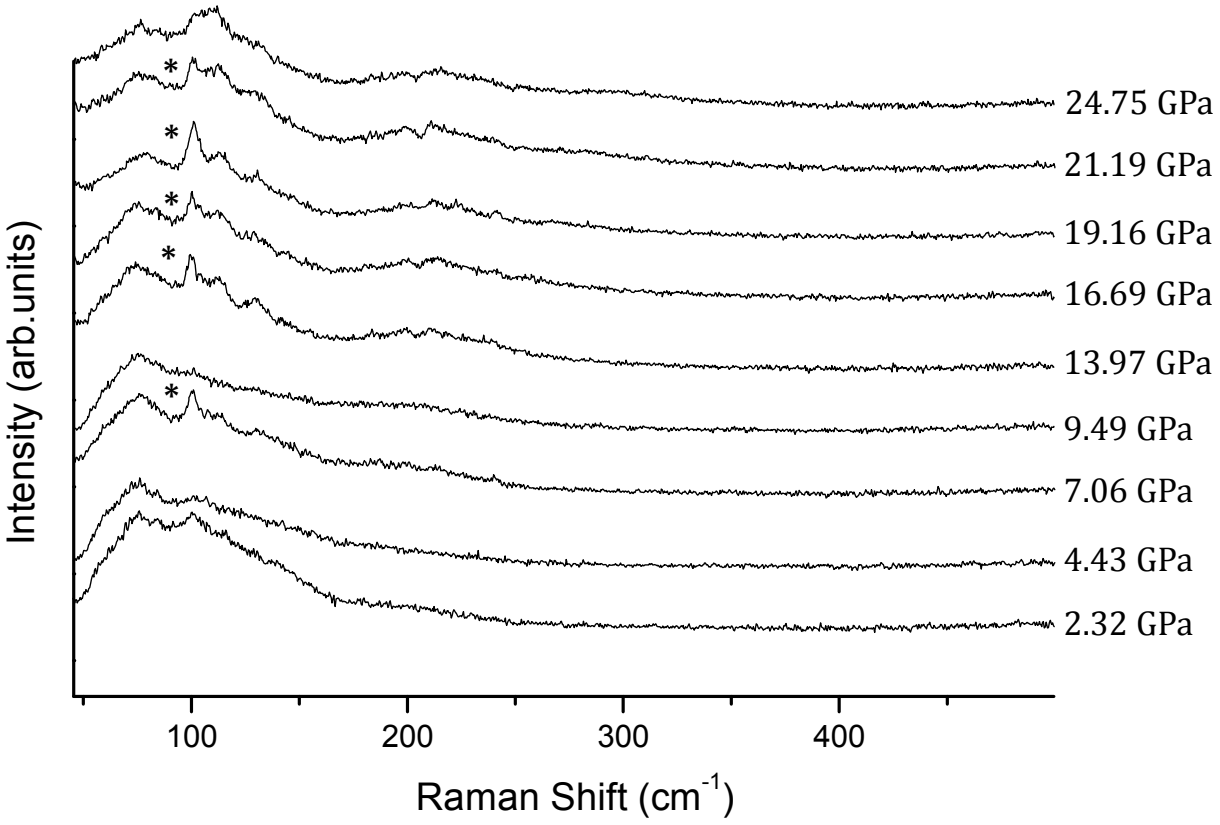

Figure 5.4: Low energy Raman spectra of *NAr8xx* with 0.10<x<0.20.

Figure 5.5 displays Raman spectra for *NAr2xx* with a N_2 mole fraction of x = 0.04. This sample had no experimental issues such as gasket failure and that enabled for the recording of the Raman spectra of the sample upon compression and decompression several times. For samples with x < 0.10, it was difficult to observe the fluid-solid transition at low pressure; however, following a second compression of the *NAr2xx* sample, after taking it to the liquid state, a double Raman peak,

corresponding to stretching vibrations at around 2330 cm^{-1}, was observed at 1.38 GPa (Figure 5.5). Lotz *et al.*[2] also observed two peaks at the fluid-solid transition for various concentrations of the N_2-Ar system. They attributed the two peaks as belonging to the coexistence of liquid and β-N_2.

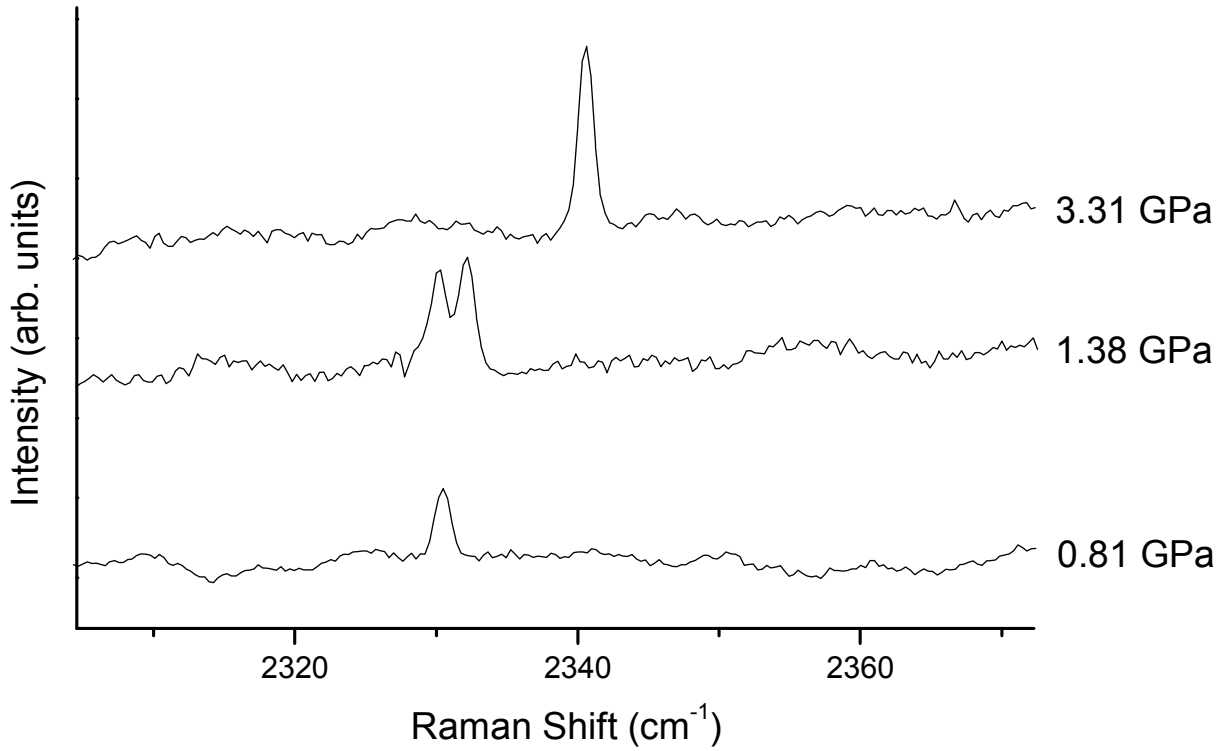

Figure 5.5: *NAr2xx* (x=0.04): The double peak was observed on the 2nd compression of the sample (after taking it to liquid). This was the only instance that a double peak was observed in any sample containing 25% or less of N_2.

The vibrational frequencies for *NAr2xx* as a function of pressure are presented in Figure 5.6 along with a summary of all samples investigated with lower concentrations of N_2. It includes a comparison to pure N_2 (dashed lines) and the results obtained by Lotz *et al.*[2] (hollow symbols), both of which aided in determining the final concentrations of the samples. The Raman frequencies were found to increase with pressure and the frequency for a given pressure did not deviate when either compressed or decompressed. After the fluid-solid transition, samples with lower mole fractions of N_2 tended to change from a lower shift in frequency (with respect to pure N_2) of about 0.5 cm^{-1} into

a higher (~ 1 cm^{-1}, with respect to β-N_2) shift that increased with pressure. For pure N_2, a shift in frequency is expected at the fluid-β transition by about 0.95 cm^{-1} upwards.[2]. The samples of pure N_2 that were investigated in this work were not brought to liquid, however, after calibration of the spectrometer the vibrational frequencies measured with pressure had, at maximum, ~0.08 % difference when compared to the results found in the literature.[1,3,4,5] In this work, a frequency jump at the fluid-solid transition by ~2 cm^{-1} was observed for mixtures that were brought to the liquid-solid transition.

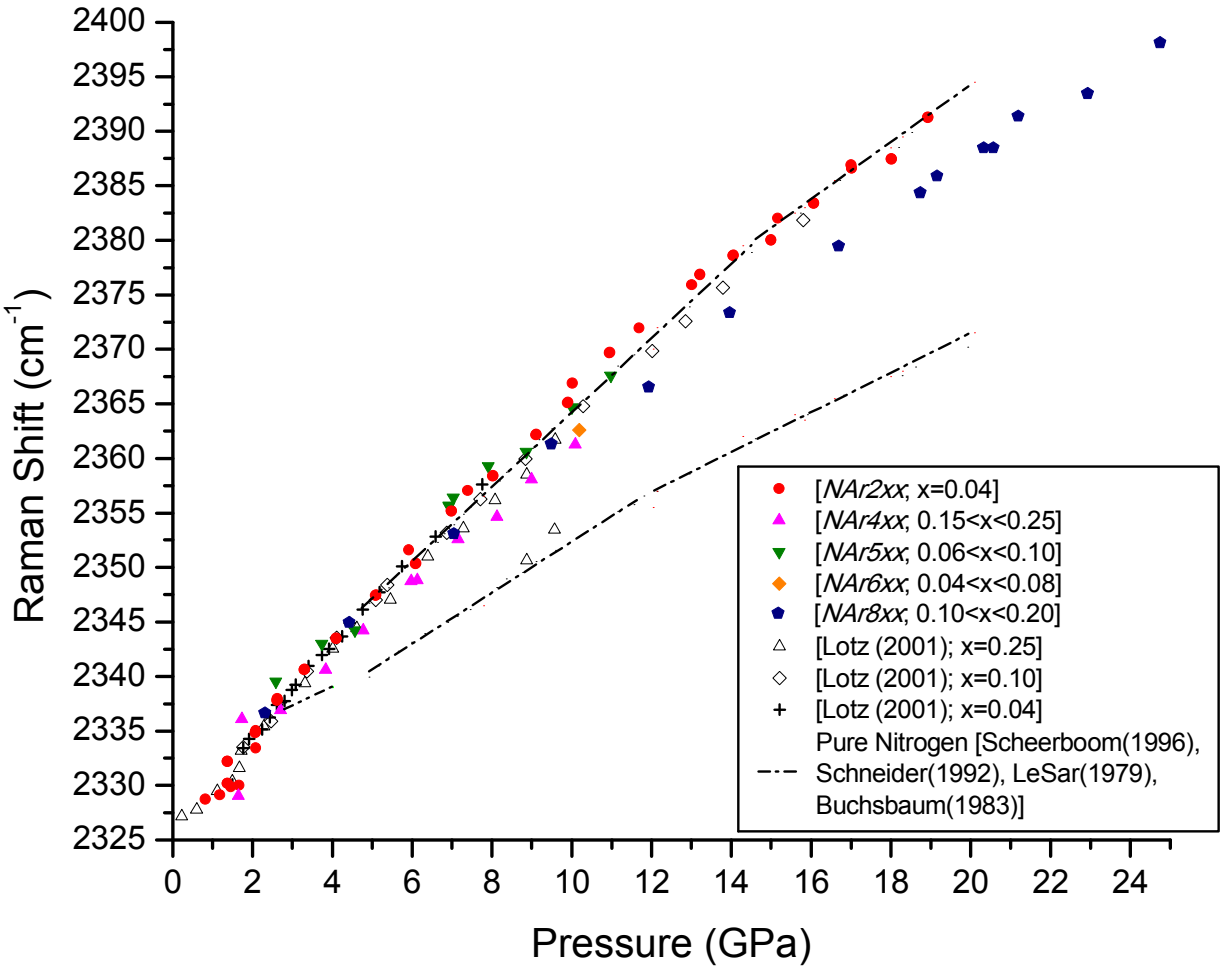

Figure 5.6: Raman shift as a function of pressure for samples with lower concentrations of nitrogen compared to pure nitrogen[1,3,4,5] (dashed lines) and results obtained for the N_2-Ar system by Lotz *et al.*[2] (hollow symbols).

5.2.2 High N_2 Concentrations

As an example of the Raman intensity associated for a sample with a higher N_2 concentration, Figure 5.7 displays the Raman spectrum obtained for *NAr9xx* at 11.93 GPa. The N_2 mole fraction in this case is x = 0.75 and the closer look in the oval shows the intensity of the molecular stretching modes with respect to the 2nd order Raman intensity due to diamond. The higher concentration of N_2 within the sample resulted in a higher intensity. To give an idea of the intensity dependence on the N_2 concentration, the intensity measured for υ_2 (lower frequency vibron) in Figure 5.7 with x = 0.75 is ~40000 times more intense than the vibron measured in Figure 5.1, which had only 0.10<x<0.20. At 11.93 GPa, the nitrogen in *NAr9xx* has undergone phase transitions and is in the δ phase, which is represented by two stretching modes in pure N_2.

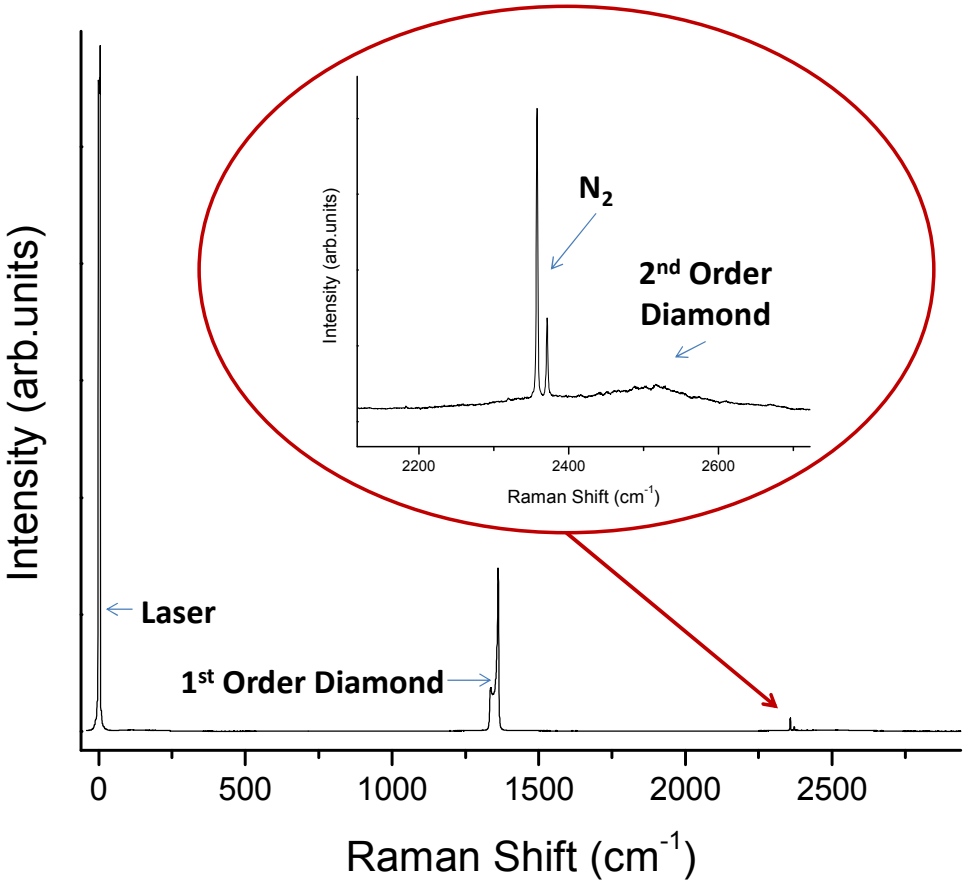

Figure 5.7: Raman spectrum of *NAr9xx* (x = 0.75) at 11.93 GPa showing Rayleigh intensities from the laser, and Raman signals from diamond and N_2.

Raman spectra for the vibrational modes of samples with higher N_2 concentrations displayed the noticeable phase changes associated to that of pure N_2. A single vibron line was observed for β-N_2 and two vibron lines were recorded for the δ phase of N_2. Figure 5.8 shows the vibrational spectra at various pressures for two different samples; *NAr3xx* with x = 0.80 and *NAr9xx* with x = 0.75.

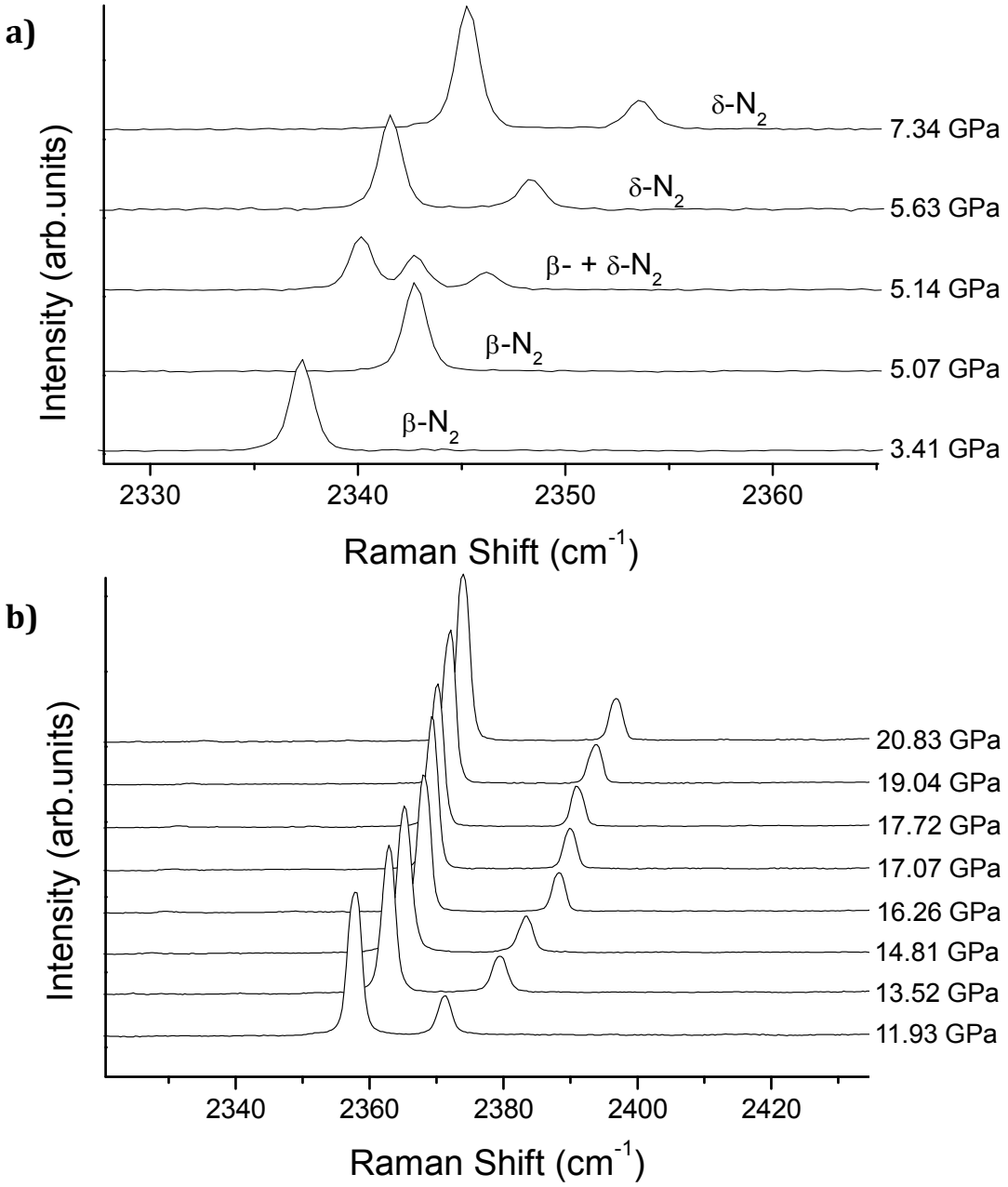

Figure 5.8: Raman spectra for the molecular stretching modes of N_2 in **(a)** *NAr3xx* (x = 0.80) and **(b)** *NAr9xx* (x = 0.75) at various pressures.

The frequencies are observed to increase with pressure and in Figure 5.8, a), a double phase is observed with β- and δ-N_2 at 5.14 GPa. Phase transition pressures were found to shift to higher pressures than that of the pure systems. These results are in agreement with findings by Lotz *et al*.[2] The ratio of the integrated intensities of the vibron lines, υ_1 and υ_2, is around $^1/_4 - {}^1/_5$, and did not change when the position of the laser spot over the sample was varied. This is an indication of the sample uniformity in composition. In pure N_2 this ratio is about $^1/_3$. This indicates that the mixing of argon into nitrogen changes the Raman scattering probability.

In the pure system, N_2 undergoes a phase transition from δ- to ε-N_2 at 16.3 GPa.[6] This transition can be observed by a splitting of the υ_2 vibron line as well as a change in the slope of the Raman linewidth as a function of pressure. It was difficult to observe a splitting of the vibron line due to line broadening, however, Figure 5.9 gives the FWHM as a function of pressure for *NAr9xx* with x = 0.75 and *NAr3xx* with x = 0.80. A jump in the slope is observed around 16.5 GPa for *NAr9xx*, signifying the δ-ε transition. In addition and similar to pure N_2, the phase change was visually observed as the sample became textured. Figure 5.10 shows images of *NAr9xx* (x = 0.75) in the δ and ε phases. A change in slope is also observed ~17.5 GPa for the compression and 16 GPa for the decompression *NAr3xx*.

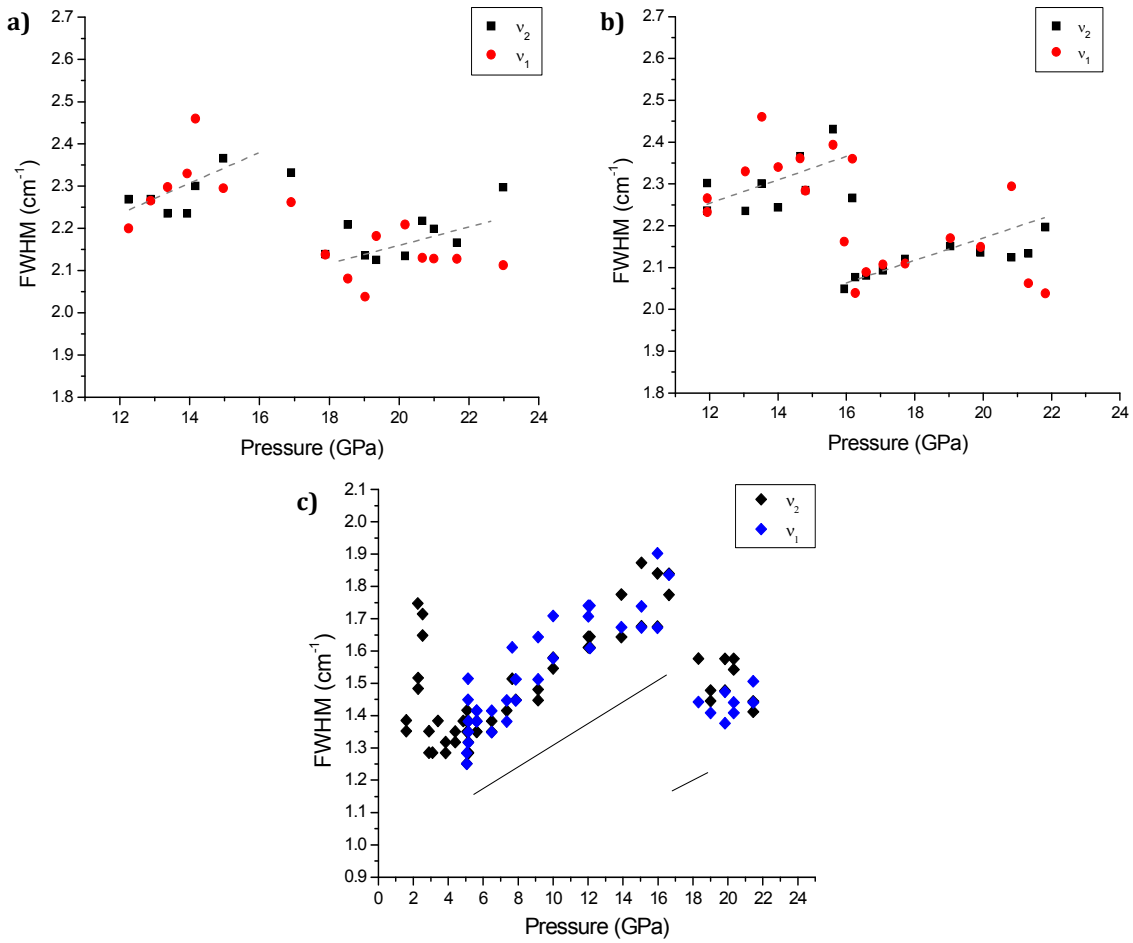

Figure 5.9: FWHM of the molecular stretching modes of N_2 for the **(a)** compression and **(b)** decompression of *NAr9xx* (x = 0.75) and **(c)** *NAr3xx* (x = 0.80). The dashed lines in (a) and (b) are an aid to the eye to show the drop in FWHM around 16 GPa, corresponding to the δ-ε phase transition of N_2. The solid lines in (c) represent data points of pure N_2 from this work.

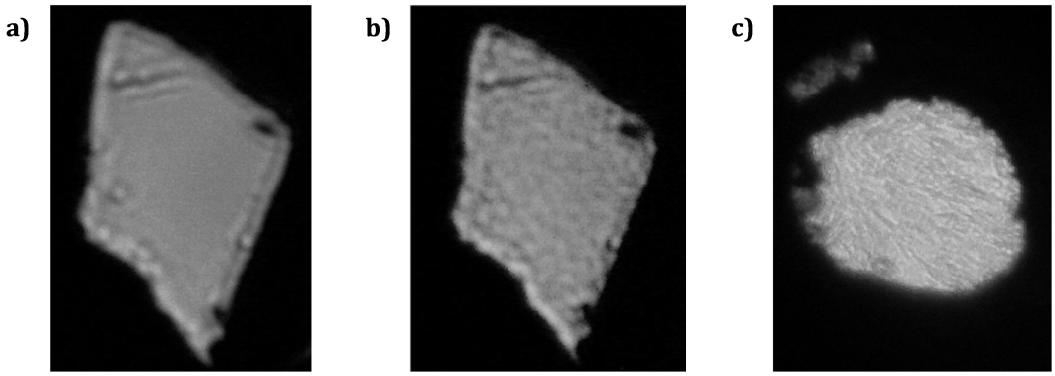

Figure 5.10: Images of samples of *NAr9xx* (x = 0.75) at **(a)** 14.36 GPa and **(b)** 22.82 GPa, and **(c)** *NAr3xx* (x = 0.80) at 18.31 GPa. Once in the ε phase (above ~16 GPa), the sample is visually observed to be "textured". Note that the sample is losing its circular shape, especially in (a) and (b). This is due to gasket failure.

As seen in Figure 5.9, a lower concentration of N_2 shifts the δ-ε transition to a slightly higher pressure. The Raman linewidths plotted in Figure 5.9 a) and b) are broader than that of pure N_2 by about 1 cm^{-1} and in c), the linewidths are approximately 0.2 cm^{-1} larger. Lower concentrations of N_2 result in larger linewidths. In addition to the observations of a δ-ε transition from the molecular stretching modes, the Raman spectra of the lattice modes (Figure 5.11) also show the addition of new features above 16 GPa. These possible new modes appear at similar frequencies to those observed by Schneider *et al.*[1], and belong to the ε phase of N_2.

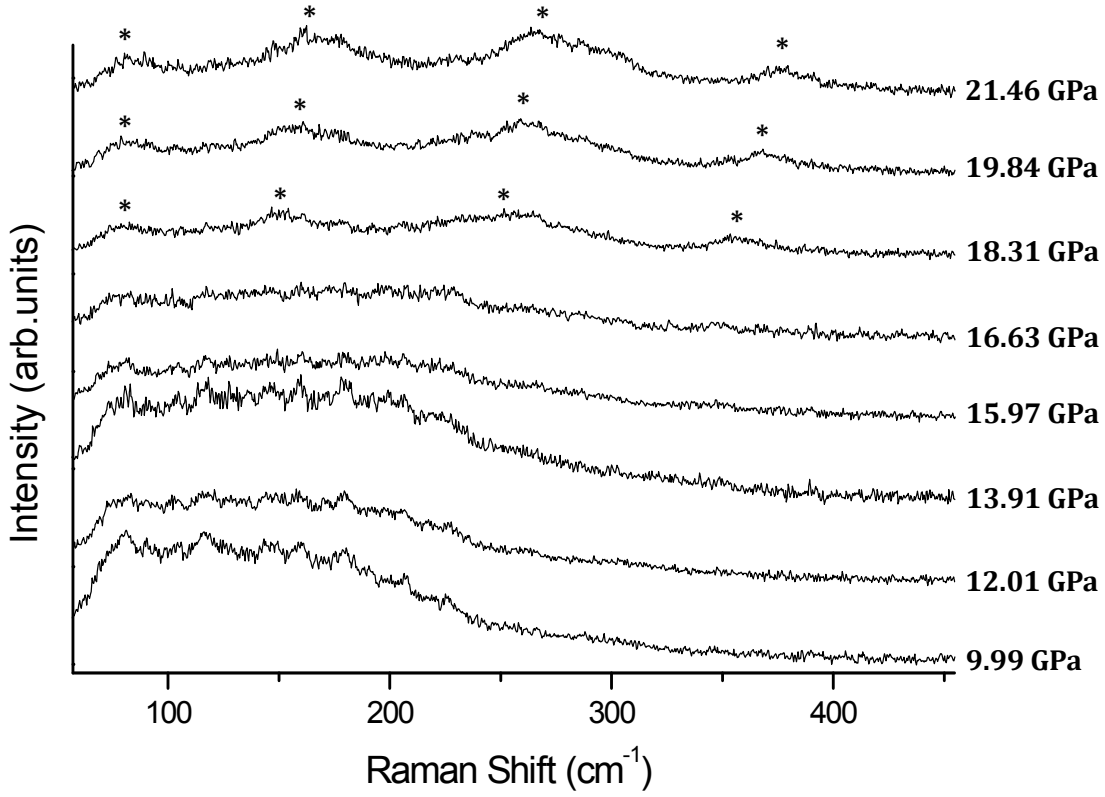

Figure 5.11: Raman spectra of the low energy lattice modes for *NAr3xx* at x=0.80. The asterisk (*) points to wavenumbers of new lattice modes.

The vibrational frequencies of samples containing high concentrations of N_2 are plotted as a function of pressure with pure N_2 (dashed lines) and results obtained by Lotz *et al.*[2] (hollow

symbols) in Figure 5.12. The dependence with pressure of the vibrational frequencies is different for different compositions. As an example, the change in vibrational frequency indicating the β-δ transition for *NAr9xx* (x = 0.75) was found to occur at 6.08 GPa and the frequencies were shifted lower with respect to pure N_2. Around 12 GPa and again at about 16 GPa the frequencies have a slight change in slope. For *NAr3xx* (x = 0.80), the β-δ transition occurs at 5.14 GPa, closer to the pure system at 4.9 GPa, and is shifted to lower frequencies (when compared to pure N_2) to the highest pressure investigated. All of the vibrational frequencies obtained for the various concentrations in this work are summarized as a function of pressure in the plot presented in Figure 5.13. The next section will present the x-ray diffraction (XRD) results and analysis for the samples *NAr1xx, 4xx, 5xx, 6xx, 7xx* and *9xx*. Mixtures not discussed in the following section were only investigated with Raman spectroscopy.

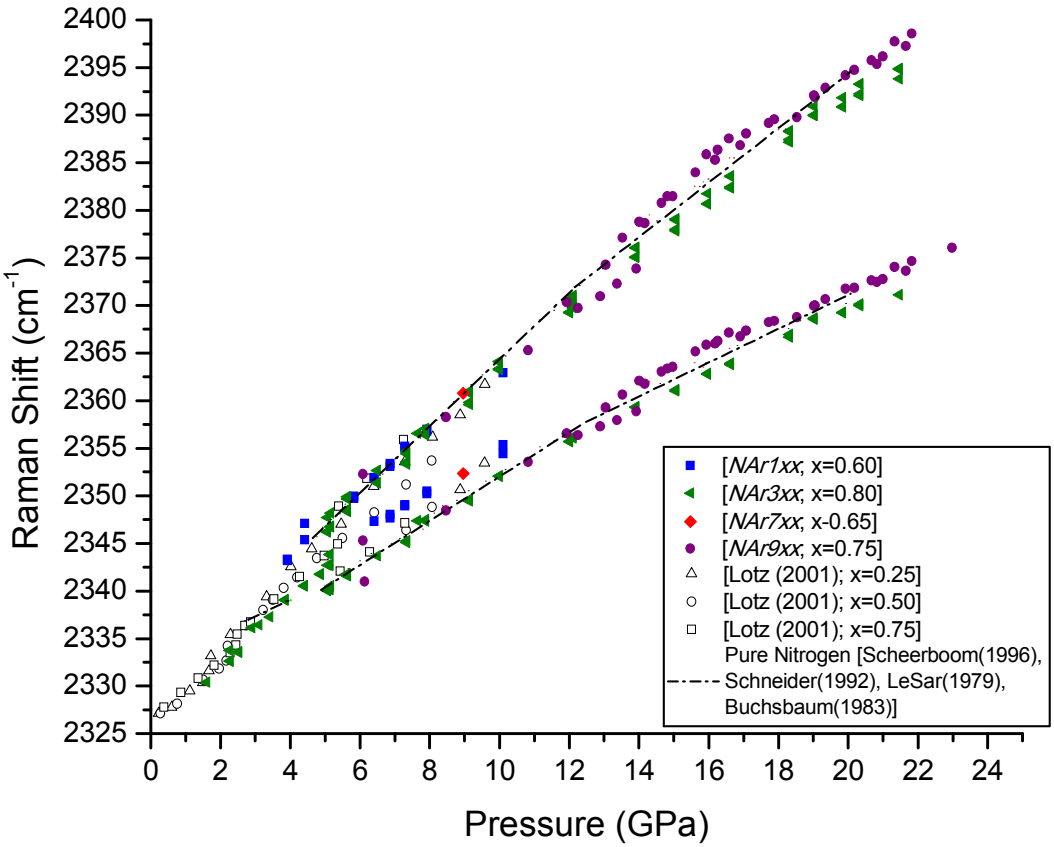

Figure 5.12: Raman shift as a function of pressure for samples with higher concentrations of nitrogen compared to pure nitrogen[1,3,4,5] (dashed lines) and results obtained for the N_2-Ar system by Lotz *et al.*[2] (hollow symbols).

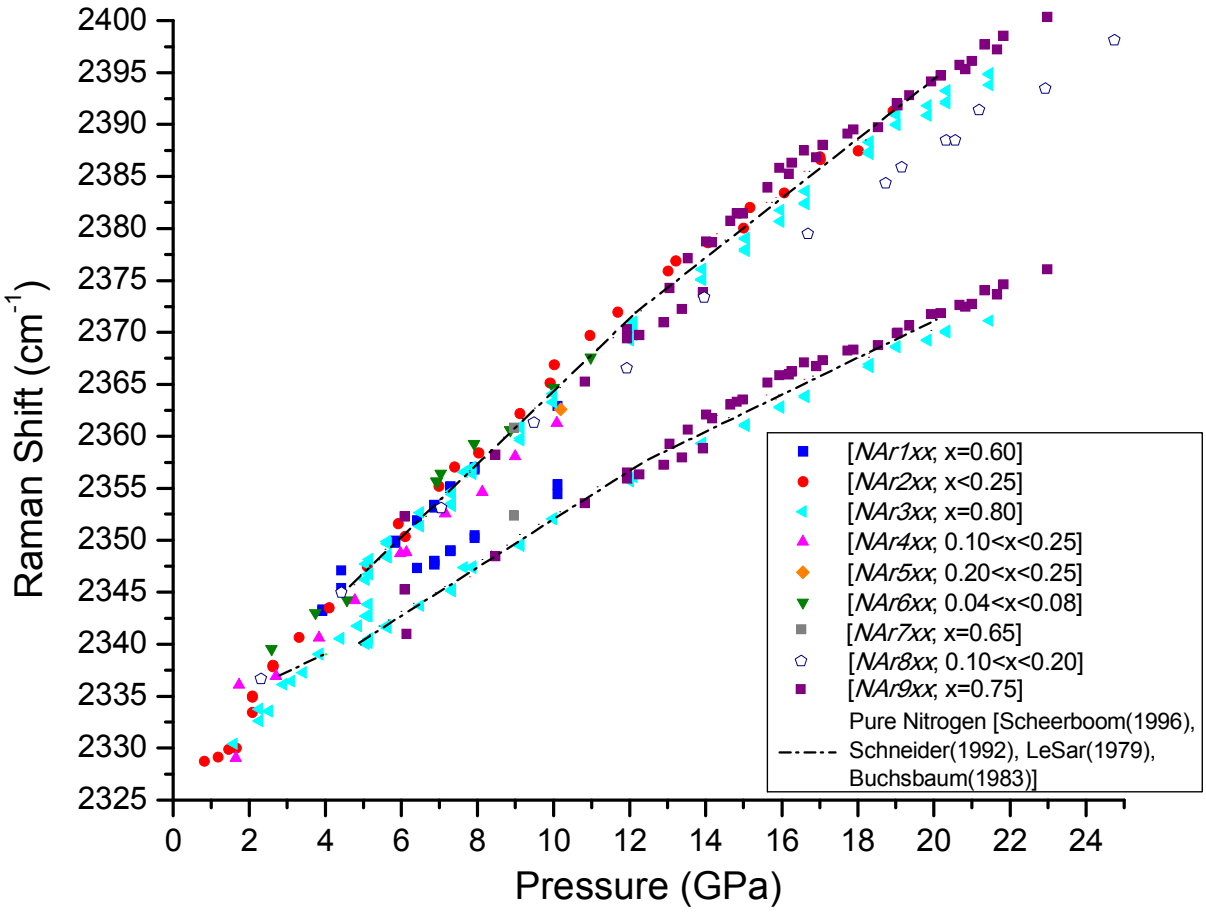

Figure 5.13: Raman shift results for all samples compared to pure nitrogen[1,3,4,5] (dashed lines).

5.3 X-ray Diffraction Results

5.3.1 Low N_2 Concentrations

To give an example of how an XRD image is analyzed, the steps are shown in Figure 5.14. This figure gives the diffraction image containing the Debye rings obtained for a sample with a low concentration of nitrogen ($0.15<x<0.25$) in part a) of Figure 5.14. In part b) the intensities are then integrated to give diffraction peaks. As seen in Figure 5.14 a), the Debye rings are not perfectly uniform; some contain regions of larger intensities. This is most likely due to larger crystals and/or preferred orientation in the powder. The face-centered cubic (FCC), (111) orientation in Figure 5.14 had the highest diffraction peak intensity due to the structure factor (discussed in Chapter 3, Section 5). Its corresponding Debye ring had regions where the image was oversaturated and this was due to an overexposure of the image. Any diffuse scattering between the rings may be due to stacking faults in the FCC lattice or stress on the system. Conversion of the diffraction peak positions on the image to d-spacings allows identification of the structure because each structure has a set of unique d-spacings. Typically, this is achieved by comparison of d-spacings with standard reference patterns when available; otherwise a systematic unit cell search is required using programmed algorithms. The pattern indexed in Figure 5.14 is that of an FCC unit cell with a lattice parameter of a = 4.560 ± 0.006 Å corresponding to a volume of 14.28 cm^3/mol. Keeping the naming scheme introduced by Lotz *et al.*[2], this structure corresponds to the solid called S_{Ar^*}, which has an FCC-Ar lattice containing dissolved N_2 molecules at some lattice points by way of substitutional dissolution. The additional diffraction line marked with an asterisk (*) in Figure 5.14 b) belongs to an HCP structure and is discussed in more detail later in the chapter.

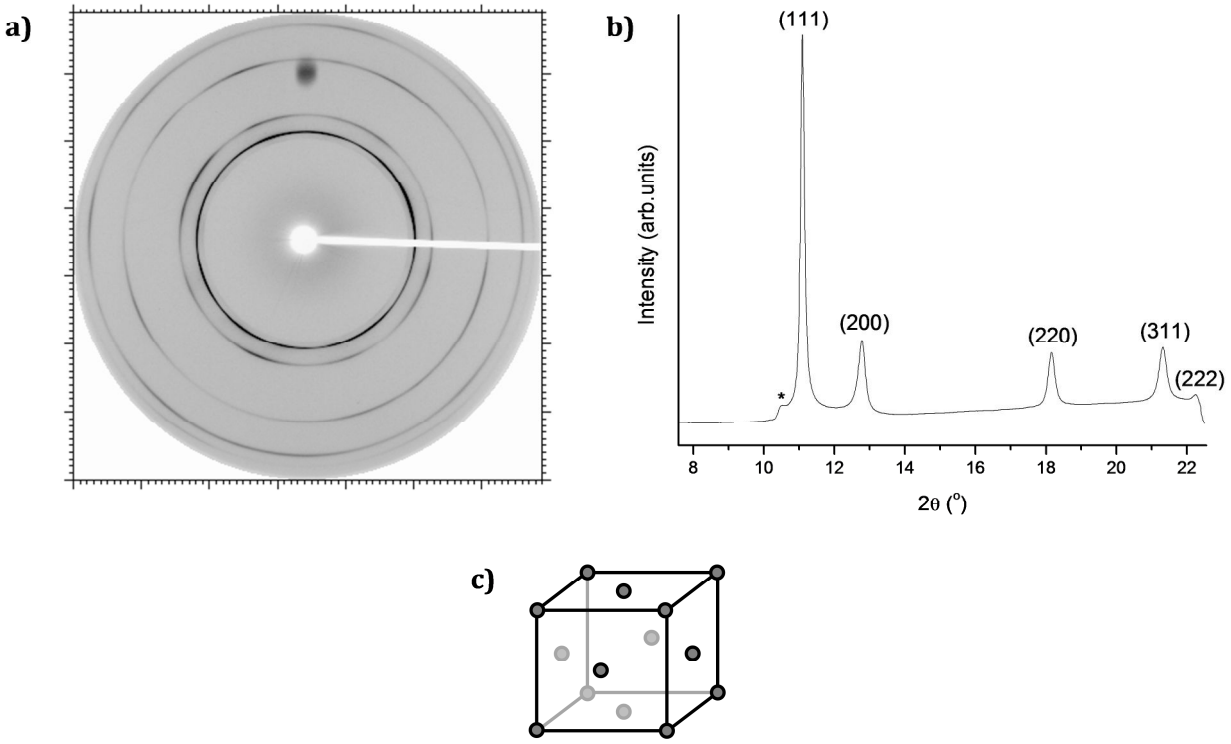

Figure 5.14: (a) XRD image of *NAr6xx* at 7.91 GPa. The spot in the top region is due to stray radiation through an opening that had not been shielded on the DAC holder. **(b)** The corresponding X-ray diffraction pattern with intense peaks indexed as those of an FCC structure. The additional diffraction line marked with an asterisk (*) belongs to an HCP structure. **(c)** The FCC structure assigned to the pattern has a lattice parameter of a = (4.560 ± 0.006) Å.

To make sure the X-ray diffraction peaks that are observed are in fact from the sample and not from an external component of the apparatus, the d-spacings are plotted as a function of pressure. If the values shift with pressure, as would be expected for the compression of the sample, then it is a confirmed structure. Figure 5.15 shows the d-spacings as a function of pressure for the FCC structure identified in *NAr4xx*. They reduce with pressure (due to the density increase), signifying that it is indeed the XRD arising from the sample. The program used to calculate d-spacings and lattice parameters, XRDA, provides only statistical uncertainties for these variables. Systematical errors were calculated and each d-spacing was found to have an uncertainty of 0.001 Å. These uncertainties are incorporated into the size of the data point when plotted in this work.

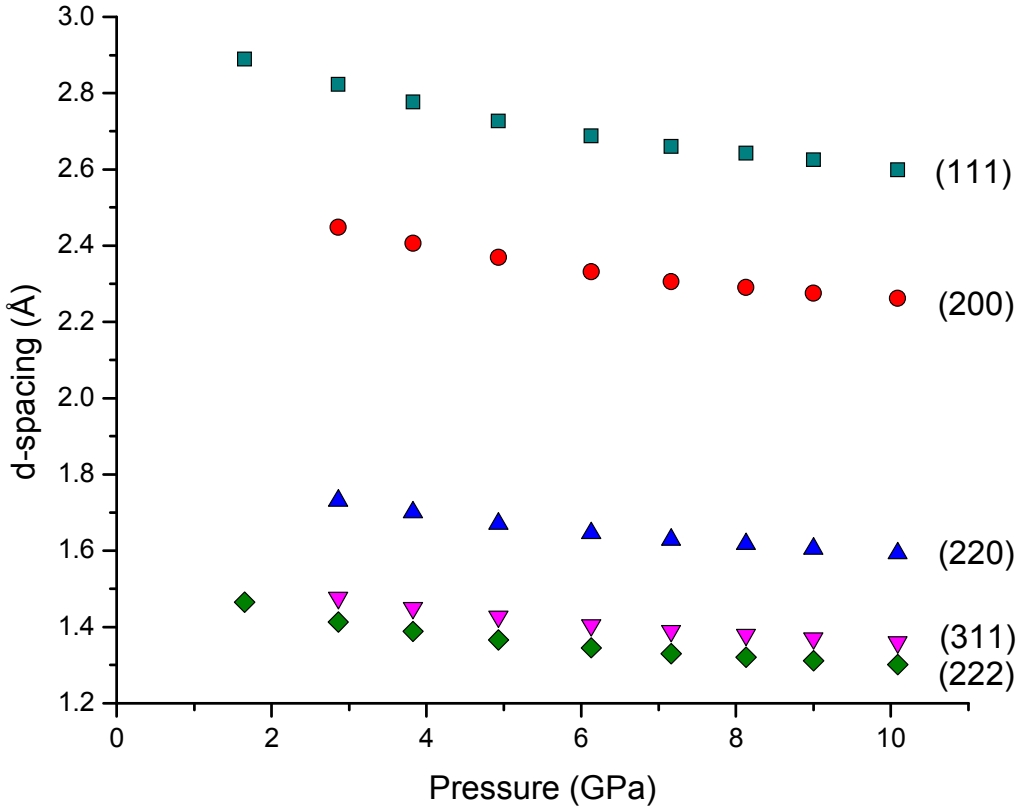

Figure 5.15: The d-spacing of an FCC structure indexed for the sample *NAr4xx* (0.15<x<0.25) as a function of pressure.

The sample *NAr6xx* (0.04<x<0.08) was decompressed to the fluid-solid phase then re-compressed to a solid. The XRD patterns are shown in Figure 5.16 for various pressures. At 5.85 GPa the intense peaks of an FCC structure at 5.85 GPa is observed to disappear at 1.57 GPa as the sample was brought to liquid. Upon compression, the solid once again reforms to the FCC structure. This is shown in the bottom spectrum at 2.58 GPa. The fluid-solid transition for pure Ar and N_2 should occur at 1.35 GPa and 2.4 GPa, respectively. The XRD patterns for all samples containing x < 0.25 were similar to Figure 5.17, where d-spacings are dependent on concentration.

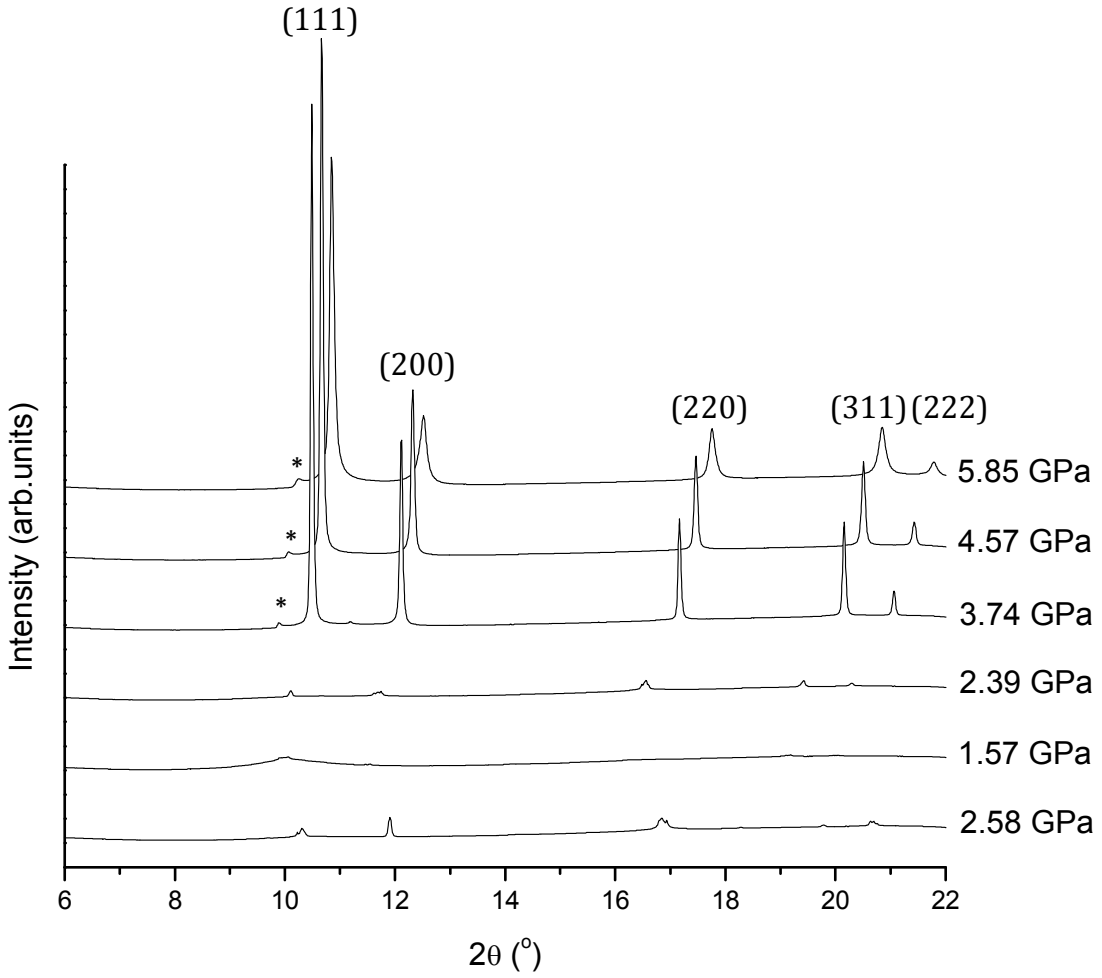

Figure 5.16: XRD patterns of *NAr6xx* (0.04<x<0.08) at various pressures down to the fluid-solid phase with λ = 0.509176 Å.

One sample with lower N_2 concentration that had particularly interesting XRD images was *NAr4xx* (0.15<x<0.25). Figure 5.17 shows a few of the XRD images obtained at different pressures from that sample. Initially, the XRD image displayed extremely non-uniform Debye rings (Figure 5.17 a)). Spots and scattering indicate larger crystals and strain within the sample. Decompression to 3.72 GPa resulted in Figure 5.17 b).

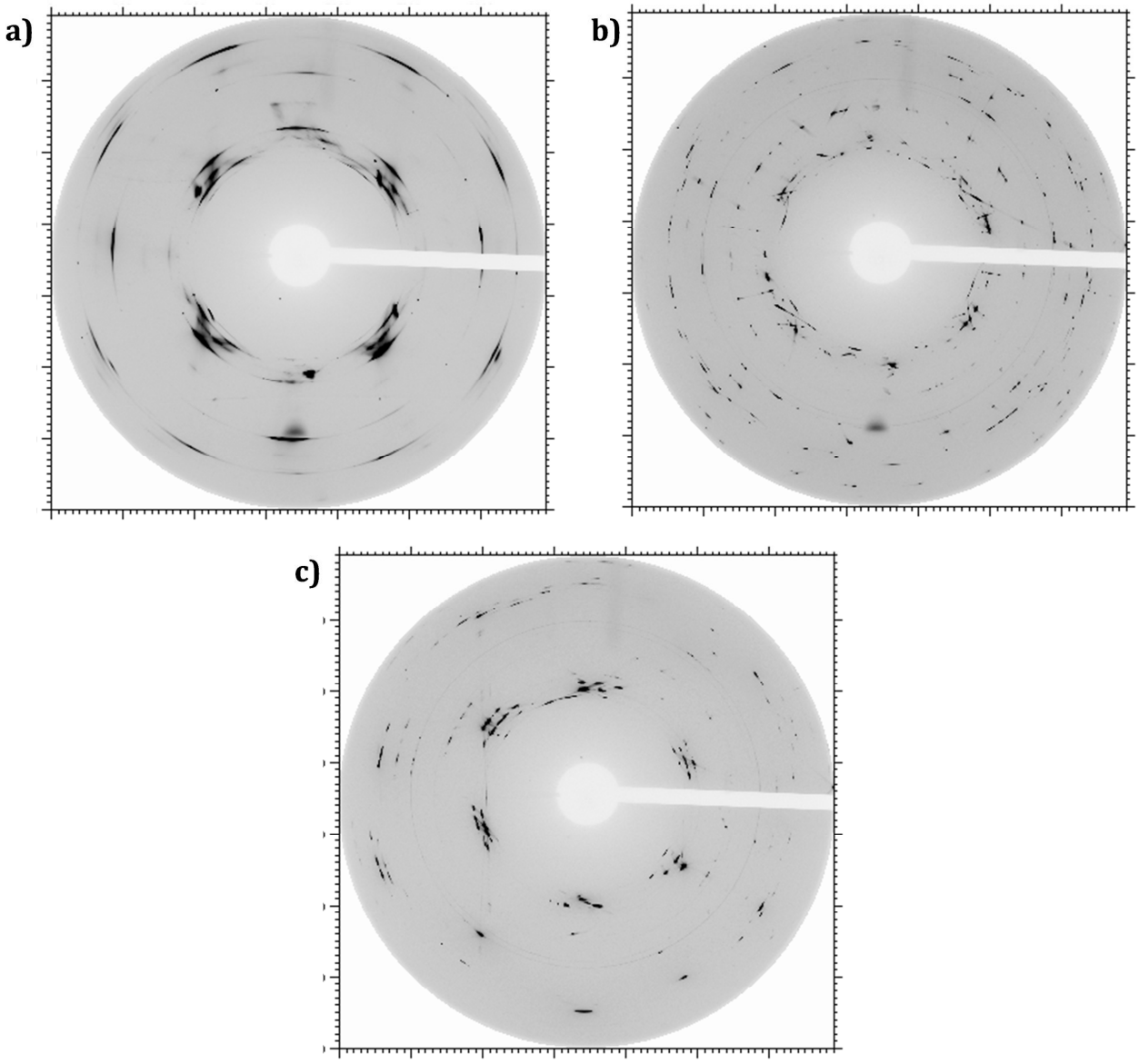

Figure 5.17: XRD images of *NAr4xx* at **(a)** 4.82 GPa, **(b)** 3.72 GPa and **(c)** 2.70 GPa. When the sample was initially decompressed, the image became increasingly distorted with many spots and "streaks". After compression from liquid the images all resembled c).

The image became very spotted and the diffuse scattering between the spots and rings was more pronounced. The sample was brought to the liquid state and compressed to 2.70 GPa (Figure 5.17 c)). A good powdered sample was not obtained by doing this as non-uniform Debye rings were still

observed, however, the amount of spots and scattering had reduced. Figure 5.18 provides a closer look at some of the spots and the scattering from Figure 5.17 b).

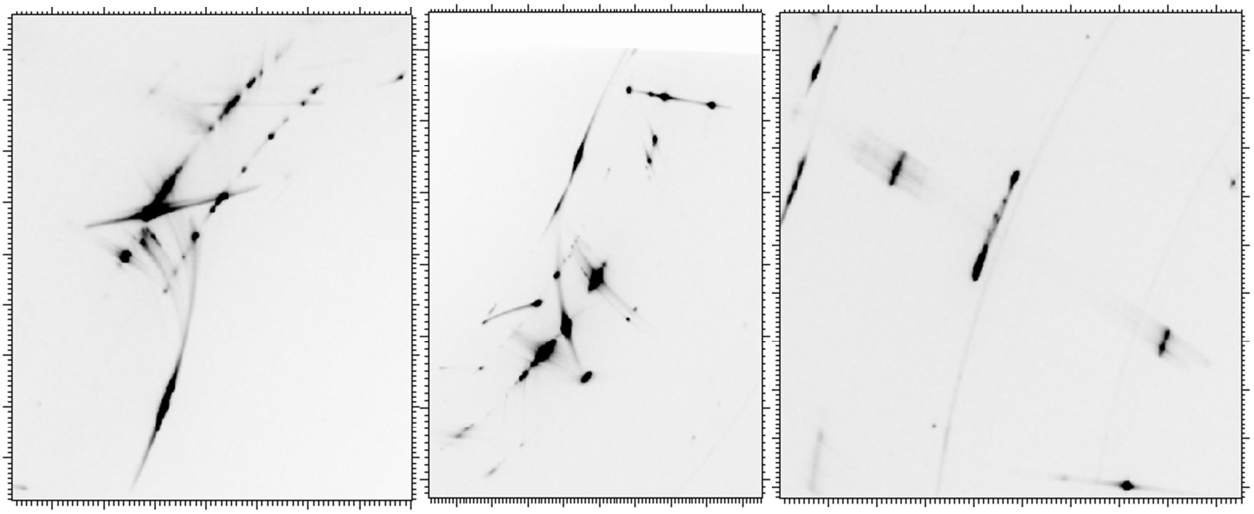

Figure 5.18: A closer look at the XRD image of *NAr4xx* (0.15<x<0.25) at 3.72 GPa.

The XRD images for *NAr4xx* may not have had perfect Debye rings; however the diffraction patterns could still be indexed as corresponding to FCC and HCP structures. At 3.72 GPa (Figure 5.17, b)), the FCC structure had a lattice parameter of a = (4.872 ± 0.006) Å and volume of 17.42 cm^3/mol and an HCP structure with lattice parameters a = (3.448 ± 0.006) Å and c = (5.624 ± 0.006) Å and volume of 17.44 cm^3/mol. The percent difference between the calculated and observed d-spacings for both structures was 0.085 % or less. *NAr4xx* was the only sample with x < 0.25 where the HCP structure observed in the XRD pattern contained more than three diffraction peaks and appeared more prominently and was indexed with better accuracy than the FCC structure. Table 5.2 summarizes the d-spacings observed and calculated (using the d_{hkl} formula for cubic and hexagonal unit cell found in Table 3.2) for *NAr4xx* at 3.72 GPa. The percent differences for all planes (*hkl*) are less than 0.12%.

Table 5.2: The d-spacings for the FCC and HCP structures indexed for *NAr4xx* at 3.72 GPa; λ = 0.509176 Å.

Structure		**Lattice Parameter (Å)**		**Volume (cm³/mol)**	
FCC		a = 4.872 ± 0.006		17.42	
(*hkl*)	**$d_{calculated}$ (Å)**	**$2\theta_{observed}$ (°)**	**$d_{observed}$ (Å)**	**$\lvert d_{calc} - d_{obs} \rvert$ (Å)**	**Difference (%)**
(111)	2.813	10.393	2.811	0.002	0.07
(200)	2.436	12.000	2.435	0.001	0.04
(220)	1.722	16.985	1.724	0.002	0.12
(311)	1.469	19.941	1.470	0.001	0.07
(222)	1.406	20.860	1.406	0	0
Structure		**Lattice Parameters (Å)**		**Volume (cm³/mol)**	
HCP		a = 3.4481 ± 0.006	c = 5.6260 ± 0.006	17.44	
(*hkl*)	**$d_{calculated}$ (Å)**	**$2\theta_{observed}$ (°)**	**$d_{observed}$ (Å)**	**$\lvert d_{calc} - d_{obs} \rvert$ (Å)**	**Difference (%)**
(100)	2.986	9.790	2.983	0.003	0.10
(002)	2.813	10.388	2.812	0.001	0.04
(101)	2.637	11.078	2.637	0	0
(102)	2.047	14.280	2.048	0.001	0.05
(110)	1.724	16.984	1.724	0	0
(103)	1.588	18.450	1.588	0	0
(200)	1.493	19.633	1.493	0	0
(112)	1.469	19.942	1.470	0.001	0.07
(201)	1.443	20.317	1.443	0	0
(202)	1.318	22.258	1.319	0.001	0.08

5.3.2 High N_2 Concentrations

Higher concentrations of N_2 resulted in XRD patterns containing intense peaks corresponding to HCP, cubic and rhombohedral structures, associated with the β, δ and ε phases of N_2. Figure 5.19 shows the XRD patterns of *NAr7xx* (x = 0.65) for the compression and decompression of the sample.

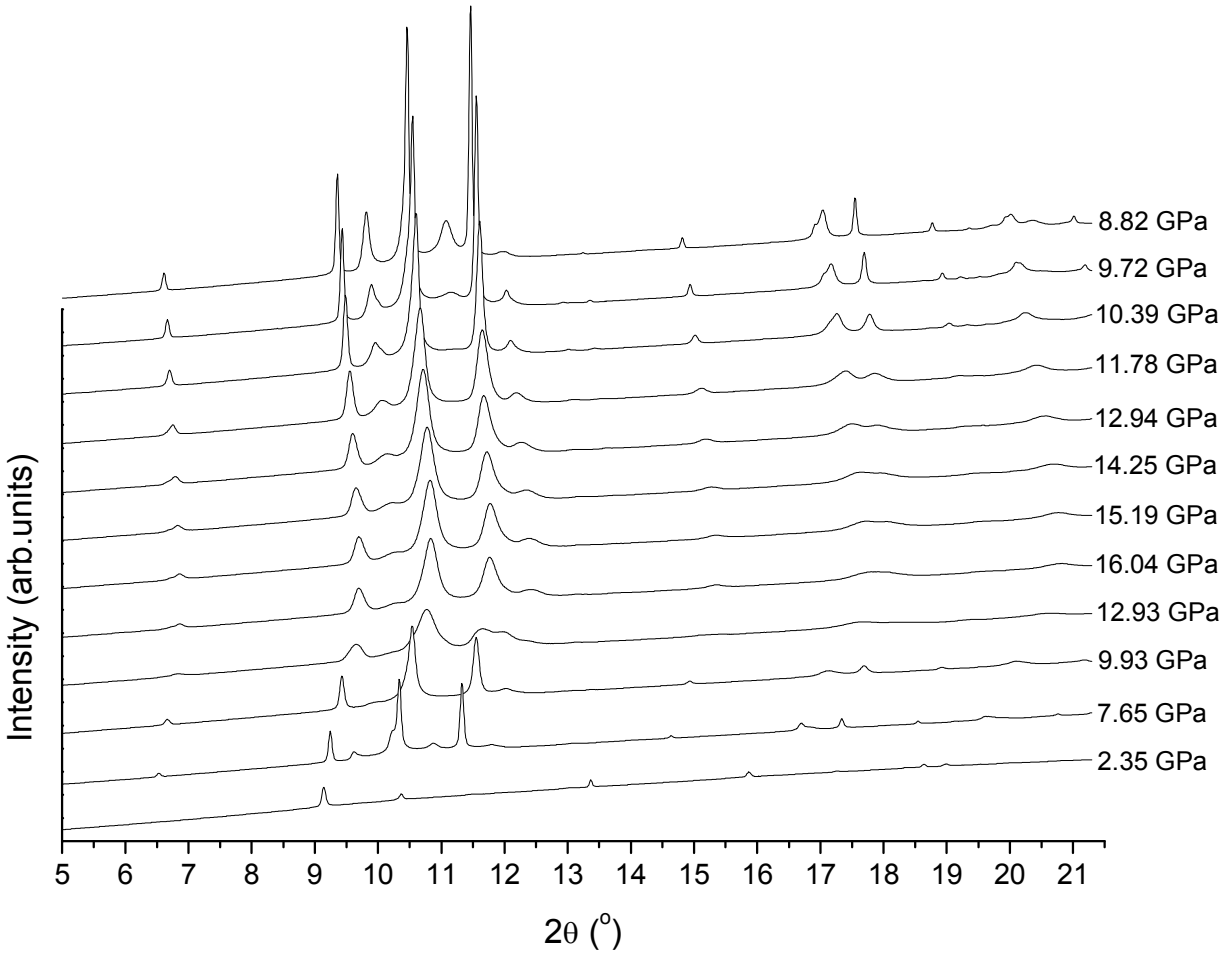

Figure 5.19: XRD patterns of *NAr7xx* with x = 0.65 recorded at various pressures at the CLS@APS with λ = 0.47684 Å.

At 8.82 GPa, the XRD pattern was indexed for a cubic structure with lattice parameter a = (5.848 ± 0.006) Å and volume 15.06 cm^3/mol, as well as for an HCP structure with lattice parameters a = (3.219 ± 0.006) Å and c = (5.331 ± 0.006) Å and a volume of 14.41 cm^3/mol. To support this result, Table 5.3 summarizes the d-spacings observed and calculated (using the d_{hkl}

formula for cubic unit cell found in Table 3.2) for *NAr7xx* at 8.82 GPa. The percent differences for all planes (*hkl*) are less than 0.06%.

Table 5.3: The d-spacings for the cubic structure (δ*) indexed for *NAr7xx* at 8.82 GPa; a = 5.848 Å, V = 15.06 cm^3/mol, λ =0.47684 Å.

(*hkl*)	$d_{calculated}$ (Å)	$2\theta_{observed}$ (°)	$d_{observed}$ (Å)	$\lvert d_{calc} - d_{obs} \rvert$ (Å)	Difference (%)
(110)	4.135	6.610	4.135	0	0
(200)	2.924	9.354	2.924	0	0
(210)	2.615	10.458	2.616	0.001	0.04
(211)	2.387	11.462	2.387	0	0
(220)	2.067	13.243	2.067	0	0
(310)	1.849	14.814	1.849	0	0
(320)	1.622	16.911	1.621	0.001	0.06
(321)	1.563	17.548	1.563	0	0
(400)	1.462	18.770	1.462	0	0
(410)	1.418	19.354	1.418	0	0
(330)	1.378	19.924	1.378	0	0
(420)	1.307	21.010	1.307	0	0

Again, to maintain the naming scheme for these structures introduced by Lotz *et al.*[2], the phase with the cubic structure will be called δ* (δ-N_2) and the phase with the HCP structure will be called β* (β-N_2), where the asterisk indicates a mixed solid with Ar substitutionally replacing N_2 within the lattice. The red lines in Figure 5.20 designate the cubic structure at 8.82 GPa. As pressure is

increased to 16.04 GPa, the narrow and intense peaks of δ* shift with pressure and transform into broader, less intense peaks. Larger linewidths are a sign of stress within the system. The diffraction peaks associated with β* reduce and disappear at 16.04 GPa. The peaks at 16.04 GPa were indexed for a cubic structure, however there was uncertainty with some of the peaks. ε-N_2 is expected at 16.3 GPa for the pure system, therefore an attempt was made to index for the ε phase of N_2 using the method described by Olijnyk *et al.*[6], where the diffraction peaks are indexed to a hexagonal unit cell (24 molecules per unit cell). Note that following this indexing method, with regard to systematic extinctions and energy minimizing procedures, the rhombohedral unit cell (*R*3*c*) was found to best describe the ε phase of N_2 (see Chapter 2, Section 3). In this work, there was also a large uncertainty after using this method (on *NAr7xx*) due to the broadened peaks.

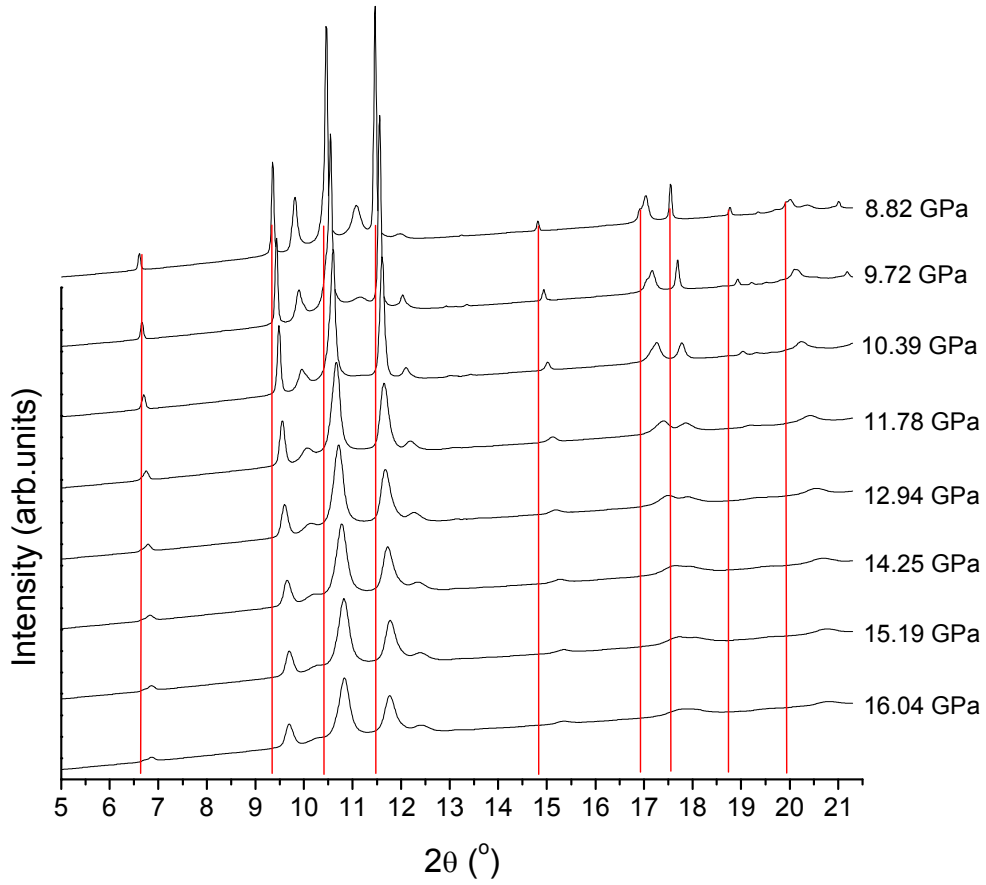

Figure 5.20: XRD patterns of *NAr7xx*. Red lines mark Bragg angles that correspond to a cubic structure at 8.82 GPa with lattice parameter a = 5.848 Å. The additional peaks observed in these patterns belong to a HCP structure.

Figure 5.21 gives a comparison between the XRD patterns of 8.28 GPa and 16.04 GPa. Less intense peaks and/or shoulders of the diffraction patterns designated by (°) appear to belong to FCC-Ar. The two patterns show major dissimilarities, which may be due to strain within the system and a possible phase transition. Figure 5.22 shows the d-spacing for the cubic structure as a function of pressure, which are found to decrease slightly with pressure.

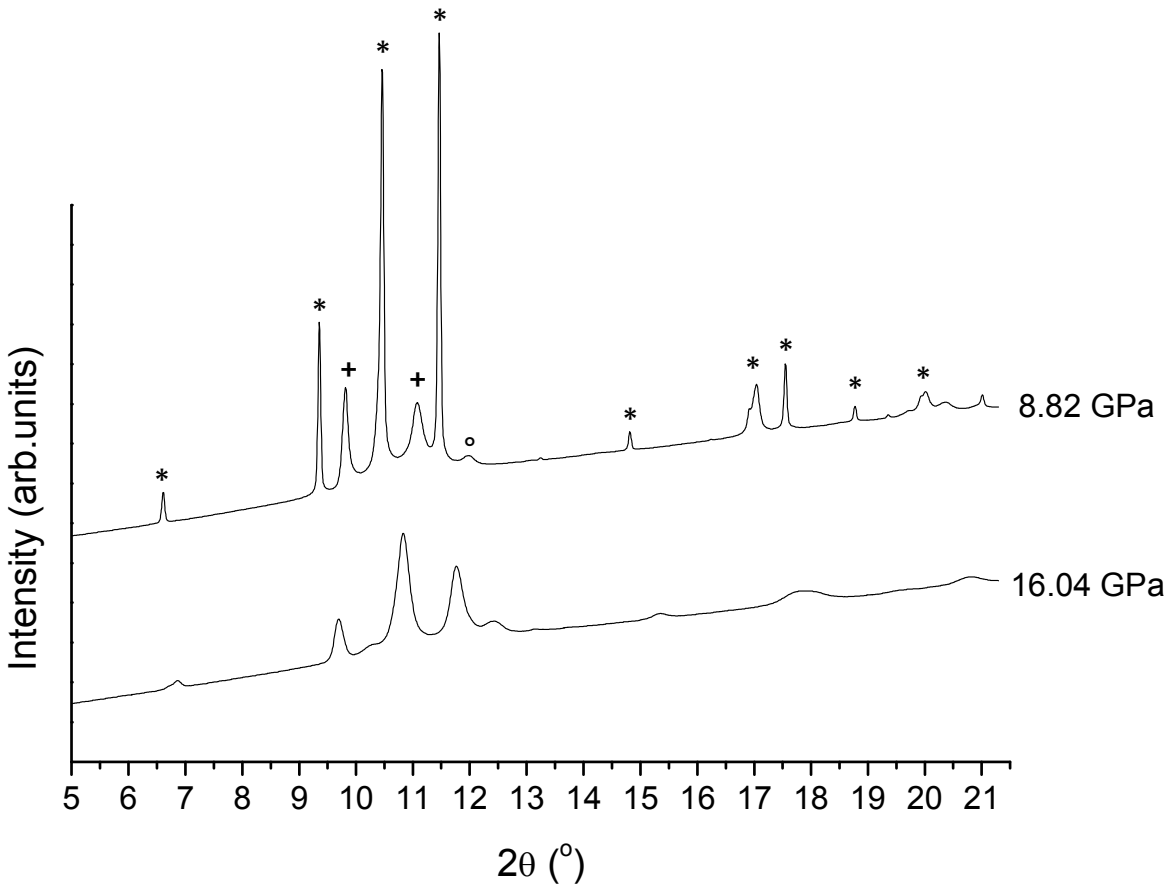

Figure 5.21: XRD patterns of *NAr7xx* at 8.82 GPa with cubic (*), HCP (+), and possibly FCC (°) structures, and 16.04 GPa showing a phase transformation and broadening.

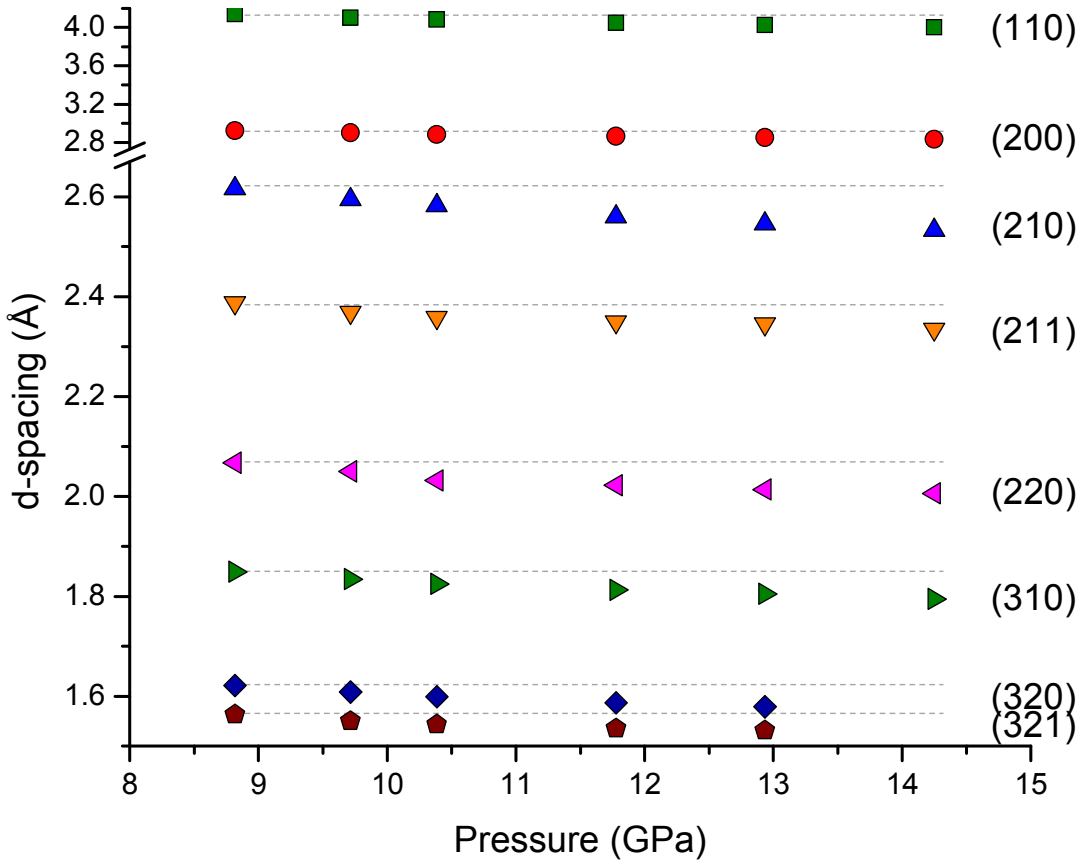

Figure 5.22: The d-spacings for a cubic structure (δ^*-N_2) indexed from *NAr7xx*. The horizontal dashed lines help to show the slight decrease with pressure, indicating the X-ray diffraction lines observed are those from due to the sample.

Due to time and technical constraints, *NAr9xx* (x = 0.75) was the only other sample investigated in this work with a higher concentration of N_2. The XRD patterns for the compression of the sample to 22.82 GPa are presented in Figure 5.23. At 5.63 GPa, the diffraction peaks were indexed for the cubic structure of δ^*. The red lines show the evolution of these peaks as the pressure increases. The XRD patterns of 17.28 GPa and above show intense, broad peaks (at approximate Bragg angles, 2θ, of 12.4, 14.1 and 21.6) that are due to diffraction from the gasket.

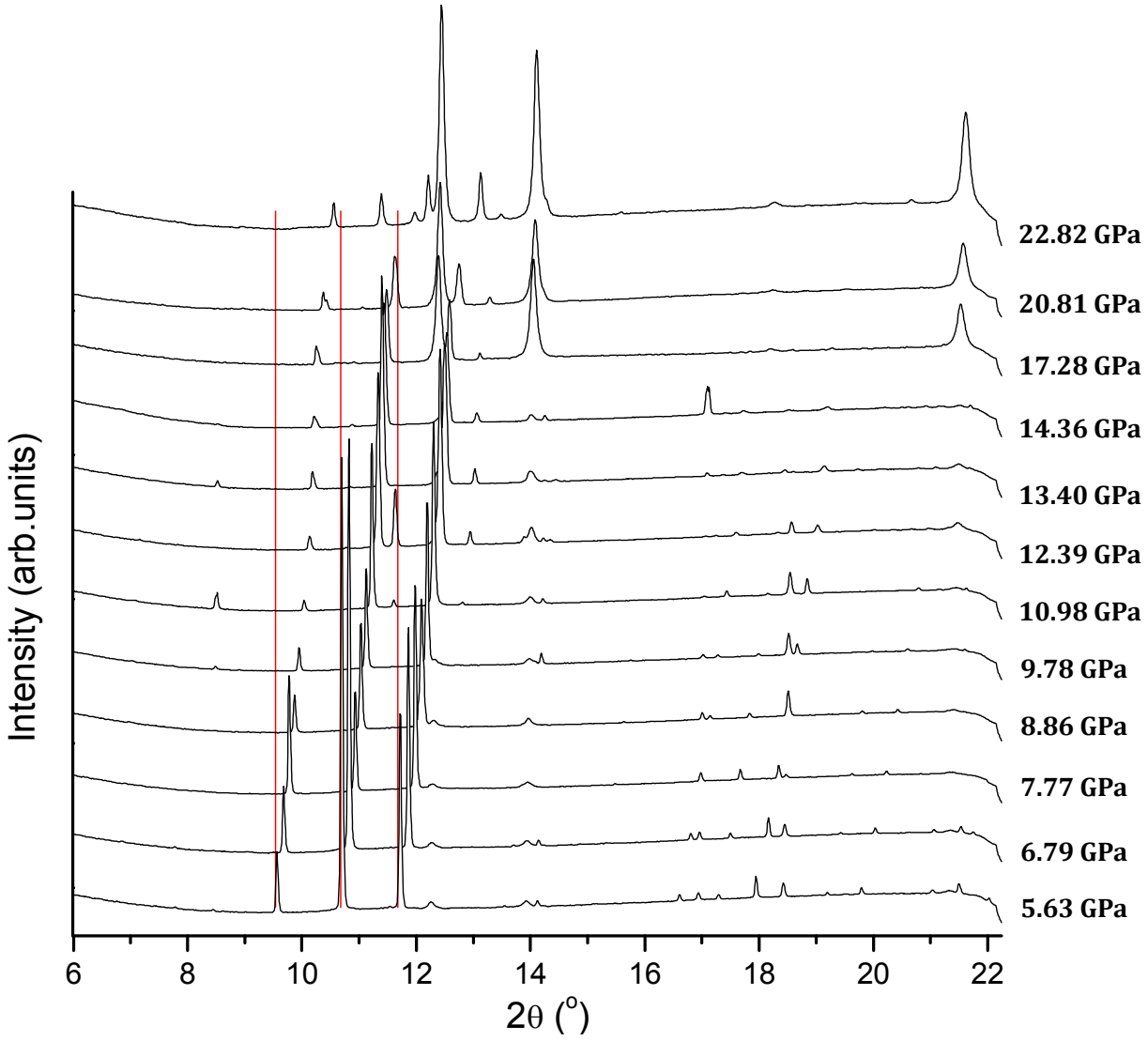

Figure 5.23: XRD patterns of *NAr9xx* at various pressures. The red lines are meant as an aid to the eye to show the phase transformation of the most intense peaks of δ* at 5.63 GPa to ε* at 22.82 GPa. NOTE: Most of the less intense peaks on the lower pressure diffraction patterns correspond to the cubic structure of δ*.

As the pressure was increased, the gasket began to fail and metallic debris started to fill the sample area. The result was intense diffraction peaks arising from the gasket material and less intense peaks from the sample. These patterns were indexed successfully for ε-N_2 using the method (previously discussed) described by Olijnyk *et al.*[6] The lattice parameter for δ* at 5.63 GPa was (6.106 ± 0.006) Å with a volume of 17.14 cm^3/mol. The rhombohedral structure of ε* was indexed

with a unit cell containing 24 molecules with lattice parameters of a = (7.503 ± 0.006) Å and c = (10.531 ± 0.006) Å corresponding to a volume of 12.88 cm^3/mol at 22.82 GPa. No Ar structures were observed in the *NAr9xx* XRD patterns. For the remainder of this work, the rhombohedral structure will be called ε*, where the asterisk represents a mixed solid. Figure 5.24 gives a comparison of the XRD patterns from 5.63 GPa and 22.82 GPa.

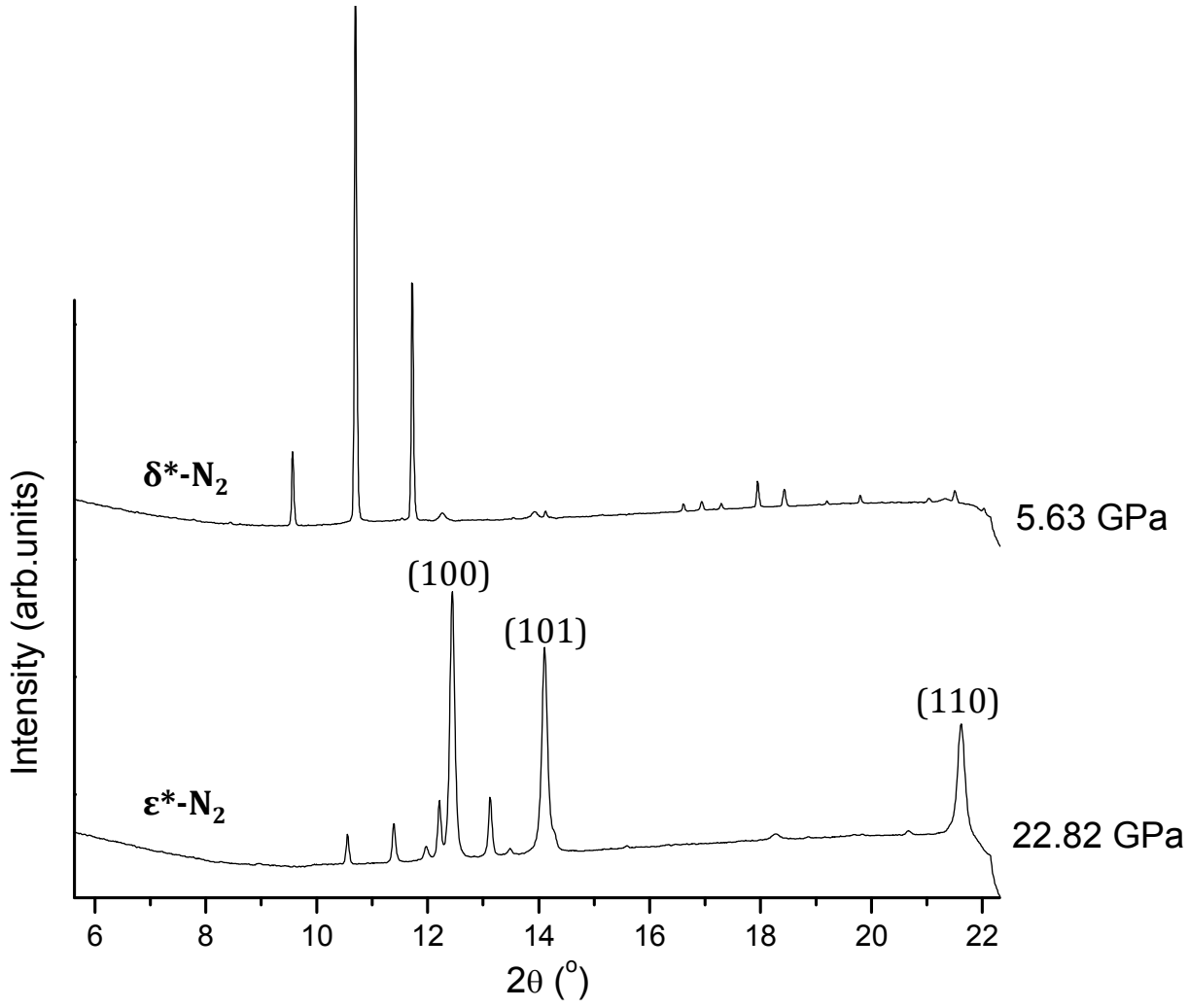

Figure 5.24: XRD patterns for *NAr9xx* at 5.63 GPa and 22.82 GPa. At 5.63 GPa, the pattern shows lines corresponding to the cubic structure of δ*. At 22.82 GPa, we see peaks corresponding to the ε phase of N_2. The (*hkl*) on the pattern of *NAr9xx* at 22.82 GPa indicate the intense peaks corresponding to the gasket (rhenium).

To support the results for the lattice parameters obtained for δ* and ε*, Tables 5.4 and 5.5 provide the observed d-spacings and a comparison to the calculated (using the d_{hkl} formula for cubic and hexagonal unit cell found in Table 3.2) for *NAr9xx* at 5.63 GPa and 22.82 GPa. The percent differences for the cubic and rhombohedral structures are < 0.07 % and < 0.04 %, respectively.

Table 5.4: The d-spacings for the cubic structure (δ*) indexed for *NAr9xx* at 5.63 GPa; a = 6.106 Å, V = 17.14 cm^3/mol, λ =0.509176 Å.

(hkl)	$d_{\text{calculated}}$ (Å)	$2\theta_{\text{observed}}$ (°)	d_{observed} (Å)	$\lvert d_{calc} - d_{obs} \rvert$ (Å)	Difference (%)
(200)	3.053	9.565	3.053	0	0
(210)	2.731	10.697	2.731	0	0
(211)	2.493	11.721	2.493	0	0
(220)	2.159	13.546	2.158	0.001	0.05
(222)	1.762	16.609	1.762	0	0
(320)	1.693	17.291	1.693	0	0
(321)	1.632	17.947	1.632	0	0
(400)	1.526	19.196	1.526	0	0
(410)	1.481	19.794	1.481	0	0
(420)	1.365	21.502	1.364	0.001	0.07
(421)	1.332	22.027	1.332	0	0

Table 5.5: The d-spacings for the rhombohedral structure (ε*) indexed for *NAr9xx* at 22.82 GPa; a = 7.503 Å, c = 10.531 Å, V = 12.88 cm^3/mol, λ =0.509176 Å.

(*hkl*)	$d_{\text{calculated}}$ **(Å)**	$2\theta_{\text{observed}}$ **(°)**	d_{observed} **(Å)**	$\lvert d_{calc} - d_{obs} \rvert$ **(Å)**	**Difference (%)**
(202)	2.765	10.563	2.765	0	0
(113)	2.563	11.399	2.563	0	0
(104)	2.440	11.979	2.439	0.001	0.04
(211)	2.391	12.222	2.391	0	0
(212)	2.225	13.138	2.225	0	0
(300)	2.166	13.499	2.166	0	0

5.3.3 Comparisons to the Equation of State

This section will provide a comparison of volumes recorded as a function of pressure of the structures indexed for all samples of the N_2-Ar binary system investigated in this work to that of the known pure systems. Equations of state (EOS) will be created to estimate the concentration of N_2 and Ar within each structure based on the change in volume.

XRD patterns of samples *NAr4xx, 5xx, 6xx, 7xx*, and *8xx* all contained lines associated with an FCC structure. The volumes of these solids are plotted (in cm^3/mol) as a function of pressure and compared to the EOS of pure N_2 and FCC-Ar in Figure 5.25.

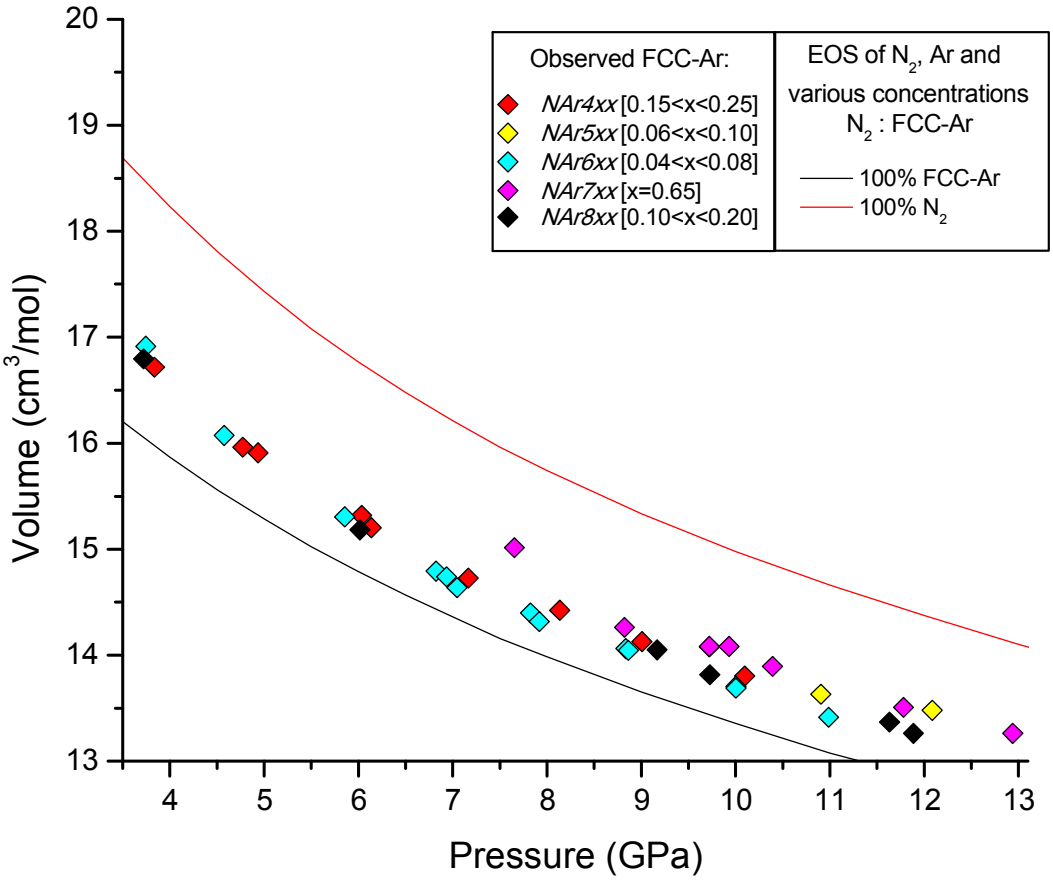

Figure 5.25: Volumes of the indexed FCC structures plotted with the volumes for pure N_2 and FCC-Ar.[6,7,8,9,10,11]

The experimental volumes of solids formed under pressure fall in between those of the pure systems. This is understandable as the N_2 molecule and Ar atom (in gas phase), though similar, are not the exact same sizes with Ar having a van der Waals (vdW) radius of ~1.9 Å and N_2 being slightly larger a vdW radius of ~1.95 Å.[12,13] If N_2 molecules are substitutionally replacing Ar within the FCC lattice, a larger volume than that of the pure FCC-Ar unit cell would be expected. In an attempt to estimate the amount of N_2 with the FCC lattice, the EOS of pure FCC-Ar and N_2 were combined to create new EOS for various concentrations. Figure 5.26 displays these EOS of the solids formed along with the EOS for the pure components and the experimental results of this work.

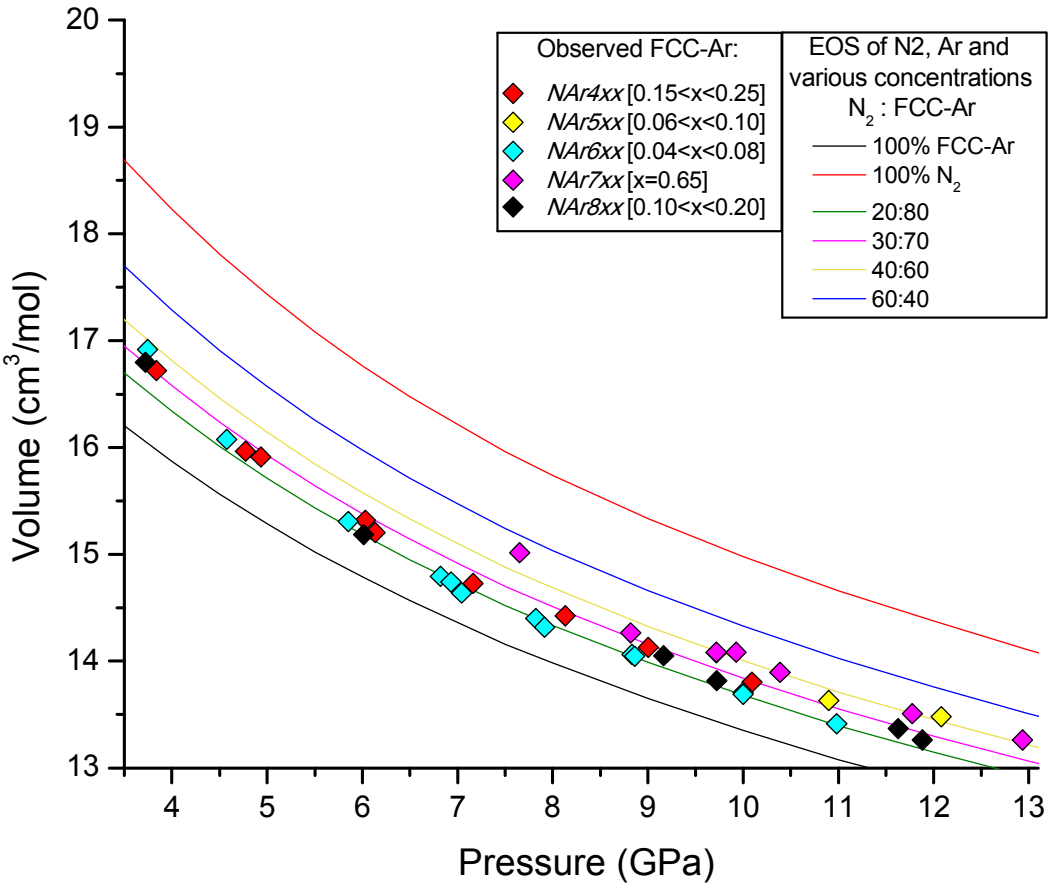

Figure 5.26: Volumes of the indexed FCC structures plotted with the EOS for various concentrations of N_2 and FCC-Ar.

From Raman spectroscopy, *NAr4xx* was estimated to be between 0.15 < x < 0.25. The XRD patterns of this sample displayed intense diffraction peaks for an FCC structure and less intense peaks corresponding to an HCP structure. Base on the volume comparison in Figure 5.27, there is an increase that corresponds to an FCC structure containing about 25% N_2 and 75% Ar. *NAr6xx* was also estimated to have a low concentration of N_2 (0.04<x<0.08) based on Raman spectroscopy results, however the volume increase corresponds to about 20% N_2 and 80% Ar. This is similar for *NAr5xx* which has an FCC structure with about 30% N_2 and 70% Ar. Unfortunately, the *NAr5xx* sample was lost early in the experiment and additional data points were not obtained to verify this structure's volume. *NAr8xx* was also estimated to have a low concentration of N_2 (0.10<x<0.20) and

the FCC volume is in agreement with this estimation. An FCC structure was indexed for *NAr7xx* (x = 0.65), though the intensity of the peaks was very low. From Figure 5.26, the volume has increases greatly to contain about 40% N_2 and 60% Ar.

Figure 5.27 provides a comparison of the experimental HCP volume to the EOS of the pure components and the EOS of solids with various concentrations of N_2 and Ar. Going back to Figure 5.15, the asterisk (*) belongs to a peak that is observed in all diffraction patterns and up to the highest pressures investigated for samples with x < 0.25. In a few cases, there were a set of peaks

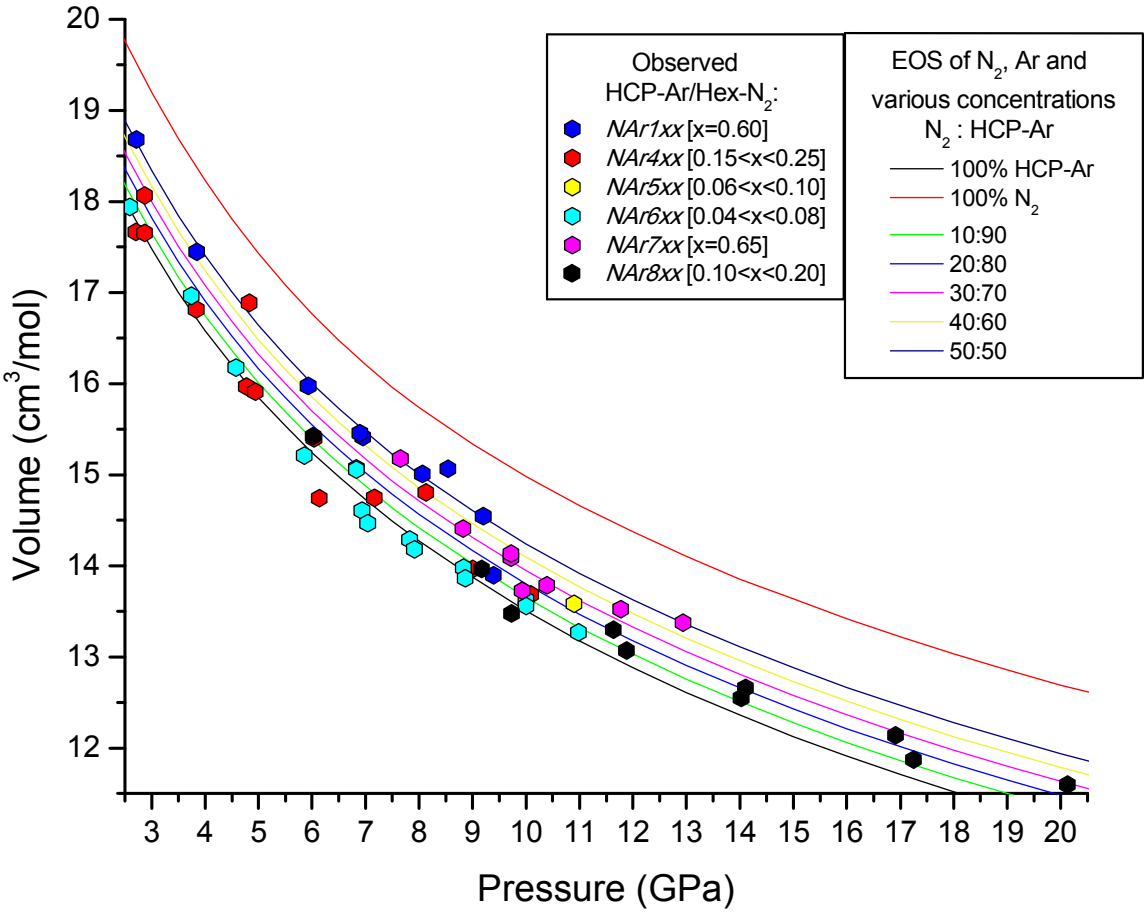

Figure 5.27: Volumes of the indexed HCP structures plotted with the EOS for the pure components[6,9,10,11,14] and various concentrations of N_2 and HCP-Ar.

that were indexed as an HCP structure. In the patterns where only a single peak was observed, such as Figure 5.14 b), the volume of the HCP unit cell was calculated by assuming an ideal c/a ratio of 1.633 and with the d-spacing of the single diffraction peak which indexed as (100).

Most of the volume data points for the samples in Figure 5.27 tend to follow the EOS for which the structure is nearly pure Ar, such as for *NAr6xx*. This contradicts what Lotz *et al.*[2] reported, i.e., the formation of β*. *NAr6xx* shows a slight volume increase and *NAr4xx* and *8xx*, for example, are following an EOS with about 10-15% N_2 substitutionally replacing Ar atoms within the FCC lattice. The data points for *NAr4xx* are somewhat scattered, and this may be due to the poor quality of the powder as the XRD images of this sample contained many spots and scattering. The HCP structure for *NAr5xx* was not verified due to loss of sample due to technical reasons. For *NAr1xx* and *NAr7xx*, samples with higher N_2 concentrations, the volume of the HCP structure is found to contain closer to 50% N_2. As this structure is not observed at higher pressures, as is the case with HCP-Ar, it appears to belong to β*.

The last EOS (Figure 5.28) will now focus on the δ* and ε* solids that were observed in *NAr1xx, 7xx* and *9xx*. Recall that the δ-ε phase transition occurs at 16.3 GPa in pure N_2. Only δ* was observed from the XRD patterns of *NAr1xx*, as it was only investigated up to 9.39 GPa. The EOS that most closely fits the data points for this sample contains about 80% N_2 with 20% Ar within the cubic lattice, as seen in Figure 5.28. Below ~12 GPa, the δ* observed in *NAr7xx* contains about 75% N_2 and 25% Ar. Above 12 GPa, there is a change in the slope and the volume decreases less with pressure. At 15.19 GPa, the volume of δ* is on the EOS of pure N_2. *NAr9xx* is unusual in that the volumes are larger than expected from both the pure components. The results for this sample follow a similar trend that is observed with *NAr7xx*, where the volume decreases less at higher pressures. This appears to occur around 15 GPa. Unfortunately, data points were not obtained

between 14-17 GPa due to technical issues. The structure above 17 GPa, for *NAr9xx*, was indexed as ε*. It should be noted that there was also a noticeable broadening of the X-ray diffraction peaks at these pressures, possibly due to crystalline strain, causing some difficulty with indexing the correct angles for some peaks in the diffraction patterns at 17.28 GPa and 20.81 GPa. The structure for ε* at 22.82 GPa was indexed reasonably well and the comparison to the calculated d-spacings are found in Table 5.5. Also, the spectrum from the ruby microspheres (rhombohedral Al_2O_3) were showing signs of strain so the pressure was also measured using the Raman signal from 1st order diamond. When the measurement of pressure using ruby luminescence becomes difficult, as was the case with *NAr9xx*, measurements of the high pressure first-order Raman signal of diamond can provide a relatively accurate and alternate method for determining pressure. Measuring the Raman signal from the diamond anvil allows the pressure of the sample to be determined as the vibrational levels in a diamond will shift with pressure according to a known relationship.[15]

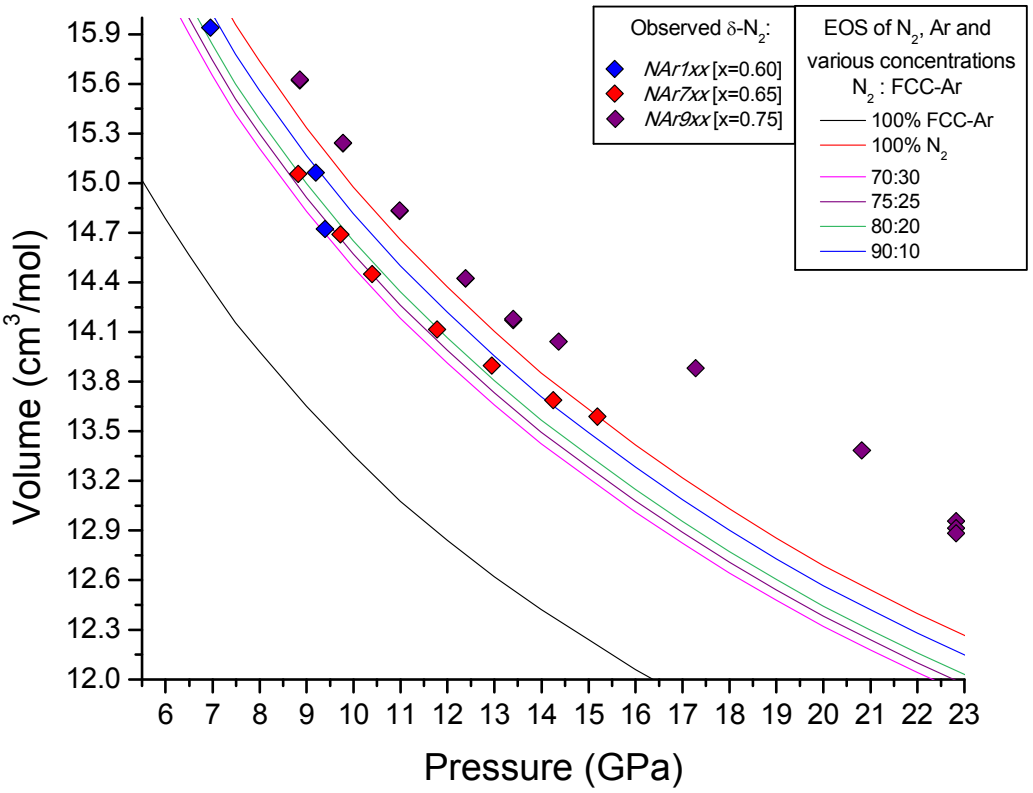

Figure 5.28: Volumes of the indexed cubic and rhombohedral structures plotted with the EOS for the pure components[6,7,8,9,10,11] and for various concentrations of N_2 and FCC-Ar.

5.4 Extension of the N_2-Ar Phase Diagram

Table 5.6 summarizes all the structures that were detected and characterized for each concentration of the N_2-Ar system investigated in this work. Only Raman spectroscopy was performed on *NAr2xx* and *NAr3xx*. *NAr3xx* had a higher N_2 concentration (x = 0.80) and phase changes of β*, δ* and ε* were more easily observed. *NAr2xx* is identified as only containing S_{Ar*} and HCP-Ar* as it contained less N_2 (x = 0.04) and only a single vibron line was observed above the fluid-solid transition. HCP-Ar* was included because it was observed in all XRD patterns with x < 0.25.

Table 5.6: Solid structures observed via Raman spectroscopy and XRD for each sample.

Sample	N_2 Mole Fraction (x)	Structures
NAr1xx	0.60	Disordered Hexagonal-N_2 (β*), Disordered Cubic-N_2 (δ*)
NAr2xx†	0.04	FCC-Ar (S_{Ar*}), HCP-Ar*
NAr3xx†	0.80	Disordered Hexagonal-N_2 (β*), Disordered Cubic-N_2 (δ*), Rhombohedral-N_2 (ε*)
NAr4xx	0.15<x<0.25	FCC-Ar (S_{Ar*}), HCP-Ar*
NAr5xx	0.06<x<0.010	FCC-Ar (S_{Ar*}), HCP-Ar*
NAr6xx	0.04<x<0.08	FCC-Ar (S_{Ar*}), HCP-Ar*
NAr7xx	0.65	Disordered Hexagonal-N_2 (β*), Disordered Cubic-N_2 (δ*), FCC-Ar (S_{Ar*})
NAr8xx	0.10<x<0.20	FCC-Ar (S_{Ar*}), HCP-Ar*
NAr9xx	0.75	Disordered Cubic-N_2 (δ*), Rhombohedral-N_2 (ε*)

(*) = *denotes a mixed solid.* (†) = *Samples were investigated with only Raman spectroscopy.*

The experimental results of this work were overlaid on the cross section of the N_2-Ar phase diagram at room temperature proposed by Lotz *et al.*[2] This is presented in Figure 5.29. Unfortunately, due to time and technical constraints, concentrations 0.25<x<0.50 were not investigated in this work. For samples that were taken to the fluid-solid transition, the transition pressures are very similar to those observed by Lotz *et al*. *NAr2xx* (x = 0.04) was the only sample that had spectra containing coexisting fluid and solid, while spectra such as this was observed for x > 0.10 by Lotz *et al*. Phases detected for x ≥ 0.60 were also in agreement with the two-phase and three-phase regions, and for x = 0.75 and 0.80, the phase diagram was extended to higher pressures to include the ε* phase. Differences arise for x < 0.25, where Lotz *et al*. reported observing the β* structure. XRD results from this work detected an HCP structure for all diffraction patterns where

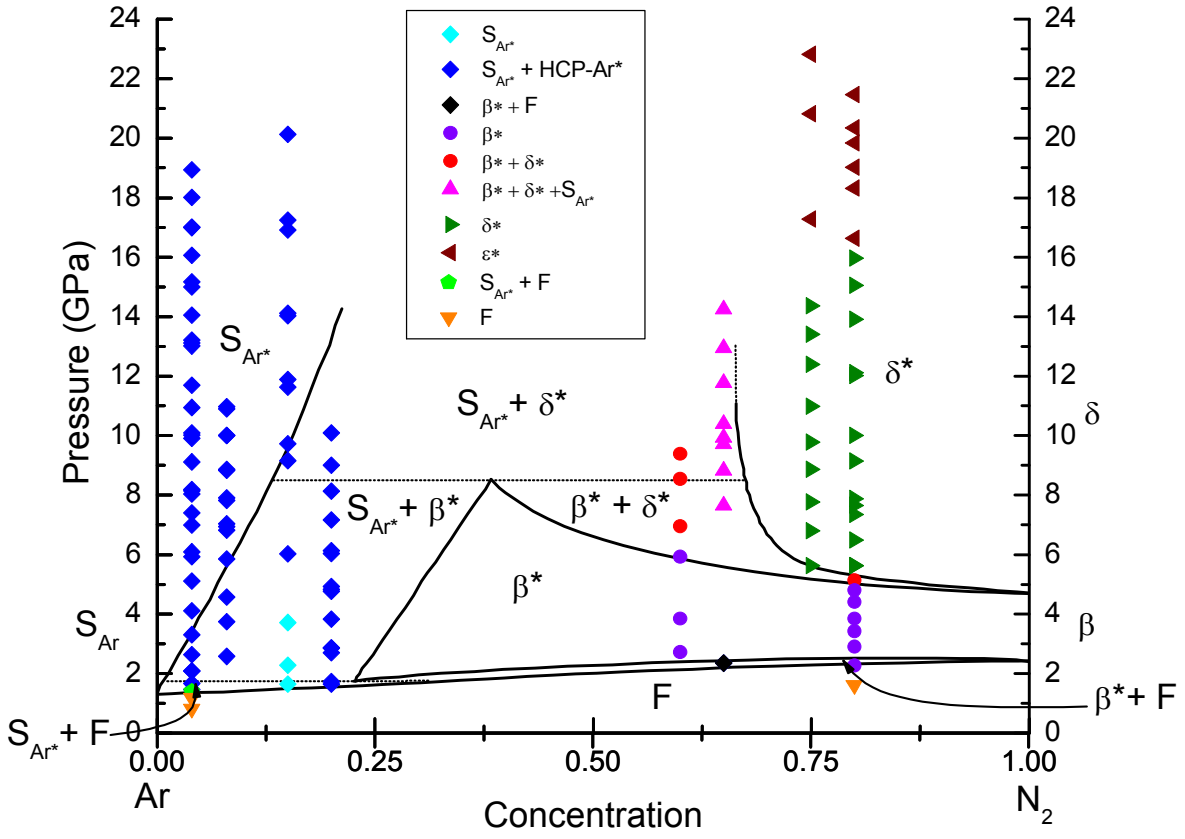

Figure 5.29: The N_2-Ar phase diagram proposed by Lotz *et al.*[2] at room temperature with data points overlaid which represent the various structures observed in this work. Solid lines: 2-phase lines; dotted lines: 3-phase lines.

$x < 0.25$; however, the volume associated with the structure was closer to the HCP-Ar EOS, rather than that of pure N_2. The single vibron line that is observed with pressure for $x < 0.25$ appears to be due to a mixed solid (S_{Ar^*}) and not that of β*. Therefore, the three-phase region that was initially labelled for F – β* - S_{Ar^*} has been changed to F - HCP-Ar* - S_{Ar^*}. The β* and δ* phases were not observed for $x < 0.25$ and instead will be replaced with S_{Ar^*} + HCP-Ar*.

Based on the experimental results of this work and those by Lotz *et al.*[2], a new proposed phase diagram for the N_2-Ar binary system is presented in Figure 5.30. This phase diagram has been extended to higher pressures and includes phases observed with XRD in addition to Raman spectroscopy. Dashed lines and regions between $x = 0.25$ and 0.60 have yet to be studied with XRD and require further investigation.

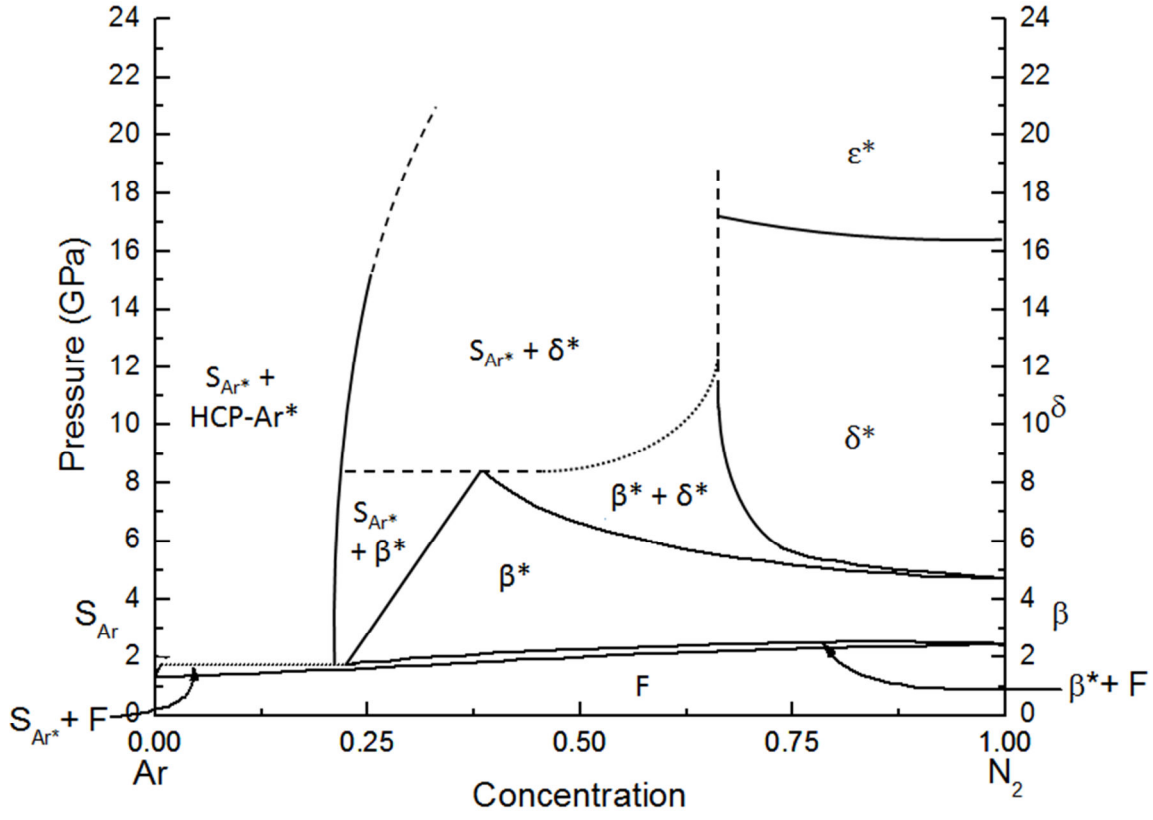

Figure 5.30: The proposed N_2-Ar phase diagram based on experimental results of this work. Solid lines: 2-phase lines; dotted lines: 3-phase lines; dashed lines: possible phase lines that would require confirmation.

5.5 Discussion

Concentrations for each sample were determined using Raman spectroscopy and comparing the experimental vibrational frequencies to accepted values for pure N_2 and to the results obtained on the N_2-Ar system by Lotz *et al*.[2] For samples with lower concentrations of N_2, it is more difficult to determine the exact concentration, hence the larger uncertainty (± 5%) for some samples.

Raman spectra for samples with lower concentrations of N_2 resulted in a single vibron line with pressure. For samples with higher concentrations of N_2, the β*-δ* transition was easily identifiable from Raman spectra by the addition of a second vibron (υ_1 and υ_2). In agreement with Lotz *et al*.[2], this transition was shifted to higher pressures and was dependant on concentration. A β* + δ* coexistence was observed in *NAr3xx* (x = 0.80) at 5.14 GPa. The ratio of the intensities of the vibrons, υ_1 and υ_2, in mixtures of x ≥ 0.60 was about $^1/_4 - {}^1/_5$, where in pure N_2 this ratio is $^1/_3$. The reduction in the intensity for υ_1 shows that about 30-50% of the sphere-like sites in δ* are occupied by Ar atoms. This is in agreement with previous studies where it was stated that Ar atoms show a preference for the sphere-like sites as opposed to the disk-like sites.[16]

With respect to pure N_2, vibrational frequencies for samples with lower N_2 concentrations tend to change from a lower shift in frequency (with respect to pure N_2) into a higher shift with pressure above the fluid-solid transition. For mixtures with higher concentrations of N_2, the behaviour of the vibrational frequencies differed for different concentrations. Frequencies for *NAr3xx* (x = 0.80), for example, remained shifted lower with respect to pure N_2 with pressure, while frequencies for *NAr9xx* (0.75) were shifted lower up to ~16 GPa where there was a slight change in slope. The shifting observed for all samples may be caused by a difference in the vibrational frequency of N_2 within the mixed solid. Compression of the N_2 molecule within the FCC-Ar lattice, for example,

would result in a higher frequency compared to the pure component. *NAr2xx* (x = 0.04) was the only sample where the fluid-solid coexistence was observed with Raman spectroscopy, which occurred at 1.38 GPa. Lotz *et al*.[2] also observed a fluid-solid coexistence in their Raman spectra for x ≥ 0.25. They attributed the solid to β*. XRD experimental results from this work have shown that S_{Ar^*} + HCP-Ar* and not the β* structure is observed for x < 0.25. The vibron line observed with pressure for x < 0.25 appears to be due to a mixed solid, with N_2 molecules dissolved within the FCC and HCP lattices of Ar.

The vibrational linewidths (FWHM) for all concentrations investigated were observed to increase with pressure when compared to pure N_2. This broadening was more significant for concentrations between 0.10<x<0.25. Below 8-10 GPa, for these concentrations, the linewidths were about 1 cm^{-1} broader than pure N_2, a significant difference. For *NAr8xx* (0.10<x<0.20), the increase in linewidth is even more prominent with a difference of more than 4 cm^{-1} above 17 GPa. Samples with higher concentrations of N_2 resulted in vibrational linewidths that were closer to pure N_2. Samples with x = 0.75 and 0.80 had linewidths that were 1 cm^{-1} and 0.2 cm^{-1} broader than pure N_2, respectively. The broadening may be due to variation in the local composition around the molecules and vibrational coupling between N_2 molecules and Ar. This could result in the detection of more vibrational frequencies and lead to an increase in the linewidth.[17] Also, the vibrational frequencies of N_2 in FCC- and HCP-Ar may be very similar and this could result in a line broadening as opposed to two discrete peaks. Changes in the slope of the FWHM as a function of pressure are a good indicator of possible phase changes. For x < 0.25, there were no obvious changes in slope with pressure. Mixtures with higher concentrations of N_2 displayed a jump in the slope at the δ*-ε* transition around 16.5 GPa for x = 0.75 and ~17.5 GPa for the compression and 16 GPa for the decompression of x = 0.30. In addition, the phase change was visually observed as the sample became textured. Low energy Raman spectra for mixtures containing x < 0.25 did not show any of

the additional lattice modes that are observed with pure N_2 for high pressure phase changes (e.g. ε-N_2 at 16.3 GPa). However, these lattice modes were observed for the mixtures in this work with higher N_2 concentrations.

A frequency jump was observed for the vibrational frequencies at the fluid-solid transition for all samples brought to the liquid state. The diameter ratio (α) for N_2-Ar is 0.94, with Ar being the slightly smaller component. Calculations on hard sphere systems have predicted that α above 0.94 will result in a monotonic incline of the fluid-solid phase lines toward the component with the higher solidification pressure with a small coexistence region.[2,18,19] In this case the component with the higher solidification pressure would be N_2 (2.4 GPa for N_2 and 1.3 GPa for Ar)[2,20]. Lotz *et al*.[2] reported an incline up to higher concentrations of N_2 and the samples that were brought to the fluid-solid transition in this work also showed this behaviour. When Ar dissolves into β-N_2, the mixture solidifies as the fluid phase is not favored. On the other hand, the FCC-Ar lattice will become distorted with the introduction of N_2 within the lattice, which will hinder the rotation of the N_2 molecules.[2]

The unusual XRD images of *NAr4xx* (Figure 5.17) may be due to complex single crystals of N_2. XRD images are not unlike those corresponding to incommensurate structures[21], however this only a qualitative assessment. These structures form when an atom (or molecule) is located slightly off from where the lattice point is expected. Each unit cell differs, however there is a periodicity that forms a larger unit cell. XRD images of such structures result in spots with symmetries.[20] The study of complex crystal structures, such as incommensurate structures, is continually expanding and if these patterns do indeed belong to such structures, it may be an area that could be investigated further with this system.

FCC-Ar* was observed prominently in mixtures with x < 0.25. The experimental volumes (calculated from lattice parameters obtained via XRD) fall in between the EOS of the pure systems. N_2 and Ar have similar sizes, with Ar being the smaller component. Substitutional replacements occurring within the lattice would result in changes in unit cell volume with respect to that of the pure components. If N_2 molecules are substitutionally replacing Ar within the FCC lattice, the result should be a larger volume than that of the pure FCC-Ar unit cell. In an attempt to estimate the amount of N_2 with the FCC lattice, the EOS of pure FCC-Ar and N_2 were combined to create new EOS for various concentrations. This method was employed for all structures (FCC-Ar*, HCP-Ar*, β* and δ*). The volumes obtained for x < 0.25 tend to follow an EOS for an FCC-Ar structure containing about 20-25% N_2. An FCC structure was observed in the XRD patterns for *NAr7xx* (x = 0.65), however the intensity of the peaks was very low compared to β* and δ*. The volumes obtained followed an EOS for an FCC-Ar structure containing about 40% N_2. The concentrations in this work were determined with Raman spectroscopy, and the method to determine the EOS for the observed volumes is a rough estimate. The increase in volume shows that N_2 is dissolving within the FCC-Ar lattice and for x < 0.25, N_2 is getting completely dissolved into solid Ar.

As stated previously, the HCP structure indexed for x < 0.25 resulted in volumes that were similar to pure HCP-Ar as opposed to β*. Mixtures with 0.08<x<0.25 lead to increased volumes that corresponded to an EOS that contained up to 25% N_2 within the HCP-Ar lattice. For *NAr1xx* (0.60) and *NAr7xx* (0.65), the volume of the HCP structure is found to contain closer to 50% N_2. The intensities associated with these HCP structures are also more intense than the ones observed in samples with x < 0.25 and disappear at higher pressures (above ~13 GPa). These structures may be the β* phase with a high quantity of Ar within the lattice.

An HCP structure was not observed in *NAr9xx* (x = 0.75). This was the only sample with a higher N_2 concentration where both the δ* and ε* phases were reached and observed with XRD. The lattice parameter for δ* at 5.63 GPa was a = (6.106 ± 0.006) Å corresponding to a volume of 17.14 cm^3/mol. The rhombohedral structure of ε* was indexed with a unit cell (24 molecules per unit cell) with lattice parameters of a = (7.503 ± 0.006) Å and c = (10.531 ± 0.006) Å with a volume of 12.88 cm^3/mol at 22.82 GPa. The ratio of these lattice parameters is 1.404, in agreement with Olijnyk *et al*.[6], who reported a c/a ratio of 1.396 at 16.3 GPa and room temperature. The volumes for these structures were unexpectedly larger than the pure N_2 EOS and the decrease in volume with compression of the sample was more evident in the ε* phase. If the pressures were not calibrated properly (due to stress on rubies), the data points for *NAr9xx* in Figure 5.28 may be shifted a little higher than the actual pressure, however, that would not account for the jump observed in the slope above 16 GPa. The data points corresponding to *NAr7xx* (x = 0.65) also show a change in slope nearing the δ*-ε* phase transition pressure. Unfortunately, the sample was lost before the transition was complete.

Lotz *et al*.[2] reported the solubility of Ar into N_2 to be ~35%. XRD experiments from this work show that the solubility is up to ~50% for HCP and up to ~40% for FCC structures for all pressures investigated. No indication of a compound was found in mixtures below x < 0.25. In this work, δ* and ε* were only observed in mixtures with higher concentrations of N_2 (x ≥ 0.60). The solubility for the δ* (disordered cubic) structure was ~25% up to about 12 GPa. Above 12 GPa, the volumes of the δ* and ε* structures indexed did not follow any of the combined EOS and were found to decrease more slowly with pressure. What is causing this phenomenon is unknown and the XRD results for mixtures with x > 0.50 should be verified. The phase diagram proposed by Lotz *et al*.[2] has been extended up to ~24 GPa for mixtures with x < 0.25 and 0.60<x<0.80. Based on the experimental result of this work a new phase diagram for the N_2-Ar binary system is presented in

Figure 5.30. Due to time and technical constraints, mixtures with concentrations between $0.25<x<0.60$ were not investigated in this work.

References

1. Schneider, H., Häfner, W., Wokaun, A. & Olijnyk, H. Room temperature Raman scattering studies of external and internal modes of solid nitrogen at pressures 8≤P≤54 GPa. *J. Chem. Phys.* **96,** 8046 (1992).

2. Lotz, H. & Schouten, J. Phase behavior of the N2-Ar system at high pressures: A Raman spectroscopy study. *Phys. Rev. B* **64,** 1–6 (2001).

3. Scheerboom, M. I. M., Michels, J. P. J. & Schouten, J. A. High pressure study on the Raman spectra of fluid nitrogen and nitrogen in helium. *J. Chem. Phys.* **104,** 9388 (1996).

4. LeSar, R. *et al.* Raman spectroscopy of solid nitrogen up to 374 kbar. *Solid State Commun.* **32,** 131–134 (1979).

5. Buchsbaum, S., Mills, R. L. & Schiferl, D. Phase diagram of nitrogen determined by Raman spectroscopy from 15 to 300 K at pressures to 52 GPa. *J. Phys. Chem.* **88,** 2522–2525 (1984).

6. Olijnyk, H. High pressure x-ray diffraction studies on solid N2 up to 43.9 GPa. *J. Chem. Phys.* **93,** 8968 (1990).

7. Finger, L. W., Hazen, R. M., Zou, G., Mao, H. K. & Bell, P. M. Structure and compression of crystalline argon and neon at high pressure and room temperature. *Appl. Phys. Lett.* **39,** 892–894 (1981).

8. Ross, M., Mao, H. K., Bell, P. M. & Xu, J. A. The equation of state of dense argon: A comparison of shock and static studies. *J. Chem. Phys.* **85,** 1028–1033 (1986).

9. Schiferl, D. *et al.* Structure of N2 at 2.94 GPa and 300 K. *Acta Crystallogr. Sect. C Cryst. Struct. Commun.* **39,** 1151–1153 (1983).

10. Mills, R. L., Olinger, B. & Cromer, D. T. Structures and phase diagrams of N2 and CO to 13 GPa by x-ray diffraction. *J. Chem. Phys.* **84,** 2837 (1986).

11. Cromer, D. T., Mills, R. L., Schiferi, D. & Schwalbe, L. A. The structure of N2 at 49 kbar and 299 K. *Acta Crystallogr. Sect. B Struct. Crystallogr. Cryst. Chem.* **37,** 8–11 (1981).

12. Vogt, J. & Alvarez, S. van der Waals Radii of Noble Gases. *Inorg. Chem.* **53,** 9260–9266 (2014).

13. Batsanov, S. Van der Waals radii of elements. *Inorg. Mater.* **37,** 871–885 (2001).

14. Wittlinger, J., Fischer, R., Werner, S., Schneider, J. & Schulz, H. High-Pressure Study of h.c.p. Argon. *Acta Crystallogr. Sect. B Struct. Sci.* **53,** 745–749 (1997).

15. Akahama, Y. & Kawamura, H. Pressure calibration of diamond anvil Raman gauge to 310 GPa. *J. Appl. Phys.* **100,** 21–24 (2006).

16. Kooi, M. E. & Schouten, J. A. Raman spectra and phase behavior of the mixed solid N2 -Ar at high pressure. *J. Low Temp. Phys.* **57,** 407–413 (1998).

17. Scheerboom, M. I. M. & Schouten, J. A. Critical broadening of the vibrational linewidth by concentration fluctuations. *Phys. Rev. E* **51,** (1995).

18. Kranendonk, W. G. T. & Frenkel, D. Thermodynamic properties of binary hard sphere mixtures. *Mol. Phys.* **72,** (1991).

19. Kranendonk, W. G. T. & Frenkel, D. Computer simulation of solid-liquid coexistence in binary hard-sphere mixtures. *Phys. Condens. Matter* **1,** (1989).

20. Schiferl, D., Buchsbaurn, S. & Mills, R. L. Phase Transitions in Nitrogen Observed by Raman Spectroscopy from 0.4 to 27.4 GPa at 15 K. *J. Phys. Chem.* **89,** 2324–2330 (1985).

21. McMahon, M. I., Loa, I., Stinton, G. W. & Lundegaard, L. F. Determining complex crystal structures from high pressure single-crystal diffraction data collected on synchrotron sources. *High Press. Res.* **33,** 485–500 (2013).

Chapter 6
NITROGEN-KRYPTON

This chapter outlines the results of Raman and XRD measurements taken for a sample of the nitrogen and krypton binary system. Due to time (and technical) constraints, only a single sample was investigated for this system.

6.1 Raman Spectroscopy Results

Raman spectroscopy was performed using an argon ion laser (λ = 488 nm) as the excitation light source and calibrated using the method described in Chapter 4. Figure 6.1 shows a Raman spectrum for *NKr1xx* at 20.5 GPa.

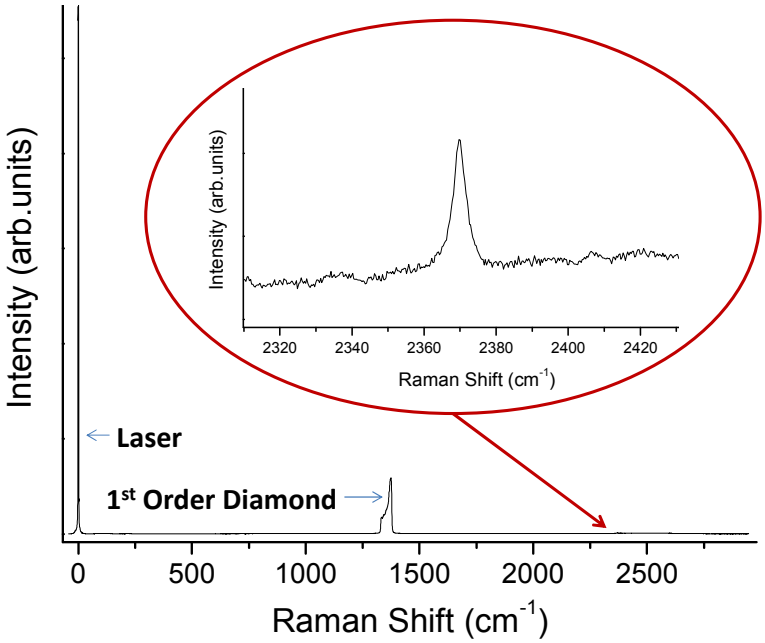

Figure 6.1: The Raman spectrum of *NKr1xx* at 20.5 GPa, displaying intensities from the laser source, diamond and nitrogen. A closer look at the nitrogen vibron line is shown inside the oval.

In this Raman spectrum, the intensity of the vibrational (stretching) mode associated with N_2 is very weak when compared to that of diamond. The uncertainty for each vibrational frequency and linewidth (FWHM) is 1 cm^{-1}. The low intensity with respect to the intensity observed for diamond (in this case, the 2nd order Raman signal) results from to a lower concentration of N_2 within the N_2-Kr sample. Figure 6.2 presents Raman spectra for the vibrational mode of N_2 under compression up to 21.67 GPa. For the entire pressure range studied, only a single peak (corresponding to the molecular stretching mode) was observed, showing no phase changes.

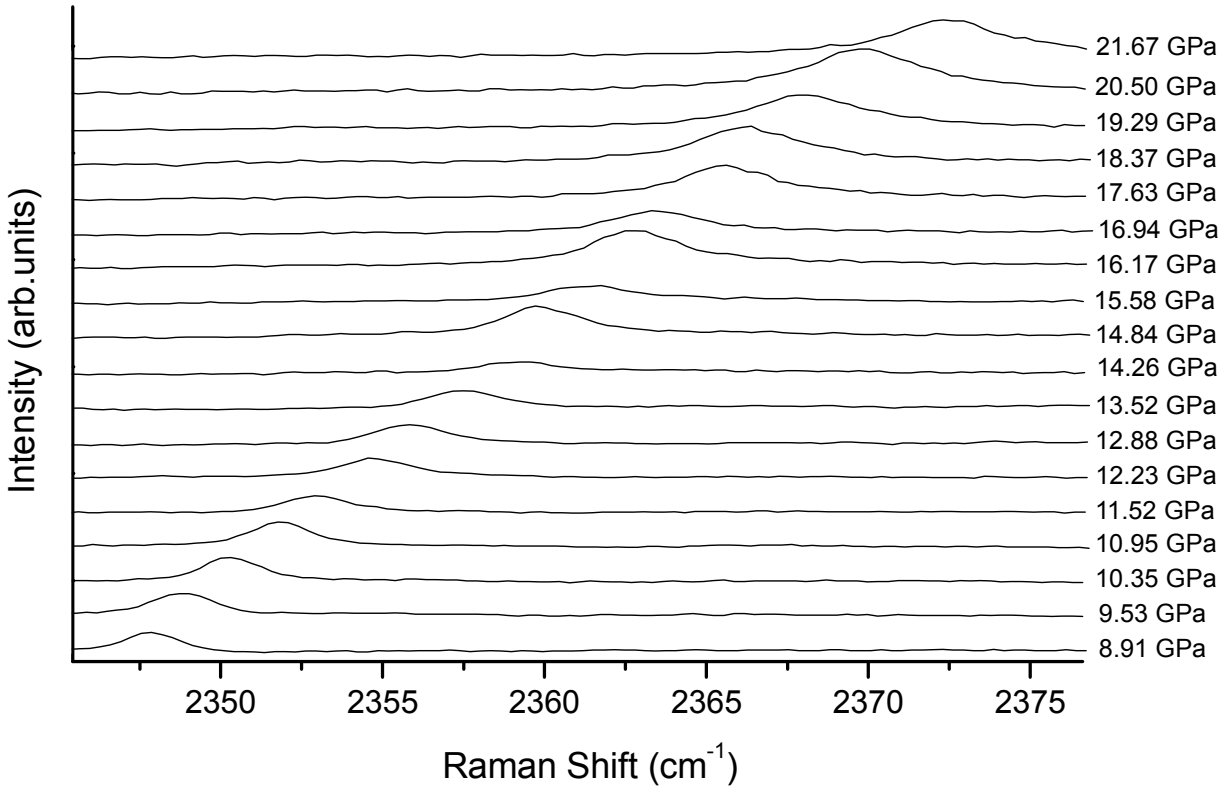

Figure 6.2: Raman spectra of the vibrational (stretching) mode of nitrogen in *NKr1xx* at various pressures showing broad linewidths compared to pure N_2.

The linewidths were all larger compared to those for pure N_2; they also required a fit to a Gaussian profile as opposed to a Lorentzian one. Observations of the low energy region (lattice modes; 0 - ~400 cm^{-1}) also did not show much change with pressure. Figure 6.3 shows the Raman spectra of

the low energy lattice modes for *NKr1xx* up to 21.67 GPa. There may be a peak or anomaly at around 20 GPa, however it is not observed in the spectrum at 21.67 GPa. Issues raised here will be addressed further in the discussion.

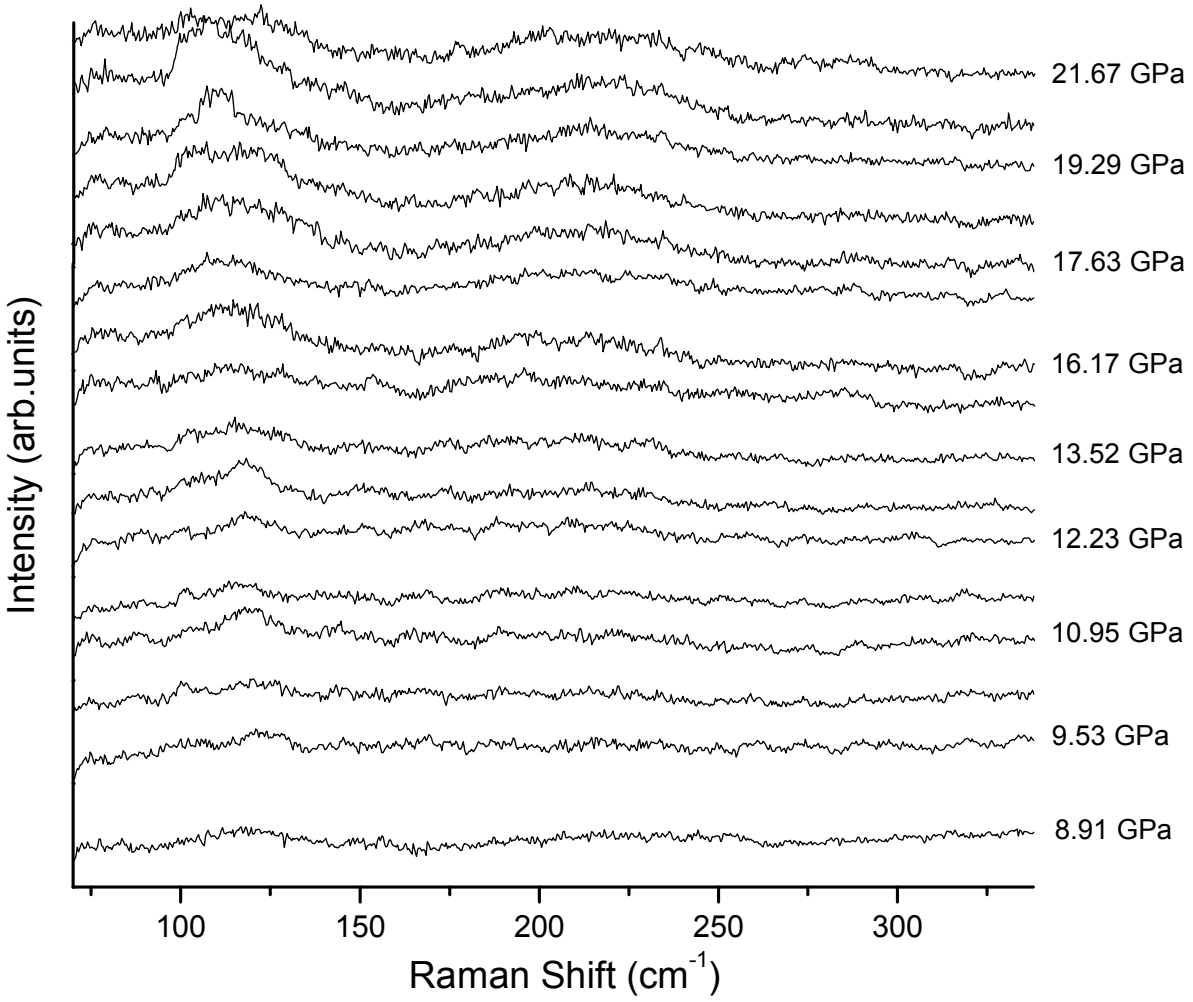

Figure 6.3: Raman spectra of the low energy lattice modes of *NKr1xx* at various pressures.

Figure 6.4 displays the full-width-half-maximum (FWHM) obtained for *NKr1xx* as a function of pressure. The FWHM increases with pressure, similar to the N_2-Ar system, and there is no obvious change in the slope, as is expected with the δ- to ε-N_2 phase change at 16.3 GPa.

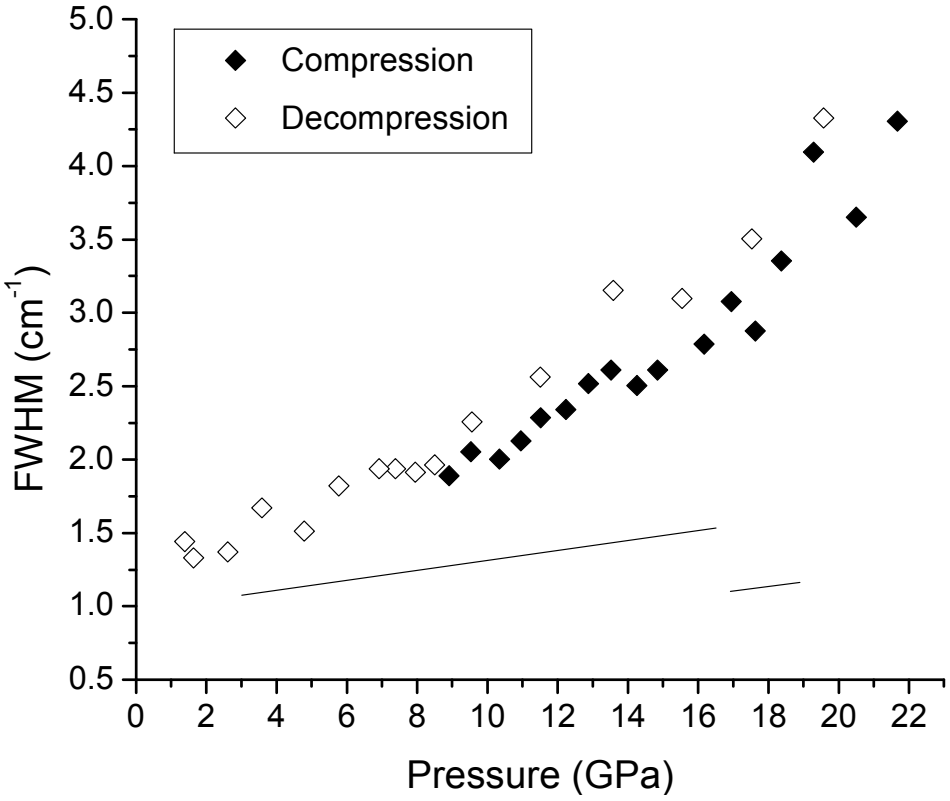

Figure 6.4: The full-width-half-maximum (FWHM) of *NKr1xx* as a function of pressure. Solid lines represent pure N_2 data from this work.

Broader peaks were observed and are more evident at higher pressures, which is in agreement with results obtained by Lotz *et al.*[1] This broadening was attributed to rapid exchange of the positions of the molecules within the mixed solid.[1] It was discussed in more detail in Chapter 2. Based on the comparison of the Raman shift results to both pure N_2 and the N_2-Kr binary system studied by Lotz et al.[1], the experimental Raman shift as a function of pressure is very similar to the x=0.06 results from Lotz *et al.*[1], where "x" represents again the mole fraction of N_2 in the sample. This shows that the sample was low in N_2. The fluid-solid transition was observed to occur at 1.1 GPa, in agreement with Lotz *et al.*[1] No other phase transitions were visually observed. The vibrational frequencies as a function of pressure, obtained in this work for the N_2-Kr system, are summarized in Figure 6.5.

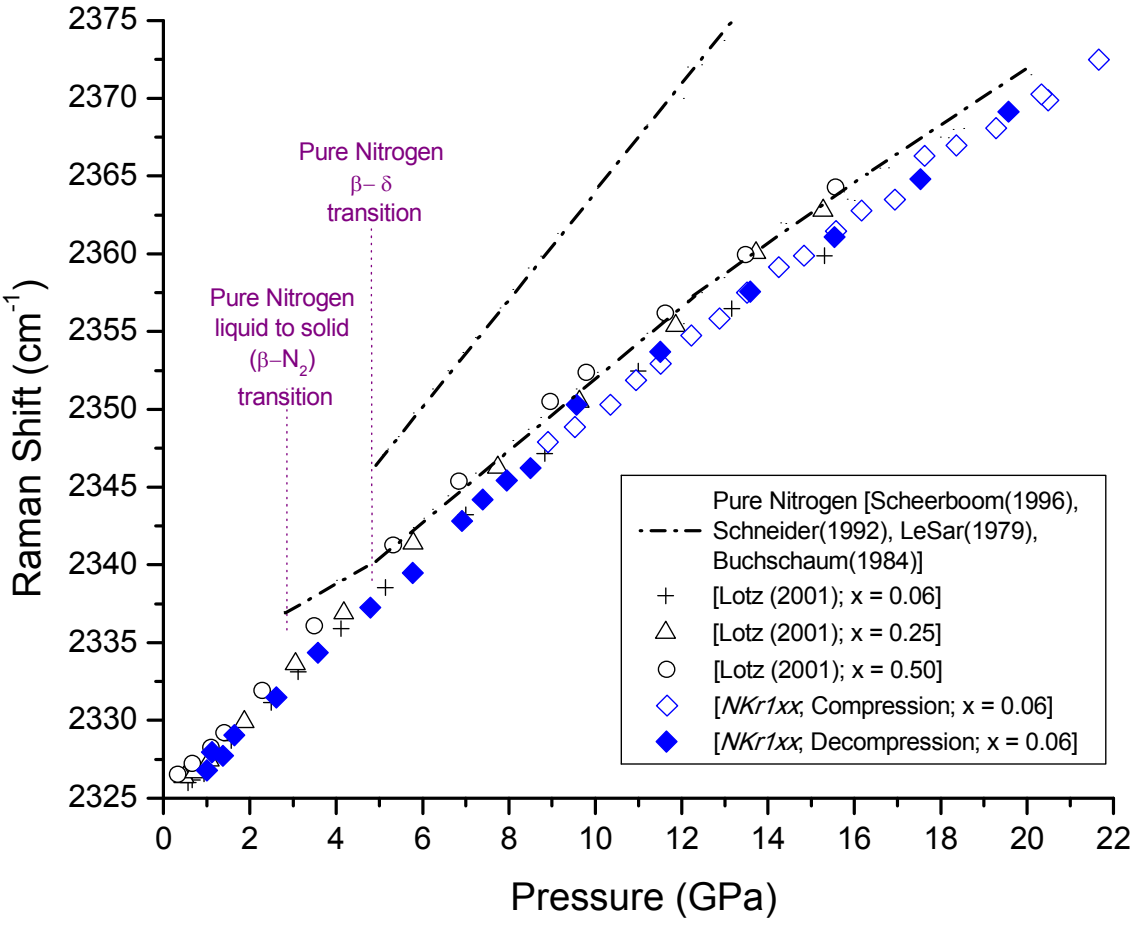

Figure 6.5: Raman spectroscopic results for *NKr1xx* at various pressures compared to pure nitrogen[2,3,4,5] and N_2-Kr data from Lotz *et al.*[1] "x" denotes the nitrogen concentration within the sample.

6.2 X-ray Diffraction Results

A single x-ray diffraction (XRD) pattern was obtained for *NKr1xx*. Figure 6.6 shows the XRD image which contains intense spots within the Debye rings and individual spots not associated to Debye rings, which are most likely due to components of the apparatus. The non-uniform Debye rings recorded on the XRD image indicate that this sample was not an ideal powder. Regions of higher

intensity were most likely due to larger crystals and/or preferred orientation within the sample. The diffuse scattering between rings may be due to stacking faults in the FCC lattice or stress on the system.

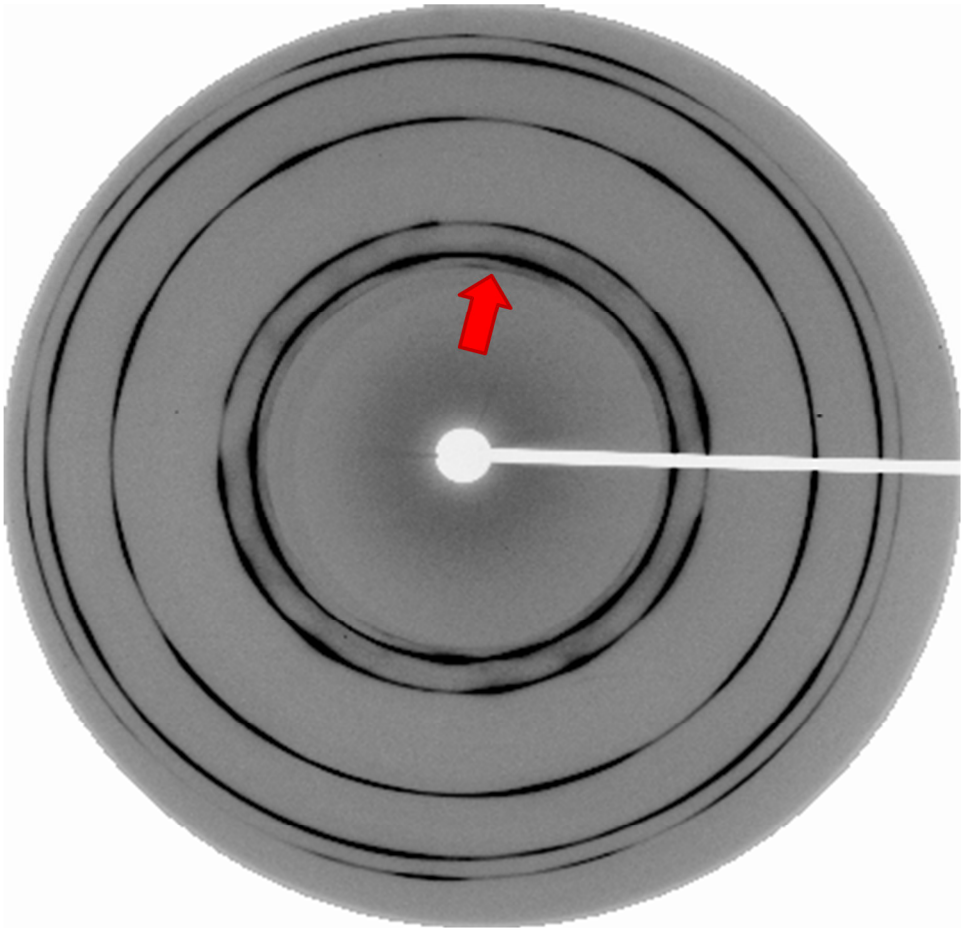

Figure 6.6: XRD image presenting Debye rings for *NKr1xx* collected at 8.28 GPa and room temperature. Non-uniform rings suggest larger crystals and/or preferred orientation within the polycrystalline sample. The five darker, most intense set of rings belong to a FCC structure of Kr. The red arrow shows a less intense ring that may belong to a HCP structure, arising also from Kr.

Figure 6.7 gives the corresponding x-ray diffraction pattern for the image shown in Figure 6.6. This pattern contains intense peaks associated with an FCC structure of Kr having a lattice parameter of a = (4.830 ± 0.006) Å. To support this result, Table 6.1 summarizes the d-spacings observed and calculated (using the d_{hkl} formula for cubic unit cell found in Table 3.2) for *NKr1xx* at 8.28 GPa. The percent differences for all planes (hkl) are less than 0.43 %.

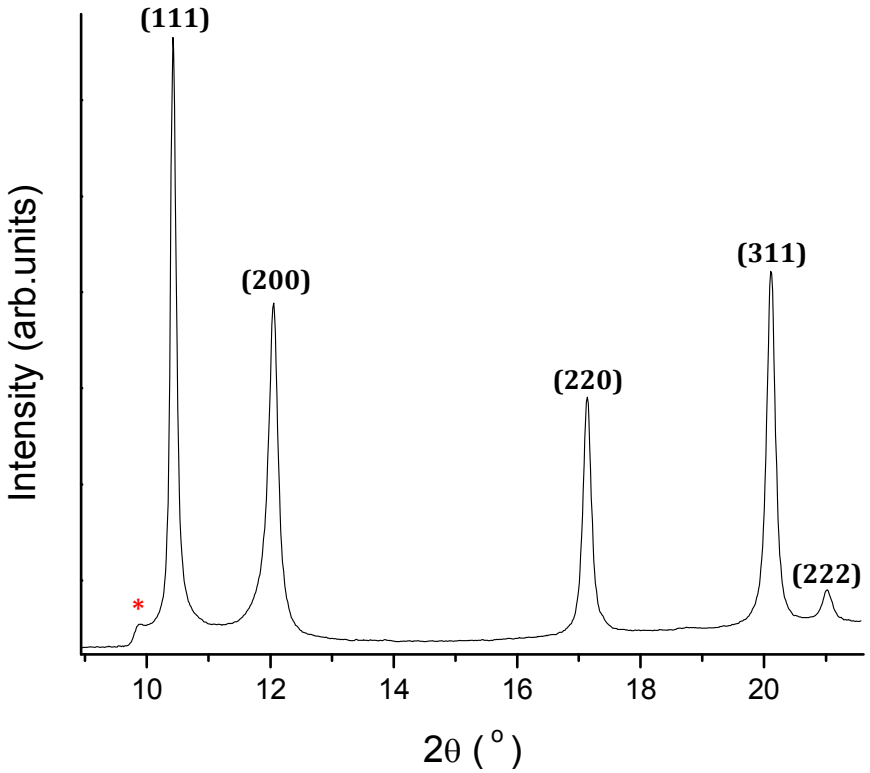

Figure 6.7: XRD pattern of *NKr1xx* at 8.28 GPa and room temperature with lattice parameter a = 4.830 Å. The peaks belonging to the S^*_{Kr} structure are designated with their corresponding planes. The asterisk (*) on the plot represents a less intense line that may belong to HCP-Kr.

Table 6.1: The d-spacings observed and calculated for the FCC structure indexed in *NKr1xx* at 8.28 GPa, using the relevant *hkl* and λ = 0.509176 Å.

(*hkl*)	$d_{calculated}$ (Å)	$2\theta_{observed}$ (°)	$d_{observed}$ (Å)	Difference (Å)	Difference (%)
(111)	2.788	10.431	2.800	0.012	0.43
(200)	2.415	12.048	2.425	0.010	0.41
(220)	1.707	17.135	1.708	0.001	0.06
(311)	1.456	20.113	1.458	0.002	0.14
(222)	1.394	21.023	1.395	0.001	0.07

Using the lattice parameter for this structure, a cubic volume was calculated to be 17.03 cm^3/mole and plotted with the equation of state (EOS) of pure N_2 and pure FCC-Kr. This is shown in Figure 6.8. The volume of the structure indexed from the diffraction pattern (Figure 6.7) falls in line with the EOS of pure Kr.

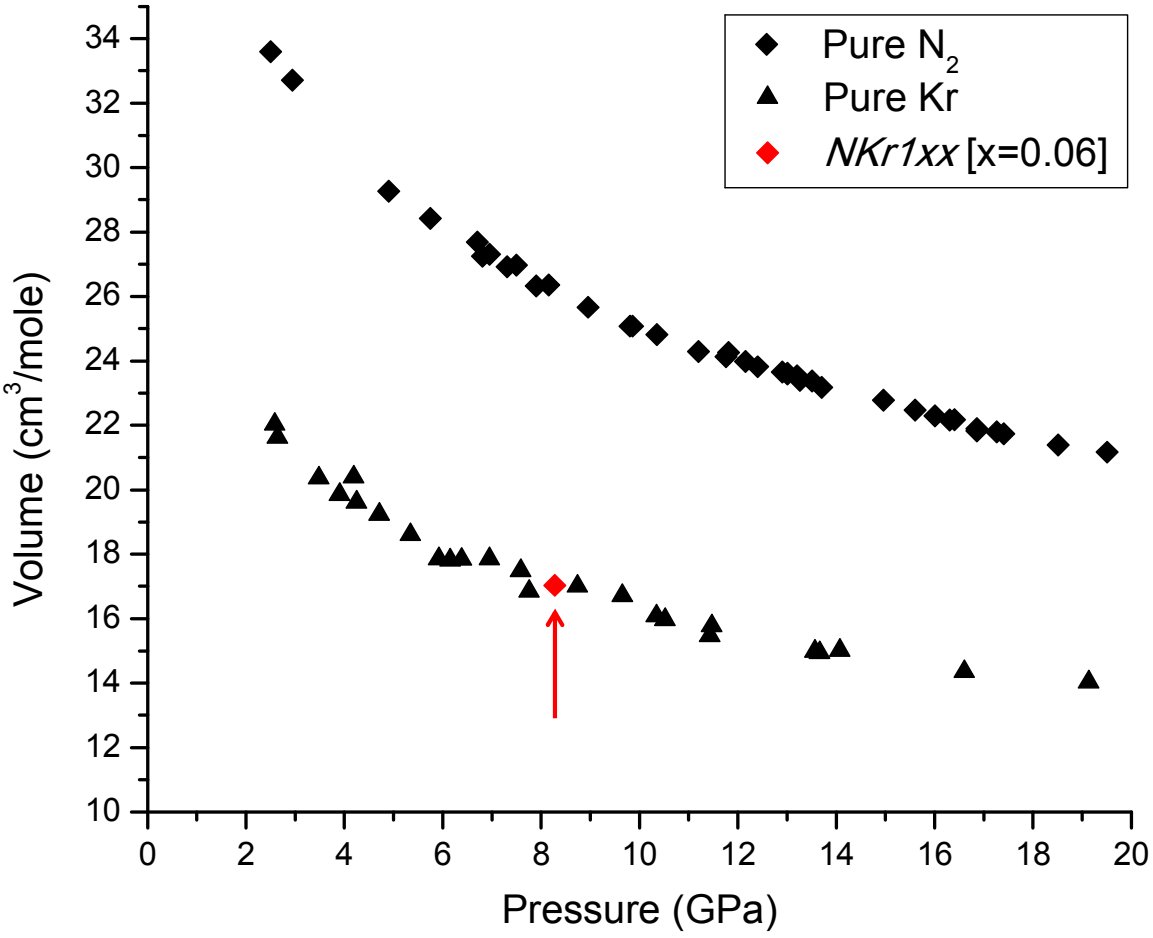

Figure 6.8: The volume of the FCC structure is plotted with the EOS of pure nitrogen[6,7,8,9] and FCC-Kr[10,11]. The arrow is meant as an aid to locate the *NKr1xx* data point.

6.3 Discussion

At room temperature, pure Kr solidifies at ~0.9 GPa and N_2 at 2.4 GPa.[12,13,14] For *NKr1xx*, the fluid-solid transition occurred at 1.1 GPa. A single vibron was observed for all pressures investigated and showed a lower intensity with respect to diamond. This helps to give a rough estimate of the concentration of the sample. A lower intensity will mean less N_2 within the sample. The vibrational frequencies were found to be shifted lower than that of pure N_2. Lotz *et al*.[1] also observed this shift in frequencies from their experiments and found that they were dependant on concentration. A smaller concentration of N_2 corresponded to a higher redshift. From a comparison of the Raman shift of *NKr1xx* to that of pure N_2 and results obtained by Lotz *et al*. (Figure 6.5), the concentration of the sample studied in this work had a nitrogen mole fraction of x = 0.06.

The vibron lines associated with pure N_2 have Lorentzian line profiles while the N_2-Kr mixture was fit with Gaussian line profiles at the fluid-solid transition and with pressure. Lotz *et al*. also observed broadening in the N_2-Kr system and attributed it to rapid exchange of the positions of the molecules within the mixed solid. The FWHM as a function of pressure (Figure 6.4) displays no obvious change in slope that is associated with higher pressure phase transitions in solid N_2. In addition to the observations from the high energy Raman spectra of no phase changes above the fluid-solid transition, intensities representing additional lattice modes belonging to ε-N_2 (discussed in Chapter 4) are not observed in the low energy Raman spectra.

An FCC structure with lattice parameter a = (4.830 ± 0.006) Å and a volume of 17.03 cm^3/mole was indexed according to the structure observed from the diffraction pattern for *NKr1xx* at 8.28 GPa. When compared to the EOS for pure N_2 and pure Kr, the volume of the structure matches that of FCC-Kr. The data point fits in well with the pure Kr EOS, and there is no obvious change in

volume due to N_2 molecules within the lattice. In agreement with the Raman experiments performed on *NKr1xx*, the N_2 concentration is very low and is most likely completely dissolved in the FCC-Kr structure, creating a mixed solid.

In Figure 6.7, the diffraction pattern was indexed for an FCC structure, however, a separate and less intense peak is also observed next to (lower angle) the FCC (111) peak. This "shoulder" is also observed in N_2-Ar mixtures with low N_2 concentrations and was shown in Chapter 5 as almost certainly belonging to an HCP structure of the noble gas. An HCP structure occurs as a result of stacking faults, or defects, within the crystal, hence the lower intensity when compared to the FCC structure. No other XRD image was taken for different pressures; though, due to the similarity of this peak found in both N_2-Ar and N_2-Kr mixtures with low N_2 content, it is most likely the result of stacking faults within FCC-Kr and not due to β-N_2. The vibrational mode that is observed with pressure (Figure 6.2) appears to be due to dissolved N_2 in the mixed solid.

Raman spectroscopy experiments confirmed the vibrational frequencies observed by Lotz *et al*.[1] for x = 0.04 up to ~16 GPa. In this work, the mixture was brought to 21.67 GPa and there was no indication of higher pressure phase transitions that are expected for pure N_2. Lotz *et al*.[1] experiments on this system only included Raman spectroscopy; however in this work XRD complimented the Raman spectroscopy. With XRD, the mixture was found to be a mixed solid at 8.28 GPa with N_2 molecules substitutionally replacing Ar atoms in the FCC lattice, rather than β-N_2 and Ar within the lattice. Though only a single mixture was studied in this work, it would be interesting to investigate other concentrations and higher pressures of the N_2-Kr binary system. The δ and ε phases of pure N_2 are rather complex, and this could lead to unusual behaviour. Adding dopants, such as Kr, to N_2 may result in novel compounds, or perhaps the Kr atoms will behave as stabilizers for a network of polymeric nitrogen.

References

1. Lotz, H. & Schouten, J. Vibrational line broadening in the mixed solid N2–Kr: A high-pressure Raman study of the phase diagram. *Phys. Rev. B* **64,** 1–8 (2001).

2. Buchsbaum, S., Mills, R. L. & Schiferl, D. Phase diagram of nitrogen determined by Raman spectroscopy from 15 to 300 K at pressures to 52 GPa. *J. Phys. Chem.* **88,** 2522–2525 (1984).

3. LeSar, R. *et al.* Raman spectroscopy of solid nitrogen up to 374 kbar. *Solid State Commun.* **32,** 131–134 (1979).

4. Scheerboom, M. I. M., Michels, J. P. J. & Schouten, J. A. High pressure study on the Raman spectra of fluid nitrogen and nitrogen in helium. *J. Chem. Phys.* **104,** 9388 (1996).

5. Schneider, H., Häfner, W., Wokaun, A. & Olijnyk, H. Room temperature Raman scattering studies of external and internal modes of solid nitrogen at pressures 8≤P≤54 GPa. *J. Chem. Phys.* **96,** 8046 (1992).

6. Schiferl, D. *et al.* Structure of N2 at 2.94 GPa and 300 K. *Acta Crystallogr. Sect. C Cryst. Struct. Commun.* **39,** 1151–1153 (1983).

7. Mills, R. L., Olinger, B. & Cromer, D. T. Structures and phase diagrams of N2 and CO to 13 GPa by x-ray diffraction. *J. Chem. Phys.* **84,** 2837 (1986).

8. Cromer, D. T., Mills, R. L., Schiferi, D. & Schwalbe, L. A. The structure of N2 at 49 kbar and 299 K. *Acta Crystallogr. Sect. B Struct. Crystallogr. Cryst. Chem.* **37,** 8–11 (1981).

9. Olijnyk, H. High pressure x-ray diffraction studies on solid N2 up to 43.9 GPa. *J. Chem. Phys.* **93,** 8968 (1990).

10. Alexandrov, I. V., Zisman, A. N. & Stishov, S. M. An investigation of the equations of state of the isoelectronic substances Csl-Xe and RbBr-Kr. Phase transitions in Csl and Rbl. *JETP* 371–375 (1987).

11. Polian, A., Besson, J. M., Grimsditch, M. & Grosshans, W. A. Solid krypton: Equation of state and elastic properties. *Phys. Rev. B* **39,** 1332–1336 (1989).

12. Schiferl, D., Buchsbaurn, S. & Mills, R. L. Phase Transitions in Nitrogen Observed by Raman Spectroscopy from 0.4 to 27.4 GPa at 15 K. *J. Phys. Chem.* **89,** 2324–2330 (1985).

13. Westerhoff, T., Wittig, A. & Feile, R. High-pressure Raman scattering of the stretching mode in nitrogen along the 300-K isotherm. *Phys. Rev. B* **54,** 14–17 (1996).

14. Young, D. Phase diagrams of the elements. *Lawrence Livermore Lab.* 64 (1975). doi:10.2172/4010212

Chapter 7
SUMMARY & FUTURE PROSPECTS

Lotz *et al.*[1,2] studied both N_2-Ar and N_2-Kr systems with Raman spectroscopy up to a maximum of about 15 GPa, though only the x = 0.10 mixture was brought above 10 GPa for the N_2-Ar system. Their conclusions regarding the phase stability and phase diagrams were based solely on results obtained from vibrational spectroscopy. In this work, the intention was to revisit those binary systems with the goals to extend the pressure range and, more importantly, to obtain, in addition to lattice dynamics, structural results from X-ray diffraction. Over nine mixtures have been investigated with Raman spectroscopy as well as XRD for the N_2-Ar system with concentrations varying between $0.04<x<1$, where x is the N_2 mole fraction. A single mixture of N_2-Kr was also studied for x = 0.06. Both systems were explored up to a maximum of ~24 GPa. The results were compared to those published and new findings were presented, analysed, and discussed.

Raman spectroscopic measurements carried out on mixed solids as a function of pressure gave vibrational (i.e., N_2 stretching) frequencies that were shifted higher than that of pure β-N_2 with $x < 0.25$ for N_2-Ar and N_2-Kr. Also, all vibrational linewidths were found to increase with pressure. Regarding the N_2-Ar system, mixtures with higher concentrations ($x \geq 0.60$) of N_2 resulted in vibrational frequencies with different pressure dependencies that were reliant on the concentration. When compared to pure N_2, vibrational frequencies for x = 0.80, for example, were shifted lower with pressure, while frequencies for x = 0.75 were shifted lower up to ~16 GPa where there was a slight change in slope. The observed shifting is likely due to a difference in the vibrational frequency of N_2 within the mixed solid. The pressure at which the fluid-solid

coexistence occurred was observed to monotonically incline toward samples with 100% N_2. Solid-to-solid phase transitions were dependant on concentration and were pushed to higher transition pressures for mixtures with less N_2 in the system. As the mixture of N_2 increased within the system, the solid-to-solid transitions were observed closer to that of the pure system. The present Raman spectroscopic results regarding phase transition pressures and the vibrational frequency dependence on pressure and concentration were in agreement with Lotz *et al*.[1] up to ~15 GPa. Two Raman peaks were observed in the fluid-solid phase for x = 0.04. Lotz *et al*.[1] also observed these peaks for x ≥ 0.25 and attributed them to the fluid + β* coexistence, as a single vibron line is expected for pure β-N_2. Conversely, the β* phase was not observed, based on the XRD analysis of mixtures with x < 0.25 for N_2-Ar and N_2-Kr. The only HCP structure detected was that of the noble element, due to stacking faults within the FCC lattice. The single vibron line that was observed with pressure did not belong to β*, but instead to the molecular stretching mode of N_2 dissolved within the Ar lattices. The expected diffraction peaks were observed for the FCC- and HCP-Ar structures, indicating the N_2 molecules were substitutionally replacing Ar atoms within the lattices. Comparisons of the experimental volumes of the structures observed in each mixture to the volumes of pure N_2 and Ar, and to various concentrations were also in agreement with structures of mixed solids having similar concentrations as those determined via Raman spectroscopy. The unit cell volume obtained for the single sample of N_2-Kr was compared to the pure substances and the sample contained a volume that was expected for pure FCC-Kr, which was indicative of a very low concentration of N_2. This was in agreement with the concentration estimated by Raman spectroscopy, with comparisons to that of pure N_2 and the results reported by Lotz *et al*.[2] of x = 0.06. No indication of a compound was found in all mixtures below x < 0.25, as was expected based on computer simulations previously made for binary systems with similar diameter ratios ($\alpha > 0.94$).[3,4]

The β*, δ*, and ε* phases were observed for N_2-Ar mixtures with x > 0.60 with Raman spectroscopy and confirmed by XRD. In addition, the pressure-induced δ*-ε* phase change was corroborated visually for x = 0.75 and 0.80, with an obvious change in the sample microstructure. The integrated intensities of the vibron lines (υ_1 and υ_2) confirmed what has been previously reported in the literature[1,5,6] that the Ar atoms preferably sit at the N_2 sphere-like sites as opposed to the disk-like sites within δ* and ε*. As the concentration of N_2 decreases from x = 0.80 to 0.75, the δ*-ε* transition pressure (as the sample was decompressed) was observed to increase slightly by about 0.5 GPa. The unit cell volume obtained for x = 0.65 and 0.75 become rapidly less compressible above ~12 GPa. This is observed by a change in the slope of the EOS. The mixture with x = 0.75, in particular, had larger volumes than that of pure N_2 for all pressures investigated. It should be noted that the pressures measured for this sample and could have been ~0.5 GPa higher than the actual due to non-hydrostatic stress on the ruby microspheres used for the pressure gauge; this however does not account for the change in slope and lower compressibility observed above ~12 GPa. The reason for this behaviour is unknown and results obtained with XRD for mixtures with x > 0.50 should be verified to confirm the observation.

Unfortunately, due to time and technical constraints, ideal powder samples were not obtained in this work. The XRD images showed many spots and non-uniform scattering as observed are indications of the presence of larger crystallites, strain on the system and/or preferred orientation within the sample. For powder samples that are not ideal, an analysis of the azimuthal intensity (along the Debye rings) could be made in combination with the corresponding (*hkl*) and this should tell about the crystallite preferred orientation. If an ideal powder were attained, the relative XRD intensities from a given phase would change when the concentration of one component is increased with respect to the other within the structure. This can be used to determine the most probable locations for specific atoms or molecules within the lattice using computer simulations (i.e.

Diamond 4.0.1, CHEKCELL).[7,8] This method could be used to verify where the N_2 molecules are located within the different lattices (FCC-Ar*, HCP-Ar*, β*, δ* and ε*). In addition, ideal powders should show less stress with pressure as they do not contain larger crystals and this can help to reduce the strain-induced broadening of the diffraction peaks. This will help to establish more precise unit cell parameters and lead to a more accurate determination of the equation of state for the various concentrations.

The unusual XRD images recorded from NAr4xx (Figure 5.17), upon recrystallization, may be due to the formation of complex single crystals. A qualitative assessment of the XRD images shows a striking similarity to those reported for incommensurate structures.[9] The study of complex crystal structures, such as incommensurate structures, is continually expanding and if these patterns do indeed belong to such structures, it may be an area that could be investigated further with this system. Single crystal diffraction would also provide more insight into these structures. Growing good quality single crystals at high pressure is, however, a genuine challenge to experimentalists.

In this work, phases of the N_2-Ar binary system have been identified and defined using Raman spectroscopy as well as XRD. Both methods complement each other well and enable a better refinement of boundaries in the phase diagram. With this contribution, the previously unexplored phase diagram of the N_2-Ar system above 10 GPa (and 15 GPa for x = 0.10) has been extended up to ~24 GPa for mixtures with $x < 0.25$ and $0.60<x<0.80$. Based on the experimental results presented in this thesis, an updated phase diagram for the N_2-Ar binary system is presented. Figure 7.1 illustrates the proposed updated phase diagram in comparison with that reported in literature. In addition to the extension to higher pressures, phase lines have been refined. This was only possible by combining Raman spectroscopic and XRD results, a contribution from this study.

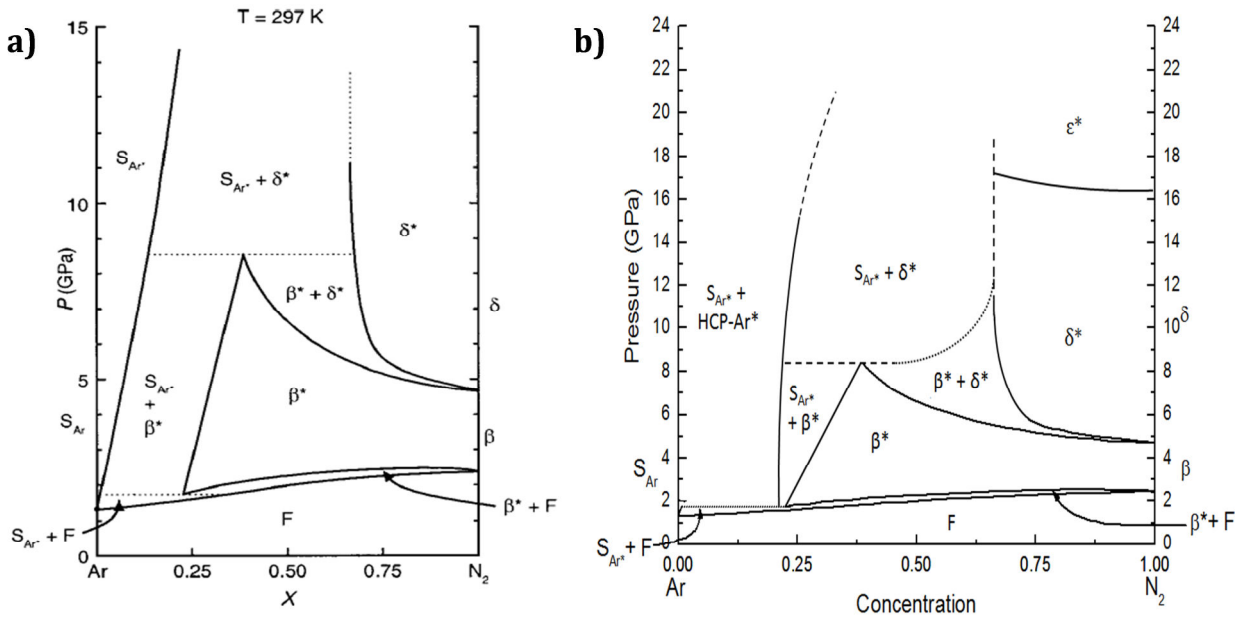

Figure 7.1: Proposed updated pressure-concentration phase diagram for the N_2-Ar binary system at room temperature by **(a)** Lotz *et al.*[1] and **(b)** from this work. (*a) Reprinted with permission from the American Physical Society, Copyright 2001.*

The N_2-Ar and N_2-Kr binary phase diagrams would benefit from the study of additional concentrations and pressures. Further refinement on the N_2-Ar phase diagram could include a search for the stability limits of the structures observed in this work and possibly discovering novel compounds in the process. In this work, there are mixtures and pressures, between $0.25<x<0.60$ and above 24 GPa, respectively, that remain uninvestigated due to time and technical constraints. Higher pressures for some samples in this work were not obtained due to the limitations of the diamond anvil cell utilized and also due to the type of gasket used. Thus, experimentally, going to higher pressures will present technical challenges. High pressure results in a reduction of the compression chamber and, consequently, the observed intensities for XRD and Raman spectroscopy will be reduced due to a smaller sample volume. A stronger metal for the gasket material should reduce the distortion and translation of the compression chamber, however, gasket failure did occur due to a less-than ideal wall cavity smoothness resulting from the laser drilling process. Furthermore, better sample preparation with pre-mixed gases (at controlled concentrations) would

certainly help. The concentration determination method utilized in this work could also see improvement. For instance, other proposed methods for concentration determination include calibration of the boiling temperature of the liquid mixture and the use of mass spectrometry to measure the relative abundance of the components. Some of the samples were measured with a different Raman spectroscopy set-up located at the Canadian Light Source (excitation light at 532 nm) while most samples were measured at the Laboratoire de physique des solides denses (excitation light at 488 nm). Improvements could be made by using the same apparatus for all measurements.

In this work, the introduction of small dopants (Ar and Kr) to pure N_2 was explored to see if they might act as stabilizers or catalysts to high-density phases of N_2. This idea could lead to new compounds or structures for the system at very high pressures. A great effort is currently underway to recover single-bonded nitrogen at ambient conditions, due to its potential as an energetic material. This avenue should be pursed.

With the exception of the "odd" behaviour observed with the EOS for N_2-Ar mixtures with $x = 0.65$ and 0.75, which requires verification, neither vdW compounds nor networks of single bonded nitrogen were observed in this work. Perhaps much higher pressures ($P > 24$ GPa) or even higher temperatures ($T > 300$ K) may facilitate the transformations required for such compounds. The search for compounds and polymeric networks can be challenging and it is still a relatively new area of research, with many components and methods that have yet to be investigated theoretically and experimentally.

References

1. Lotz, H. & Schouten, J. Phase behavior of the N2-Ar system at high pressures: A Raman spectroscopy study. *Phys. Rev. B* **64,** 1–6 (2001).

2. Lotz, H. & Schouten, J. Vibrational line broadening in the mixed solid N2–Kr: A high-pressure Raman study of the phase diagram. *Phys. Rev. B* **64,** 1–8 (2001).

3. Kooi, M. & Schouten, J. High-pressure Raman investigation of mutual solubility and compound formation in Xe-N2 and Ne-N2. *Phys. Rev. B* **60,** 12635–12643 (1999).

4. Vos, W. L. *et al.* A high-pressure van der Waals compound in solid nitrogen-helium mixtures. *Nature* **358,** 46–48 (1992).

5. Kooi, E. & Schouten, J. Influence of Argon on the Phase Behavior and Vibrational Properties of Solid Nitrogen at High Pressure. *J. Low Temp. Phys.* **111,** 349–355 (1998).

6. Kooi, M. E. & Schouten, J. A. Raman spectra and phase behavior of the mixed solid N2 -Ar at high pressure. *J. Low Temp. Phys.* **57,** 407–413 (1998).

7. Crystal Impact. Diamond: Crystal and Molecular Structure Visualization. (2016). at <http://www.crystalimpact.com/diamond/Default.htm>

8. CCP14, Laugier, J. & Bochu, B. Basic Demonstration of Chekcell Graphical Powder Indexing Helper and Spacegroup Assignment Software on a Cubic Cell. (2016). at <http://www.ccp14.ac.uk/tutorial/lmgp/chekcell.htm>

9. McMahon, M. I., Loa, I., Stinton, G. W. & Lundegaard, L. F. Determining complex crystal structures from high pressure single-crystal diffraction data collected on synchrotron sources. *High Press. Res.* **33,** 485–500 (2013).

Appendix A
Copyright Permissions

Figure No:	Reference	Licence No.
2.3	Eremets [2004]	3735381090163
2.4	Tomasino [2014]	3735390211773
2.5	Tomasino [2014]	3735390456039
2.6	Yakub [2015]	3735401117124
2.8	Kooi [1998]	3734970645344
2.9, 2.10, 7.1	Lotz [2001]	3735390866203
2.11, 2.13	Lotz [2001]	3735391069435
2.12	Lotz [2001]	3735391260326
2.14	Gregoryanz [2007]	3735401335664
2.21	Scheerboom [1993]	3735410153055
2.25	Westerhoff [1996]	3738270157499
4.3	Schneider [1992]	3767801067379